UNIVERSITÀ
DEGLI STUDI
DI PADOVA

Università degli Studi di Padova
Dipartimento di Ingegneria Civile, Edile e Ambientale

Scuola di dottorato in Scienze dell'Ingegneria Civile ed Ambientale
Ciclo XXVI

PIPING DETECTION IN DIKE FOUNDATIONS BY DISTRIBUTED TEMPERATURE SENSING

UNDERSTANDING THE DEVELOPMENT OF THERMAL ANOMALIES

INDIVIDUAZIONE DEL SIFONAMENTO NELLE FONDAZIONI ARGINALI MEDIANTE MISURE DISTRIBUITE DI TEMPERATURA

COMPRENDERE LO SVILUPPO DELLE ANOMALIE TERMICHE

Direttore della Scuola: Ch.mo Prof. STEFANO LANZONI

Supervisore: Ch.mo Prof. PAOLO SIMONINI

Co-supervisore: Dr. ANDRÉ R. KOELEWIJN

Dottorando: SILVIA BERSAN

Luglio 2015

Sommario

L'erosione interna è causa di una percentuale significativa di danni riguardanti le opere di ritenuta idraulica. Nella maggior parte dei casi tuttavia l'identificazione precoce del fenomeno permette di evitare incidenti drammatici. Sviluppare tecniche di monitoraggio in grado di individuare l'erosione interna in atto con sufficiente anticipo rappresenta pertanto un passo significativo verso una maggiore sicurezza idraulica.

Questo lavoro indaga l'efficacia della misure distribuite di temperatura per l'individuazione precoce dell'erosione interna negli argini fluviali e costieri. La ricerca si concentra sugli argini suscettibili a sifonamento, intesa come l'erosione retrogressiva che interessa lo strato di fondazione di strutture poggianti su terreni sabbiosi.

Vengono presentate e discusse le misure realizzate in un esperimento di sifonamento a grande scala. Il test ha permesso l'identificazione dei principali fattori che influenzano l'insorgenza delle anomalie termiche nelle regioni affette da sifonamento.

Successivamente, l'effetto dei suddetti fattori è stato studiato quantitativamente con l'ausilio della modellazione agli elementi finiti e dell'analisi dimensionale. È emerso che l'individuazione precoce del sifonamento si non può basare esclusivamente sulla propagazione di un fronte termico (caldo o freddo a seconda della stagione) che si muove dal fiume verso campagna con velocità differente nelle zone integre ed erose. Infatti, in funzione della permeabilità e spessore dello strato sabbioso e della dimensione del rilevato, la durata della piena può non essere sufficiente affinché il fronte raggiunga un sifone non ancora pienamente sviluppato. Tuttavia si può sfruttare un meccanismo alternativo: l'effetto della velocità del flusso idraulico sul gradiente verticale naturale. Poiché tale gradiente diminuisce con la temperatura, l'efficacia di questo meccanismo dipende dalla profondità a cui il sifonamento si manifesta.

La tesi contiene anche acuni consigli per una modellazione numerica efficiente del problema di avvezione-diffusione in terreni permeabili, sia integri che affetti da sifonamento.

Infine la tesi descrive un apparato sperimentale sviluppato per studiare in piccola scala la distribuzione di temperatura nei dintorni di un sifone. Il modello incorpora un sensore distribuito in fibra ottica con risoluzione spaziale sub-centimetrica. Tale risoluzione è stata ottenuta adottando una tecnica di misura innovativa basata sull'analisi della componente di Rayleigh nel dominio delle frequenze. I risultati preliminari mostrano l'influenza sulle misure della contemporanea sensibilità del sensore a temperatura e deformazione e come questo problema è stato parzialmente risolto.

Abstract

Internal erosion is the cause of a significant percentage of damages involving water-retaining structures all over the world. In most cases, however, early detection of the phenomenon allows avoiding dramatic accidents. Developing monitoring techniques capable of detecting ongoing internal erosion with sufficient advance represents therefore a significant step towards a higher level of flood safety.

Temperature measurements performed in embankment dams have been proven to be effective in identifying leakages consequent to internal erosion. This work investigates the effectiveness of distributed fibre-optic temperature sensing for the early detection of internal erosion in river and sea dikes. The attention is focused on dikes prone to backward erosion piping, a mechanism that affects the foundation layer of structures resting on sandy soils.

The measurements performed in a large-scale piping test are presented and discussed. The test enabled the recognition of the main factors that influence the onset of thermal anomalies in regions affected by piping.

Subsequently, the effect of the above-mentioned factors was quantitatively studied with the aid of finite element modelling and dimensional analysis. It was discovered that early detection of piping cannot completely rely on the propagation of a thermal front (hot or cold depending on the season) that moves from the waterside to the landside with different speed in intact and eroded regions. Indeed, depending on the permeability and thickness of the sandy layer and on the size of the embankment, the duration of the flood event might not be sufficient for the front to reach a pipe not yet fully developed. However, another mechanism is exploitable for detection: the effect of the flow velocity on the natural vertical temperature gradient. Since this gradient decreases with depth, the effectiveness of this mechanism depends on the depth at which piping occurs.

The thesis also contains some tips for an effective numerical modelling of the advection-diffusion equation in permeable soils, both intact and affected by piping.

Finally, the thesis describes a small-scale setup that was developed to investigate the temperature distribution in the surroundings of a pipe. The model incorporates a distributed fibre-optic sensor with a sub-centimetre spatial resolution. Such resolution was achieved adopting a novel sensing technology, in which the spectral shift of the Rayleigh backscatter is measured using optical frequency-domain reflectometry. Preliminary results show how the cross-sensitivity of the sensor to temperature and strain influenced the measurements and how this was partially overcome.

Acknowledgements

PhD was a hard proof for me. I felt supported and at the same time alone, not understood and incapable. It was only writing these acknowledgements that I realized how many people took part in this adventure.

The most important role in a PhD, but also the most controversial, is played by the supervisor. The relationship between student and supervisor is rarely easy. I initially felt frustrated as I did not get the kind of support I was expecting, but year after year I realized I was learning from my supervisor many important things that cannot be found in books. After four years I must admit I had much more support than could be expected. Prof. Paolo Simonini, thanks for keeping believing in me despite the difficulties that made this path long and tortuous.

I am very glad I had the opportunity to have Dr. André Koelewijn as co-supervisor, a personality and engineering mind with no equals. I would like to express my very great appreciation to all the people at Deltares (the Netherlands) that dedicated part of their time to share their knowledge and that made me feel part of a group. I am also thankful to prof. Cristina Jommi from TU Delft for the fruitful discussions and to prof. Adam Bezuijen and Kristine Vandenboer from Ghent University for sharing their experience.

Cooperation with prof. Luca Palmieri (Photonics and Electromagnetics group) and Dr. Luca Schenato (CNR-IRPI) has been instructive and enjoyable. Their being passionate, curious, thorough as well as cheerful and patient was greatly appreciated.

I want to express my gratitude to prof. Mario Putti, department of Mathematics, for his help with the numerical modelling and his faith in the potentialities of this work.

I am also grateful to the foundation Cariparo that partially financed the research and to Dr. Alessandro Pasuto (CNR-IRPI) to whom I must recognize the merit of suggesting a very exciting and challenging research topic.

Personal acknowledgements go to the colleagues of the geotechnical group in Padova, that shared everyday coffees, technical issues and general complaints with great spontaneity. Special thanks go to prof. Simonetta Cola for being always present and supportive.

The colleague and friend Alberto Dacome also deserves a place in this list: he was for me a precious link between the academy and the territory.

I would like to extend my thanks to the friends in my home town and those spread around Europe that kept being my friends even when I was too busy or thoughtful to dedicate my time to let our friendship grow.

Finally, I must acknowledge the people that provided the most sincere and unconditioned support, my parents and sister and my boyfriend Michele. They have been the most affected by my worries and bad mood in these years and yet forgave me and did their best to cheer me up and make me feel beloved and understood.

Table of Contents

List of Figures

List of Tables

Abbreviations

CPTu	Cone Penetration Test with pore pressure (u) measurement
DFOS	Distributed Fibre Optic Sensor
DTS	Distributed Temperature Sensing
EM	Electromagnetic Methods
ERT	Electrical Resistivity Tomography
FBG	Fibre Bragg Grating
FDEM	Frequency Domain Electromagnetic Methods
FE	Finite Elements
FOS	Fibre Optic Sensor
GPR	Ground Penetrating Radar
LiDAR	Light Detection And Ranging
OFDR	Optical Frequency Domain Reflectometry
OBR	Opticl Backscatter Reflectometer
OTDR	Optical Time Domain Reflectometry
SAR	Synthetic Radar Aperture
SNR	Signal to Noise Ratio
SP	Self-Potential
SVD	Singular Value Decomposition

Physical Constants

Speed of light	c	$=$	$2.997\ 924\ 58 \cdot 10^{8}$ m s^{-1}
Plank's constant	h	$=$	$6.62606957 \cdot 10^{-34}$ m^{2} kg s^{-1}
Boltzmann's constant	k	$=$	$1.3806488 \cdot 10^{-23}$ m^{2} kg s^{-2} K^{-1}

Symbols

erfc	complementary error function	
∇	gradient operator	
$\nabla\cdot$	divergence operator	
∇^2	Laplace operator	
δ_{ij}	Kronecker delta	
α	coefficient of thermal expansion	m m^{-1} K^{-1}
α_L	longitudinal dispersivity	m
α_T	transverse dispersivity	m
β	pipe friction factor	-
γ	coefficient of cubical expansion	-
δ	thickness of intermediate layer	m
ε	soil porosity	-
ε	strain	-
θ	dimensionless temperature	-
θ'	dimensionless horizontal temperature	-
κ	permeability	m^2
κ^*	pipe fictitious permeability	m^2
λ	thermal conductivity of the porous medium	W m^{-1}K^{-1}
Λ	geometry scale factor	-
λ_o	thermal conductivity of minerals other than quartz	W m^{-1}K^{-1}
λ_q	thermal conductivity of quartz	W m^{-1}K^{-1}
λ_s	thermal conductivity of solid	W m^{-1}K^{-1}
λ_w	thermal conductivity of fluid (water)	W m^{-1}K^{-1}
μ	dynamic viscosity of the seepage fluid	Pa s

μ'	Brinkman effective viscosity	Pa s
ν	kinematic viscosity	$m^2\ s^{-1}$
ν	optical frequency	s^{-1}
ν_B	optical frequency of the Brillouin component	s^{-1}
ξ	tracer concentration	$kg\ m^{-3}$
ξ_0	tracer concentration at inflow	$kg\ m^{-3}$
ρ	volumetric mass density of the seepage fluid	$kg\ m^{-3}$
ρ_{dry}	bulk density of dry soil	$kg\ m^{-3}$
ρ_s	volumetric mass density of solid	$kg\ m^{-3}$
ρ_{sat}	bulk density of saturated soil	$kg\ m^{-3}$
σ'_y	yield stress	kPa
σ_v	total vertical stress	kPa
σ'_{v0}	effective overburden stress	kPa
τ	time scale of interest	s
τ_{res}	residence time of water	s
φ	total hydraulic head	m
X_f	fluid coefficient of compressibility	Pa^{-1}
X_m	soil coefficient of compressibility	Pa^{-1}
a	thermal diffusivity	$m^2\ s^{-1}$
A	aquifer aspect ratio	-
A_0	amplitude of annual temperature fluctuations	℃
A_p	pipe cross−section area	m^2
b	pipe thickness (for a rectangular cross-section)	m
c_f	specific heat capacity of fluid	$J\ Kg^{-1}K^{-1}$
c_s	specific heat capacity of solid	$J\ Kg^{-1}K^{-1}$
C	volumetric heat capacity of the porous medium	$J\ m^{-3}K^{-1}$
C_a	volumetric heat capacity of air	$J\ m^{-3}K^{-1}$
C_{creep}	percolation factor	-
C_s	volumetric heat capacity of solid	$J\ m^{-3}K^{-1}$
C_w	volumetric heat capacity of fluid (water)	$J\ m^{-3}K^{-1}$
d	damping depth of annual temperature fluctuations	m
d_c	thickness of clogged layer	m

D	aquifer thickness	m
D	computational domain	-
∂D	boundary of the computational domain	-
d_i	largest particle size in the smallest i% of particles	mm (μm)
D'	coefficient of hydrodinamic dispersion	$m^2\ s^{-1}$
D_h	pipe hydraulic diameter	m
D_H	aquifer thickness (when smaller than the thickness of the computational domain)	m
h	grid size	m
H	hydraulic head over a water retaining structure	m
H_c	critical hydraulic head for piping	m
i_c	heave critical gradient	-
I_a	intensity of the Raman Anti-Stokes component	W
I_s	intensity of the Raman Stokes component	W
K	hydraulic conductivity	Pa^{-1}
K_e	Kersten number	-
l	length of the pipe	m
l^*	characteristic length	m
L	horizontal length of seepage domain and/or seepage length	m
L_p	pipe length	m
n	refractive index of the optical fibre	-
p	pore fluid pressure	Pa
P	pipe wetted perimeter	m
Pe	Péclet number	-
Pe_g	geothermal Péclet number	-
Pe_h	element Péclet number	-
Q	mass source (or sink)	$kg\ m^{-3}\ s^{-1}$
Q_{disp}	energy flux due to dispersion	$J\ m^{-2}\ s^{-1}$
q_H	average horizontal flow	$m\ s^{-1}$
Q_H	total horizontal flow	$m^2\ s^{-1}$
q_V	average vertical flow	$m\ s^{-1}$
Q_V	total vertical flow	$m^2\ s^{-1}$
Re	Reynolds number	-

$S_{0\varphi}$	specifc volumetric storativity related to potential changes	m^{-1}
S_{0p}	specifc volumetric storativity related to pressure changes	Pa^{-1}
S_r	relative saturation	-
t	time	s
T	temperature	℃
t_0	time of occurrence of minimum annual temperature	days
T_a	annual average soil temperature	℃
T_i	temperature at inflow	℃
T_o	temperature at outflow	℃
T_B	temperature at bottom of the domain	℃
T_T	temperature at top of the domain	℃
T_w	temperature of the reservoir water	℃
$\mathbf{u}$	$= (u, v, w)$ Darcy velocity or specific discharge	m s^{-1}
Δu	excess pore water pressure	kPa
$\overline{U}$	average velocity in pipe cross-section	m s^{-1}
$\mathbf{U}$	=(U,V,W) dimensionless Darcy velocity	m s^{-1}
U_b	bulk volume of a reference porous medium element	m^3
$\mathbf{v}_\varepsilon$	pore velocity of fluid	m s^{-1}
$\mathbf{v}_T$	$= (u_T, v_T, w_T)$ advective thermal velocity	m s^{-1}
w_p	pipe width (for a rectangular cross-section)	m
(x, y, z)	space variables	m
(X, Y, Z)	dimensionless space variables	-

Chapter 1

Introduction

1.1 Why monitoring dikes?

The demand for protection from floods has drastically increased in the last decades due to the increasing value of the riparian and coastal areas. The latter indeed, because of the uncontrolled urbanization, include nowadays crowded industrial and residential districts. Flood protection is mainly entrusted to river and sea dikes. Their failure, intended as the unintentional inundation of the area they are meant to protect, can occur: (1) without prior damage to the elements of the dike system or (2) by a breach in the dike system that results from damages affecting at least one of the elements of the system. CIRIA et al. (2013) define the first case as *hydraulic failure* and the second one as *structural failure*. Hydraulic and structural failure are not necessarily unrelated as one can lead to the other: the most common example is the failure by external erosion consequent to overtopping. Hydraulic failure is much more frequent than structural failure, but the latter can be more dangerous, since the damage caused by a breach is larger than that caused by overtopping in terms of size of the flooded area and impact on it. Among the mechanisms of structural failure, internal erosion is very frequent in France (Fry et al., 2012), Germany (Horlacher et al., 2007), the Netherlands (Vrijling, 2010), Italy (Simeoni et al., 2008; Squeglia et al., 2013; D'Alpaos et al., 2014) and, more specifically, in the district of Padova (§ **??**).

Several criteria are available to assess the risk of internal erosion, but the improvement of all the existing dikes not complying with the rules is highly demanding. Moreover, since some rules are still under revision, in some cases the uncertainty on the

safety level can be high. Monitoring systems that make use of advanced technologies can increase the safety level of not complying structures. Of course the increase in safety level they provide is not comparable with that offered by a properly designed and built structural intervention, but also the costs are not comparable, even if the long term costs connected with the management of a monitoring system are considered.

1.2 Early detection of internal erosion

Early detection of internal erosion has received considerable attention in the past and keep receiving it given the importance of this failure mechanisms for dam safety. Statistics claim (Foster et al., 2000) that internal erosion is indeed responsible for about 50% of failures of embankment dams. A number of geophysical methods have been developed for early detection of internal erosion in embankment dams, among which the thermometric method. It dates back to the late 1980s; back then temperature measurements were performed in standpipes by means of thermocouples.

The basic principle of the thermometric method is that heat transfer in soils generally occurs by conduction, but when the pore water flows at significant velocity, as occurring in regions affected by internal erosion, the heat transferred by *advection*, i.e. by the moving fluid, becomes predominant over the heat transferred by conduction. An increase in seepage velocity can therefore cause a variation of the temperature field in the soil.

A big impulse to the diffusion of the thermometric method was given by the availability on the market of distributed fibre-optic sensors that made possible to perform spatially continuous measurements by deploying hundreds of metres of optical cable along the embankment. To date leakage detection in embankment dams by means of distributed fibre-optic temperature sensors is state of the art, as testified by the numerous installations worldwide.

For what concerns river and sea dikes the first installation of a distributed temperature sensor was made in France by EDF (Albalat and Garnero, 1995; Fry, 1997, as cited in Johansson and Sjödahl, 2004). Since then several installations were made in France along intake channels but, to the author knowledge, a single installation was made so far along a river: the Rhine river in Germany (Pyayt et al., 2014).

1.3 Thesis objective and research approach

This work investigates the effectiveness of temperature measurements for the early detection of internal erosion in dikes. The attention is focused on dikes prone to *backward erosion piping*, a mechanism that affects water retaining structures founded on a sandy layer and consists in the formation of small channels at the interface between the sandy layer and the impervious base of the dike (or other impervious soil between the dike and the sandy layer).

Great care should be taken in transferring to dike monitoring the experience gained in decades of temperature monitoring in embankment dams. The reason is that dikes present a few differences respect to dams that might have an influence on the temperature distribution that occurs in the embankment - and foundation soil - as the result of the interaction between soil, atmosphere and the water body that is retained. These differences are (1) the size and (2) the duration of the hydraulic loads. The large size of many dams results in a large part of the embankment being unaffected by the annual temperature variation. Moreover, significant, nearly constant hydraulic loads persist for long time on dams, so that previous research (Claesson et al., 2001) reasonably treated the problem as a stationary one, with the embankment subject to a constant hydraulic load and a cyclic thermal load. On the contrary, in river and sea dikes significant hydraulic loads persist from 12 hours to a few days, so that considering transient hydraulic loads seems to be more appropriate and could reveal new aspects of the problem.

It should be also considered that in most cases the distributed optical sensors would be installed in existing structures, limiting the possibilities for what concerns the position of the sensor. In existing embankments optical fibres can be easily deployed at the toe and less easily underneath the slope surface, but installation inside or below the embankment is invasive and very expensive.

Recent research concerning the monitoring of canal dikes in France has mainly focused on data interpretation techniques. Some of them are fully statistical (Khan et al., 2008a,b; Khan et al., 2010), others also have a physical base (Radzicki and Bonelli, 2010b).

In this work the problem is approached from a different perspective, partly as a consequence of the geotechnical background of the author and partly because a large amount of field data was not available for analysis.

The onset of temperature variations in permeable foundation layers affected by

seepage anomalies and, more specifically, by backward erosion piping, is called into question. Through the study of heat transfer in permeable dike foundations it is explained how and under what conditions the above-mentioned thermal anomalies can arise.

1.4 Relevance of internal erosion in the Padova district

During the last six years, three dike breaches occurred along the main rivers flowing through the Padova district: Muson dei Sassi River at Loreggia, Frassine River at Saletto and Bacchiglione River at Ponte San Nicolò. They have been all ascribed to internal erosion: the first two were ascribed to erosion triggered by nutria burrows within the dike body, the latter is likely to be due to erosion at the contact between the dike and an old culvert.

Although animal burrows can have an effect on river embankments, it seems that lately too often they are fingered as the prime cause of failure when the true causes are unknown. There is evidence that the breach along the Frassine River could also have been triggered by backward erosion piping. I fact, during the flood events following the reconstruction of the dike, sand boils appeared close to the landside toe, indicating that there is a high piping potential at that location.

The dikes of the Frassine and Gorzone River, in the southern area of the Padova district, suffer from heavy underseepage which manifests with stagnant water and softening of the soil at the landside. *Sand boils* as the one depicted in Fig. 1.1a appear frequently during significant flood events, often at the same locations. Failure is avoided by the intervention of the Civil Protection that stops or slows down the erosion process by building sandbag rings around the sand boils (Fig. 1.1b).

Local experience confirms that, as observed in other countries, sand boils can appear far from the dike toe (more than 50 m) and inside draining ditches. The example depicted in Fig. 1.2 shows that even sand boils occurring at the dike toe might be difficult to detect since they can be masked by heavy underseepage. In the case depicted in the figure, a sand boil had been detected close to the toe before the seepage water submerged it.

1.5 Brief outline of the thesis

The thesis contains an extended literature review (Chapter 2 to 5) in which the information for understanding the problem and the tools to answer the research question has been gathered, organised and re-elaborated. Such extension of the literature review partly stems from the multidisciplinarity of the research topic.

The order of the chapters coming after does not follow the logical sequence usually adopted in experimental studies. The description of a large-scale test (Chapter 6) and the analysis of its outcomes (Chapter 7) precede the description a of a small-scale facility realized in the lab (Chapter 8). This order reflects the chronological sequence of the activities. The author, in fact, participated in a large-scale failure test that took place before the small-scale modelling could be undertaken and that was designed and run by engineers familiar with the physical modelling of dike failure mechanisms.

(a)

(b)

FIGURE 1.1: Sand boil and sandbag ring along the Gorzone river at Vighizzolo d'Este, February 2014 (courtesy of Alberto Dacome)

FIGURE 1.2: Heavy underseepage occurring at Vescovana, along the Gorzone river, in February 2014

Chapter 2

Internal erosion

Internal erosion occurs when soil particles are removed from their position and transported by seepage flow within an embankment or its foundation.

Foster et al. (2000) analysed the statistics of failures of large dams constructed between 1800 and 1986 and found that internal erosion was responsible for about half of embankment dam failures where the mode of failure is known. It is approximately equal in importance to failures by overtopping due to inadequate spillway capacity or malfunction of gates and other outlets. By comparison embankment slides and failures due to earthquakes account for only 4% and 1.7% of embankment dam failures in operation respectively. The statistics of embankment dam incidents show that internal erosion is also a significant cause of incidents, including new or increased seepage and leakage, sinkholes and accelerating settlements of the dam.

Given the threat that internal erosion poses to dam safety, a large amount of research has been conducted in the last decades to clarify this phenomenon and learn how to prevent it. The research focused on:

- clarification of the mechanisms that can result in dam failure by internal erosion;
- definition of criteria to predict soil erodibility;
- prediction of time between initiation of erosion and failure;
- definition of design rules to prevent internal erosion (filter rules);
- design of products to prevent internal erosion (geotextile filters);
- techniques for detection of ongoing internal erosion.

This chapter provides a brief description of the multiple erosion mechanisms. Then it focuses on the erosion mechanism addressed by this work: backward erosion piping. The literature review on backward erosion piping is a selection - despite being quite broad - of the aspects that play a role in the way the areas affected by erosion influence the seepage flow velocity and, in turn, the temperature field in the dike. Those aspects include for example the geometry of the eroded volumes and the configuration of the exit point of the seepage flow. For sake of completeness, a brief review of the methods for assessing the likelihood of backward erosion piping is also given.

2.1 Classification of soils susceptible to erosion

The first condition for internal erosion to occur is particle detachment. Seeping water must provide sufficient energy to detach particles from the soil structure. The nature of the soil in the dam determines its vulnerability to erosion. Three classes of soils have to be distinguished, based on their susceptibility to erosion and their capability to hold a roof.

Non plastic (cohesionless) soils, such as silts, sands and gravels, are relatively easily eroded. These may collapse and will not sustain a crack when saturated under flooding.

Plastic soils, such as clays, clayey sands, and clayey sandy gravels are generally more resistant to erosion than cohesionless soils. Clay soils will hold a crack even when saturated.

Dispersive soils are plastic (clay) soils in which the chemistry of the seeping water causes dispersion (de-flocculation) of the clay flocs, breaking them down into smaller, easily eroded, particles.

2.2 Erosion mechanisms

Initiation of erosion follows four mechanisms.

Concentrated leak erosion. Where there is an opening through which concentrated leakage occurs, the sides of the opening may be eroded by the leaking water. Such concentrated leaks may occur through cracks caused by differential settlement, desiccation or frost. Concentrated leaks may also occur around conduits or other through-penetrating structures. Here cracks are caused by hydraulic fracture due to low stresses or collapse settlements in poorly compacted material. Moreover, concentrated leaks can

occur due to the action of animals burrowing into dikes and small dams and tree roots rotting and forming holes. Concentrated leaks can only occur in soils that are able to sustain a crack, as plastic soils, or unsaturated silt, silty sand or silty sandy gravel.

Contact erosion. It occurs where a coarse soil such as a gravel is in contact with a fine soil and flow parallel to the contact in the coarse soil erodes the fine soil. Contact erosion initiates when the velocity of flow in the coarse soil is sufficient to initiate erosion of the fine soil, placed either above or below the coarse soil. For example, flow through gravel alluvium in the foundations of a dam or dike may erode the base of an overlying silt layer. Contact erosion can occur in both plastic and non plastic soils.

Suffusion. It occurs when the small particles are transported by the seepage flow through the pores of the coarser particles, within the same soil. The coarser particles are not transported and the effective stresses are largely transferred through the matrix of the coarser particles. Suffusion results in an increase in permeability, greater seepage velocities, and potentially higher hydraulic gradients, possibly accelerating the rate of suffusion. Suffusion occurring within an embankment core or the foundation of a dam may also lead to some settlement of the embankment. Suffusion cannot occur in plastic soils under the gradients normally experienced in dams and their foundations.

Backward erosion. Backward erosion can only occur in non-plastic plastic soils under the gradients normally experienced in dams and their foundations. There are two kinds of backward erosion:

- *Global backward erosion* occurs in narrow or even reasonably wide sloping or partially sloping core dams if they are not properly protected by filters or a transition zone. Particles are detached at the downstream surface of the core; the progression of erosion leads to development of a near-vertical pipe in the core of the embankment. The process is assisted by gravity, and there is no need for a cohesive soil layer to form the roof for the pipe.

- *Backward erosion piping* consists in the formation of a thin pipe below a roof provided by a layer of cohesive soil or a rigid structure. The experience in the USA and Europe is that backward erosion piping mostly occurs in the foundations, as in Fig. 2.1, where the eroding soil is fine to medium grain size sand, with a uniformity coefficient $Cu < 3$. However, it can also affect the embankment. Here erosion can be promoted by heterogeneity, as illustrated in Fig. 2.3, or can occur under revetments as in Fig. 2.2. It initiates where critically high vertical hydraulic

gradients at the toe of a dam erode particles. Subsequently a pipe grows towards upstream due to the progressive erosion of its back end and to the transport of the eroded particles towards downstream.

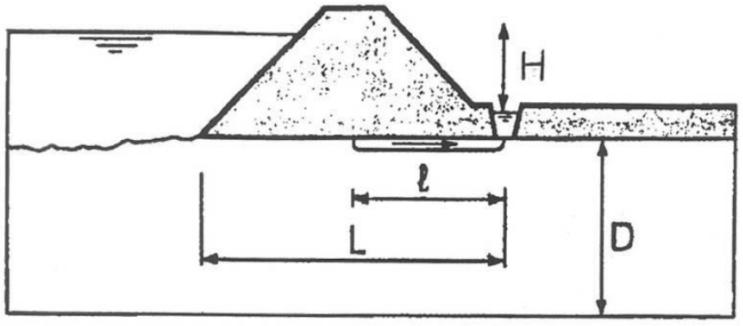

FIGURE 2.1: Backward erosion piping in a dike foundation (ICOLD, 2015)

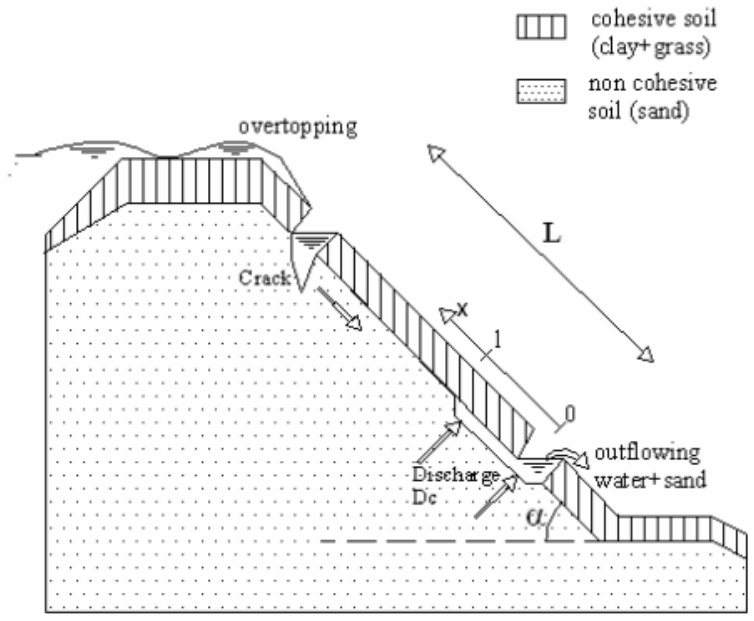

FIGURE 2.2: Piping under the cover layer of the inner slope following dike overtopping (Galiana, 2005)

Once initiated erosion will continue unless (1) the eroding forces are reduced or (2) the passage of the eroded particles is impeded in some way.

For concentrated leak erosion, the erosion leads to development of a pipe. For suffusion, some of the finer fraction is eroded leaving the coarse matrix of the soil behind. The permeability may be increased significantly and backward erosion piping might occur in the coarse matrix or the matrix may collapse. For contact erosion, the erosion of the finer soil into the coarser soil might lead to development of a pipe in the finer soil. In global backward erosion, sinkholes (vertical pipes) form. For backward erosion

the process extends upstream from the point of initiation, and a network of pipes forms beneath the soil or embankment providing the roof.

If the erosion processes are not arrested the dam/dike will eventually breach because of a gross enlargement of the pipe, overtopping due to settlement of the crest or instability/liquefaction of the downstream slope.

This work focuses on backward erosion piping. Backward erosion piping can be an issue wherever a layer of uniform sand is present at the ground level or few meters below the ground level. Backward erosion piping strongly affects river dikes in the Venetian plain (see § 1.4) as well as the Netherlands (Vrijling, 2010), Hungary (Imre et al., 2015), China and USA (Cao, 1994; Mansur et al., 2000, as cited in Van Beek et al., 2014a).

Since in most cases internal erosion leads to the formation of one or more pipes, the term *piping* is sometimes used generically to indicate internal erosion; often piping refers to concentrated erosion. In this work the term "piping" will be used with reference to backward erosion piping, while "internal erosion" will be used as a general term including all the specific mechanisms.

2.2.1 Erosion starting at the river side

In most cases internal erosion is triggered by seepage flow going from the reservoir or river to the landside. In riverbanks (and sea banks) erosion can also be triggered at the riverside, due to the seepage flow directed towards the river. The mechanism is well described in Hagerty (1991). It is typical of natural banks, which are characterized by high heterogeneity, but its occurrence cannot be excluded in man-made river embankments.

Source of water for the erosion mechanism is often the stream itself. When the stream rises against the face of the bank, water enters the bank. Recharge will happen preferentially into those soil zones that have the highest hydraulic conductivity. Outflow will occur during the descending phase of the flood, when the head within the outflow zone exceeds the head in the stream. The source of water for piping may also be subsurface leakage from buried conduits or containment vessels.

Piping cavities form where there is an exit point at which water can leave the bank, dislodge surface particles and carry away the dislodged grains. Undercutting of soil strata above the eroded area can cause failures in those zones. The slabs or blocks of soil displaced during the failures will accumulate on the lower portions of the bank or shore, together with the soil removed by the piping/sapping directly. In order for

the erosion process to continue, the accumulated failure debris must be removed. The process is sketched in Fig. 2.3.

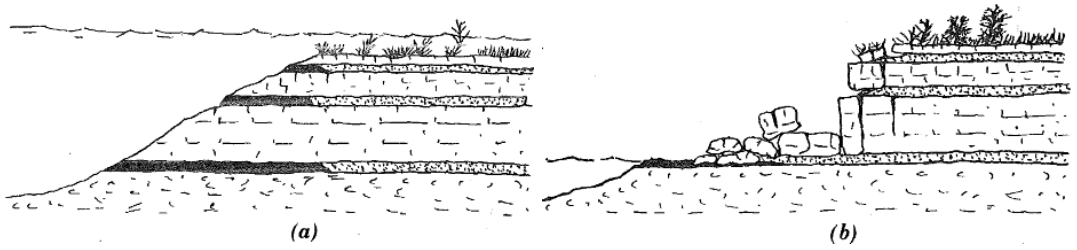

FIGURE 2.3: Bank subject to backward erosion: (a) inundation and recharge of the pervious zones; (b) backward erosion and collapse of undercut zones (Hagerty, 1991)

2.3 Backward erosion piping: experimental observations

This section aims at providing the reader with knowledge of the object to monitor: the erosion channels. Information on their geometry (shape, size and pattern) and the time required for their development are given in the following.

Since the 1980s many lab experiments have been conducted to clarify the mechanism of backward erosion. Experiments at different scales have been carried out at Delft Hydraulics / Delft Geotechnics Laboratories, today Deltares (De Wit et al., 1981; Weijers and Sellmeijer, 1993b). Large-scale experiments have been carried out at University of Florida (Pietrus, 1981; Townsend et al., 1988; Schmertmann, 1995, as cited in Schmertmann, 2000). In all these experiments the test sand is placed in a flume under water to ensure near-saturation and a transparent cover is placed over to simulate the presence of an impervious structure yet allowing the erosion process to be visible. Indeed, in this kind of set up the pipes always develop and propagate at the interface between the sand and the cover.

Experimental work has been also conducted in the 1980s in Germany (Müller-Kirchenbauer et al., 1993) and Japan (Kohno et al., 1987).

More recently, a big experimental program have been carried out at Deltares, including small-scale and medium-scale lab tests, large-scale field tests and centrifuge tests (Van Beek et al., 2010, 2011). Small-scale tests have also been performed at Gent University, Belgium, to investigate the 3D character of backward erosion piping (Vandenboer et al., 2014). A medium-scale facility has been built at the University of New South Wales, Sydney, Australia, with the aim of investigating piping in well graded

sands and gravels (Douglas et al., 2013). Richards and Reddy (2010) used a true triaxial apparatus to investigate the influence of effective stress conditions and angle of seepage path on the initiation of erosion in non-cohesive soils.

The experiments shows that backward erosion piping can be subdivided in three processes: initiation, progression and widening. Initiation concerns the onset of erosion in an intact sand layer, progression is the growth of a pipe in the upstream direction until the reservoir is reached and widening is the enlargement of the pipe occurring once upstream and downstream are in direct connection through the pipe.

2.3.1 Initiation

Initiation of internal erosion requires the existence of an unfiltered exit for the water flow. For what concerns dike foundations this occurs at the following locations.

1. If a low permeability layer (also referred to as impervious layer or blanket) is present downstream of the dike, the transport of sand particles can only occur
   (a) where the sand layer surfaces, often at the bottom of a ditch, or
   (b) where a crack cut through the blanket. It is likely that cracks arise in the blanket because of excessive underpressure: (i) where the blanket is thinner, for example at the bottom of a ditch, (ii) where flow lines converge close to the dike toe because of some seepage barrier, for example geomorfological features as clay-filled swales, or (iii) where the blanket is discontinuous, for example at the interface between soil and structures like wells and deep foundations.
2. If no blanket is present downstream of the dike, initiation of erosion generally occurs at the dike toe.

Different setups have been designed to reproduce the configurations that are found in the field (Fig. 2.4). The plane type exit reproduces case (2): no blanket downstream; the ditch type exit reproduces case (1a): surfacing of the sand layer; the circular exit reproduces case (1b): initiation in a crack; the slope type exit is not representative of a common situation in the field but it is often adopted in laboratory experiments because it is easier to construct.

When flow velocities sufficient to cause fluidization of sand are reached at some unfiltered exit point, a *sand boil* forms. If the fluid flow is sufficient to carry soil particles outside the fluidized zone, the particles deposit outside the sand boil centre creating a

small volcano. If erosion progresses backwards, the volcano grows in size. When the "plane" exit type (Fig. 2.4) is adopted, usually several discrete sand boils occur, not a smeared situation as could be imagined.

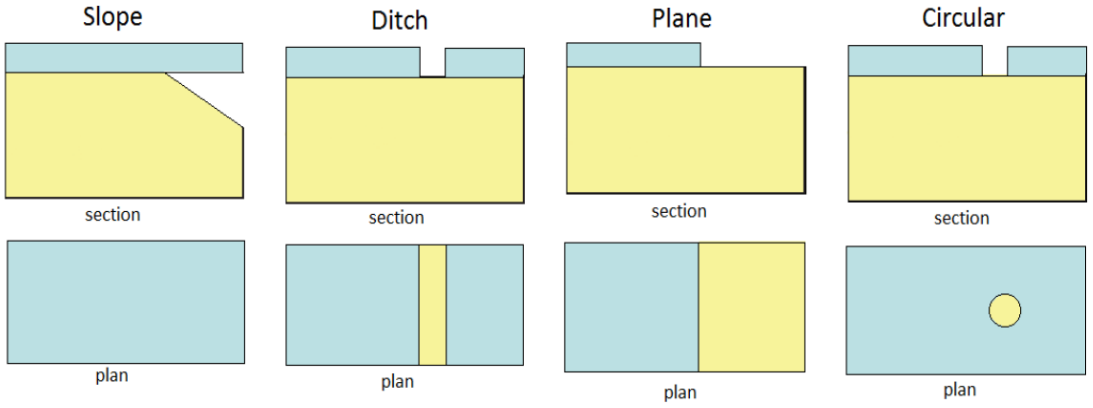

FIGURE 2.4: Different exit types adopted in experimental setups (Van Beek et al., 2013)

2.3.2 Progression

The tests are typically performed increasing the hydraulic head in small steps: a new step is undertaken only if no sand transport is occurring. Van Beek et al. (2014a) pointed out that the kind of progression of the pipe observed in the experiments can be classified in two groups.

- **Progressive erosion.** After initiation, sand transport stops and the hydraulic head need to be increased to allow the pipe to progress backwards. More steps are to be completed before the *critical head* is exceeded, i.e. the limit above which continuous erosion occurs.

- **Continuing erosion.** After initiation the pipe grows under constant hydraulic head since it reaches the upsteam side. The critical head coincides with the initiation head.

The exit type strongly influences the type of progression. For exit configurations that concentrates the flow lines more (hole type, ditch type), the head required for initiation is lower than the head required for continuous progression. Conversely, exit configurations that concentrates the flow lines less (plane type) require a higher head for initiation than for progression.

Details on the shape and size of the pipes are found in Müller-Kirchenbauer et al. (1993), Van Beek et al. (2011) and Vandenboer et al. (2014). In the progression phase,

pipes have an elongated cross-section. In small- and medium-scale tests, their thickness is a couple of millimetres and remains constant during progression. Their width at the *tip* (upstream end) of the pipe is pretty constant upon lengthening: it ranges from 5 to 10 mm in small- and medium-scale tests and a positive correlation exists with the average grain size. The pipes broaden toward the exit point (*tail*). The width at the tail increases significantly as a result of lengthening, due to erosion of the lateral walls of the pipe. Two-dimensional Sellmeijer's theory (§ 2.4) cannot describe the three-dimensional features of the process and therefore it only attributes the pipe growth to scour at the pipe bottom. Consequently the pipe elongates and deepens as erosion progresses, resulting in a channel which thickness increases towards downstream. The width of the pipe in small-scale experiments is in the order of one centimetre. Figure 2.5 illustrates the concept of pipe progression according to Müller-Kirchenbauer et al. (1993), based on the outcome of their small-scale experiments.

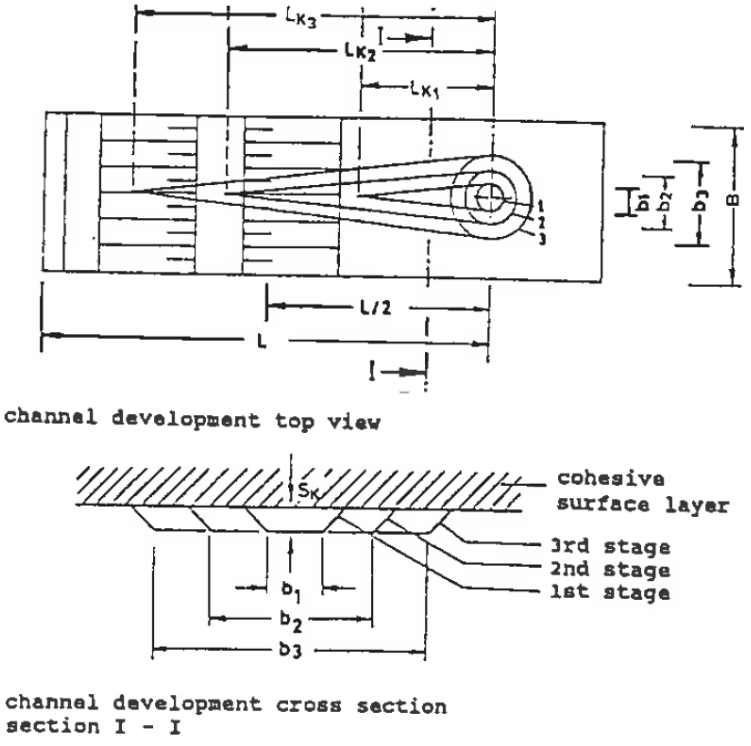

FIGURE 2.5: Principle of development of erosion channels according to Müller-Kirchenbauer et al. (1993)

In many experiments, meandering of the pipe is observed and the meandering character increases with increasing scale. Moreover, the pipe often branches so that in front of a single sand boil a network of pipes forms. The width of the network can increase with scale but the network does not extend indefinitely at the sides; rather, in

case of a ditch or plain type exit, more sand boils form along the exit line, (see examples in Fig. 2.6 and § 6.4.4).

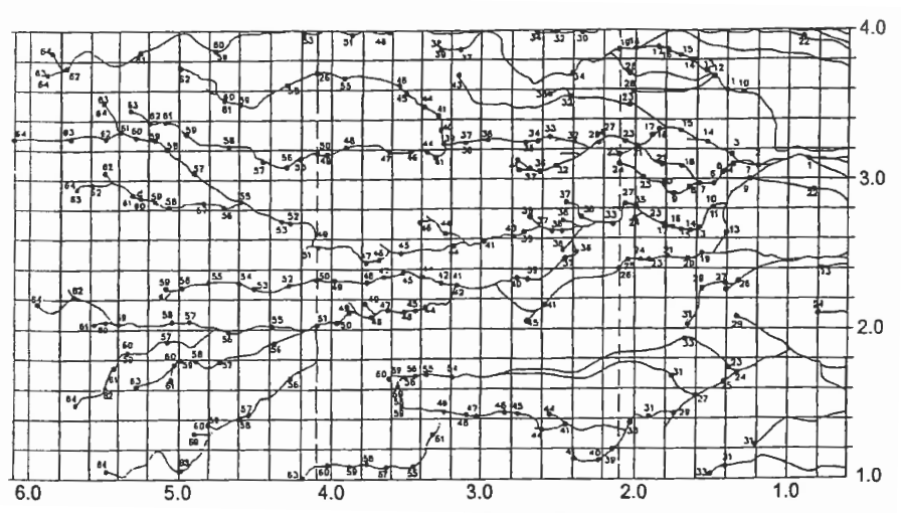

FIGURE 2.6: Delft Hydraulics flume test (seepage length=12 m, model width=5 m) showing branching of the pipes (Weijers and Sellmeijer, 1993b)

Sometimes a single broad channel forms in lab experiments, with a main stream migrating within the channel, as in braiding rivers (Fig. 2.7). The main stream deposits material at the inside of the bends and erodes in the outside. This results in a large channel with a cross-section of non-constant depth.

For what concerns the location of the piping channels, we have earlier said that they always form at the interface between the permeable, erodible layer and the above impervious layer. This is always true for uniform aquifers in absence of seepage barriers as cutoffs. The pattern is slightly more complicated for multilayer aquifers. When a gravelly, highly permeable layer underlies a sandy layer, some almost vertical piping channels grow towards the gravelly layer, following the main direction of the seepage flow. However these pipes stop when they reach the coarse, not erodible layer (Imre et al., 2015), while the horizontal pipes developed at the interface with the upper impervious layer can progress backwards up to failure, as sketched in Fig. 2.8.

2.3.3 Widening

As soon as the pipe makes contact with the upstream side, a pressure surge accompanies the flow through the pipe. This pressure surge in turn causes a large quantity of sand to be eroded. In the experiments described in Van Beek et al. (2011), during the widening process the flow and sand transport at the exit point do not increase significantly;

(a)

(b)

FIGURE 2.7: Similarity between erosion channels and braiding rivers: (a) University of Florida flume test (seepage length=18 m) (Pietrus, 1981) and (b) Piave river crossing the high Venetian plain

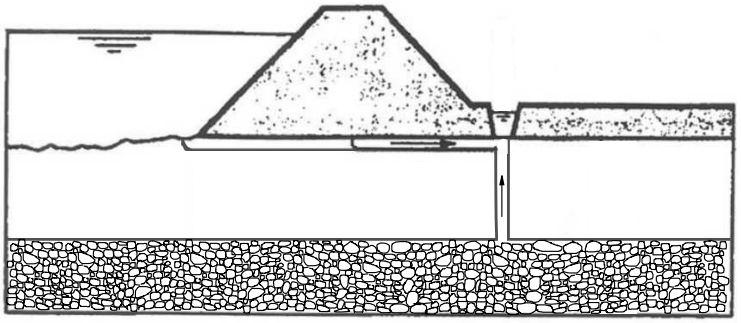

FIGURE 2.8: Possible piping paths in multilayer aquifers (modified after ICOLD, 2015)

therefore any observation made there cannot determine whether the upstream water body has been reached or not. Only when the widened pipe has almost reached the downstream side flow and sand transport increase sharply. Although the process of widening is very fast in the small-scale experiments, it took up to a few days in the large-scale experiments.

2.3.4 Time for development of erosion

Fell et al. (2003), analysing dam failures and accidents, asserts that backward erosion in foundation soils develops slowly (over weeks or months) until a pipe breaks through to the reservoir. From that moment on the erosion is rapid (many hours or days) to very rapid (<3 h). In the large-scale field tests described in Van Beek et al. (2011) failure occurs in few days. Imre et al. (2015) reports the erosion process to be generally slow, but they also mention two cases of very rapid failure (described in Szepessy, 1983; Imre and Rétháti, 1991), where the pipe reached the riverside few seconds after a geyser had suddenly appeared adjacent to the landside toe.

Van Beek et al. (2011) observed that the time required for progression increases with increasing scale. They also observed that the amount of transported sand per time unit remains more or less constant as long as the head is kept constant and increases with increasing head. However, in 2012 large-scale tests (described in Koelewijn et al., 2014), where the pipes did not reach the upstream water body, the rate of sediment transport seemed to be independent on the hydraulic load (A.R. Koelewijn, personal communication, June 2015).

The time to failure is also influenced by phenomena other than erosion. In the medium- and large-scale experiments described in Van Beek et al. (2011), blockage of the pipes took place during widening, increasing the time to failure. The material in the blockages was subsequently removed during a new process of backward erosion. Such material can both be sand (in the lab tests this is the only option) and clay particles or clay chunks detached from the above layer. Deformation of the upper cohesive layer is also considered a possible cause of blockage during the widening phase. This has been observed in a centrifuge test described in Van Beek et al. (2011). The authors pointed out that the deformations of the clay may have been governed by the presence of a relatively large channel, as the grain size is not scaled down in these small-scale experiments.

TABLE 2.1: Values of percolation factor C_{creep} in expression $H_c = L/C_{creep}$ according to Bligh

Soil type	C_{creep}
Fine silt and sand	18
Fine micaceous sand	15
Ordinary coarse sand	12
Gravel and sand	9
Boulders, gravel and sand	4 to 6

2.4 Backward erosion piping: prediction models

Prediction tools for backward erosion have been developed since the early 1900s. However, the ongoing experimental work shows that the problem has not yet been solved satisfactorily. Bligh (1910) deduced a purely empirical rule from failures of river diversion weirs which occurred under stress. He defined safety thresholds for the ratio between critical head and seepage length. The critical head H_c is defined as the value of the head H that leads to ongoing erosion, while the seepage length L is the shortest distance between the upstream and downstream levels (see Fig. 2.1). He called the ratio "percolation factor" but it was later defined as "creep ratio". The threshold values are dependent on grain size, as Table 2.1 illustrates.

Lane (1934) contributed to this empirical formulation by introducing different weight factors for horizontal and vertical sections in the seepage path, in order to take into account the higher resistance encountered by the flow along vertical sections.

The first analytical study was by Terzaghi (1922). He recognized that the onset of particle motion requires uplift of the particles. Imposing the vertical equilibrium of granular material, he determined the critical heave gradient (i_c) that causes fluidization:

$$i_c = -(1-\varepsilon)\left(\frac{\rho_s - \rho}{\rho}\right) \tag{2.1}$$

where ε is the soil porosity, ρ_s is the particle density and ρ is the water density. Since then, many studies and lab experiments investigated fluidization and erosion due to an upward flow (see for instance Wilhelm (2000)).

Terzaghi's approach is followed in the USA. The U. S. Army Corps of Engineers (USACE, 2005) prescribe a maximum value of 0.5 for the upward exit gradient. This value is purely empirical, deduced by data collected along the Mississippi River during 1950 flood (WES, 1956). With reference to Terzaghi's critical gradient, it means applying a safety factor around 1.6 (in terms of effective stress) or 1.2 (in terms of total stress)

(Sillis, 2012). The safety factor takes into account the reactivation of old sand boils, where soil density is locally lower. In USACE (2000) "blanket theory" equations are given to calculate the exit gradient for a standard configuration with a pervious layer covered by a low permeability top stratum. For more complex configurations the use of computer programs is recommended.

Dutch and German codes (TAW, 1999; DWA, 2007) rely on Sellmeijer's model for safety assessment against piping. Sellmeijer (1988) combined two-dimensional groundwater flow equations with equations for the micro-scale processes in the pipe: grain equilibrium and Posseuille flow. It was assumed that a pipe continues to grow when the seepage force on the grains at the bottom of the pipe exceeds the stabilising forces. For each pipe length, the head drop across the structure at which the grains in the pipe are in the limit equilibrium state, was calculated by solving the equations. The maximum equilibrium head found in this way is referred to as critical head for the progression of the pipe, because continuous erosion will occur when this maximum head is exceeded. The model was calibrated using large-scale experiments in the Delta flume (Silvis, 1991) and a practical rule was derived for a standard configuration: a levee overlying a confined homogeneous aquifer of constant thickness (Weijers and Sellmeijer, 1993b). Deviating configurations can be analysed using a finite-element method (FEM) code in which the model has been integrated (Sellmeijer, 2006). A non-standard configuration that is often observed is a fine sand top layer overlying a more permeable layer consisting of coarse grains. In this situation, the water flow is governed largely by the flow through the coarse layer, whereas the piping process is likely to take place in the fine layer.

While Terzaghi's approach determines the critical head for the initiation of erosion, Sellmeijer's model determines the critical head for the progression of erosion. His theory assumes that the head required for initiation is always lower that the head required for progression. Van Beek et al. (2014a) pointed out that this assumption is not always in agreement with experimental observations. Therefore, they investigated the process of initiation to provide rules for determination of the critical head in initiation-dominated configurations. They provided relationships between the average gradient H/L and the exit gradient for different exit types. They assumed that initiation of erosion occurs when the exit gradient exceeds Terzaghi's critical gradient (Eq. 2.1) over a minimum number of soil grains. While Terzaghi's criterion holds for upward vertical flow only, Richards and Reddy (2014) developed an initiation criterion that takes into account the

effect of seepage direction; it is based on the kinetic energy of the seepage flow, rather than on pressure gradients.

Schmertmann (2000), based on the results of 115 piping tests carried out in Florida, the Netherlands, and Germany, designed a semi-empirical method to predict the factor of safety vs. piping. The method consists in adjusting the results of laboratory tests to the field conditions, by means of correction factors (for geometry, grain size etc.) that he determined theoretically. Schmertmann visualizes the erosion process as progressive liquefaction occurring on a micro-scale at the advancing tip of the pipe. He considers the magnitude of the vertical hydraulic gradient at the pipe tip determining its advance. He does not consider the transport of the eroded sand up to the discharge point.

Recently, an analytical model that takes explicitly into account both the erosion at the bottom of the pipe and the fluidization of grains occurring at tip of the pipe has been developed in the Netherlands (G.J.C.M. Hoffmans, personal communication, March 2013).

Chapter 3

Dike monitoring

Knowledge of the expected failure mechanism(s) is paramount for the design of an effective dike monitoring system, including the choice of the physical parameters to measure and the position of the instruments. It is also very important, despite maybe less obvious, ask ourself what is the purpose for which the system is required. Indeed, reviewing Italian experiences on dike monitoring from the past 25 years and recent international experiences, it was noticed that monitoring systems can provide support in different tasks. This chapter describes the possible purposes of dike monitoring making use of Italian examples. It subsequently focuses on internal erosion and presents the sensing techniques which are more suitable to detect it.

3.1 Purposes of dike monitoring

The dike-related activities that can take advantage of monitoring systems are:

- design, construction and testing of new dike stretches and dike improvements;
- scientific studies on dike behaviour and failure mechanisms;
- management of dike networks.

The last item is the most challenging and can be articulated in the following objectives:

- localization of critical stretches;
- safety assessment of critical segments (or of the entire network where required by law);
- early warning.

3.1.1 Construction of new dikes and improvement of existing ones

Monitoring is a fundamental part of the construction process when the design of the dike is based on the *observational method* (CEN, 2004). Such method is often adopted when the foundation soils are highly compressible and it is desired to follow the time trend of the settlements and optimize the construction stages.

Vertical displacements are the parameter that is measured most frequently, followed by horizontal displacements in case instability is considered an issue. However, CIRIA et al. (2013) considers pore pressure measurements the most reliable tool to control the construction. Figure 3.1 shows how the measurements should be used. The ratio between the increment of pore pressure Δu and the increment of total vertical stress $\Delta\sigma_v$ is an indicator of the risk of instability: as soon as the slope of the line is greater than unity there is a risk of failure occurring and it is recommended interrupting the construction in order to allow the soil to consolidate. The line portion (O-A) represents the overconsolidated state, before the yield stress σ'_y is reached; the portion (A-B) represent the normal consolidated state; the portion (B-C) corresponds to the onset of local failure. Projecting on the $\Delta\sigma_v$ axis the straight line portion (A-B) the yield stress σ'_y is obtained.

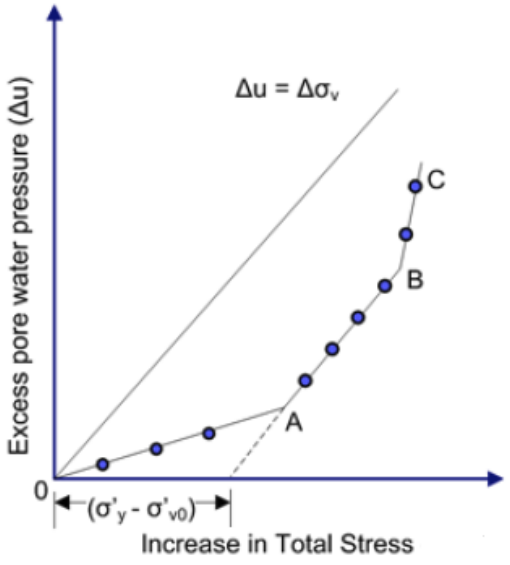

FIGURE 3.1: Pore pressure increase induced by excess load. The line portion (O-A) represents the overconsolidated state, the portion (A-B) the normal consolidated state and the portion (B-C) the onset of local failure. Projecting on the $\Delta\sigma_v$ axis the line portion (A-B) the yield stress σ'_y is obtained. (CIRIA et al., 2013)

An example of a monitoring system aimed at supporting the construction of a river embankment is given in Fig. 3.2. Settlement plates, extensometers and inclinometers

were used to monitor displacements. Casagrande, pneumatic and BAT piezometers were used to monitor pore pressures. After the construction stage, the monitoring system, integrated by new pore pressure sensors, was used to control the dike behaviour during a piping test (Colleselli et al., 2004). The latter was conducted increasing the water level in a reservoir that was enclosed between the new dike and the old one.

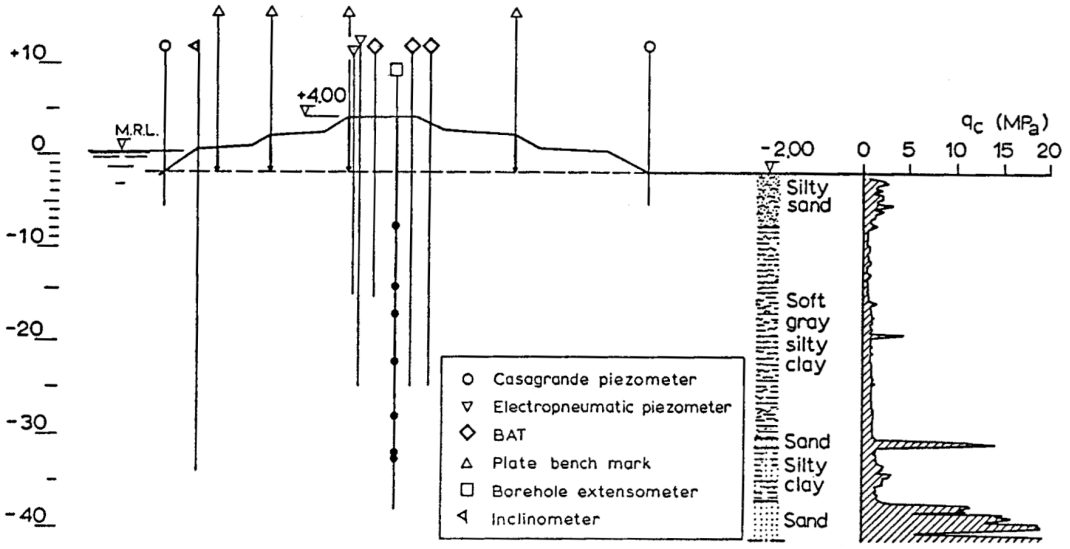

FIGURE 3.2: Monitoring system aimed at supporting the construction of a river embankment along the Po river delta (Italy). (Colleselli and Cortellazzo, 1992)

Construction of new dikes in not as common as improvement of existing ones. Testing the effectiveness of improvement works is another, more common function of monitoring systems. Besides testing the quality of the intervention, much information on the behaviour of the dike can be obtained by monitoring a significant dike improvement, especially if the measurements are continued for sufficient time after completion of the works. To this end, maintenance of the instrumentation installed (or of a small part of it) and continuous transfer (or periodic collection) of the data can provide valuable information at a small additional cost.

The effectiveness of seepage screens is traditionally assessed measuring the pore pressure response to the natural variations of the water body. In addition to pore pressure sensors, Dacome and Bersan (2014) used a chemical tracer injected in the embankment during a flood event. Lo Presti et al. (2014) and Cosanti and Lo Presti (2014), in addition to pose pressure sensors, used capacitive sensors to measure the variation of the water content in the unsaturated part of the dike, waterside and landside of the seepage screen.

3.1.2 Scientific studies

Monitoring is a fundamental part of scientific studies performed both on existing and on purpose-made dikes. If the study is performed on an existing dike, the possibility that no significant flood event will occur in the coming years should be considered. Therefore, the option of testing a dike along a channel or river stretch where the water level can be controlled should be evaluated. Alternatively, purpose-made dikes can be built. Calabresi et al. (2013) describe a seepage test performed on a test dike built riverside of the actual Po dike. The construction of the new dike provided a reservoir where the level could be increased as desired (Fig. 3.3).

Use of a made-on-purpose embankment is generally necessary when the final collapse is sought. This is the case of a number of test dikes built in the Netherlands between 2007 and 2012, within the framework of the IJkdijk ("calibration dike") project. Chapter 6 deals with the failure test performed on one of these dikes.

3.1.3 Safety assessment

The results of stability analyses are often affected by high uncertainties due both to the difficulties encountered in defining an accurate hydrogeological-geomechanical model and to the limited knowledge of the initial conditions.

In-situ measurements of piezometric levels under significant hydraulic loads enable the calibration of the hydrogeological-geomechanical model of the dike, which is used for safety assessment and, if needed, for the design of restoration works. The hydraulic parameters and, if necessary, also the stratigraphic model are adapted to fit the measured pore pressure values. Moreover, strength parameters are adapted to higher values if the model predicts failure while this has not occurred (*proven strength*). As suggested by Schweckendiek et al. (2013) and Van der Meij (2013), it is also possible to take advantage of data collected by means of visual inspection for calibrating the calculation models employed in stability and piping safety assessment.

Once the model is calibrated, conventional or dynamic safety assessments can be performed. In the first case the river level predicted for a given return period is assigned as hydraulic load. In the second case a real-time estimation of the current safety factor is provided based on real-time pore pressure measurements. The safety factor can be determined by continuously running numerical simulations in which the measured values are incorporated or by interrogating a *look-up table* (Simm et al., 2013). Look-up tables

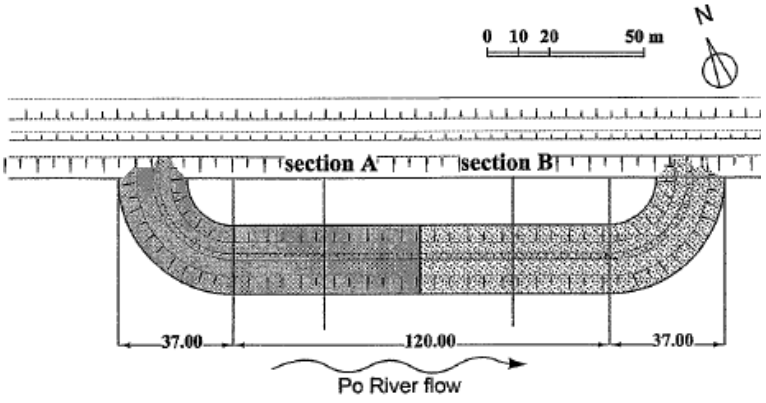

(a)

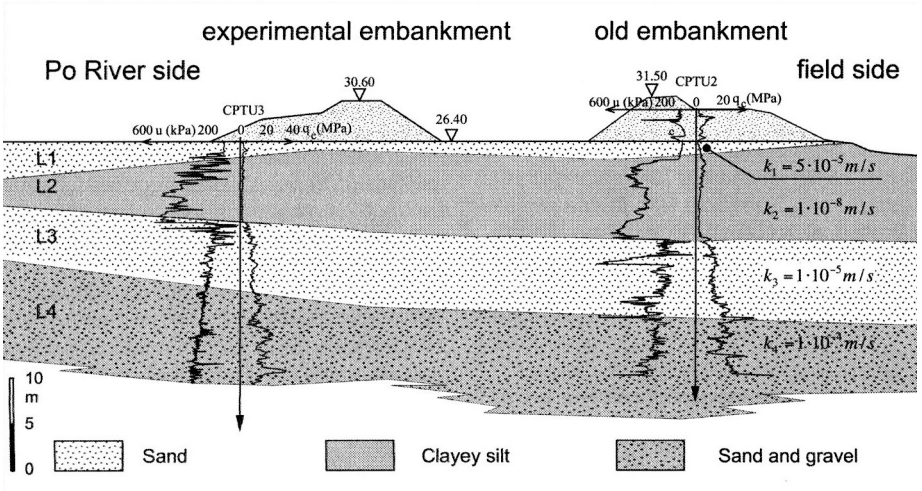

(b)

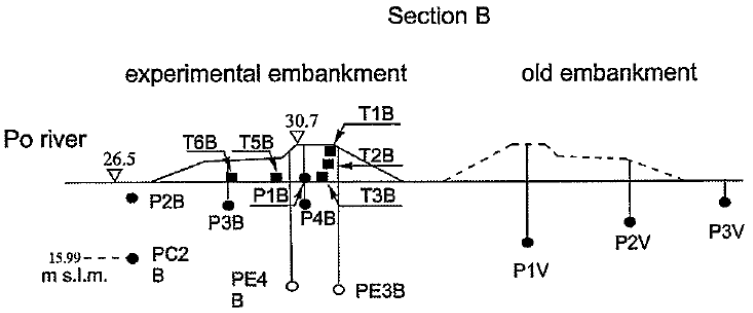

(c)

FIGURE 3.3: Test dike built at the aim of studying the hydraulic response of the typical Po riverdikes (Northern Italy): (a) plan view; (b) cross-section; (c) position of the instrumentation: tensiometers (T) and piezometers (P). (Calabresi et al., 2013)

are generated in advance by running a number of safety analyses for a range of potential pore pressures readings. A table is the compiled in which a safety factor is associated to each value of pore pressure.

Even more useful is the calculation of near-future safety factors. This is performed for instance by the module FEWS-DAM developed by Deltares (Lam et al., 2013). During high waters, hydrodynamic forecast models are run to predict near future river stages. The current pore pressures and the current water level are assigned as initial conditions in the groundwater flow model, then the time-dependent pore water distribution is calculated as a function of the forecast water levels; the resulting piezometric levels are used to perform strength calculations in order to predict safety levels during the coming flood (the critical situation is usually slightly after the maximum water level).

Figure 3.4 summarizes how pore pressure measurements can be integrated in both traditional and dynamic safety assessment procedures.

3.1.4 Management of dike systems

Long-term monitoring of a dike network pursues the ambitious objective of ensuring the safety of the entire network, by means of both default periodical safety assessments and real-time assessments performed during flood events. These two sub-objectives translate in different requirements for what concern the frequency of data acquisition, transmission and elaboration; in turn, these requirements influence the choice of the technology to adopt.

To date, it does not exist in Europe any rule that requires the adoption of dike monitoring systems aimed at increasing the safety of river and sea dikes. The only reference, despite not so explicit, is contained in the European Directive 2007/60/EC (European Parliament and Council, 2007). The directive prescribes that all the member countries devise risk management plans involving all the aspects connected to flood risk, including the development of prediction methods and early-warning systems.

Monitored objects as large as a dike network requires technologies that allow to cover large distances with limited financial resources. Conventional geotechnical instrumentation, with its point nature, is suitable for situations where detailed knowledge of the behaviour of a few representative cross-sections is sought-after. The management of a whole dike system would benefit from the adoption of a *multiscale approach*. Such

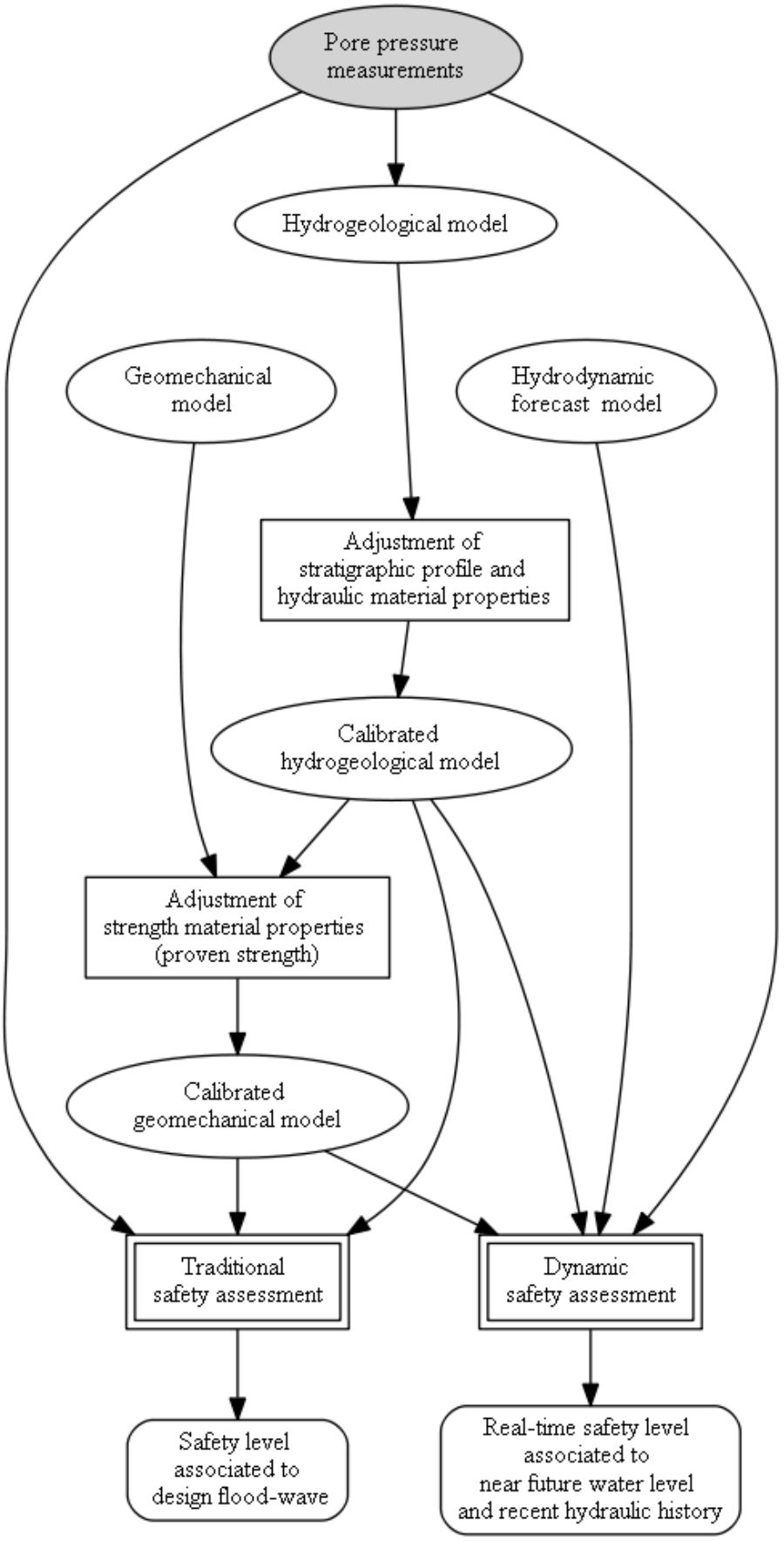

FIGURE 3.4: Use of pore pressure measurements to improve traditional dike safety assessment and enable real-time safety assessment

approach consists in integrating periodical checks of the whole network, made with extensive technologies, with continuous and detailed measurements performed at the most critical points. The concept is illustrated in Fig. 3.5.

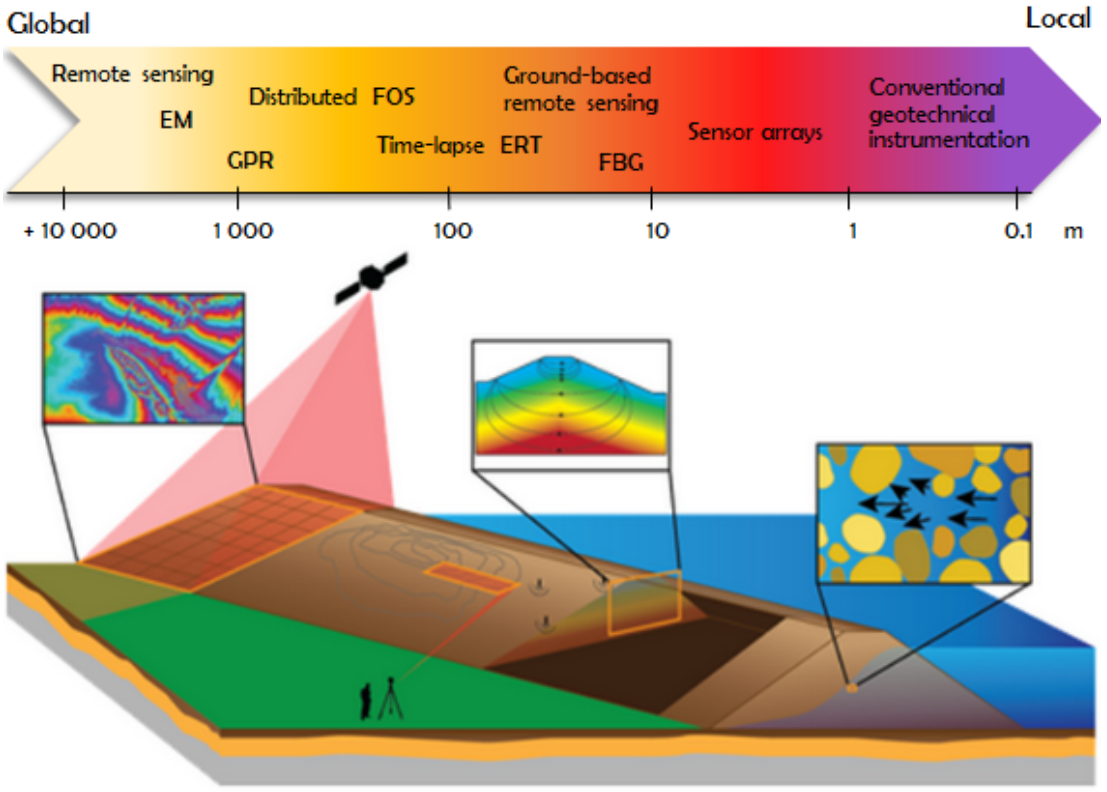

FIGURE 3.5: Multiscale approach for dike monitoring (concept from Mooney (2014))

3.2 Early detection of internal erosion

Internal erosion is triggered by high seepage velocities and causes a local decrease of the pore pressure and increase of the matrix porosity. Since an increase in porosity means an increase in hydraulic conductivity, internal erosion is always accompanied by a local increase of seepage velocity.

Pore pressure measurements are not good indicators of ongoing internal erosion because of the point nature of both the sensing technique and the erosion mechanism. Theoretical considerations by Ng and Oswalt (2010) show that the radius of influence of a pipe is in the order of few metres. Field observations of backward erosion piping show that the radius of influence of a pipe in its initial stage is on the order of 1 metre (see § 6.4.4). Consequently, an effective monitoring system would require a pore pressure sensor about every 2 metres. Therefore early detection of internal erosion cannot rely

on conventional geotechnical instrumentation even when a short dike stretch has to be controlled.

Pore pressure monitoring systems as those described in Del Grande (2008) and Simeoni et al. (2008) - to keep quoting Italian examples - are not believed to be very effective for detection of ongoing internal erosion. On the other hand they can be helpful for real-time safety assessments, as explained in § 3.1.3, if they are associated to a hydrogeological-geomechanical model.

Seepage anomalies are good indicators of internal erosion and a number of techniques have been devised to detect them. Other techniques have been proposed for monitoring porosity variations induced by internal erosion.

The disadvantage of all these techniques is that the parameters measured are also sensitive to other quantities, besides seepage velocity or porosity, that can vary in space and time because of soil heterogeneity. Integrated systems that measure more physical quantities susceptible to internal erosion can help in solving the ambiguities.

A brief description of the techniques suitable for early detection of internal erosion is given in the following sections. Distributed fibre-optic sensing is addressed in depth in Chapter 5.

3.3 Remote sensing

Thanks to its ability to cover large areas, remote sensing is highly suitable to large-scale monitoring. Its main limit is the frequency of the measurements. For satellite measurements the frequency is determined by the satellite revisit time, that can vary between one month and one day. This makes satellite imaging not a suitable technique for real-time detection of dike malfunctioning. Airborne sensing is more adaptable, as both periodic and emergency flights can be arranged. Diffusion of UAV (Unmanned Aerial Vehicles), best known as drones, is making remote sensing more accessible and economical.

Remote sensing techniques are commonly used in civil and environmental engineering for detection of surface displacements. They include InSAR (Interferometric Synthetic Radar Aperture), ground-based radar, photogrammetry and LiDAR. A limiting factor in natural areas is the low coherence between images shot at different times due to the seasonal variations of the vegetation cover. However, by positioning reflecting

objects characterized by high coherence (*corner reflectors*) a millimetric precision can be achieved.

The use of remote sensing for identification of seepage anomalies and other precursors of dike malfunctioning is not so common and its effectiveness is still under investigation.

At the Mississippi State University, researchers have worked on a procedure to detect and classify vulnerable stretches within the vast national dike network (Aanstoos et al., 2010; Dabbiru et al., 2010; Aanstoos, 2012). They have identified features of polarimetric SAR images that allow identification of slough slides. The latter are of great interest as they make the dike more vulnerable to significant hydraulic loads. Moreover they can extract from SAR images information related to the soil water content and vegetation quality, which in turn is related to the soil water content.

In the framework of the Flood Control 2015 project, Cundill et al. (2013) investigated the effectiveness of remote sensing to monitor peat dikes. Temperature maps obtained with a thermographic camera and satellite radar images at different wavelengths have been compared to maps of water content and vegetation determined respectively by sampling and direct observations (Fig. 3.6). Although spatial variations of water content produced spots in the radar images, it was only combining different wavelengths that was possible to identify anomalies strongly correlated to subsoil features.

Among remote sensing techniques, passive microwave radiometry should be mentioned as a suitable method for large-scale mapping of the soil water content (Laymon et al., 1998; Schmugge, 1998). It exploits the principle that the emissivity of an area depends on the water content of the first few metres of soil. Waves emitted in C, X and L band are recorded by radiometers mounted on satellites, airborne and land vehicles. Accuracy and penetration depth are higher for terrestrial measurements. Passive radiometry has been used, in combination with many other techniques, to study the effect of drought on the stability of peat dikes, in a pilot carried out at de Veenderij, South of Amsterdam (Van den Berg and Koelewijn, 2014).

3.4 Geophysical methods

Geophysical methods are mostly used for *una tantum* investigations aimed at evaluating the safety level of dikes. To date the most interesting techniques are surface geophysical

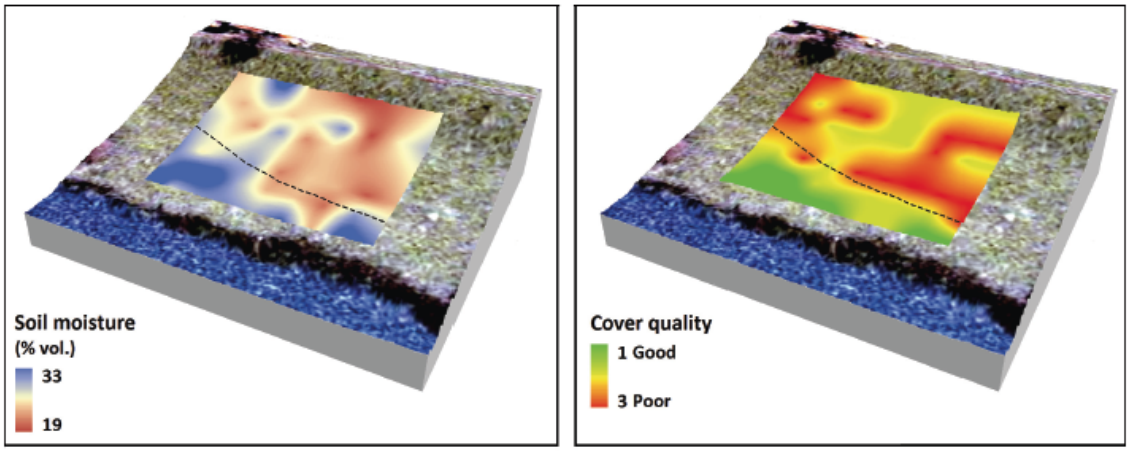

(a)

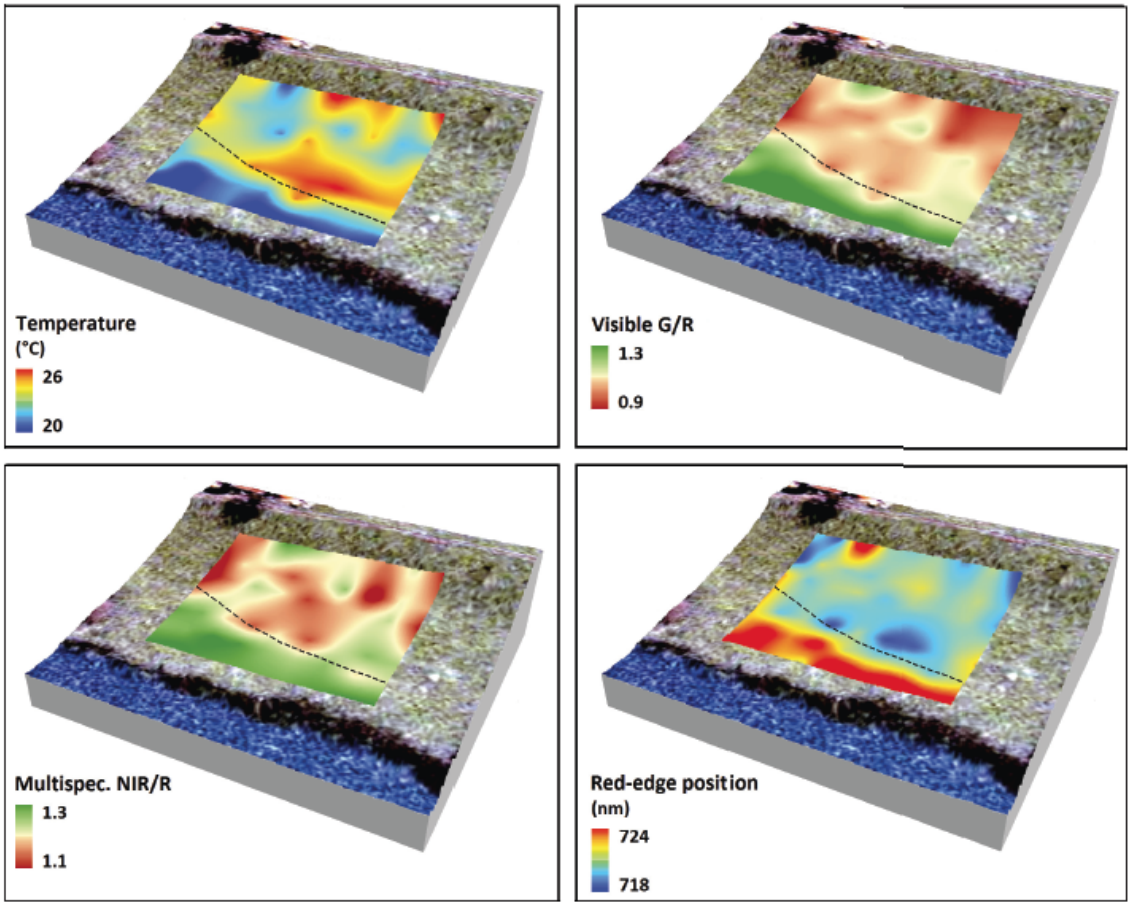

(b)

FIGURE 3.6: Correlation between key features of a peat dike and satellite data at different wavelengths: (a) validation data; (b) satellite data (Cundill et al., 2012)

methods: since they do not require the introduction of any tool at depth, they are non-invasive, more economical and faster. By continuous investigation over medium-long distances they allow to subdivide the dikes in homogeneous segments and to identify anomalous zones.

Geophysical methods can also be adopted for monitoring purposes if the measurements are repeated over time. Although their suitability for dam monitoring has been studied for years and guidelines by the CEATI Dam Safety Interest Group are available (Corwin, 2007; Dahlin et al., 2008; etc.), their employment in river and sea dikes is quite recent and still under study (see for instance Royet, 2012).

Geophysical methods measure physical parameters that are dependent on more than one soil parameter (mineralogy, water content, density etc.). In addition, inverse modelling has to be applied to retrieve the actual distribution of the measured parameter. This can lead to a non-univocal interpretation of the geophysical data if the latter are not supported by data obtained through a geotechnical investigation (boreholes, cone penetration tests etc.).

The methodologies described in the following sections include Electrical Resistivity Tomography (ERT), ElectroMagnetic surveys in the Frequency Domain (FDEM), Self-Potential (SP) and Ground Penetrating Radar (GPR). These methods are designed to produce an image of the investigated subsurface in terms of electrical conductivity (ERT and FDEM), dielectric constant (GPR) or electric potential (SP), which are strongly related to the subsurface lithology and water content. The methodologies differ in spatial resolution and operating modes. The FDEM and GPR methods do not require any direct contact with the ground and therefore are better suited to cover large areas in a relatively short time; the ERT technique, on the other hand, requires a galvanic contact with the surface and thus longer operating times, but offers a higher resolution and a greater control over signal penetration as compared to FDEM and GPR.

3.4.1 Electrical Resistivity Tomography

Electrical Resistivity Tomography consists in generating an electric field in the soil, through the transfer of a direct current between two source electrodes rooted in the soil, and in measuring the induced potential difference by means of a number of couples of electrodes, different from the source ones.

ERT can be employed in time-lapse mode for identifying zones affected by strong seepage. Its application is based on the dependency of soil resistivity on temperature and ion concentration, which are parameters that vary seasonally as a function of seepage velocity: zones affected by stronger seepage present larger seasonal variations (Sheffer et al., 2009).

Figure 3.7 shows the results of the monitoring conducted at the Sädva dam (Sweden) between 2001 and 2015 (Johansson et al., 2005). The resistivity at 20 m depth is determined by inversion of daily data recorded by fixed electrodes deployed on the crest. The resistivity at the chainage 450 m is lower and shows large seasonal variations, which is synonym of higher seepage velocity.

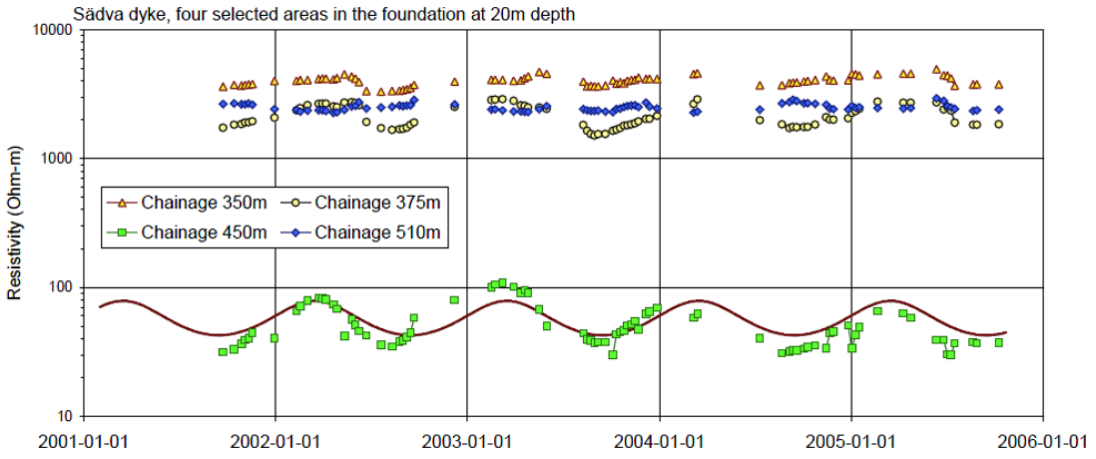

FIGURE 3.7: Sädva dam, Sweden: temporal variation of the resistivity at the depth of 20 m at four progressive distances (Johansson et al., 2005)

Also high resistivity anomalies can be a signal of internal erosion, as they can be synonym of an increase in porosity. Resistivity measurements are more effective in identifying high porosity zones when the saturation degree is higher, for instance after precipitations and when the seepage flow is fully developed (Case, 2012). This occurs because of the resistivity contrast between the pore water and the soil matrix is larger than the contrast between air and soil. In a lab experiment Burns et al. (2006) were able to identify piping by means of miniaturized sensors suitable for identification of structures at the millimetre scale.

An increase in porosity can also translate in a decrease of electrical resistivity; this occurs in fine-grained unstable soils, where the selective transport of the clay fraction produce a change in the mineralogy on the soil (Bergström, 1998, as cited in Sheffer et al., 2009).

An interesting case of dike monitoring by means of resistivity measurements is described in Mériaux et al. (2012). On a 100 m dike segment along the Loire river two parallel lines have been deployed along the crest, 4 m from each other, in order to obtain a three-dimensional model of the dike resistivity. Each line was made of 48 electrodes installed 1.2 m below the soil surface, at a distance of 2 m from each other. Preliminary results show that using a double acquisition line associated to a 3-d interpretation model is paramount to retrieve high quality information from raw data. Indeed when a single longitudinal profile is acquired a 2-d model has to be used to invert data, in which the dike is assimilated to an infinite half-space. Such hypothesis is never satisfied for a longitudinal profile. On the other hand, the infinite half-space hypothesis is satisfied for transversal profiles (Perri et al., 2014). The information obtained by the latter is therefore more accurate.

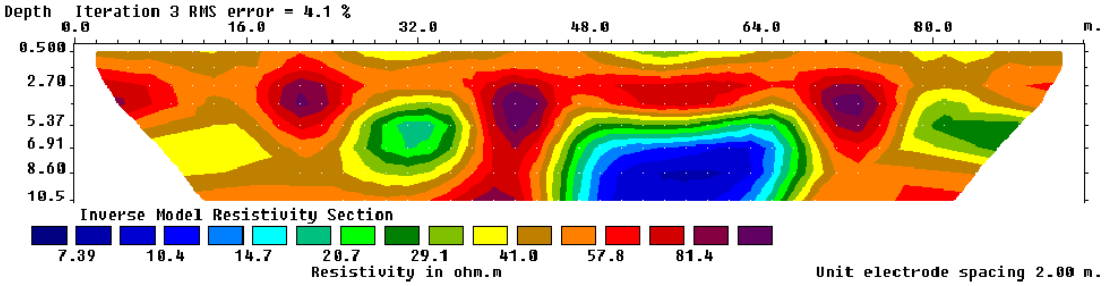

(a)

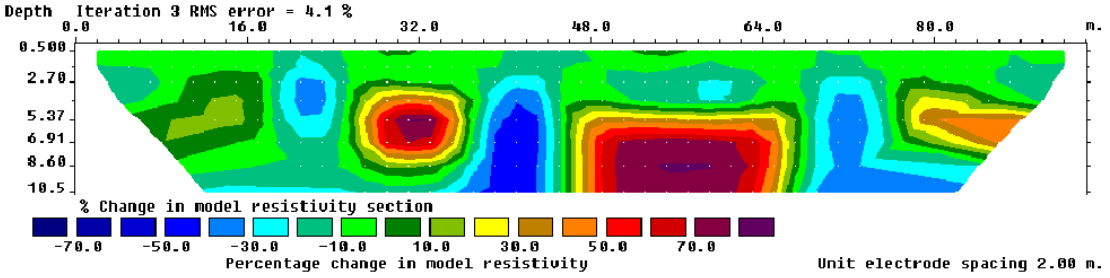

(b)

FIGURE 3.8: Loira river dike, longitudinal section at the riverside: (a) inverted resistivity on May 2009; (b) relative variations (%) of inverted resistivity obtained comparing June 2010 and May 2009 data. (Mériaux et al., 2012)

ERT has also been proved useful to monitor sub-surface cracks in clay dikes. These cracks have a key role in a number of dike failure occurred in the UK and the depth at which they extend is difficult to determine visually. Sentenac and Zielinski (2009) have tested miniaturized electrodes on a small-scale embankment. Sentenac et al. (2013) suggest to perform preliminary investigations with ERT and EM to locate the most

fissured zones and here installing miniaturized electrodes for a detailed monitoring of the cracks.

3.4.2 Frequency Domain Electromagnetic method

Frequency Domain Electromagnetic method (FDEM) involves generating, through a transmitter loop, an electromagnetic field that induces eddy currents in the subsoil, which in turn cause the subsurface to create a magnetic field. By measuring the magnitude and phase of the induced electromagnetic field through a receiver loop, the electrical resistivity of the subsoil is inferred. For surface FDEM, transmitter and receiver are fixed at a certain distance forming a mobile instrument that does not require direct contact with the soil and can be moved along the dike using a hand truck. The investigation depth does usually reach 6 m.

For its speed of execution FDEM is suitable for frequent measurements over large distances. This also allows to get information under different load conditions. The principles that make FDEM suitable for detection of internal erosion are the same explained in § 3.4.1, as FDEM produces a map of the subsurface electrical resistivity. On the other hand, the method is much less accurate than ERT, since FDEM measurements represent a weighted average of electrical resistivity over the depth investigated. For this reason FDEM measurements are suitable for identifying anomalies, but need to be integrated by higher resolution techniques like ERT to get a better understanding of the anomalies.

3.4.3 Self-potential

The self-potential method (SP) is sensitive to the seepage flow, as the thermometric method, and is effective only if the flow is fully developed.

The occurrence of self-potential signals with groundwater flow is well explained in (Bolève et al., 2011). The surface of mineral grains in contact with water is generally negatively charged. In order to compensate for the imbalance of electrical charges attached to the mineral grains, an excess of electrical charges concentrates in the vicinity of the mineral surface in the so-called electrical *double layer*. The mobile part of this excess of electrical charges (forming the so-called *diffuse layer*) is dragged by the flow of the pore water. The net flow of charges per unit surface area of porous material and per unit time is an electrical current density proportional to the Darcy velocity. The polarity, as well as the magnitude of the electrical field can give indications on the direction and

the velocity of the leakage flow. Bolève et al. (2011) show how time-lapse self-potential measurements in combination with a salt tracer allow not only identification of a seepage area, but also estimation of the flow velocity.

The electrical field can be measured at the ground surface by a voltmeter and a set of non-polarizing electrodes in contact with the soil. The cost of the equipment is much lower compared to the other geophysical methods, especially if geophones are manufactured at home.

Since the distribution of the source current density is also shaped by the distribution of the electrical resistivity, inversion of SP data requires that the resistivity distribution in the domain is known. Therefore coupling of ERT and SP is advised (Titov et al., 2000). The coupling with temperature measurements also looks promising (Revil and Bolève, 2007).

Rittgers et al. (2015) demonstrated that the spatial accuracy of a model of source current density is improved when acoustic emissions are utilized to constrain the inversion of self-potential data. Acoustic emissions are generated by collapses, water or soil particle movements (as well as by vehicles and people movements) and are recorded by means of geophones installed below the surface. The method is also called *passive seismic*. Rittgers et al. (2015) tested the effectiveness of coupled self-potential and passive seismic in a 7-d full-scale dike failure test, conducted in the Netherlands and aimed at testing the capability of a geotextile filter to prevent backward erosion piping (see § 6.1). Since the geotextile allows a certain amount of piping to develop, a series of sand boils appeared in the central part of the landside toe and eventually local liquefaction of the embankment toe occurred at that position. Correspondingly, the development of a positive self-potential anomaly was identified near the toe of the embankment. Fig. 3.9 shows the self-potential distribution.

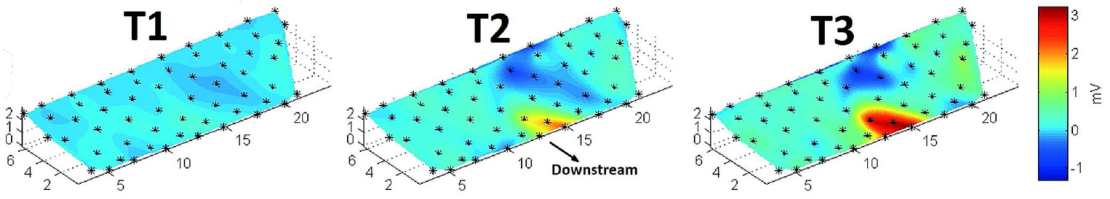

FIGURE 3.9: Self-potential data from a full-scale dike failure test at three progressive stages. A positive anomaly appears at the landside toe, after progressive increase of the hydraulic load. The anomaly is consistent with the observation of a liquefaction area at the same location (Rittgers et al., 2015)

3.4.4 Ground Penetrating Radar

Ground Penetrating Radar (GPR) is a very popular tool for dike investigation as surveys are pretty fast and it is claimed to be able to detect one of the major elements of concern regarding dike safety: animal burrows.

GPR makes use of high-frequency electromagnetic pulses emitted by mobile antennas close to the surface. The system measures the time of flight of the EM wave reflected because of a variation in the EM impedance between two different media. These variations are produced by soil stratifications, buried objects or cavities. The depth of the element that has generated the reflection can be calculated once the speed of propagation of the wave in the soil - which in turn depends on the dielectric permittivity - is known (calibration in homogeneous field is needed). Figure 3.10 shows an example of the hyperbola-shaped reflections of the electro-magnetic wave caused by an animal burrow.

The depth of penetration of the signal varies between 10 m and less than 1 m. Signal damping depends on soil mineralogy, water content and chemistry of the pore water, as well as the frequency of the pulse. The depth of penetration is high in coarse soils and very low in saturated clayey soils.

Another factor that can limit the depth of investigation is the trade-off between signal frequency and spatial resolution. Low frequency signals can reach larger depths but have spatial resolutions that might be not sufficient to detect objects on the orders of few tens of centimetres, as animal burrows and buried pipes. Di Prinzio et al. (2010) show that running the investigation from a riverside bank can be helpful in this sense, because there the distance between the burrow and the soil surface is smaller.

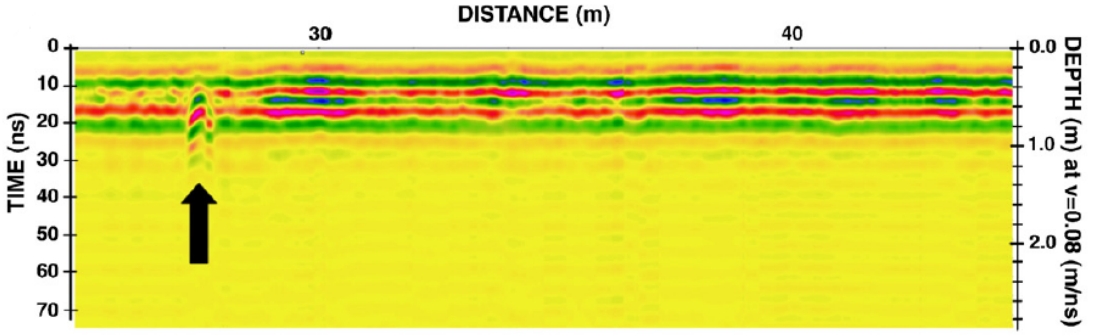

FIGURE 3.10: A GPR application on dikes: hyperbola-shaped reflections of the electro-magnetic wave caused by an animal burrow (Di Prinzio et al., 2010)

3.5 Visual inspection and social sensors

Remarkable advances have been accomplished in sensor technology in the last decades, allowing to achieve both good spatial coverage and acceptable resolution in the measurements. Nevertheless, the lack of financial resources makes a capillary control by means of sensors very difficult. Moreover, new technologies cannot replace the historical memory and knowledge that hydraulics officers accumulated visiting repeatedly the same dike segments. Visual inspection remains the most important tool for a sustainable management of a dike network. Sensors are to be considered as "extra eyes", with the aim of extending the control domain besides the visible, anticipating the detection of anomalies and providing a quantitative description of the ongoing processes. This way they can assist engineers and stakeholders in making predictions and assigning priorities for further inspections, maintenance and improvement works (Peeters et al., 2013).

During their inspections patrollers should note uprooted trees, or trees with invasive roots, signs of external erosion, areas where the grass cover is absent or deteriorated, crest and slope depressions, bulging of the landside toe, slough slides, cracks, animal burrows, ponds, springs and turbidity of the water seeping out of them, sand boils (CIRIA et al., 2013).

Guaranteeing an effective dike patrolling is hard when budget is limited. In Italy, during high waters, the Civil Protection coordinates visual inspections and emergency interventions, that are mainly carried out by volunteers. Lack of financial means makes difficult to organize more regular and capillary visual inspections.

A European research project aimed at involving a large part of citizens in flood risk management is ongoing (Ciravegna, 2013). The researchers claim that citizens can be social sensors, both conscious and unconscious. In the first case they can collect data (staff gauge readings, pictures) and communicate them through dedicated channels; in the second case they can provide useful information through their activity on the social networks. The concept is illustrated in Fig. 3.11. The project also aims at devising techniques for translating the information from social sensors into data to feed to calculation models.

In order to get the best out of social sensors, investing resources in their formation is important. A curious example comes from the Netherlands, where resources have been invested in the creation of serious games. Among these there is Levee Patroller, a software that simulates critical situations as sand boils, uprooted trees etc. on a virtual

dike. It is meant to teach both technicians and volunteers what are the aspects to which pay attention during inspections and how to correctly report observations (Harteveld, 2010). An application for smartphones with a simplified version of the game has been developed to promote the diffusion of the game among the citizenry.

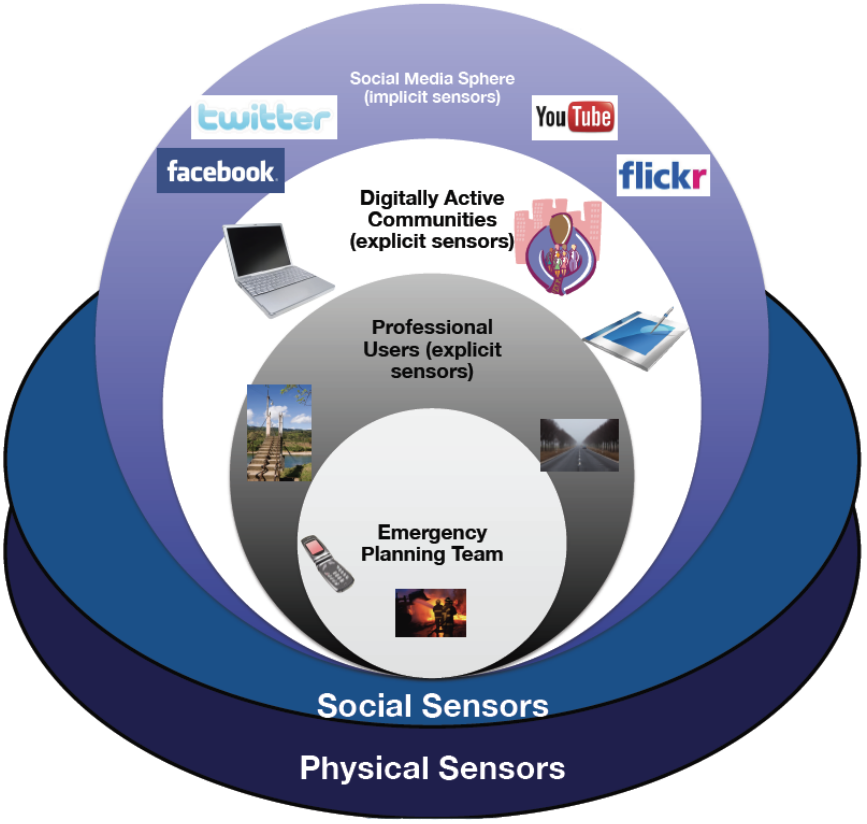

FIGURE 3.11: Concentrinc partecipation model for dike management (Ciravegna, 2013)

Chapter 4

Heat transfer in soils

Heat transfer in soils can be described by the general physical laws that regulate heat transfer in porous media. Heat is transported through porous media by means of mainly two mechanisms. *Conduction* is the transfer of heat caused by a temperature gradient and occurs through both the solid matrix and the pore fluid(s). *Advection* is the transfer of heat by means of the motion of a fluid and its magnitude is a function of the fluid velocity. The term convection is sometimes used as a synonym for advection; however, by definition, convection is the sum of transport by conduction and advection.

This chapter presents the equations that govern fluid flow in soils and allow to calculate the flow velocity responsible for heat advection. A section is dedicated to interface problems between piping channels and porous matrix, that arise because different equations hold in the two domains. Following, the equations governing heat transfer in porous media are reported. A few pages are dedicated to dimensionless numbers that give a measure of the relative importance of conductive and convective heat transfer. Moreover, a detailed literature review is reported, regarding the thermal properties of soils. The last section gives an overview of the temperature distribution in the subsurface as a function of depth.

4.1 Theory of mass transport in porous media

The flow of a homogeneous fluid through a porous medium is addressed in this section. This is, for example, the case of a water saturated soil. Mass conservation applied to a control volume gives:

$$\frac{\partial(\rho\varepsilon)}{\partial t} + \nabla \cdot (\rho \mathbf{u}) = Q \tag{4.1}$$

where ρ is the fluid density, ε is the medium porosity, Q is an internal source or sink and $\mathbf{u}$ is a vector describing the rate of flow through a surface element of unit area, and is named *specific discharge*.

The specific discharge is also called Darcy velocity, as it can be expressed through the Darcy's empirical law:

$$\mathbf{u} = -\frac{\kappa}{\mu}(\nabla p + \rho g z). \tag{4.2}$$

where κ is the permeability of the porous matrix, μ is the dynamic viscosity of the fluid, p is the pore pressure and z is the elevation.

Expanding the first term of Eq. (4.1) the following equation are obtained:

$$\frac{\partial(\rho\varepsilon)}{\partial t} = \frac{\partial(\rho\varepsilon)}{\partial p}\frac{\partial p}{\partial t} \tag{4.3}$$

$$\frac{\partial(\rho\varepsilon)}{\partial p} = \varepsilon\frac{\partial\rho}{\partial p} + \rho\frac{\partial\varepsilon}{\partial p} = \rho\left(\varepsilon\frac{1}{\rho}\frac{\partial\rho}{\partial p} + \frac{\partial\varepsilon}{\partial p}\right). \tag{4.4}$$

The definition of *fluid coefficient of compressibility* can now be introduced:

$$X_f = \frac{1}{\rho}\frac{\partial\rho}{\partial p} \tag{4.5}$$

together with the definition of *soil coefficient of compressibility*:

$$X_m = \frac{\lim_{\Delta V\to 0}\partial(\Delta V)/V}{p} \tag{4.6}$$

as given in (Gamboloati, 1973). ΔV is the bulk volume of a porous medium element. As the soil grains are assumed incompressible, the dilatation is only due to variations of the pore volume caused by rearrangements of the spatial distribution of the soil grains. It is thus correct assuming $X_m = \partial\varepsilon/\partial p$. According to the above definitions Eq. (4.4) can be written as follows:

$$\frac{\partial(\rho\varepsilon)}{\partial p} = \rho(\varepsilon X_f + X_m) = \rho\, S_{0p}, \tag{4.7}$$

where

$$S_{0p} = \varepsilon X_f + X_m \tag{4.8}$$

is the *specific volumetric storativity related to pressure changes*. S_{0p} is defined as the volume of water released from (or added to) a unit soil volume per unit decline (or rise)

of pressure.

The problem is often formulated in terms of *total hydraulic head*,

$$\varphi = \frac{p}{\rho g} + z \tag{4.9}$$

rather than in terms of pore pressure. In such case, Eq. (4.2) becomes

$$\mathbf{u} = -K\nabla\varphi \tag{4.10}$$

where K is the *coefficient of hydraulic conductivity.* K depends on both the permeability of the solid skeleton and the fluid properties:

$$K = \kappa\frac{\rho g}{\mu}. \tag{4.11}$$

Written in terms of hydraulic head, Eq. (4.7) becomes:

$$\frac{\partial(\rho\varepsilon)}{\partial\varphi} = \rho^2 g(\varepsilon X_f + X_m) = \rho\, S_{0\varphi}, \tag{4.12}$$

where

$$S_{0\varphi} = \rho g(\varepsilon X_f + X_m) = \rho g\, S_{0p} \tag{4.13}$$

is the *specific volumetric storativity related to potential changes.* $S_{0\varphi}$ is defined as the volume of water released from (or added to) a unit soil volume per unit decline (or rise) of head.

4.2 Theory of fluid flow in a piping channel

Flow in piping channels is described by the mass conservation equation:

$$\frac{\partial\rho}{\partial t} + \nabla\cdot(\rho\mathbf{u}) = 0 \tag{4.14}$$

and the Navier-Stokes equations for the conservation of the momentum :

$$\rho\frac{\mathrm{d}\mathbf{u}}{\mathrm{d}t} = -\nabla p + \mu\nabla^2\mathbf{u} + \frac{1}{3}\mu\nabla(\nabla\cdot\mathbf{u}) + \rho\,\mathbf{g}. \tag{4.15}$$

If ρ is constant and $\mathbf{u}$ is small enough for the viscous forces to dominate the dynamics (*Reynolds number*$\ll 1$), the *Stokes* approximation applies, which leads to a system of

linear equations:

$$\nabla \cdot \mathbf{u} = 0 \tag{4.16}$$

$$\nabla p = \mu \nabla^2 \mathbf{u} + \rho \, \mathbf{g}. \tag{4.17}$$

The inherent order difference between the Darcy's law (Eq. 4.2) that is solved in the porous matrix and the Stokes equations that are solved in the pipe generates a difficulty at the interface between the domains. The Darcy's law is indeed of first order in the spatial derivatives so that only one boundary condition can be applied, either on the pressure or on the velocity component normal to the boundary. If the normal velocity is assigned, the other components of the velocity have arbitrary values at the wall. In the following, three possible approaches are presented to overcome this difficulty.

4.2.1 Slip boundary condition

Beavers and Joseph (1967) suggested to impose a slip boundary condition at the interface between a porous matrix and free fluid. They defined an empirical slip coefficient that expresses the relationship between the flow velocity and the flow velocity gradient at the interface. They found experimentally that this coefficient is sensitive to the characteristics of the porous medium. An overview of the coupling of the Navier-Stokes and Darcy's equations and algorithms to compute the solution of its numerical approximation are given in Discacciati and Quarteroni (2009).

4.2.2 Brinkman equations

The second approach consists in using the Brinkman equations

$$\nabla p = -\frac{\mu}{\kappa}\mathbf{u} + \mu' \nabla^2 \mathbf{u} + \rho \, \mathbf{g} \tag{4.18}$$

to describe both the flow in the porous matrix and the free flow in the pipe. The coefficient μ' is an effective viscosity, that Brinkman set equal to μ. Equations (4.18) are an extension of the Darcy's law that take into account the dissipation of the kinetic energy by viscous shear (the Laplacian term), which is not negligible for high permeabilities. For this reason, they are often referred to as the Brinkman's extension of the Darcy's law. However this is a misleading expression, as (Brinkman, 1949) did not just add a term to the Darcy's law; he rather obtained a relationship between permeability and porosity for an assembly of spheres through a consistent procedure. Later derivation of the

Brinkman equations from the Navier-Stokes equations by means of a volume-averaging technique gave $\mu' = \mu/\varepsilon$ (see Le Bars and Worster, 2006 for a simplified approach or Ochoa-Tapia and Whitaker, 1995 for a more complex and general approach).

4.2.3 Hagen-Poiseuille formula

Three-dimensional finite element discretization of the Navier-Stokes and Brinkman equations implies four degrees of freedom for each node. This makes the computation very expensive. In addition, the discretization of a Navier-Stokes domain requires to adopt along the walls a few layers of very thin elements (boundary layer mesh), thus increasing the overall number of elements necessary.

A drastic simplification of the problem is obtained if the flow in the channels is treated as a Hagen-Poiseuille flow, that is one-dimensional laminar flow through a tube.

The hypothesis of laminar flow is reasonable, given the small size of the pipes and the limited velocities that can be reached in the pipes under the hydraulic loads applied to small and medium water retaining structures. The other features of a Hagen-Poiseuille flow are:

- the component of the velocity perpendicular to the walls is null;
- the components of the velocity parallel to the walls vanish at the walls (no-slip condition).

Levy and Sanchez-Palencia (1975) (as cited in Discacciati and Quarteroni, 2009) found that, since the velocity in a free fluid overlying a porous layer is much larger than the Darcy velocity in the porous layer itself, as a first approximation the flow around the porous medium is the same as if the porous body were impervious. The asymptotic matching of the free fluid with the flow in the porous body occurs within an intermediate layer of thickness equal to the characteristic length of the matrix pores (Fig. 4.1). It is

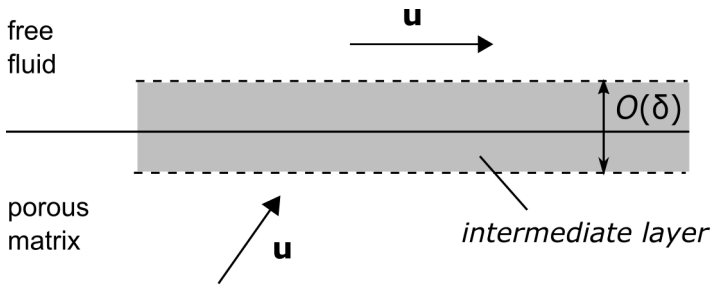

FIGURE 4.1: Intermediate layer of thickness δ between free fluid and porous body (Discacciati and Quarteroni, 2009)

TABLE 4.1: Friction factor for fully developed laminar flow in pipes of various cross-sections ($Re = UD_h/\nu$).

Tube geometry	Aspect ratio w_p/b	Friction factor β
Circle	-	64.00/Re
Rectangle	1	56.92/Re
	2	62.20/Re
	3	68.36/Re
	4	72.92/Re
	6	78.80/Re
	8	82.32/Re
	∞	96.00/Re

concluded that the portion of the pipe where the flow is not one-dimensional should be thin, compared to the size of the pipe. It follows that the no-slip condition should be a reasonable approximation.

Hagen-Poiseuille flow in tubes of general shape is described by the following equation:

$$\overline{U} = -\frac{2D_h^2}{\beta\mu}\rho g\frac{\Delta\varphi}{l} \tag{4.19}$$

where $\overline{U}$ is the average velocity across the section, l is the length of the pipe, β is a friction factor depending on the shape of the section (see Table 4.1) and D_h is named *hydraulic diameter* and is a ratio between the area of the section and its wetted perimeter ($D_h = 4A_p/P$). Comparing Eq. (4.19) with Eq. (4.2) it is clear that a Hagen-Poiseuille flow can be described by the Darcy's law, if a fictitious permeability is used:

$$\kappa^* = \frac{2D_h^2}{\beta}. \tag{4.20}$$

When the cross-section of the tube is elongated, with the thickness b much smaller than the width w_p: $w_p/b \to \infty$, as for the pipes observed in small- and medium-scale lab tests, we obtain

$$\kappa^* = \frac{b^2}{12} \tag{4.21}$$

and the flow in the pipe is given by

$$Q = -\frac{\rho g}{\mu}\,\frac{b^3 w_p}{12}\,\frac{\Delta\varphi}{l}. \tag{4.22}$$

Equation (4.22) is the well known *cubic law* that describes flow in fractures.

If a Hagen-Poiseuille flow is assumed to occur in the piping channel, the Darcy's

law can be solved in the whole domain by assigning a fictitious permeability in the pipe as given by Eq. (4.20) or Eq. (4.21). In such case, only a single unknown (pressure or hydraulic head) is associated to each node and the solution of the system of equations is much cheaper. Figure 4.2 shows the velocity profiles obtained using the formulations presented. The sketch refers to a Poiseuille flow in a channel formed by an impermeable wall at $z = +h$ and a permeable wall at $z = 0$, corresponding to the upper surface of a semi-infinite porous medium saturated with the same fluid.

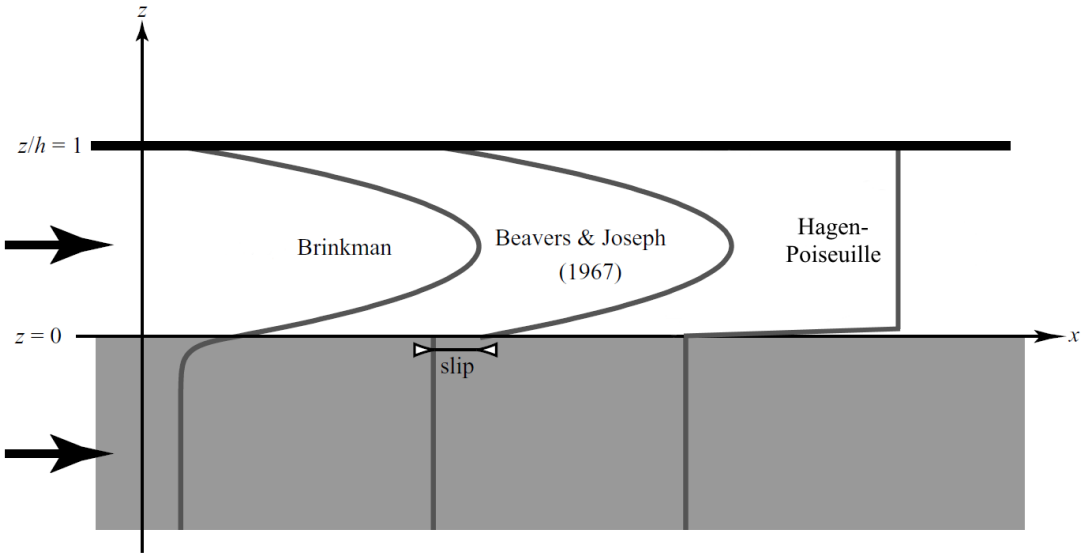

FIGURE 4.2: Poiseuille flow in an open channel overlaying a porous layer: flow velocity profiles obtained with Brinkman formulation, Stokes-Darcy formulation with Beavers and Joseph (1967) interfacial conditions and Darcy-Darcy formulation with the flow in the channel described by the Hagen-Poiseuille formula (modified after Le Bars and Worster, 2006).

4.3 Theory of heat transfer in porous media

Application of the law of conservation of energy to a control volume, gives the conduction-advection equation for heat transfer, that reads:

$$C\frac{\partial T}{\partial t} + C_w\,\mathbf{u}\cdot\nabla T = \nabla\cdot(\lambda\nabla T) + Q_{disp} \tag{4.23}$$

where

T is the temperature;

C_w is the volumetric heat capacity at constant pressure of the fluid (water);

C is the volumetric heat capacity at constant pressure of the porous medium (water);

ρ_f is the fluid density;

λ is the thermal conductivity of the porous medium (a scalar or a tensor if the medium is anisotropic);

$\mathbf{u}$ is the Darcy velocity;

Q_{disp} is the energy flux due to mechanical and thermal dispersion.

Temperature variations cause changes in fluid density and fluid viscosity. If these changes are neglected the problem of fluid flow and heat transfer are uncoupled.

Equation (4.23) can be further simplified by neglecting heat dispersion and assuming the medium to be homogeneous and isotropic with respect to the thermal properties (but not necessarily to the hydraulic ones):

$$C\frac{\partial T}{\partial t} + C_w\,\mathbf{u}\cdot\nabla T = \lambda\nabla^2 T \tag{4.24}$$

Rearranging Eq. (4.24) as follows:

$$\frac{\partial T}{\partial t} + \frac{C_w}{C}\mathbf{u}\cdot\nabla T = \frac{\lambda}{C}\nabla^2 T \tag{4.25}$$

two new parameters are obtained: the *thermal diffusivity*

$$a = \frac{\lambda}{C} \tag{4.26}$$

and the *velocity of the thermal advective front*

$$\mathbf{v}_T = \frac{C_w}{C}\mathbf{u}\,. \tag{4.27}$$

A high thermal diffusivity implies a capability for rapid and considerable temperature changes in time. $\mathbf{v}_T$ is sometimes referred to as the "thermal front velocity", but this definition can be misleading, as the term does not include conductive thermal fluxes.

If temperature is compared to other tracers, it can be useful to recall that natural or chemical solutes, which movement is governed by a similar equation, travel with pore

velocity $\mathbf{v}_\varepsilon = \mathbf{u}/\varepsilon$, which is about twice $\mathbf{v}_T$. Moreover, temperature is a not conservative tracer, as it also depends on heat conduction.

4.4 Péclet number

In the steady state ($\partial T/\partial t = 0$) one-dimensional case, Eq. (4.24) can be rearranged as follows:

$$u\frac{\partial T}{\partial x} = \frac{\lambda}{C_w}\frac{\partial^2 T}{\partial x^2} \tag{4.28}$$

On a domain of length l, with boundary conditions of Dirichlet type:

$$T(0) = T_i\,; \qquad T(l) = T_o \tag{4.29}$$

the variables can be made dimensionless as follows:

$$X = x/l\,; \qquad \theta = (T - T_i)/(T_0 - T_i) \tag{4.30}$$

The derivatives in Eq. (4.28) are now expressed in term of the new dimensionless variables:

$$\begin{aligned} &\frac{\partial X}{\partial x} = \frac{1}{L}\,; \qquad \frac{\partial T}{\partial \theta} = T_0 - T_i\,; \qquad \frac{\partial T}{\partial x} = \frac{\partial T}{\partial \theta}\frac{\partial \theta}{\partial X}\frac{\partial X}{\partial x} = \frac{T_0 - T_i}{L}\frac{\partial \theta}{\partial X} \\ &\frac{\partial^2 T}{\partial x^2} = \frac{\partial}{\partial x}\left(\frac{T_0 - T_i}{L}\frac{\partial \theta}{\partial X}\right) = \frac{\partial}{\partial X}\frac{\partial X}{\partial x}\left(\frac{T_0 - T_i}{L}\frac{\partial \theta}{\partial X}\right) = \frac{T_0 - T_i}{L^2}\frac{\partial^2 \theta}{\partial X^2} \end{aligned} \tag{4.31}$$

By substituting Eq. (4.31) in Eq. (4.28) the latter becomes:

$$Pe\,\frac{\partial \theta}{\partial X} = \frac{\partial^2 \theta}{\partial X^2} \tag{4.32}$$

where the dimensionless group:

$$Pe = \frac{u\,l^*\,C_w}{\lambda} \tag{4.33}$$

is defined as the Péclet number for heat transfer in porous media and is a measure of the importance of convective versus conductive heat transfer on a distance l^* representative of the phenomenon under investigation, which is called characteristic length.

The Péclet number is not characterized by the existence of an exact critical value below which the system is purely conductive. However, for Péclet numbers much less than unity the system is conduction dominated, while for values significantly greater

than unity the system is advection dominated. An order of magnitude of one indicates a conductive-advective system.

4.4.1 Geothermal Péclet number

The Péclet number defined in the previous section refers to a situation where heat flow and fluid flow are parallel. In natural hydrogeological systems, where the heat flow due to the natural geothermal gradient is mainly vertical and the fluid flow can be both horizontal and vertical, two distinct Péclet numbers should be used.

Van der Kamp and Bachu (1989), applying dimensional analysis theory to natural hydrogeological systems, showed that it is possible to give an estimate of the relative magnitude of convective and conductive heat transfer by means of a single Péclet number, if an appropriate definition of this dimensionless quantity is given.

They discriminate between closed and open systems (Fig. 4.3). A closed groundwater system is a system for which no fluid crosses the subsurface boundary and the inflow/outflow is given by recharge/discharge. An open hydrogeological system is characterized by subsurface inflow and outflow from or to other systems.

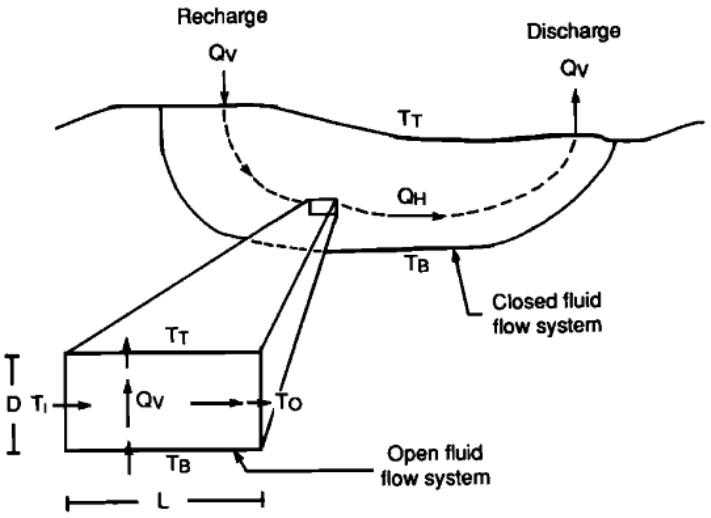

FIGURE 4.3: Schematic representation of open and close hydrogeological systems (Van der Kamp and Bachu, 1989)

In a two-dimensional domain Eq. (4.23) becomes:

$$C\frac{\partial T}{\partial t} + C_w\left(u\frac{\partial T}{\partial x} + w\frac{\partial T}{\partial z}\right) = \lambda\left(\frac{\partial^2 T}{\partial x^2} + \frac{\partial^2 T}{\partial z^2}\right) \tag{4.34}$$

where u and w are the horizontal and vertical components of the specific discharge.

A closed system characterized by the following characteristics is considered: horizontal length L, thickness D, temperatures T_T at the top and T_B at the bottom, total horizontal and vertical fluid flow Q_H and Q_V. The time scale of the processes under study is defined as τ . Horizontal and vertical characteristic specific discharge are defined as as $q_H = Q_H/D$ and $q_V = Q_V/L$. In order to perform a dimensional analysis of the importance of convective versus conductive heat transfer in the representative element, the variables are made dimensionless:

$$\begin{gathered} X = x/L\,; \qquad Z = z/D\,; \qquad \theta = (T - T_T)/(T_T - T_B)\,; \\ U = u/q_H\,; \qquad W = w/q_V\,; \qquad t^* = t/\tau \end{gathered} \tag{4.35}$$

By substitution of Eq. (4.35) into Eq. (4.34), the latter becomes:

$$\frac{D^2}{a\tau}\frac{\partial\theta}{\partial t^*} + Pe_g\left(U\frac{\partial\theta}{\partial X} + \frac{Q_V}{Q_H}W\frac{\partial\theta}{\partial Z}\right) = A^2\frac{\partial^2\theta}{\partial X^2} + \frac{\partial^2\theta}{\partial Z^2} \tag{4.36}$$

where the dimensionless group:

$$Pe_g = \frac{q_H C_w D A}{\lambda} \tag{4.37}$$

is defined as the geothermal Péclet number and $A = D/L$ is the aspect ratio of the representative element of the aquifer. The characteristic length is taken in the main direction of heat flux, which, in the case of terrestrial heat flow is vertical. Therefore the characteristic length l^* in Eq. (4.33) becomes the thickness D of the hydrogeological system. In a hydraulically non-homogeneus system where horizontal fluid flow is concentrated in a layer of limited thickness compared to the depth of the system, the question arises about which value of D should be used. Van der Kamp and Bachu (1989) suggest either the average depth of fluid flow or the depth of the bottom of the permeable part of the system. The value of L is given by the horizontal size of the flow path.

In the case of an open hydrogeological system with mainly horizontal fluid flow, the temperature T_i at the inflow is different from the temperature T_o at the outflow. By neglecting horizontal conduction of heat and defining a horizontal dimensionless temperature $\theta' = (T - T_i)/(T_o - T_i)$, the ratio of horizontal convective heat transfer to the vertical conductive heat transfer is given by

$$Pe_g\,\frac{T_o - T_i}{T_B - T_T}\,. \tag{4.38}$$

4.4.2 Unsteady problem

When the problem is advection dominated ($Pe \gg 1$), unsteadiness will be observed if the time scale of interest is smaller than the *residence time*: $\tau < \tau_{res}$. The residence time is the time spent by the water particle inside the system, i.e. the time passed from the moment the particle enters the system to the moment the particle exits the system.

When the problem is conduction dominated ($Pe \ll 1$), the parameter $D^2/a\tau$ gives a measure of the unsteadiness of the problem: if $D^2/a\tau \gg 1$ then unsteadiness will be observed over the time scale of interest.

4.5 Thermal properties of sediments

4.5.1 Thermal conductivity

Thermal conductivity of sediments mainly depends on the volumetric fraction and the properties of the phases that compose the soil (solid, water and air). The thermal conductivities of these phases vary across several orders of magnitude: they are in the order of 10 W/(m·K) for mineral grains, 1 W/(m·K) for water and 0.01 W/(m·K) for air. Such a contrast in thermal conductivities leads to preferential particle-level heat transport processes in granular materials: conduction in the solid particle, solid-to-solid conduction through the contact area (this conduction path plays an important role in dry soils), solid-fluid-solid conduction (this conduction path is especially relevant in partially saturated soils with pendular water) and conduction through the fluid within the porous network. A scheme of the conduction paths is reported in Fig. 4.4. The

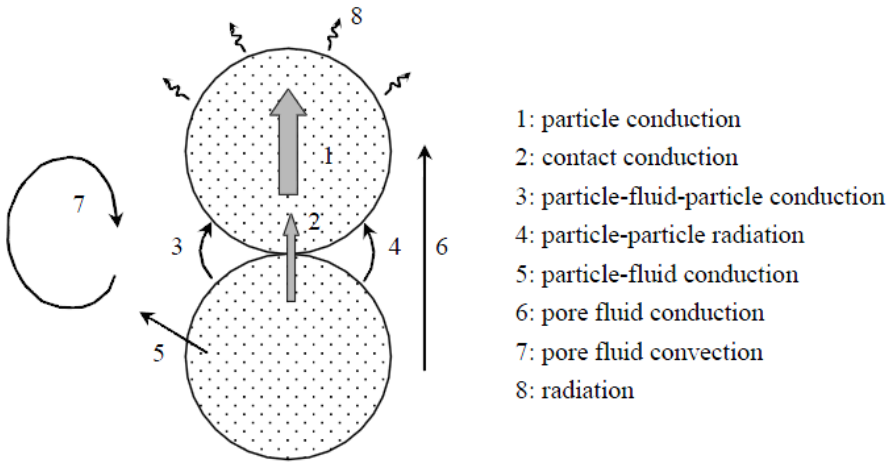

FIGURE 4.4: Thermal conduction paths in sediments (Santamarina, 2012)

intrinsic characteristics of a soil that determine its thermal conductivity are:

- mineralogy,
- particle size distribution,
- particle shape.

Mineralogy plays the main role. As the thermal conductivity of quartz is higher than that of all other common minerals and constituents found in soils, the thermal conductivity of sediments will be proportional to the volumetric fraction of quartz. Grain size distribution and particle shape determine the number of interparticle contacts: round particles and well-graded soils tend to attain denser packing, higher coordination number and thus higher thermal conductivities. This is important especially in the unsaturated condition. Mean particle size also plays a role: larger particles lead to higher thermal conductivities because the interparticle conductive heat transfer is proportional to the particle radius and inversely proportional to the inter-contact distance.

Thermal conductivity is also influenced by the state of the soil. Relevant parameters are:

- porosity,
- degree of saturation,
- effective stress,
- temperature.

Porosity and degree of saturation are key parameters in determining the thermal conductivity as they describe the volumetric fraction of the solid, liquid and gaseous phases. Thermal conductivity slightly increases with effective stress (at constant porosity) due to the improvement of the quality of particle-to-particle contacts.

Thermal conductivity of soils can be either determined through laboratory and in situ tests (see for example Witte et al., 2002) or estimated on the basis of geological and geotechnical information.

Saturated soils. Several methods have been suggested for calculating the thermal conductivity of saturated soils based on the thermal conductivity of their components. Any equation adopted should give a result lying between the upper limit, obtained from

the parallel flow model, and the lower limit, given by the series flow model. With the assumption that heat flows through fluid and solids in parallel, the equation is

$$\lambda = \varepsilon\lambda_f + (1-\varepsilon)\lambda_s \tag{4.39}$$

where λ_f and λ_s are the fluid and soil conductivities. In the series flow model the resistivities are added together giving

$$\frac{1}{\lambda} = \varepsilon\frac{1}{\lambda_f}(1-\varepsilon)\frac{1}{\lambda_s} \tag{4.40}$$

An average of the parallel and series thermal conductivities is obtained by taking the geometric mean

$$\lambda = \lambda_f^{\varepsilon}\ \lambda_s^{1-\varepsilon} \tag{4.41}$$

More complex models have been proposed by De Vries (1975) and by Woodside and Messmer (1961). However these models contain coefficients which are difficult to assess.

The geometric mean model (Eq. 4.41) has been proven to provide good estimates of the thermal conductivity of saturates sands. For pure quartz sands, evaluation of λ is straightforward due to known sand mineralogy, i.e., $\lambda_s = \lambda_q$, where λ_q denotes the thermal conductivity of quartz. The model can also be successfully applied to soils of diverse mineralogy by assessing the thermal conductivity of solid particles as the geometric mean of the thermal conductivities of quartz and other components:

$$\lambda_s = \lambda_q^{\theta_q}\ \lambda_o^{1-\theta_q} \tag{4.42}$$

where θ_q is the volumetric content of quarts and λ_o denotes the average thermal conductivity of minerals other than quartz. Thermal conductivities of common minerals in sedimentary rocks are reported in Table 4.2. At high quartz contents, the thermal conductivity of the minerals other than quartz plays a little role and can be assumed 2.0 W/(m·K). For coarse soils with a quartz content of less than 20%, Johansen (1975) suggested to use λ_o=3.0 W/(m·K).

Thermal conductivity of saturated sands is also influenced by temperature. Its variation is around 4 to 15% over a temperature range from 4 ℃ to 20 ℃. The thermal conductivity of quartz and other minerals noticeably decreases with temperature. Only feldspar shows an exceptional behaviour, with its thermal conductivity increasing as the

TABLE 4.2: Thermal conductivities of common minerals in sedimentary rocks determined at room temperature (Horai, 1971)

Mineral	**Thermal conductivity W/(m·K)**
Quartz	7.8
Calcite	3.4
Dolomite	5.1
Anhydrite	6.4
Pyrite	19.2
Siderite	3.0
Orthoclase	2.3
Albite	2.3
Halite	6.5
Mica	2.3
Chlorite	5.1
Kaolinite	2.8
Smectite (BMT)	1.8
Illite	1.8
Mixed-layer I-S	1.9
Water	0.60
Air	0.03

temperature decreases. On the other side, the thermal conductivity of water weakly increases with temperature. Consequently, for saturated sands a decreasing tendency of λ with T is present. Figure 4.5 shows experimental results presented by Tarnawski et al. (2011). At larger porosities the decrease of λ with T becomes weaker because of the higher water content.

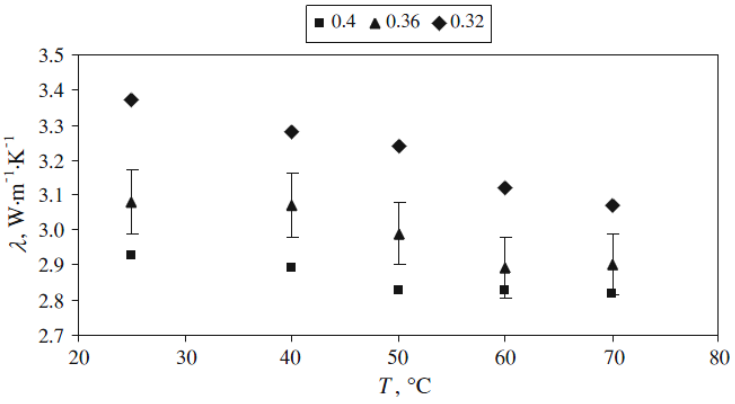

FIGURE 4.5: Experimental trend of thermal conductivity versus temperature for a pure quartz saturated sand (Ottawa sand C-109) at three different porosities. Uncertainty limits are reported for ε=0.36. (Tarnawski et al., 2011)

Fine inorganic soils contain clay sheet minerals (i.e. kaolinite, illite, montmorillonite) which average thermal conductivity is around 2.0 W/(m·K). But they can also contain feldspar, mica, quartz, calcite or other minerals in the clay or silt size range. Organic solids have a thermal conductivity that is about 1/10 of the conductivity of mineral solids. Values from 0.25 to 0.45 W/(m·K) are found in the literature (Farouki, 1981). Analytical models, which work well for sands, are not capable of predicting the thermal conductivity satisfactorily in clays and mudstones (Blackwell and Steele, 1989; Midttømme et al., 1998). A possible reason for the poor correlation between measured and estimated thermal conductivities is the influence of the texture of the material, which is not accounted for in the models. The measured anisotropy of thermal conductivity is an example of this influence. Thermal conductivity is shown to depend on grain size and grain size distribution: coarse grained materials have higher thermal conductivity than finer material.

The thermal conductivity of water does not change much with addition of soluble salts. Sea water has a thermal conductivity only a few percent less than that of pure water. However, the presence of ions and salts in water promotes flocculation during deposition thus affecting the structure of clay and consequently its thermal conductivity.

Partially saturated soils. As the values in Table 4.2 show, thermal conductivity of air λ_a is 22 times lower than that of water; therefore the thermal conductivity of dry soils is much lower than the thermal conductivity of saturated soils. As the degree of saturation increases, air is displaced by liquid water and the soil thermal conductivity increases. The effect of increasing moisture content on thermal conductivity depends on the type of soil (Fig. 4.6). In clayey soils thermal conductivity is less sensitive to water content, while sand and silt show a high rate of increase in thermal conductivity at the lower moisture contents. This is assumed to be mainly due to the formation of water bridges at the contact points that improve the heat transfer from grain to grain. By looking at Fig. 4.7, it is clear that thermal conductivity is related to suction, rather than to moisture content. At the same moisture content, different types of soil will have differences in the proportion of mobile water and absorbed water (water strongly held on the surface of the soil particles), because of variations in their specific surface area and their mineral nature. This will result in different suctions at the same moisture content.

The complexity of the interactions between water and soil particles, involving also hysteresis and changes of state, makes it difficult to fully evaluate by means of simple

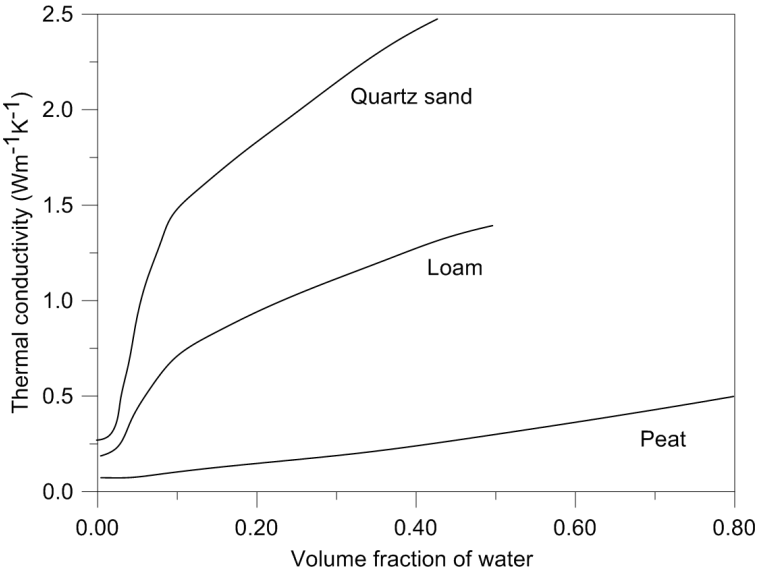

FIGURE 4.6: Thermal conductivity vs volume fraction of water (De Vries, 1975)

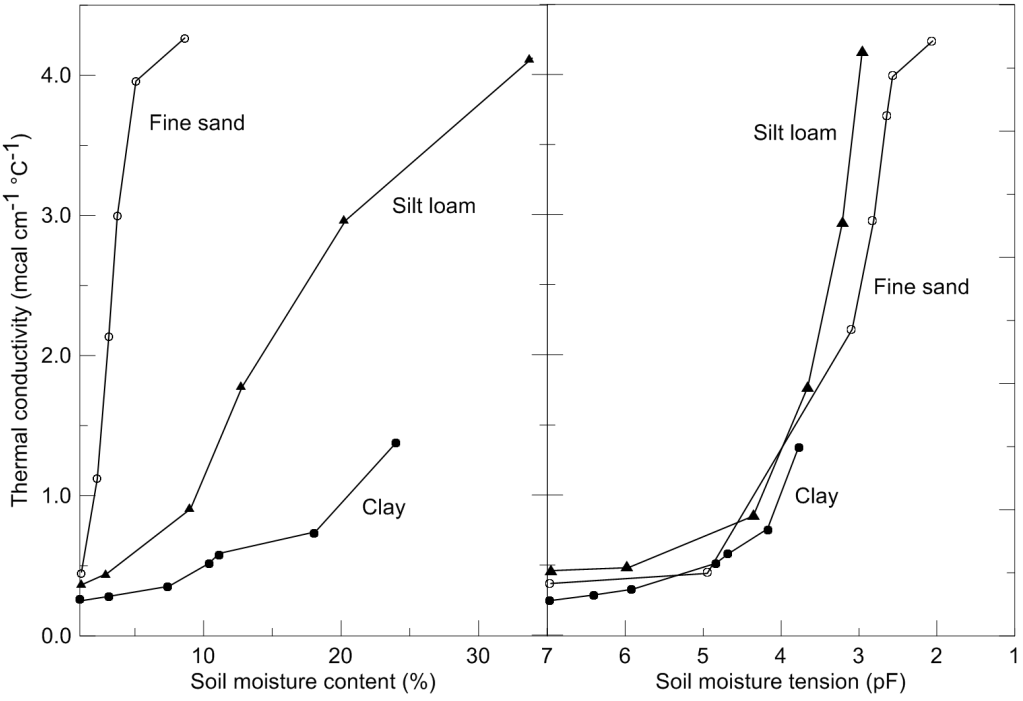

FIGURE 4.7: Thermal conductivity of different soils vs soil moisture content (left) and soil moisture tension (right). (Al Nakahabandi and Kohnke, 1965)

analytical models the effect exerted by water on the thermal conductivity of soils. At a first attempt, thermal conductivity at partial saturation can be calculated according to Johansen (1975), who suggested to interpolate between the dry and saturated values of the thermal conductivity by using the *Kesten number* (K_e):

$$\lambda = (\lambda_{sat} - \lambda_{dry})K_e + \lambda_{dry}\,. \tag{4.43}$$

For coarse unfrozen soils

$$K_e = 0.7 \log S_r + 1.0 \qquad \text{where } S_r > 0.05\,. \tag{4.44}$$

For fine unfrozen soils

$$K_e = \log S_r + 1.0 \qquad \text{where } S_r > 0.1\,. \tag{4.45}$$

4.5.2 Heat capacity

The heat capacity of a system is the sum of the capacities of its components. Therefore, the specific heat capacity of soil-water mixtures is calculated as a weighted average of the capacities of water and solids:

$$C = \varepsilon\, \rho c_f + (1 - \varepsilon)\rho_s c_s \tag{4.46}$$

where ρ and c_f are the density and specific heat capacity of the fluid while ρ_s and c_s are the density and specific heat capacity of the solid. More generally, for a partially saturated soil:

$$C = \varepsilon(1 - S_r)\rho_a c_a + \varepsilon S_r \rho c_f + (1 - \varepsilon)\rho_s c_s \tag{4.47}$$

where S_r is the degree of saturation, ρ_a and c_a are the density and specific heat capacity of air. According to Kersten (1949) the specific heat capacity of common soil minerals c_s differ only slightly, with a sufficiently accurate value of 795 J/(m·K) at 60 ℃ and 670 J/(m·K) at -18 ℃ and using linear interpolation for intermediate temperatures. Specific heat at 20 ℃ is about 730 J/(m·K). Density of the solid fraction can be assumed 2.65 kg/dm^3. Specific heat capacity of water slightly decreases with temperature between at 0 ℃ and 40 ℃ from 4218 J/(m·K) to 4178 J/(m·K). Its value is 4182 J/(m·K) at 20 ℃.

4.5.3 Thermal diffusivity

Thermal diffusivity is a measure of the thermal inertia of a medium: it characterizes the velocity at which a temperature variation is transmitted within the medium. In a substance with high thermal diffusivity, heat moves rapidly because the substance conducts heat quickly relatively to its volumetric heat capacity.

An increase in dry density causes an increase in the thermal conductivity, as seen in § 4.5.1. However, the diffusivity does not increase in proportion because the heat capacity also increases owing to an increase in the solids volume fraction (Fig. 4.8a). With increasing moisture content volumetric heat capacity and thermal conductivity increase at different rates, thus a maximum thermal diffusivity occurs at a certain water content (Fig. 4.8b).

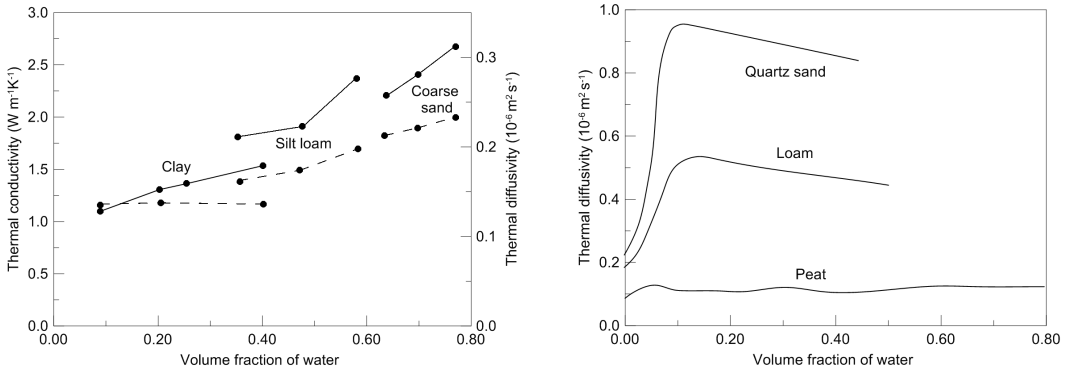

FIGURE 4.8: (a) Effect of texture and density on thermal conductivity (solid lines) and on thermal diffusivity (dashed lines) of air-dried soils (Al Nakahabandi and Kohnke, 1965); (b) effect of texture and water content on thermal diffusivity (De Vries, 1975).

4.5.4 Thermal dispersivity

In Eq. (4.23) the effect of thermal dispersion is neglected. Dispersion is the spreading of a heat (or solute) plume due to the presence of a pore system through which the fluid flow takes place. Because of the interconnected pore space, the microscopic streamlines fluctuate in space with respect to the mean flow direction (Fig. 4.9a). Flow velocity also varies through the cross-section of a single pore as in a capillary tube. It is usually assumed that the velocity is null on the solid surface and maximum at some internal point (Fig. 4.9b). Moreover, the maximum velocity itself varies according to the size of the pores. The spreading occurs both in the main direction of the flow and in the direction transversal to the flow, but the former is much higher. The transversal component of

mechanical dispersion is enhanced by diffusion across the steamtubes, promoted by the gradient between adjacent streamlines (Fig. 4.9c).

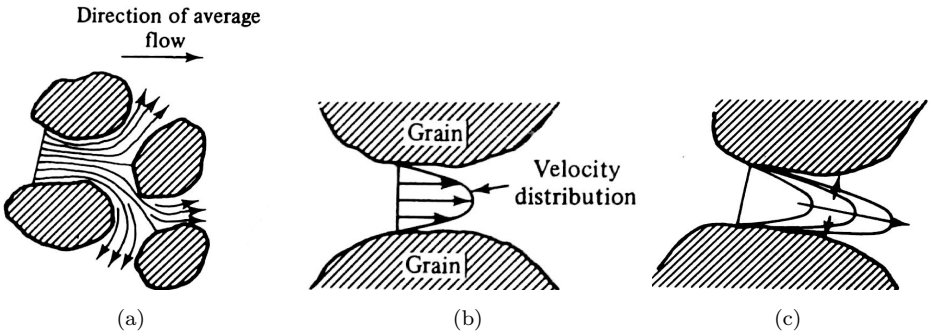

FIGURE 4.9: Spreading due to mechanical dispersion (a, b) and diffusion (c) (Bear and Verruijt, 1987)

Dispersion plays a key role in solute transport, which obeys the same law as heat transport. Here the effect of molecular diffusion and solute dispersion are described by the coefficent of *hydrodinamic dispersion*. Thermal dispersion is taken into account using an *effective thermal conductivity*, defined as the sum of two components: the bulk thermal conductivity of the porous medium in the absence of groundwater flow (λ) and a dispersive term. In the most general case the effective conductivity is a tensor. Under the assumption of isotropic thermal conductivity, this tensor can be expressed as follows (Bear, 1972; Cunat, 2012):

$$\lambda_{e,ij} = \lambda\delta_{ij} + \rho_w c_w \left[\alpha_T |\mathbf{v}|\delta_{ij} + (\alpha_L - \alpha_T)\frac{v_i v_j}{|\mathbf{v}|}\right]. \tag{4.48}$$

Two *dispersivity* terms, a longitudinal (α_L) and a transverse (α_T) one reflects the dependency of the degree of thermal dispersion on the direction of the flow. The relationship $\alpha_T = 0.1\ \alpha_L$ is commonly assumed for both solute and thermal transport but it may vary depending on the heterogeneity structure of the aquifer and the Péclet number.

The literature contains conflicting descriptions of the thermal dispersivity and of the relationship between thermal dispersivity and fluid velocity. Some authors suggested a linear relationship, as in Eq. (4.48), while others identified the possibility of a non-linear relationship (Rau et al., 2012).

Rau et al. (2012) investigated the differences between solute and heat transport in porous materials at the sub-metre scale . They reported that (1) the magnitude of conductive heat transport is orders of magnitude faster than solute diffusion and (2) the convective transport of heat is slower than that of solutes, because the thermal

capacity of the solids retard the advance of the thermal front. This results in different Péclet numbers for heat and solute which has the consequence that for the same Darcy velocity solute and heat transport are within different transport regimes (see Fig. 4.10). For example, at the Darcy velocities where advection dominates the solute transport, conduction dominates the heat transport. Consequently, thermal dispersion is much less significant than solute dispersion. Most importantly, however, the heat transport can be described by the same fundamental dispersion relationship previously established for solute dispersion. It should be specified that when defining the Péclet number, Rau et al. (2012) set the characteristic length equal to the average grain size diameter d_{50}, both for solute and thermal Péclet numbers.

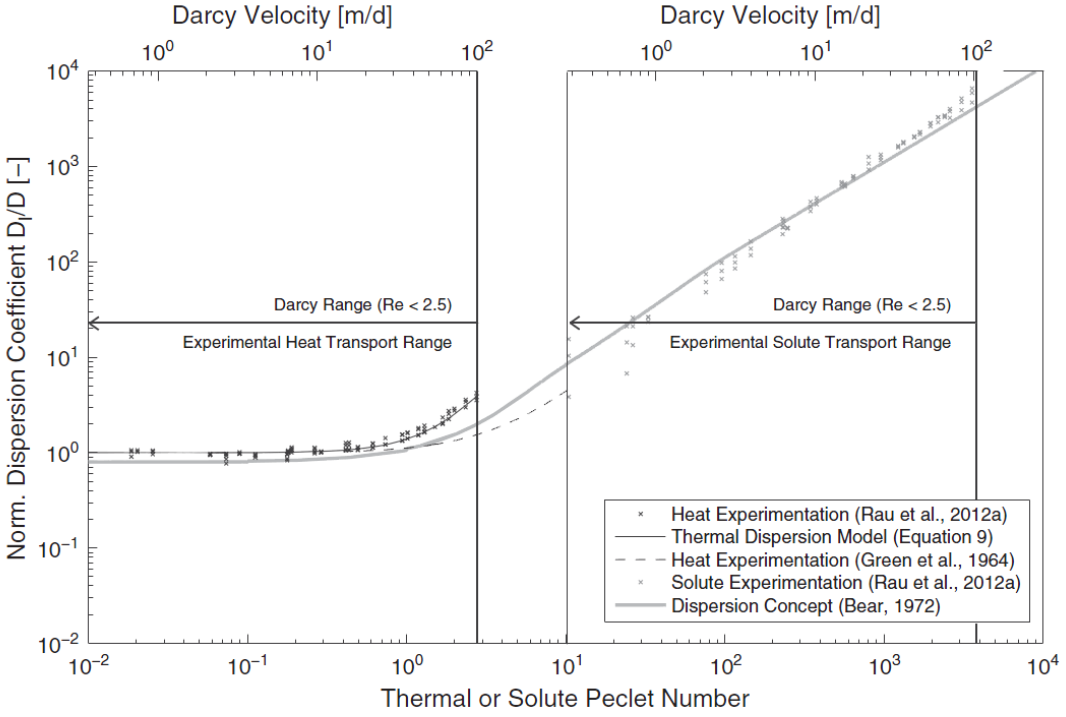

FIGURE 4.10: Experimental dispersion data at the sub-meter scale for heat and solute transport in natural homogeneous sand (d_{50} = 2 mm) as determined by Rau et al. (2012) and plotted on a conceptual graph adapted from Bear (1972). (Rau et al., 2014)

Figure 4.10 shows that at the sub-metre scale conduction is dominant with no dependency on velocity for Darcy velocities lower that 10 m/d ($\approxeq 10^{-4}$ m/s). However, differential transfer due to the heterogeneity of the hydraulic conductivity field at the macroscopic scale strongly contributes to dispersion and, as a consequence, thermal dispersion is somehow linked to the field scale. Empirical relationships of the type $\alpha_L = b\,(L)^m$ are given for solute transport, where L represents the field scale, and b and m are characteristic coefficients of the geological medium. Figure 4.11 shows longitudinal

dispersivity values reported in the literature: most of these values are located within the range given by empirical relationship for solute transport.

An analytical study performed by Molina-Gilardo et al. (2011) shows that, if thermal dispersion is assumed to be scale-dependent, neglecting thermal dispersion is critical for Darcy velocities higher than 10^{-8} m/s. Their study is based on a field scale of 10 m. In groundwater flow, where the hydraulic gradient is typically of the order of 10^{-3}, these velocities develop in medium sand to gravel aquifers. Accordingly, the range of hydrological conditions in which thermal dispersion can be ignored is large. This might be the reason why thermal dispersion has been traditionally neglected in heat transport simulation problems. The difficulty in getting a reliable estimate of the thermal dispersivity is also a factor that leads to generally neglect it.

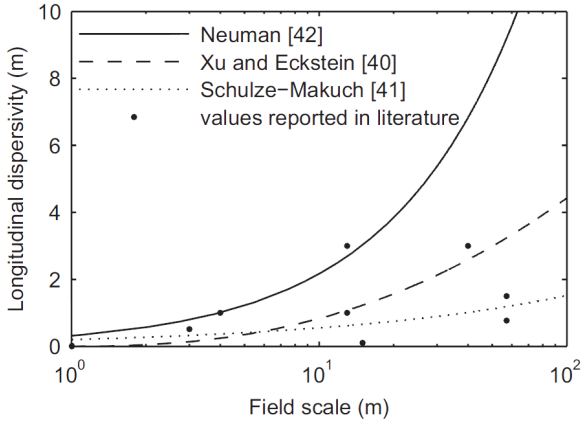

FIGURE 4.11: Relationship between field scale and solute longitudinal dispersivity according to different empirical relationships; values of thermal longitudinal dispersivities reported in literature are shown as dots (Molina-Gilardo et al., 2011).

4.6 Terrestrial heat fluxes

The temperature of the Earth is roughly constant in a zone extending from about 10 m to about 60 m deep. This constant temperature is the result of a complex interaction between heat flows from above (the sun and the atmosphere) and from below (earth interior). The heat flow coming from the earth interior is probably generated by a still cooling core or by the radioactive decay of elements.

Below this zone the temperature begins to rise: in the upper part of the crust the average geothermal gradient is about 25 ℃ for every kilometre of depth. The average continental conductive heat flux is around 60 mW/m^2 (Jessop et al., 1976). Some areas

have much higher heat flows because of deep fault zones, rifting, magmatic intrusions, or active tectonic forces (Fig. 4.12).

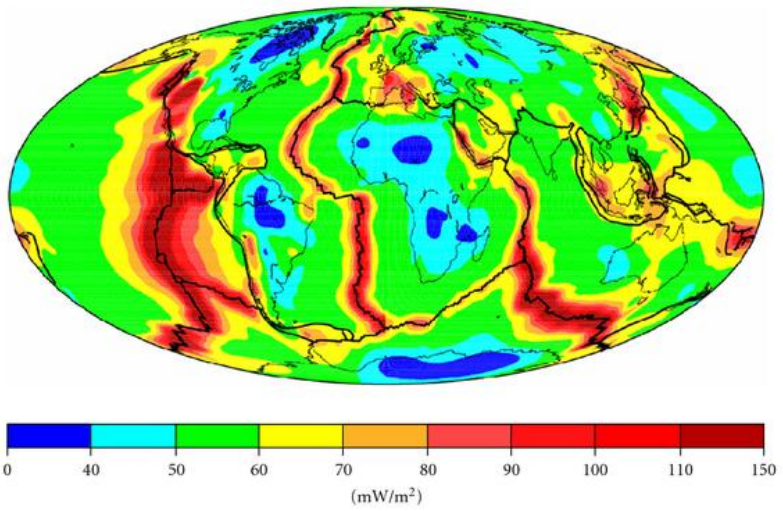

FIGURE 4.12: Map of the global geothermal heat flow (Hazma et al., 2010)

Above the zone at constant temperature, soil temperature fluctuates annually and daily as a consequence of the variations in air temperature and solar radiation. The interaction between the Earth's surface and the atmosphere includes many other factors, as depicted in Fig. 4.13, but these are often neglected in the formulation of the energy balance.

The annual variation of the daily average soil temperature at different depths can be estimated using a sinusoidal function. The sinusoidal temperature model was derived by Hillel (1982) by solving the following partial differential equation:

$$\frac{\partial T(z,t)}{\partial t} = a\,\frac{\partial^2 T(z,t)}{\partial z^2} \tag{4.49}$$

where $T(z,t)$ is the soil temperature at time t (d) and depth z (m) and a is the thermal diffusivity. The following assumptions are employed in the derivation of the model:

1. A sinusoidal temperature variation occurs at the soil surface $z = 0$:

$$T(0,t) = T_a + A_0 \sin\left[\frac{2\pi(t-t_0)}{365} - \frac{\pi}{2}\right] \tag{4.50}$$

where T_a is the average soil temperature, A_0 in the amplitude of the annual temperature function, t_0 the time lag from an arbitrary starting day to the occurrence of the minimum temperature in a year. Generally 1st January is assumed as the

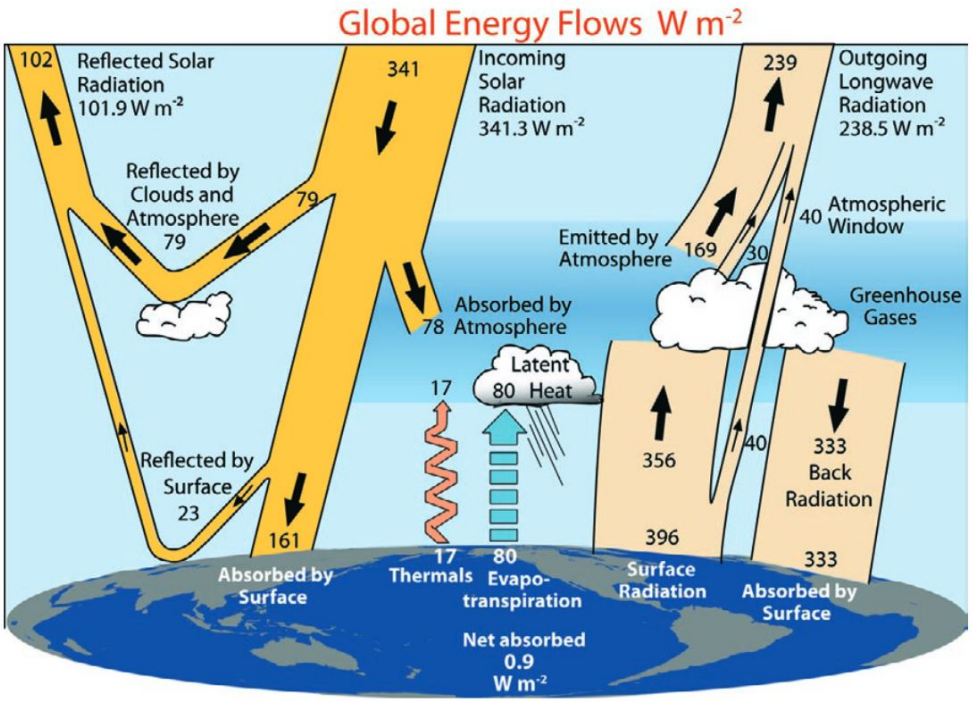

FIGURE 4.13: Estimate of the Earth's global annual mean energy balance. Over the long term, the incoming solar radiation absorbed by the Earth and atmosphere is balanced by the Earth and atmosphere releasing the same amount of outgoing longwave radiation. About half of the incoming solar radiation is absorbed by the Earths surface. This energy is transferred to the atmosphere by warming the air in contact with the surface (thermals), by evapotranspiration and by longwave radiation that is absorbed by clouds and greenhouse gases. The atmosphere in turn radiates longwave energy back to Earth as well as out to space. (Trenberth et al., 2009)

arbitrary starting day. Consequently, for central Europe a phase of $-\pi/2$ has to be added.

2. At infinite depth the soil temperature is constant and is equal to the average soil temperature.

3. The thermal diffusivity is constant throughout the soil profile and throughout the year.

According to the model the soil temperature at different depths is described by the following function:

$$T(z,t) = T_a + A_0 e^{-z/d} \sin\left[\frac{2\pi(t-t_0)}{365} - \frac{z}{d} - \frac{\pi}{2}\right] \tag{4.51}$$

where d (m) is the damping depth of annual fluctuation. The damping depth is given by

$$d = \sqrt{\frac{2a}{\omega}} \tag{4.52}$$

where $\omega = \pi/365\,\mathrm{d}^{-1}$.

It can be inferred from Eq. 4.51 that the soil temperature is a damped and delayed version of the air temperature at the surface, as the graphs in Figs. 4.14 and 4.15 show. Figure 4.14 also shows that the penetration of the daily temperature variation is generally smaller than 1 m. The maximum depth of penetration of both the daily and annual temperature variation depends on the thermal diffusivity of the soil (Fig. 4.16).

If air temperature is used as input instead of soil surface temperature, the model consistently underestimates soil temperatures by about 2 degrees Celsius (Wu and Nofziger, 1999). According to Nofziger (2005) good estimates of temperatures under bare soils can be obtained by simply increasing the maximum and minimum air temperatures by 2 degrees when defining the parameters in Eq. (4.51). The correction for soils that are not bare will likely be less since those soil temperatures are somewhat less due to shading from the plants .

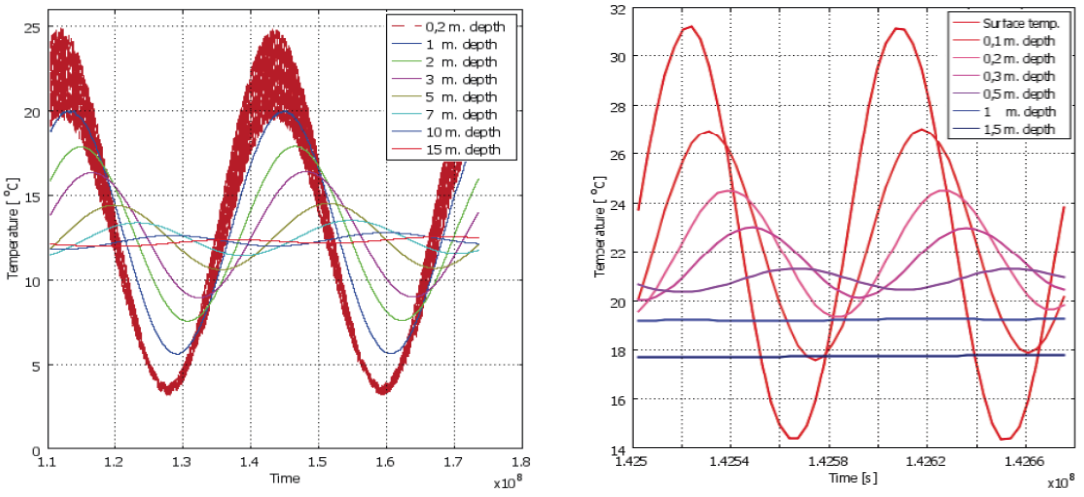

(a) (b)

FIGURE 4.14: Two year temperature (a) and two day temperature (b) at different depths in a soil with average thermal diffusivity (Eindhoven University of Technology, nd)

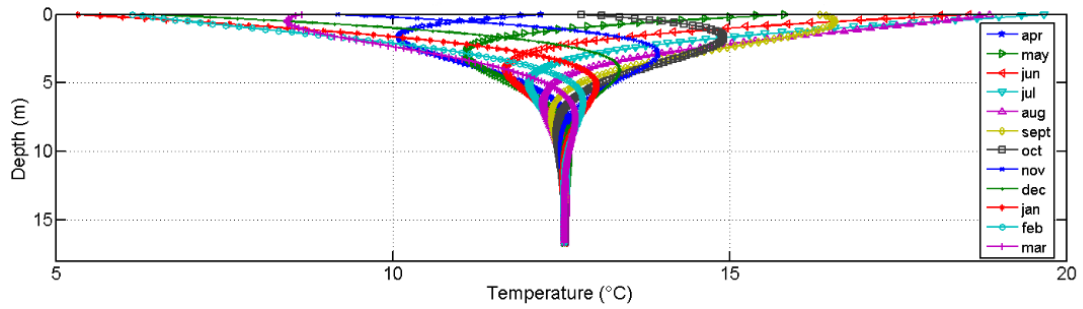

FIGURE 4.15: Evolution of temperature with depth at different times of the year (Cunat et al., 2009)

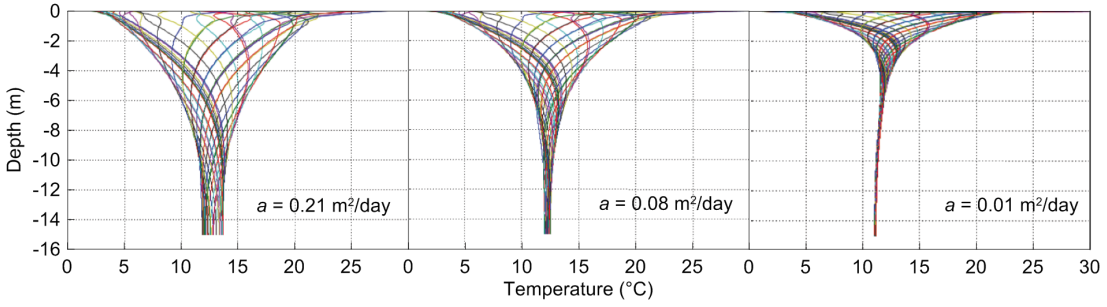

FIGURE 4.16: Evolution of temperature with depth at different times of the year for a soil with high, medium and low thermal diffusivity (Eindhoven University of Technology, nd)

Chapter 5

Distributed Temperature Sensing

Distributed Temperature Sensing (DTS) systems measure temperature by means of optical fibres. Their most attractive feature is that they provide the temperature field along an optical cable, which is the sensing element of the system, with high spatial resolution. The distributed nature of these systems has made them attractive for a number of environmental applications, including detection of seepage anomalies. This chapter contains a detailed description of the measuring principles and performances of DTS systems. Thereafter, it briefly explains the link between temperature and seepage flow and offers an overview of the available techniques for interpreting temperature data in terms of seepage anomalies.

5.1 Fibre-optic sensors

An optical fibre is a dielectric waveguide with a diameter in the order of few hundreds of μm that guides light up to several kilometres. Just to mention, it takes approximately 15 km to halve the light power in a standard silica fibre. An optical fibre is made by a glass or plastic *core* surrounded by a *cladding* of lower refractive index, which, continuously reflecting the light beam, entraps the light inside the core. Externally, one or more *jackets* protect the fibre from damage.

A large variety of fibre-optic sensors have been successfully developed and commercialized in the past three decades, mostly based on Bragg gratings and Fabry-Perot cavities (FP), providing one or several measurement points along a single cable. Generally, those technologies require special manufacturing to create a localized, sensitive element capable of producing a measurable signal. They compete effectively with other

standard sensor technologies and, in general, present the advantage of good signal stability, immunity to electromagnetic interference and the possibility of heaving multiple measurement points on a single sensor.

A feature that does not have any equivalent in standard technology is the possibility of a real spatial distributed sensing. The term *distributed sensing* designates the case in which an entire optical fibre becomes sensitive to the surrounding environment. Thus, the measurements are performed all along the fibre, connected to a proper reading device, rather than at few points.

5.1.1 Fibre Bragg Grating

A Fibre Bragg Grating (FBG) is created by "inscribing" a periodic variation of the refractive index into the core of an optical fibre using, for example, an intense ultraviolet source such as a UV laser. When the FBG is illuminated by a broadband source, a small amount of light is reflected at each position where there is a discontinuity of the refractive index. All the reflected light signals combine coherently to one large reflection at a particular wavelength when the grating period is approximately half the input light's wavelength. This is referred to as the Bragg condition; the wavelength at which this reflection occurs is called the Bragg wavelength and depends on the period of the modulation. Light signals at wavelengths other than the Bragg wavelength, which are not phase matched, are transmitted unaltered. Strains induced on the fibre by external forces or temperature variations cause a variation in the wavelength of the reflected signal, which is registered by an acquisition system (Fig. 5.1). If multiple FBGs with different index modulation periods, each one therefore producing a reflection on a different wavelength band, are inscribed on the same cable, several measurement points can be concatenated along a single fibre (Fig. 5.2). FBGs can be used directly as strain-gauges or temperature sensors; with the help of mechanical components, they can be configured as displacement, pressure (Fig. 5.3) and inclination transducers. The main limitation of the FBG method is the number of gratings that can be multiplexed in a single fibre.

5.2 Distributed fibre-optic sensors

Various techniques may be utilized to implement an optical fibre distributed measurement system. All the techniques are based on the analysis of the backscattered signal.

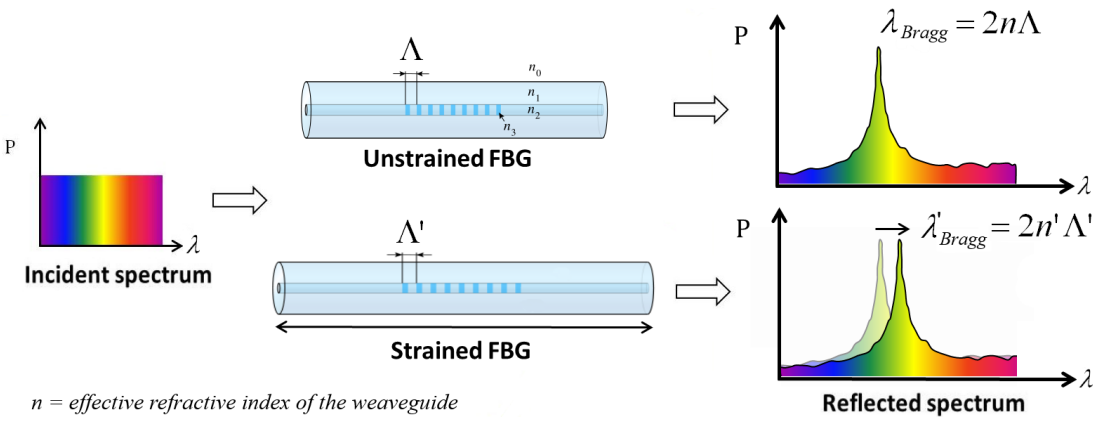

FIGURE 5.1: FBG functioning principle

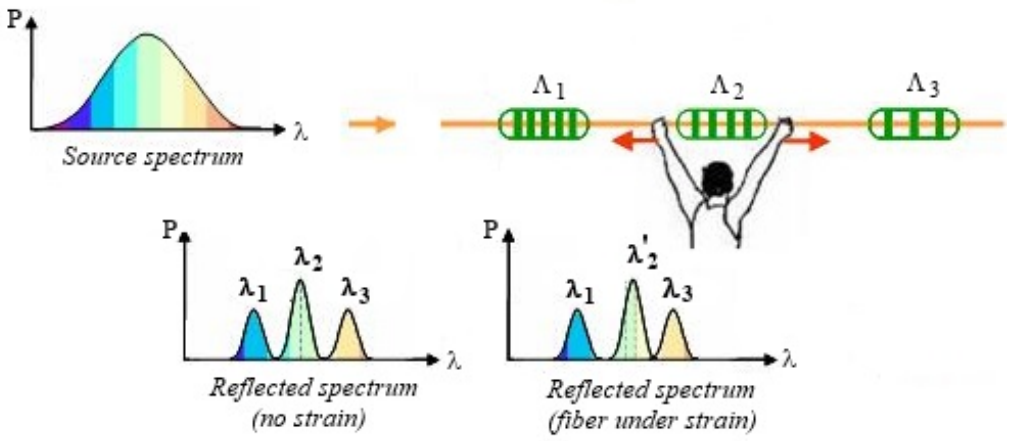

FIGURE 5.2: Concatenation of multiple FBG sensors

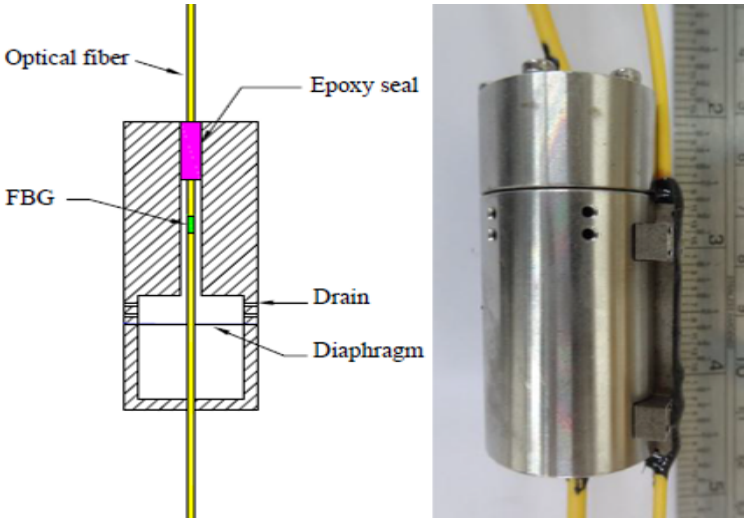

FIGURE 5.3: FBG pore pressure sensor (Disaster Prevention and Water Environment Research Center National Chiao Tung University, Hsin Chu, Taiwan)

As shown in Fig. 5.4, the light backscattered by an optical fibre segment without any defects or abnormal characteristics is spectrally decomposed into three distinct peaks corresponding to three phenomena.

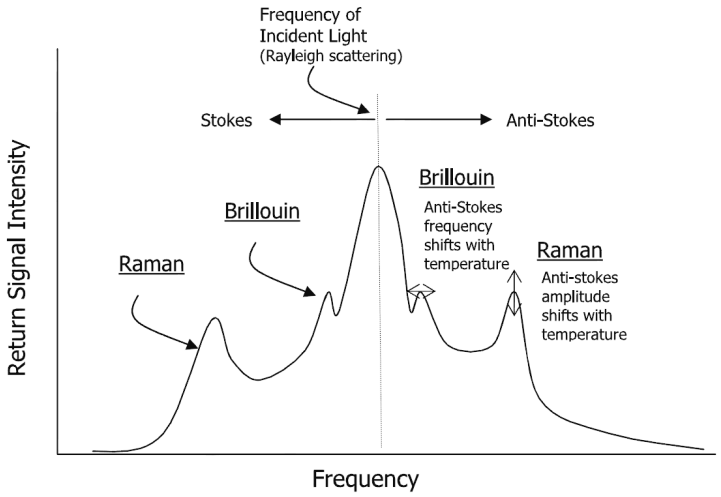

FIGURE 5.4: Backscattering spectrum of a monochromatic wave within an optical fibre (Selker et al., 2006b)

The backscattered component with the same wavelength as the injected wave relates to Rayleigh scattering, which is originated from the elastic collisions between the electromagnetic wave propagating in the fibre and the silica molecules. Intensity variations of the Rayleigh component are exploited to localize damages along optical telecommunication lines. The technique is known as Optical Time Domain Reflectometry (OTDR). It consists in injecting a laser pulse within an optical fibre and then measuring the power of the backscattered signal versus time. Time is converted in position along the fibre in the following way: a period Δt corresponds to a pulse round-trip between the end of fibre in which the signal is injected and a given point on the fibre located at a distance from that end equal to

$$\Delta x = \frac{c}{n} \cdot \frac{\Delta t}{2} \tag{5.1}$$

where c is the speed of light in vacuum and n the refractive index of the fibre.

Raman scattering, used in combination with OTDR, is the most commonly adopted technology to perform distributed temperature measurement. Raman scattering originates from laser light photon interaction with thermal vibrations of silica molecules (thermal photons). More precisely the anti-Stokes part of the Raman component (see Fig. 5.4) is mainly dependent on temperature. Therefore Raman distributed sensing

systems may use OTDR pulsed technique to perform distributed intensity measurements of the anti-Stokes backscattered light. However, the evolution of the anti-Stokes intensity must be augmented with a reference measurement since the signal loss in an optical fibre increase with time (increase with fibre ageing, connector dirt, fibre curvatures, etc.). A number of commercially available distributed temperature sensing devices automatically compensate for this loss by measuring the ratio between the Anti-Stokes and Stokes absorption line intensities, I_a and I_s respectively, being Stokes absorption temperature independent. The ratio of the two signals then allows for the calculation of the temperature of the fibre by means of the following relationship:

$$\frac{I_a}{I_s} \propto \exp\left(\frac{h\,\Delta\nu}{k\,T}\right) \tag{5.2}$$

where h is the Planck constant, k is the Boltzmann constant, T is the absolute temperature, and $\Delta\nu$ is the separation between Raman anti-Stokes and Stokes light frequencies.

Another phenomenon also occurs when an optical pulse is launched into an optical fibre, called Brillouin scattering (see Fig. 5.4). The frequency shift of the Brillouin component, ν_B, is proportional to temperature variations ΔT and strain ε:

$$\Delta\nu_B = C_T \Delta T + C_\varepsilon \varepsilon \tag{5.3}$$

where C_T and C_ε are characteristics of the type of fibre. Also Brillouin scattering employs OTDR.

Because of the cross-sensitivity to strain and temperature, measuring temperatures by using Brillouin scattering requires that the optical fibre does not experience any strain that could be misinterpreted as a temperature change. For this reason strain-free fibres have to be used to perform temperature measurements via Brillouin scattering.

On the other hand, strain measurement by means of Brillouin scattering requires that the temperature variation experienced by the fibre is know. For this reason Stimulated Brillouin scattering is often used in combination with Raman scattering when strain measurements are to be performed.

Distributed sensing based on Brillouin scattering is usually implemented in *single-mode* fibres which have a 9 μm diameter core and are a standard in telecommunications, while distributed sensing based on Raman scattering is generally exploited in *multi-mode* fibres that have a bigger core. It follows that, although Raman DTS is the favourite

method for temperature measurements, Brillouin DTS can opportunistically make use of telecommunications infrastructure.

In this work a sensing system based on Rayleigh backscatter and Optical Frequency Domain Reflectometry (OFDR) has been used for performing measurements in a small-scale model, in order to overcome the limited spatial resolution provided by OTDR. As explained in Palmieri and Schenato (2013), Rayleigh scattering is *per se* independent of almost any external physical field for a wide range of conditions. Actually, in Rayleigh-based sensing techniques the scattering itself is used only to track and to reveal propagation effects that the backscattered light experiences while travelling back into the fibre. These include attenuation and gain, phase interference and polarization variations and allow for the backscattered light to keep memory and encode any change in the surrounding environment. These propagation effects may affect also Raman and Brillouin scattering, but they are usually neglected just because Raman and Brillouin scattering offer direct sensing mechanisms. An important peculiar feature of Rayleigh-based sensing systems is that they cannot provide absolute strain/temperature, but only the variation with respect to an initial condition, assumed as reference. Although a number of propagation effects can be exploited for sensing, systems based on phase interference are the only Rayleigh-based systems successfully commercialized to date.

In this work an Optical Backscatter Reflectometer (OBR) from Luna (Gifford et al., 2005; Luna Inc., nd) has been used in combination with a standard single-mode fibre. The OBR measures the spectral shift in the local Rayleigh backscatter pattern, which is both temperature and strain dependent. Like for Brillouin systems, the cross-sensitivity to temperature and strain has to be conveniently faced.

5.2.1 Resolution

Despite the optical fibre itself constitutes the sensor, the heart of the monitoring system is the interrogator. It includes, besides many other components, a laser, which produces a light beam, a photo detector, which detects the signal backscattered by the fibre, and a CPU, which transforms the detected signal in a strain/temperature information. The resolution of the system is strongly influenced by the interrogator and by the acquisition parameters.

As reported in Tyler et al. (2009), since only a small fraction of the incident light is scattered in an optical fibre, signal strengths are very low, which is one of the main

limits of the distributed measurement, since this limits the dinamic range and the spatial resolution.

Greater signal strength may be achieved by longer integration time. For example, the resolution of Raman DTS is a function of the Stokes to anti-Stokes backscatter ratio precision, which is proportional to the number of photons collected by the detector. The number of photos collected is in turn dependent on the size of the fibre core and on the acquisition time. For this reason, multimode fibres are generally adopted in Raman DTS and, all other parameters being equal, a longer time-averaging period improves the resolution of the temperature measurement. However, longer temporal averaging reduces the probability of detecting rapid changes in the temperature signal.

The spatial resolution of OTDR, i.e. the spatial accuracy with which the specific physical field is mapped, is given by the length of the probing pulse. This occurs because the power measured at a certain time is the superposition of the scattering generated by a section of fibre with length equal to half the pulse length. For instance, a 10-ns pulse corresponds to a resolution of 1 m. Note, however, that this should be considered as a lower bound to the resolution. In fact, the spatial resolution of a distributed fibre-optic sensor depends on other factors, among which the signal to noise ratio (SNR) of the measurement.

As a rule of thumb, to increase the spatial resolution one should reduce the pulse length, but this causes a reduction of the SNR. The SNR ratio depends indeed on the power backscattered by the fibre, that is proportional to the pulse energy which, in turn, depends on the pulse duration. And compensating the reduction of the pulse length by increasing the pulse power is not recommended, since nonlinear effects would be originated and the signal would be strongly distorted.

In general there is a trade-off between spatial resolution, temperature resolution and spatial range.

In addition, the sampling rate of the instruments is limited by the circuit-processing speeds used by each component. High sampling rate can lead to signal loss at high spatial resolution. A longer time-averaging interval can significantly improve the resolution of distributed measurements and can compensate for the attenuation that affects the signal when the cable is very long.

Raman DTS systems are generally characterized by a temperature resolution of approximately 0.1 ℃. A temperature resolution approaching 0.01 ℃ is also possible with

long integration times (in the order of hours) if the DTS device itself is thermally stabilized (Selker et al., 2006b), which is hardly achievable in the field. A spatial resolution up to 1 m can be obtained for lengths up to 1000-2000 m; a spatial resolution as little as 30 cm can be achieved on shorter cables; a spatial resolution up to 2 m is guaranteed for lengths up to tens of kilometres. Resolution degrades with increasing distance but can be restored by increasing the acquisition time. Figure 5.5 shows a typical graph included in DTS datasheets where temperature resolution is depicted as a function of spatial range and integration time for a given spatial resolution. Most DTS instrument manufacturers declare the minimum spatial resolution achievable by the system, that can be adjusted upward if coarser-scale measurements are more appropriate.

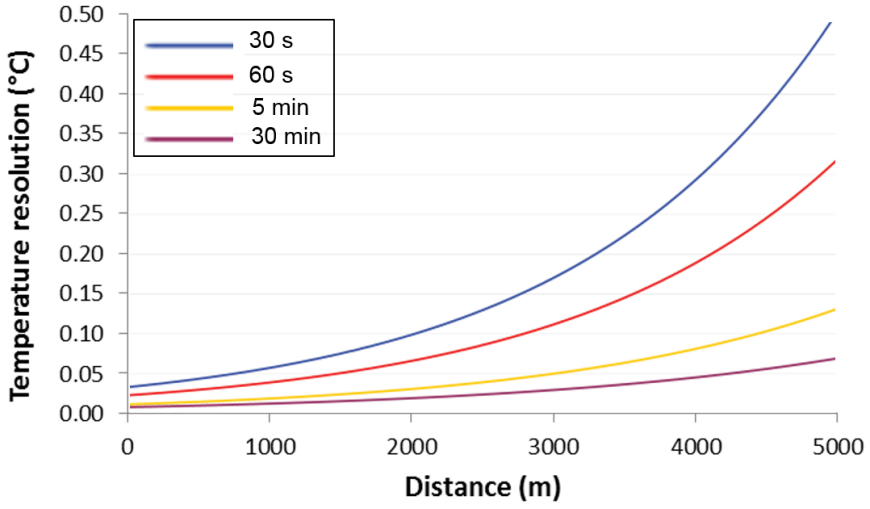

FIGURE 5.5: Temperature resolution of a commercial Raman DTS system as a function of distance and acquisition time for fixed 2 m spatial resolution

Commercial Brillouin-based systems claim an accuracy of 2 $\mu\varepsilon$ ($= 2 \cdot 10^{-6}$) or less for strain and higher than 0.1 ℃ for temperature; about range and spatial resolution, they are capable of performing measurements over few tens of kilometres, with 0.5 m or slightly better resolution.

Commercially available Rayleigh-based sensing systems are directly capable of measuring temperature and strain variations with 0.1 ℃ and 1 $\mu\varepsilon$ resolution, respectively. Range is in the order of some tens of metres, with a sub-centimetre spatial resolution. The range can be extended up to 2 km, with a 3 cm spatial resolution and 0.5 ℃ temperature resolution. Differently from standard time-domain techniques, in Rayleigh-based sensing systems based on OFDR, a non pulsed source is used. The

source is a continuous wave laser, whose optical frequency is linearly swept in a bandwidth that may extend to several tens of nanometres. Of course this advantage comes at the cost of an increased complexity and a limited range of measurement.

While the temperature resolution (or precision) is a function of the DTS system and acquisition parameters, the accuracy, i.e. the capability of measuring the absolute temperature, depends on the calibration process, that is carried out by placing the cable in an environment of known constant temperature, attaching the cable to the DTS, and taking a long-time integration data set. Details on the procedures of calibration can be found in Hausner et al. (2011).

5.2.2 Installation

The bare optical fibre (core + cladding) cannot be directly used for field applications. First, the optical cable has to be robust in order to endure civil engineering works conditions: handling, soil compaction, and so forth. Moreover, it must resist to a chemically aggressive environment (water and salinity). Finally, rodents often happen to destroy cables, which can be solved by adopting metal protected cables. Consequently, it is recommended to choose cables meant for burial.

As a side effect, the coatings isolate the fibre from its environment. For what concern temperature measurements, Selker et al. (2006a) have demonstrated that for a stainless-steel housed fibre the time to adapt to temperature changes is very acceptable: laboratory tests, consisting in applying abrupt step-wise changes in temperature, showed that 95% of the applied temperature variation was detected by the fibre within 15 seconds. For what concern strain measurements, a possibility consist in integrating the optical cables into a geotextile fabric, thus exploiting the high soil-textile interface friction properties to transfer very small strains from the soil to the fibre.

Fibre installation in existing dikes often occurs at the landside toe. This kind of installation is usually neither technically difficult nor expensive. Fibre-optic cables can be easily buried in the ground by plowing, trenching or microtrenching (Fig. 5.6); in complicated situations directional drilling can be employed.

Where the ground is soft and relatively free of rocks and the land is flat and has no obstacles for the movement of heavy equipment, direct burial by plowing is a very fast method that allows to install several km of cables in a day.

Plowing needs dedicated equipment and operators. Plowing in fibre-optic cables is indeed a process that demands care and experience because of the strict requirements for cable support, bending radius, tension or vibration.

Trenching may be easier because it requires smaller machinery and less room. All sizes of trenchers are commonly available, so specific fibre-optic equipment is not needed.

Microtrenching can be a faster alternative to trenching. A groove is sawed in the pavement or soil, few centimetres wide, the cable is dropped and the groove is refilled, often with the same material vacuumed up during the sawing. Microtrenchers are also easily available. Their main limitation is the excavation depth.

More detailed informations on installation are given by The Fiber Optic Association (FOA, 2010).

In zoned dams and dikes of new construction optical cables can be also deployed downstream of the core or deep in the foundation soil. Optical fibres can also be installed during reparation works below an impervious revetment, in order to assess its continuity.

(a) (b)

FIGURE 5.6: Installation techniques for fibre-optic cables: (a) plowing, (b) microtrenching.

5.2.3 Environmental applications of Distributed Temperature Sensing

Raman-based DTS technology was originally developed by the oil and gas industries and has been used since the late 1980s for pipeline monitoring, fire detection and protection, and other industrial applications (Hausner et al., 2011).

The use of DTS for geo-environmental applications started in the 90s when the temperature was monitored in boreholes for fluid logging, i.e. the identification of subsurface flow zones and the assessment of their hydraulic properties (Hurtig et al., 1994). In the same years the effectiveness of DTS for leakage detection in dams was assessed

(Johansson, 1997). Optical fibres are now installed at several dam sites in Sweden, Germany, France, Turkey, China, Canada etc. (Johansson and Sjödahl, 2004).

In the mid 2000s DTS systems, after achieving acceptable levels of spatial and temporal resolution, along with high temperature accuracy and resolution, became an important tool in environmental sciences.

They have been used for detection and quantification of groundwater flow in losing and gaining streams (Vogt et al., 2010; Westhoff et al., 2007; Selker et al., 2006a) as well as for detection of illicit connections in sewers (Hoes et al., 2009).

DTS has also been employed for monitoring soil moisture (Steele-Dunne et al., 2010; Striegl and Loheide, 2012) and evapotranspiration (Koonce et al., 2011), based on the fact that moisture influences the thermal properties of soils.

In the field of geothermal energy production, besides fluid logging, estimation of the thermal properties of soils and of thermal wall resistance can take advance of distributed temperature measurements (Günzel and Wilhelm, 2000).

Further applications in the environmental field are described in Selker et al. (2006b) and Suárez et al. (2011).

5.3 Leakage detection by temperature measurement

5.3.1 Basics

Temperature measurement for seepage detection was first proposed in Germany by Kappelmeyer (1957). Extensive research on the applicability of the method was performed during the 90s. Initially the measurements were carried out in standpipes, by progressively lowering a temperature probe or by permanent installations of few probes at different depths (Johansson, 1997). A big impulse to the diffusion of the method was given by the Distributed Temperature Sensing. By means of horizontal installations along a dam, with the optical cable in direct contact with the soil, DTS made possible to perform almost spatially continuous measurements.

The basic principle is that heat transfer in soils generally occurs by conduction, that is the transfer mechanism typical of solids. However, when the pore water flows at significant velocity ($u > 10^{-6} - 10^{-7}$ m/s), the heat transferred by the moving fluid (heat advection) becomes predominant over the heat transferred by conduction. Intense seepage flow can therefore cause a variation of the temperature field with reference to a

situation with no or little flow and such variation can be proportional to the intensity of the flow.

For this reason, temperature measurement allow detection of preferential seepage flows promoted by cracks, voids and permeable zones, also consequent to internal erosion. On the other hand, temperature measurement allow identification of zones where flow concentrates and thus where internal erosion is more likely to occur.

There are two approaches to detect seepage. The first one is a passive approach and is based on absolute temperature changes within the body of the dam caused by the seepage water. This method is limited to cases where a temperature gradient between the seepage water and the dam material exists (Dornstädter, 2013). That is why it is also referred to as the *gradient method*. To surpass this limitation the *heat-pulse method* or *active method* can be adopted. This method is mostly used in combination with hybrid sensing cables in which the optical fibres are coupled with copper wires. By heating the sensing cable for a short period (from 10 min to 1 h), cable sections within zones of higher water saturation or even flow zones appear as sections with increased heat transport, i.e. they heat up less. This work focuses on the passive approach, in that it purely investigates the influence of a seepage flow on the subsurface temperature distribution.

5.3.2 Data interpretation

Data interpretation techniques can be classified according to their suitability for real-time detection of leakages rather than for long-term monitoring of the conditions of the structure. In addition, some techniques have a physical base while other are purely statistical. An important difference is made by the position of the sensor: data from sensors close to the surface, as those installed at the downstream toe of a dam or dike, are treated differently form data coming from sensors located at significant depth, as those in the core or in the foundation of a dam.

When the sensor is deployed at a depth where the soil temperature is not influenced by the air temperature and other external factors ($z \gtrsim 10$ m), leakage detection relies on the seasonal temperature variation of the reservoir water. In some cases, seepage anomalies can be directly detected based on comparison between temperature changes in space or time for measuring points located along the same cable. Figure 5.7 reports the comparison between the temperature variation in time for three points similarly located

but at different chainages. Measurements with large temperature variation indicate a higher seepage flow than points with small temperature variation. Also the time-lag between the maximum temperature measured in the reservoir and the maximum temperature occurring at the measuring point can be used to identify high seepage flows.

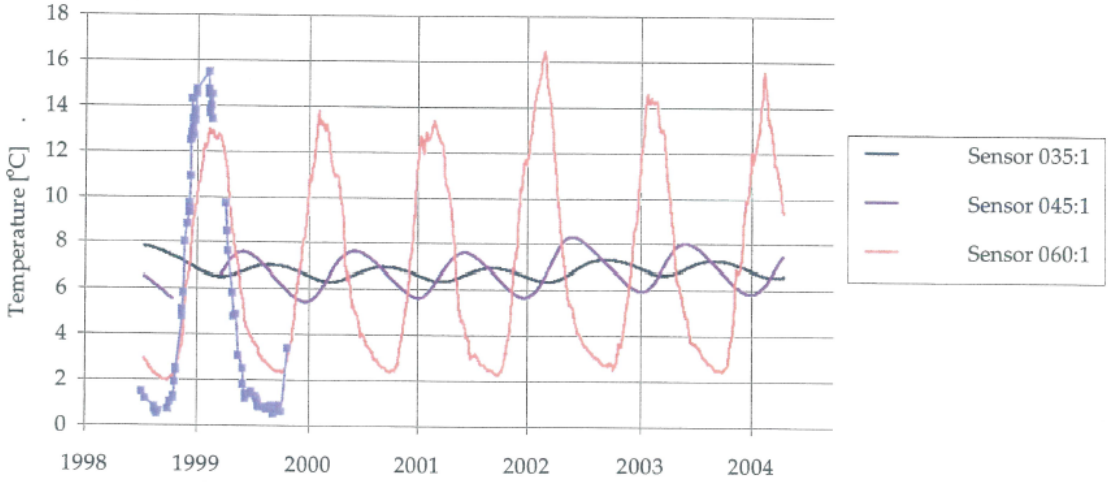

FIGURE 5.7: Temperature measurements made in piezometers similarly located in the bedrock at chainage 35, 45 and 60. The curve with markers represents the reservoir temperature. (Johansson and Sjödal, 2009)

Quantification of leakages is also possible, if analytical tools are adopted. Claesson et al. (2001) developed a numerical solution for the two-dimensional advection-diffusion problem depicted in Fig. 5.8b. The problem consists of a homogeneous aquifer layer with constant horizontal flow, confined by two impervious layers, and is representative of a defect extending from the upstream to the downstream face of a dam core at large depth. Pure heat conduction occurs in the impervious layers, while heat advection and conduction occur in the aquifer layer. Heat conduction in the x-direction is neglected. A periodic temperature is prescribed at the inlet. The thickness of the seepage zone and the magnitude of the seepage flow are estimated adjusting their value in the model as long as the measured data fit the simulated data. For univocal quantification it is to be assumed that the sensor is inside the seepage zone and not in the surroundings. Figure 5.9 shows the comparison between the real temperature data in Fig. 5.7 and the best approximation calculated by the model.

When the temperature sensor is installed at the downstream toe, and thus is quite shallow, the measured temperature is essentially influenced by the annual fluctuation of the air temperature. When a significant seepage flow develops, the saturation degree

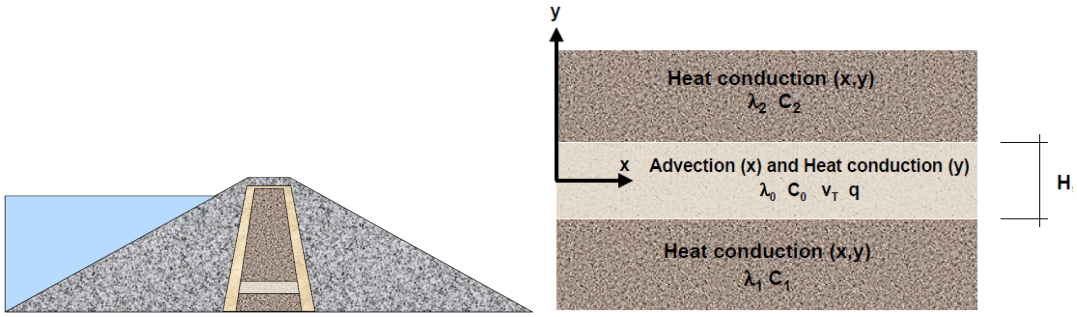

(a) (b)

FIGURE 5.8: Zone of increased seepage in a dam core: concept (a) and sketch of the two-dimensional thermal model (b) (Johansson and Hellström, 2001)

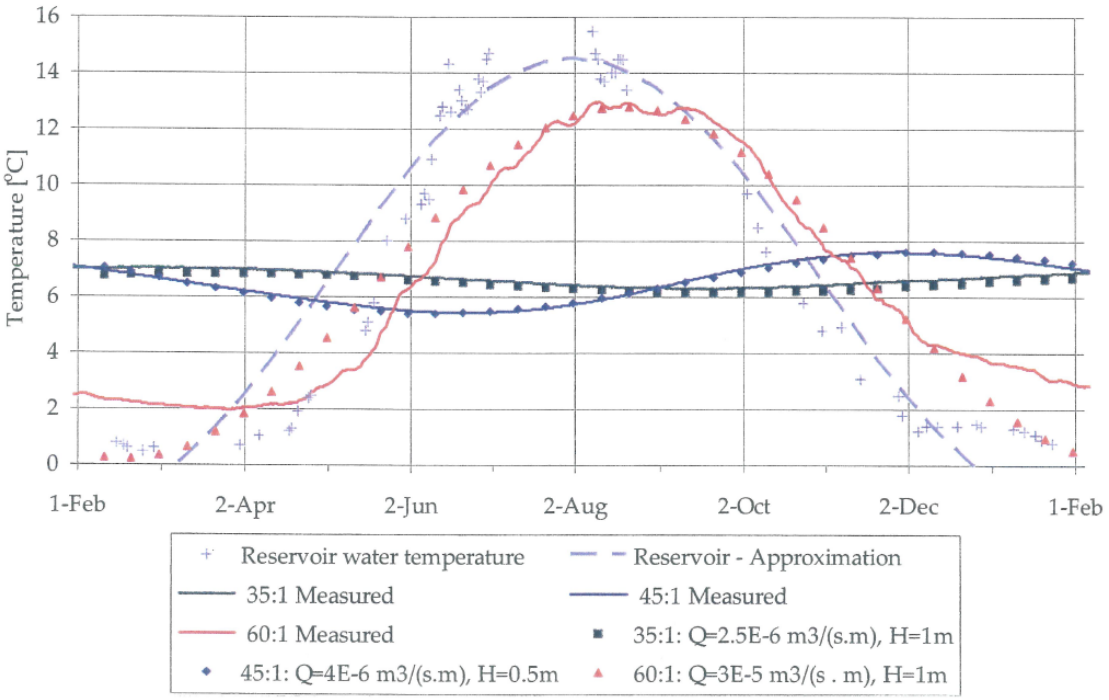

FIGURE 5.9: Fitting of measured temperature data using a two-dimensional advection-diffusion model (Johansson and Sjödal, 2009)

of the soil increases and thus the influence of the air temperature. On the contrary, when the soil is everywhere fully saturated, increased seepage velocity in the leakage zone results in a lower influence of the air temperature.

For sensors at shallow positions, automated early detection of leakages can be performed by comparing the expected temperature to the real temperature. As described in Nygren (2013), the expected temperature is calculated with a sine approximation of 100 measured data points recorded in the preceding 365 days. A sine curve is in many cases a good approximation of the temperature curve in a dam, although at high latitudes the sum of more sine functions works better. Every time a new point is measured,

a comparison between this point and the fitted curve is made to detect changes. If the temperature difference is greater than the set alarm threshold, an alarm occurs. Figure 5.10 gives an example. An alternative approach compares the slope of the line connecting the last measurements to the slope of the line connecting the corresponding measurements performed the previous week. Different threshold values should be set for points along a dam that show a different temperature excursion. It is important to do an extensive research on the dam before the choice of an alarm value is made.

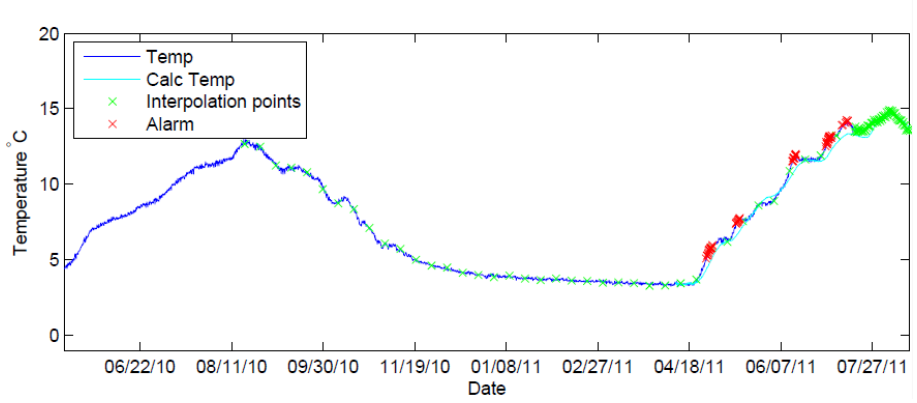

FIGURE 5.10: Comparison between expected temperature and measured temperature. The sum of two sine functions is adopted as interpolation function to determine he expected temperature. (Nygren, 2013)

An effective tool for long term monitoring is the Impulse Response Function Thermal Analysis (IRFTA) by Radzicki and Bonelli (2010b). It requires for analysis a minimum of two months temperature series and allows both identification of the leakages and estimation of their intensity. The impulse response function describes how an input temperature signal is modified by the dam to produce, as output signal, the temperature at the sensor location. In its most general version, the transfer function is a superposition of two functions that describe the response of the dam to two different inputs: the temperature of the reservoir water and the air temperature. The function has four parameters that represent time-lag and damping associated to the two input signals. The impulse response function is calculated at each point, on the basis of the data provided by the sensor; seepage anomalies are identified by local variations of the function parameters. If the influence of the air temperature is negligible or, on the contrary, there is no influence of the reservoir temperature, a two-parameter model can be adopted.

5.3.2.1 Statistical methods

The soil temperature close to the surface is not only influenced by the air temperature, but also by solar radiation, wind, precipitation, and ground heterogeneities resulting in a spatially variable response to the external factors. In order to separate from the data all factors other than flow rate that influence the soil temperature, a number of signal processing techniques have been recently developed. These techniques, that do not require any physical model of the dike, have been tested on real data collected along intake channels managed by EDF (Electricité de France). Different methods have been adopted to address the need for both real-time detection of leakages and long-term monitoring of the conditions of the structure.

The daily dissimilarity method by Khan et al. (2010) exploits the idea that daily temperature variations at "singularities" (leakages, existing structures etc.) differ from daily temperature variations at homogeneous non-singularity zones. The method consists in estimating a reference vector from the 24-h temperature variations at all sensing distances, using a common technique in signal analysis Singular Value Decomposition (SVD). A dissimilarity measure is determined for each distance, comparing the recorded data to the reference vector. Figure 5.11 shows an example of comparison between measured data and reference vectors for singular and nonsingular zones.

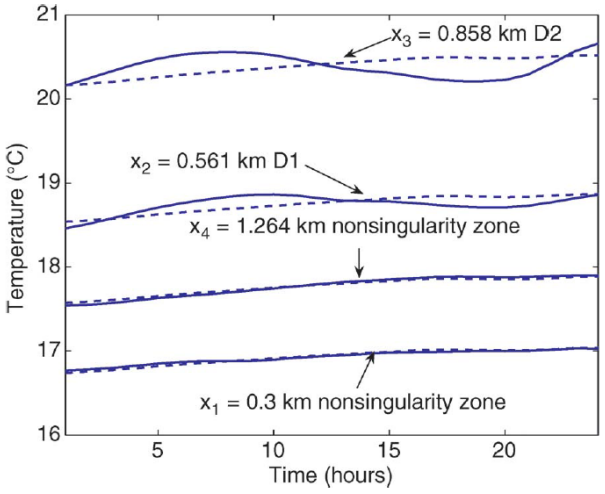

FIGURE 5.11: Solid lines: 24-hour temperature profiles at four different distances; singular zones D1 and D2 present a different trend compared with nonsingular zones. Dashed lines: estimated reference vectors (at same day and distances as solid lines); they show large deviations from the data in the singular zones than in the nonsingular ones. (Khan et al., 2010)

A variable alarm threshold needs to be applied to the dissimilarity measures, since the estimated temperature variations are not the same for each day. Integral part of

the method is therefore the calculation of a variable threshold on the basis of a prefixed probability of false alarm. Daily dissimilarity proved to be capable of detecting backward erosion piping few days before failure of the dike occurred in a large-scale test performed in the Netherlands in 2009 (see § 6.1). Some results are presented in Beck et al. (2010). Sub-daily analysis with 12-h windows proved to be helpful in improving the temporal resolution of the detection method.

The main disadvantage of SVD is that the reference vector is highly influenced by the response of the ground in which the sensor is buried. The latter, in turn, is strongly affected by ephemeral phenomena as precipitations. As a consequence, SVD does not perform well in days of intense precipitations. This is particularly disadvantageous for the monitoring of river dikes, because high water stages (and high probability of occurrence of internal erosion) often correspond to periods of heavy rains.

Khan et al. (2008b) proposed to identify data affected by precipitations using higher order statistics criteria and to neglect such data in the construction of the reference vector. A robust approach by Khan et al. (2008a) makes use of *blind source separation* techniques to separate ground response and other phenomena from the leakages. Khan et al. (2008a) also suggest to apply the source separation algorithm on spatial temperature gradients - rather than directly on temperature data - since this limits the effect of the ground response and precipitation, as well as the effect of seasonal variations. Source separation is suitable for analysis of monthly or sub-monthly data, but not for real-time monitoring.

5.4 Some considerations on the active method

Figures 5.12 and 5.13 illustrate the response of hybrid optical cable to heating. The cable has been placed in air, dry soil, saturated soil and saturated soil with significant fluid flow. It can be observed that the effect of the water content - expressed by the temperature difference between dry and saturated sand (purple and cyan curves) - is larger than the effect of the flow velocity - expressed by the temperature difference between no flow and high seepage flow, both in saturated condition (cyan and brown curve). Hence, the accuracy of the measurements that is necessary to identify leakages in saturated soils is higher than the accuracy needed to detect soil moisture changes. The effectiveness of an active system for leakage detection depends indeed on the span of

temperature difference between small and fast velocities in comparison with the accuracy of the DTS device.

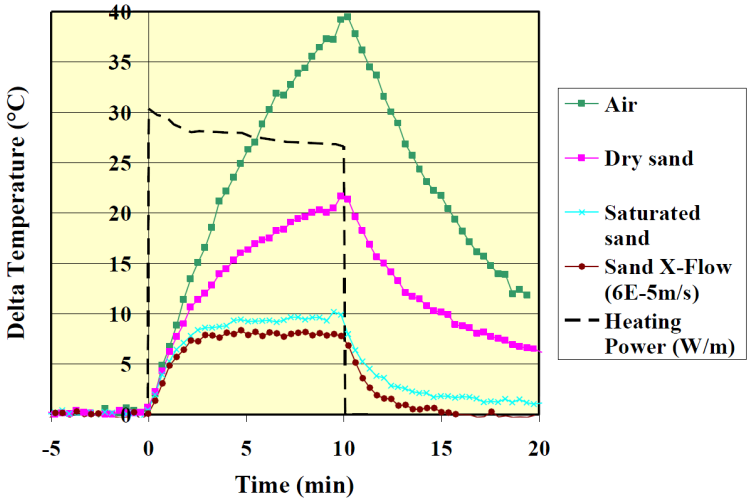

FIGURE 5.12: Laboratory test on a hybrid cable deployed in a sand sample (Côté et al., 2009)

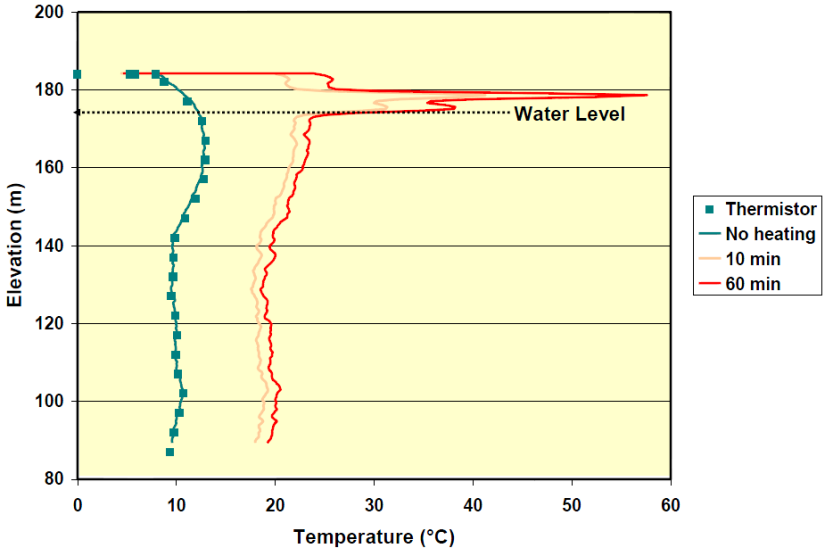

FIGURE 5.13: Temperature profile in a borehole before and after heating at Péribonka Dam (Côté et al., 2009)

As Fig. 5.14a shows, the thermal response varies with the flow velocity in the range 10^{-5} to 10^{-3} m/s. The span of temperature measurement increases with decreasing cable diameter, increasing heat input and with additional several millimetre cable coating of a geotextile fleece. By these measures the measuring range can be extended to 10^{-2} m/s (Fig. 5.14b). Being sand more permeable than dam core materials, the application of the active method to piping detection would exploit the right portion of the curve. The more permable the sand, the lower the temperature variation induced by the anomalous

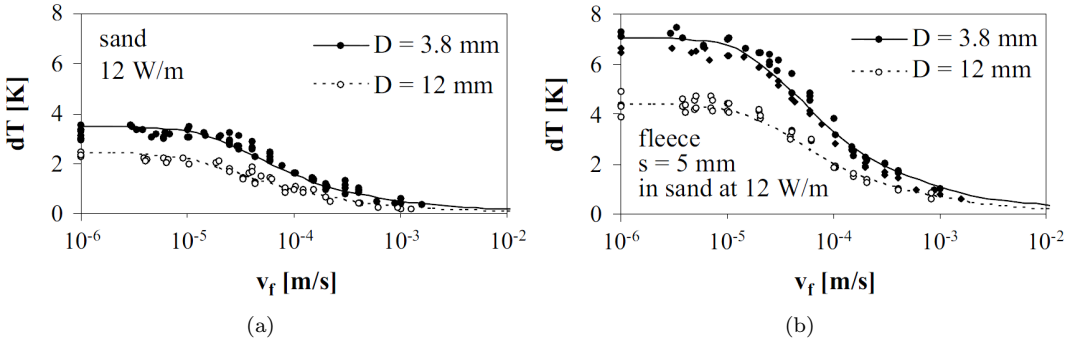

FIGURE 5.14: (a) Temperature increment in pure sand after 60 min of heating expressed as a function of Darcy velocity, for two different cable diameters D: test data (dots) and theory (lines). (b) The same, with additional fleece cable coating (Perzlmaier et al., 2007).

flow. For example, if the base soil is a clean coarse sand ($K = 10^{-3}$ m/s, $u = 10^{-4}$ m/s) and a robust cable (12 mm diameter) is used, then the temperature anomalies induced by heating will be less than 1 ℃.

A 0.1 °C temperature accuracy of the measuring system is therefore recommended. Such accuracy requires a heat input not less than 10 W/m, limiting the range from 1 to 2 km using 400 V or to 3 to 4 km if the voltage is transformed to 1000 V. Any device with better temperature accuracy will either allow for less heat input or higher accuracy of the distributed flow velocity measurement (Perzlmaier et al., 2007).

A major inconvenient of the active method is the limited range of action that is reduced to 15 cm around the optical fibre (Perzlmaier, 2007, as cited in Cunat et al., 2009).

Chapter 6

A large-scale failure test

This chapter describes a large-scale test in which backward erosion piping was induced in the foundation of a dike. The high spatial density of pore pressure and temperature measurements allowed detailed mapping of the pipes and detection of thermal anomalies induced by piping. In addition, a clear picture of the heat transport induced by the seepage flow, both in the sound foundation soil and in the eroded areas, was obtained.

6.1 The IJkdijk testing program

The IJkdijk (Dutch for "calibration dike") is a Dutch research program initiated in 2005 with the double goal of testing new monitoring techniques under field conditions and advancing the knowledge on geotechnical failure mechanisms on a large scale. In the past eight years, various large-scale experiments, mainly on dikes, have been carried out on a special test site at Booneschans, in the Northeast of The Netherlands. The program included an overtopping test on a 4 m high grass slope (2007), a slope stability test of a 100 m long, 6 m high dike resting on soft soil (2008) and a series of four tests on piping (2009). A conclusive series of tests, which are described in the following section, was carried out in 2012.

6.2 All-In-One Sensor Validation Test

In 2012 a series of three large-scale tests was carried out in Booneschans under the name of All-In-One Sensor Validation Test (AIO-SVT). The first part of the name refers to the fact that every test included more than one single possible failure mechanism. The second part of the name expresses the main purpose of the experiment, i.e. testing

the predictive power of levee sensor systems. In addition, the experiment aimed at investigating the effectiveness of failure prevention measures.

The dikes tested were named after their position in the field. East and West dikes (placed in the northern part of the test site, see Fig. A.1) had a sandy foundation soil vulnerable to piping and a sandy core vulnerable to micro-instability. The West dike was equipped with two controllable drainage tubes as prevention measures against piping and micro-instability (depending on the location of the tube); the East dike was equipped with a granular filter against piping. The South dike (on the left in Fig. A.1), was built on a very soft soil and was tested against slope instability with a deep sliding plane and local instability of the clay cover. In this chapter the piping test run on the West dike is described in detail.

After the collapsed East dike was removed, a new dike was built at the same location, as part of another project aimed at testing the capability of a geotextile filter to prevent piping. A description of all the failure prevention measures tested at the Booneschans test site can be found in Koelewijn et al. (2014).

All the dikes tested were instrumented with both new sensor technology and proven technology as reference monitoring. New sensor technology included remote sensing, as ground-based LiDAR, ground-based radar (Fig. A.19) and infrared thermography (Fig. A.12). A number of surface geophysical methods were employed: ground penetrating radar (Fig. A.20), self-potential, passive seismic and electrical resistivity. Moreover, fibre optic sensors were tested: the dikes were equipped with FBG strain and temperature sensors (Fig. A.18a), FBG pore pressure sensors (Fig. A.18b) and distributed strain and temperature sensors (Fig.A.13).

The All-In-One Sensor Validation Test aimed for more than the mere testing of innovative sensor technologies. It aimed at testing the predictive power of full-service levee sensor systems, i.e. sensors combined with data processing and an information system producing a timely, reliable warning in case failure may occur. In this framework, tools for real time data visualization, dike safety assessment and information sharing between stakeholders were also tested.

Twelve companies participated in the test providing sensors (or services) partially at their own expenses and submitting daily predictions of the failure mode and conditions at which failure would occur. The companies that provided monitoring systems used their own measurements to make predictions, while the companies providing dike safety

information systems had access to the data of most of the monitoring systems installed, being validated and shared through a central data base.

Subsequently, the performances of the monitoring systems were judged by the test leaders according to the following criteria: robustness of the instrumentation, accuracy, density and frequency of the measurements, time for installation and adjustment, processing time, interpretation and quality of prediction. The information systems were judged by their ability to combine data of different sources, the application of various techniques and methods to arrive at meaningful information, the clarity of statements and of course the quality of the prediction. The evaluations of the performances can be found in Koelewijn et al. (2013) and, more extensively, in De Vries et al. (2013).

6.3 The West dike

The piping tests were carried out in the facility showed in Fig. A.2. The facility consisted of two basins delimited by clay embankments and overlain by an impermeable foil to separate the tested soil from the subsoil. The basins were filled with sand, compacted in layers to a relative density of about 65 to 75 percent, up to a thickness of 3 metres.

The basins and the sandy foundation layer were the same as in the 2009 piping experiments, although, in order to get rid of the organic matter accumulated, the upper part of the sand layer (40 to 60 cm) was replaced by a new sand of almost the same properties.

In the West dike the new sand had a d_{50} of 0.30 mm and a uniformity coefficient d_{60}/d_{10} of 1.69. Sieve curves of the old and new test sand are given in Fig. A.7. Before the construction of the West dike, the controllable drainage tube to be tested as a piping prevention measure was installed. Afterwards, the sand was saturated using about 50 percent vacuum pressure and part of the instrumentation was installed.

The West embankment (on the right in Fig. A.2) was 3.5 m high, 19 m long and 15 m wide at its base. As depicted in Fig. A.4, the lower part of the dike was made of a 0.7 m clay layer, which separated hydraulically the foundation from the dike body. The dike body was made of a 1.7 m high small clay dike at the upstream side, a sand core behind the small clay dike and a cover of organic clay. This composition is found in many smaller dikes around the Netherlands. The layer of clay dividing the subsoil susceptible to piping from the upper part of the dike vulnerable to micro-instability and erosion from overtopping had been compacted very well, while the higher parts of the

dike (sand core, small clay dike at the upstream side and the cover layer) were hardly compacted at all.

The test dikes and the clay embankments delimiting the basins enclosed two reservoirs, each one with a volume of approximately 2000 m^3, to be filled during the test to apply the desired hydraulic load. Downstream, lower dike rings enclosed two ponds equipped with a drain, necessary to ensure full saturation of the foundation layer and to maintain a nearly constant downstream water level.

6.3.1 Reference monitoring system

A reference monitoring system adopting conventional instrumentation was installed to enable the test leaders to closely monitor the course of the test. It consisted of two liquid level sensors to record the water levels in the upstream and downstream reservoirs, a flow meter placed at the discharge point of the downstream basin and 77 pore pressure transducers placed in the dike during construction. 4 lines of 17 pore pressure sensors each were installed in the foundation and 3 lines of 3 sensors each were installed in the sand core, right above the clay layer. In addition, visual inspection was performed at regular intervals; position and size of the sand-boils were recorded and documented by pictures. The reference monitoring data were not disclosed to the participants during the tests.

The pore pressure sensors in the dike foundation (also in the core?), given their tricky position of at the interface between two soil layers, were manufactured on purpose, inserting a liquid level sensor in a parallelepiped case with a filter at the bottom (Fig. A.10). It was so ensured that the pore pressure in the sand, and not in the above clay, were measured. The transducers adopted were based on piezoresistive ceramic sensor elements and were compensated for temperature and barometric pressure. Declared accuracy ranged between 0.06 and 0.2 kPa. The instruments were deployed on the sand layer after that the latter was saturated under vacuum and before the embankment was built.

6.3.2 Temperature monitoring system

The temperature inside the dike was measured by means of distributed fibre optic sensors encased in a geotextile strip (Fig. A.13).

The high soil-textile interface friction properties and the strong link between the optical cable and the geotextile help to transfer and detect very small soil strains. Moreover, if a leak occurs far from the fibre, it can be collected and drained through the plane of the fabric faster than flowing through the soil only.

The strip contained 4 fibres, 2 for strain and 2 for temperature measurements. Stimulated Brillouin and Raman scattering were used to measure, respectively, strain and temperature. The monitoring system allowed detection of soil strains as low as 0.01%. Temperature changes were measured with an accuracy of 0.1°C and a spatial resolution of 1 m. The frequency adopted was of a measurement every 30 min.

A single strip was deployed in 5 profiles, lengthwise the dike, at the interface between the sand layer and the bottom of the dike (Fig. A.9, A.14 and A.15) and on 3 levels along the downstream slope of the dike, in trenches that were excavated a few tens of centimetres below the surface (Fig. A.16). Due to a mistake during installation, the temperature was not measured in the upstream basin.

An infrared camera was used to map the surface temperature of the downstream slope as well as part of the upstream and downstream basins.

6.4 Measurements and observations

The Cartesian system chosen to reference the monitoring data is centred on the western side of the upstream toe; the x-axis is oriented longitudinally to the dike while the y-axis is oriented transversally, from upstream to downstream. As large part of this work is dedicated to the modelling of seepage and heat transport by advection, the y-axis is oriented in the seepage direction. However, the position of the sensors was originally referred to the downstream toe, as pipes originate downstream and progress towards upstream.

6.4.1 Test execution

The test on the West dike started on Tuesday, August 21st, 2012, at 4:30 pm (local time). This moment is defined as t=0. The upstream level was increased in steps related to the expected failure mechanisms (Fig. 6.1).

1. **Initialization.** The upstream basin was filled up to 0.50 m. Stabilization of the outflow was awaited in order to determine the bulk hydraulic conductivity of the

sand layer from the flow measurements: an value of $1.25 \cdot 10^{-4}$ m/s was obtained. Afterwards, the level was increased by 0.50 m.

2. **Non-critical level for piping.** The level was increased in steps of 0.20 m each, up to 1.80 m. Each time, the next step was undertaken when the pore pressures were stable and the sand transport had stopped.

3. **Critical level for piping.** The level was increased in steps of 0.10 m each, up to 2.20 m (level that was fatal in 2009). Each time, the next step was undertaken when the pore pressures were stable and the sand transport had stopped.

4. **Critical level for microinstability (overpassing of the small clay dike).** By design, the level should have been increased in steps of 0.10 m, but time constraints did require to accelerate the failure. The water level was thus increased continuously up to 3.43 m.

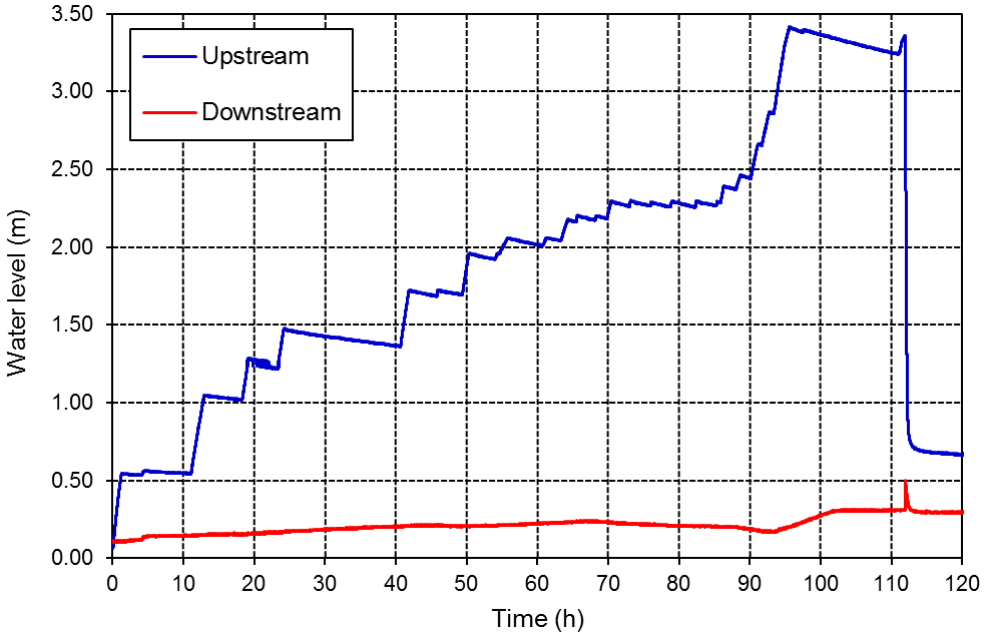

FIGURE 6.1: Water level in the upstream and downstream basins during the test

Failure by micro-instability of the sand core occurred on the sixth day of the test, on Sunday, August 26$^{\text{th}}$, at 8:24 am (t=111.9 h), while the upstream basin was being refilled after the level had decreased overnight due to seepage. Other mechanisms which played a role in the test are compaction of the dike at first filling and piping (backward seepage erosion) through the sand layer underneath the dike.

6.4.2 Compaction at first filling

Cracks appeared on the crest and on both slopes already at a water level in the upstream basin that was much lower than the top of the small clay dike, which is about 2.4 m above the top of the lower sand layer. The first cracks on the crest were discovered on at t=13.9 h (Fig. A.23), while the upstream level was only about 1.2 m above the top of the lower sand layer. At t=20 h, a large crack was discovered on the upstream slope, in the middle of the dike just above the water level (Fig. A.24). The cracks increased in size over time and a height difference developed between the two sides of the cracks on the crest: the upstream side got lower in course of time.

The pore pressures in the sand core close to the upstream side, just behind the small clay dike on top of the well-compacted clay layer, started to rise at t=21 h. First this happened only in the middle and on the east side, than, at t=24 h, also on the west side, see Fig. 6.2.

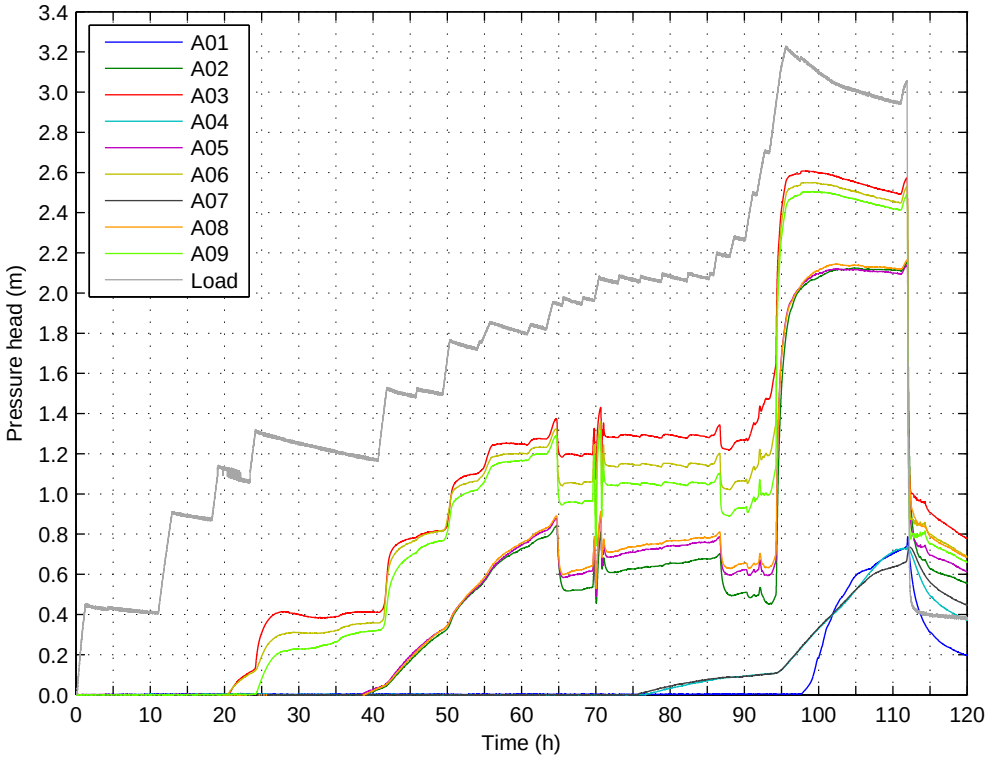

FIGURE 6.2: Pore pressures in the sand core

An explanation for these observations is that the water from the upstream basin could easily flow through the slightly compacted clay of the small clay dike, which was placed on top of the well compacted clay layer separating this small clay dike and the sand core from the lower sand layer. Through this slightly compacted clay, and

probably even through concentrated flow at the interface between well compacted clay and slightly compacted clay, the sand core got wet, causing (limited) compaction of the most upstream part of the sand core and also some compaction of the wet part of the small clay dike. This compaction caused deformations, leading to the observed cracks and uneven settlements. In turn, these cracks may have accelerated the wetting and compaction of the sand core. The presence of a preferential path is reflected by the quick reaction of pore pressure meters A03 - A06 - A09, right behind the small clay dike, to the water level rise in the upstream basin at t=42 h and t=50 h. This was accompanied by a further increase of the size of the cracks. The connection between the cracks occurring during the first days of the test and the poor compaction of the sand core and the small clay dike is supported by the observations made during the removal of the (identical) East dike, where a sharp contrast was found between the well-compacted clay layer which was still strong, and the nearly liquefied clay of the small clay dike.

It is noted that it took quite a while before the more downstream instruments in the sand core showed any reaction: 38 h for instruments A02 - A05 - A08 at 1.8 m downstream of the small clay dike and 76 h for instruments A04 - A07 (6.0 m downstream of the small clay dike and 1.4 m upstream of the downstream slope), 98 h for instrument A01. At t=63.3 h the upper controllable drainage tube was opened, which must have slowed down the filling of the sand core. The aperture of the tube was first decreased at around 70 h and then increased again at 86 h; consequent sharp variations of the pore pressures are seen in Fig. 6.2.

Internal overtopping of the small clay dike did not occurred before t=86 h.

6.4.3 Micro-instability of the sand core

6.4.3.1 Description of the mechanism

Micro-intsability relates to the stability of soil on the surface of a slope under the influence of groundwater flowing through the dike. The term indicates that the mechanism concerns very local intabilities, where the number of grains loosing stability simultaneously is very small. If equilibrium at right angles to the slope is not satisfied, soil grains are removed more or less individually (*washout*). If equilibrium parallel to the slope is not satisfied, sliding of very thin layers of soil takes place (*shearing*). These phenomena only occur with non-cohesive granular materials; with cohesive materials deeper shearing is more likely to occur.

Design rules are given in the Dutch guidelines for water retaining earth structures (TAW, 1999). More recent research by De Groot et al. (2011) has highlighted that instability may occur at gentler slopes than predicted by the simple theory included in the national guidelines. This observation is explained by the eroding effect of water flowing over the slope. However a dangerous change in profile caused by micro-instability in a gentle slope takes a long time (a day or more).

Often, the inner slope of a dike is covered by a clay layer or revetment to prevent scour due to overtopping water. The high phreatic level in the core can cause the uplift and cracking of the cover layer. The high water pressure can also reduce the shear resistance at the interface causing the sliding of the cover layer. When the cover layer has slid down or cracks are present in it, the situation at the sand surface is similar to an uncovered slope with a free surface flow (De Groot et al., 2011).

6.4.3.2 Failure of the test dike

Application of the formula given in De Groot et al. (2011) to the test dike - to be precise, to the situation with a 1:2 inner slope made of sand with only a thin cover of soft material - yields that the situation is unstable as soon as the sand gets saturated, which may take quite some time. The cover will only cause a limited delay of the failure process.

Right after closure of the upper controllable drainage tube, the pore pressures in the sand core started to rise sharp at t=94 h. At t=97.6 h, the higher pore pressures in the wet part of the sand core led to partial loss of the shear strength, causing some sliding of the downstream slope (Fig. A.25 and A.26). At this point, most of the sand core below the crest may have been filled with water. This sliding may have caused further cracking of the sand core, thereby also the last pore pressure meter there (A01) was reached by the rising water inside the core (at t=98 h). During the following night, the deformations slowly continued while the water level in the upstream basin receded (Fig. A.27 and A.28). The deformations concentrated at the east side of the dike. The next morning, at t=111.0 h the upstream basin was refilled. The pore pressures in the sand core quickly responded to that. Before the level of 3.43 metres above the lower sand level was reached again, at t=111.9 h the continued and increased deformation of the downstream slope and the crest lead to so much subsidence of the crest that overtopping at a reservoir level of 3.38 metres above the sand level occurred a few metres west of the

east side of the dike. Breaching occurred and as a result, the reservoir emptied within 10 minutes (Fig. A.29 and A.30).

It is hard to tell why the failure occurred at that location. The vicinity of the dike wrapped in foil separating the West and the East test dikes probably made that location slightly more vulnerable than the middle part of the dike. It should be noted that in order to avoid failure right at any of the ends of the West and East test dikes, an extra lump of clay had been placed near the sides, as can be seen in Fig, A.17, showing the west side of the East dike during construction.

6.4.4 Piping

The combination of careful visual inspection and pore pressure measurements allowed for a detailed reconstruction of the development of the pipes during the test. Location and degree of activity of the sand boils observed are reported in Table 6.1.

Traces of sand transport, consisting of grain movements or spots of turbid water, were recorded since 21.5 h, yet the first proper sand boil (depicted in Fig. A.21) was only discovered at 45 h, placed at x = 5.2 m. The trace of the first pipe was detected 2 hours earlier in the pore pressure measured at two locations (x = 4.8 m, x = 5.8 m) along at the most downstream line of sensors, located at 0.9 m from the toe (line 1: y=14.1 m) (Fig. 6.3, lower bundle of curves).

The pipe manifested as a small pore pressure drop. It should be noted that the recorded drop is smaller than expected from the theory; a possible explanation is that the sensors were hardly located exactly in the piping channel and the curvature of the flow lines generated by a pipe decreases very fast with distance from the pipe itself.

From the size of the first sand boil recorded during the visual inspections, the volume of the sand removed from the foundation was calculated and it was found that the cross-sectional area of a pipe (or the total area of a pipe network) at the fist stage is between 2.5 and 5 cm^2. Of course these numbers are affected by great uncertainty, concerning both the size of the sand boil and the length of the pipe(s), but they provide us with an order of magnitude of the pipe size.

At 55.5 h, after a further increase of the upstream water level, the first pressure drop occurred in the second line of pore pressure transducers (y=12.5 m, 2.5 m from d/s) at the shoulders of the first sand boil (Fig. 6.3, upper bundle of curves), indicating that the corresponding pipe(s) had grown that far. Moreover new sand boils (#2, #3,

0	Stopped / buried sand boil
2a	Traces of sand movement, no dust cloud
2b	Traces of sand movement, dust cloud (from fine sand) visible
3	Sand boil producing water only
4	Sand boil with continuous sand transport
-	Not accessible
	Assumed to be equal to the previous reading

		well number / position (m)											
Time	**Head**	1	2	3	4	5	6	10	11	12	13	14	15
hh.mm	**m**	5.2	11.7	11.2	8.7	17.4	7.0	3.0	4.0	5.8	6.5	10.3	17.3
21.31	1.15									2b			
22.24											2b		
25.07	1.34									2b	2b		
27.00													2b
29.20	1.31												2b
33.10	1.27												2b
37.30	1.23												2b
42.30	1.56											2a	
42.31	1.56											2b	
42.34	1.56							2b					
42.36	1.56									2a			
42.39	1.56			2a									
45.11	1.49	3											
47.16	1.55	3											
51.35	1.79	3							2b				
55.10			3										
55.11				3									
55.15					3								
55.17		4											
57.58	1.87	4											
58.00	1.87				3								
58.05	1.87			3									
58.09	1.87		4										
60.53	1.83					3							
60.58	1.83		4										
61.04	1.83			3									
61.07	1.83				3								
64.45	2.02		4										
64.49	2.02			4									
64.53	2.02				4								
64.55	2.02	4											
65.01	2.02						3						
69.22	2.01					3							
69.24	2.01												
76.28	2.09	3											
76.32	2.12						0						
76.34	2.12				3								
76.40	2.12			3									
76.42	2.12		3			-							
80.00	2.12			3	3								
80.00	2.12												
80.05	2.12						3						
80.06	2.12	3											
80.07	2.12		3			-							
84.59	2.12			3									
85.07	2.12				3								
85.08	2.12						3						
85.10	2.12	3											
88.15	2.30	4	3	3									

TABLE 6.1: Location and degree of activity of the sand boils observed during the visual inspections.

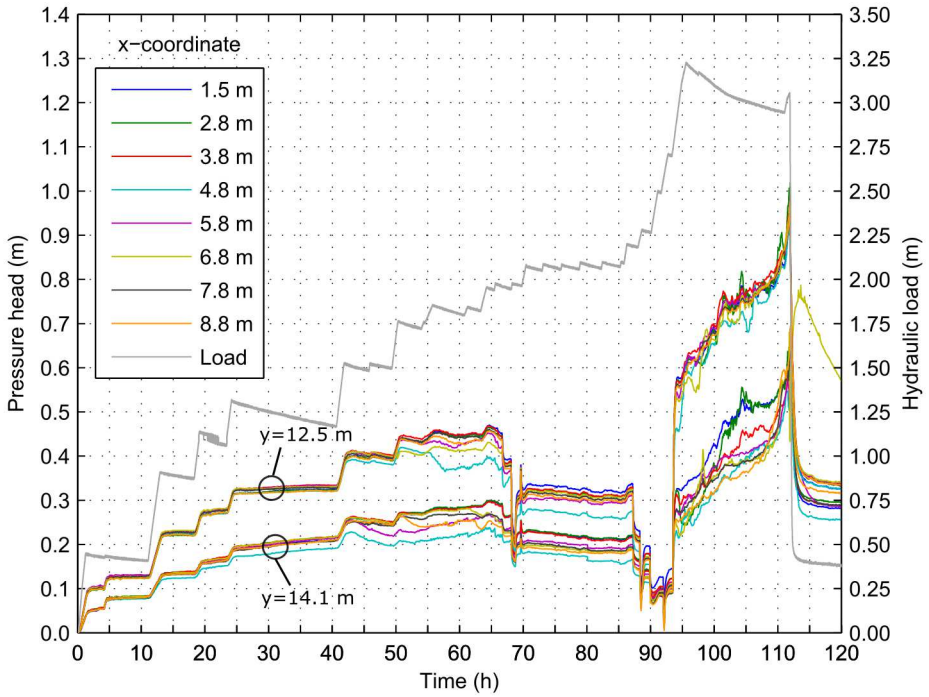

FIGURE 6.3: Pressure head measured under the dike by the two most downstream lines of sensors: western half of the dike.

#4) appeared at x=11.7, x=11.2 and x=8.7 m, followed by a drop in the pore pressure sensors placed behind them (Table 6.1, Fig. 6.4). Sand boil #2 is depicted in Fig. A.22. From that moment on, sand transport occurred continuously, as revealed by the size of the sand boils increasing with time. In the pore pressures measured by the third and fourth lines of sensors (y=10.7 m, 4.3 m from d/s; y=3.8 m, 11.2 m from d/s) no traces of piping were visible.

The opening of the lower drainage tube, starting at 67 h, had a clear effect on the pore pressures under the dike and, in turn, an effect on the sand transport that suddenly stopped. After closing the controllable drainage tube at around 94 h, the pore pressures were restored again and the erosion process restarted as before. However, from the pore pressure measurements it is possible to assert that none of the pipes reached the third line of sensors, placed at about a quarter of the seepage length.

Regarding the first 40 hours a general remark can be made that during that period the pressures are more spread on the east side (x>10 m) than on the west side and there are some locations were the pore pressures are clearly lower than in the surroundings since the beginning of the test. This can be explained with some sensors located more downstream than others and/or as a consequence of a slight heterogeneity of the sand layer caused by a non-uniform substitution of the old sand with the new sand (indeed,

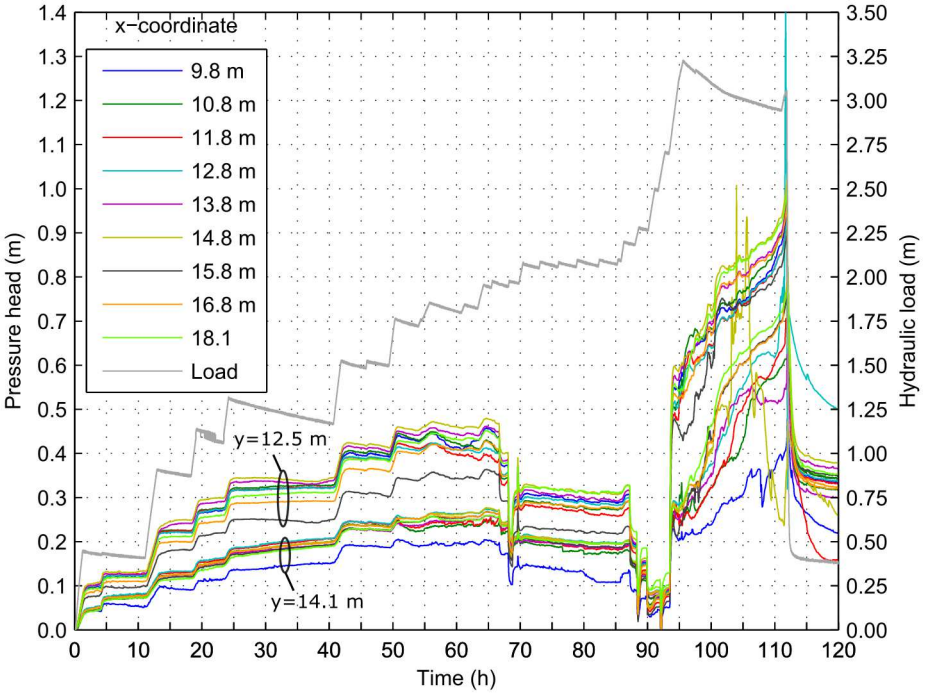

(a)

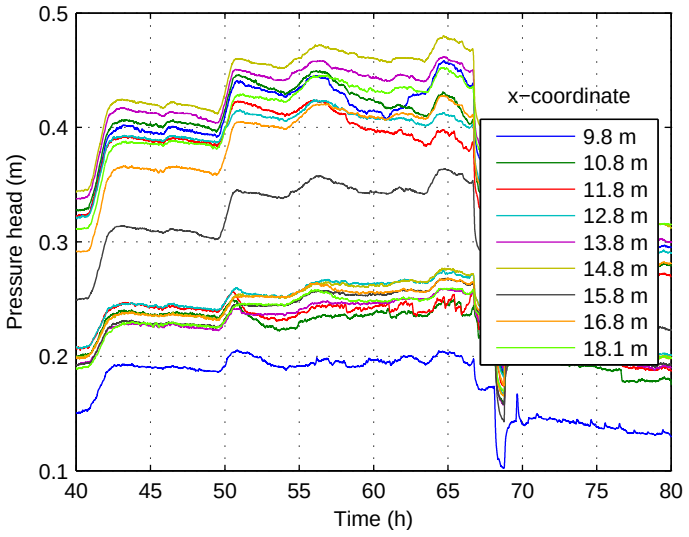

(b)

FIGURE 6.4: Pressure head measured under the dike by the two most downstream lines of sensors: eastern half of the dike (a). Zoom of the measurements between 40 and 80 h (b).

thicker replacements were done where necessary).

6.5 Temperature measurements

6.5.1 Dike foundation

6.5.1.1 Data

The measurements started 7 days before the beginning of the test and were interrupted before the end of the test, at about t=103 h, when the fibres broke due to the sliding of a large portion of the downstream slope. Thanks to the distributed nature of the sensor, temperature was measured along the entire cable and an average value was provided each metre with a frequency of 30 minutes and a resolution of 0.1°C.

Figure 6.5 shows the evolution of the temperature before and during the test, for different distances from upstream. Before the beginning of the test (at t=7 d),

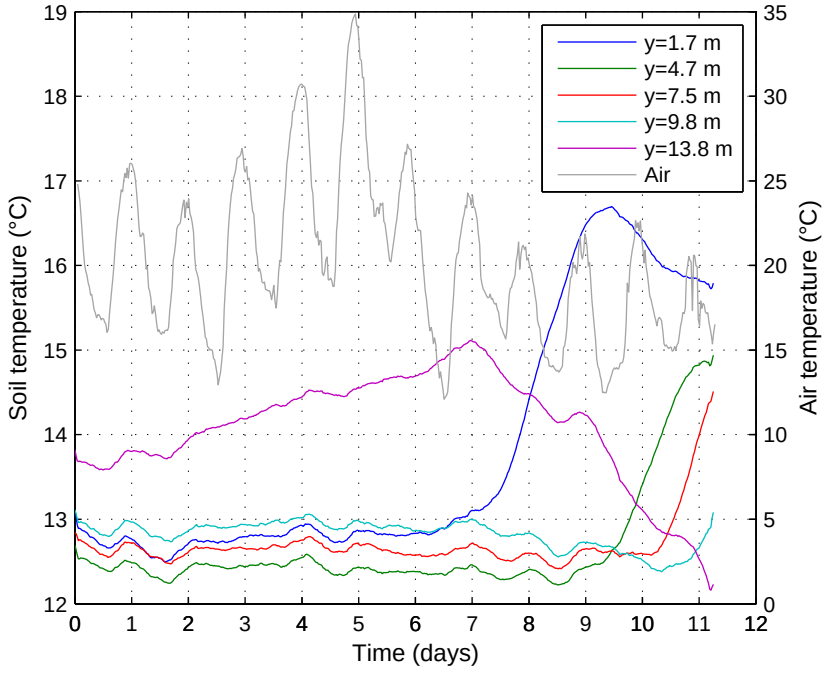

FIGURE 6.5: Temperature measured in the centre of the dike (x=10 m) at progressive distance from upstream (y)

the temperature at the base of the dike is constant. Minor differences between the measuring lines, within 1°C, are a consequence of different exposition (south or north) and depth. The temperature at the most downstream position (line 1), which is also the most shallow, is the most influenced by the external environment. It shows a positive trend, up to the beginning of the test, likely as a consequence of increasing average daily

temperature and solar radiation. Subsequently a sharp inversion of the trend occurs. The temperature at line 1, placed at 1.7 m from the upstream toe, starts increasing few hours after the beginning of the test, which means that the reservoir water was warmer than the dike body. Line 2 and 3 are reached by the warm front after 2 and 3 days respectively. At line 4, the temperature starts decreasing soon after the beginning of the test and it keeps decreasing up to the arrival of the warm front, more than 3 days later. Line 5 was never reached by the warm front.

Figure 6.6 depicts the temperature measured by line 5, placed at 1.2 m from the downstream toe and between the third and fourth line of pore pressure transducers. Despite it is not possible to differentiate between the measurements, the graph shows

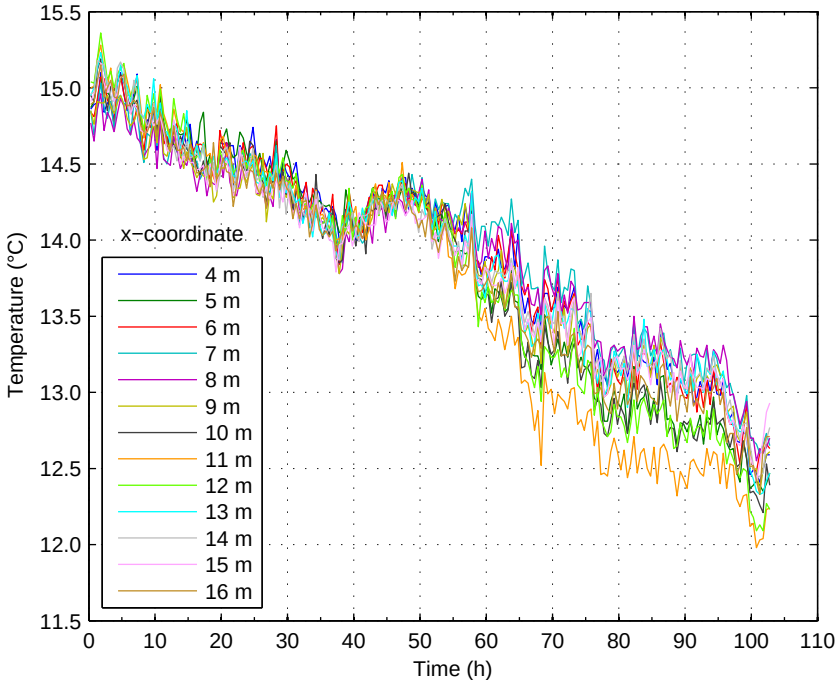

FIGURE 6.6: Temperature measured at the most downstream line (y = 13.8 m)

that the values start to diverge after 55 h, that is when the third line of pore pressure meters is reached by the pipes, while no sign is detected earlier, at 43 h, when the fourth line is reached. The graph also shows that the measured temperature variations are smaller than 1°C. Temperature data recorded along line 4 did not show any anomaly. This is in accordance with the pore pressure measurements, since this optical fibre is upstream of the second line of pore pressure sensors that was never reached by the pipes.

A graphical representation of the same data using a spectrogram, as in Fig. 6.7, is very effective for identifying the occurrence of piping. Starting from 55 h, negative thermal anomalies (lower temperature) appear at the location of the pipes, approximate

at x = 5, 11 and 17 m. Since the reservoir water was warmer than the dike, positive anomalies would be expected; the reason for this non-intuitive behaviour will be explained later. Comparing monochrome to colour scale it was observed that the first works better. A careful look at contours plotted for significant times during the test,

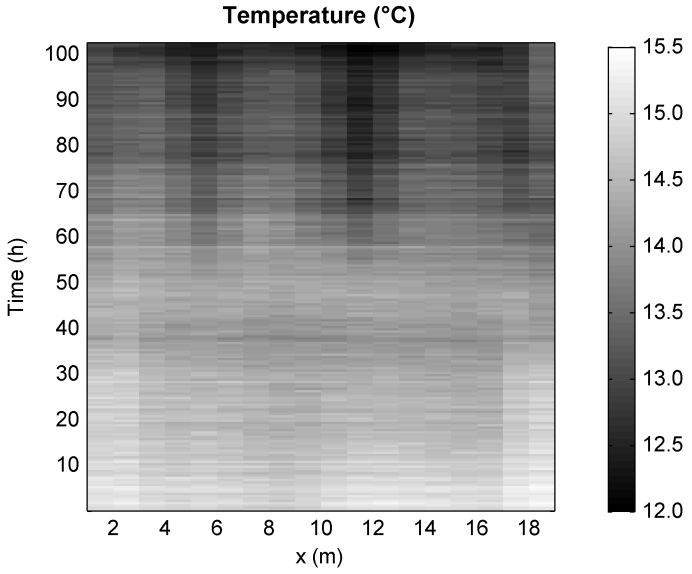

(a)

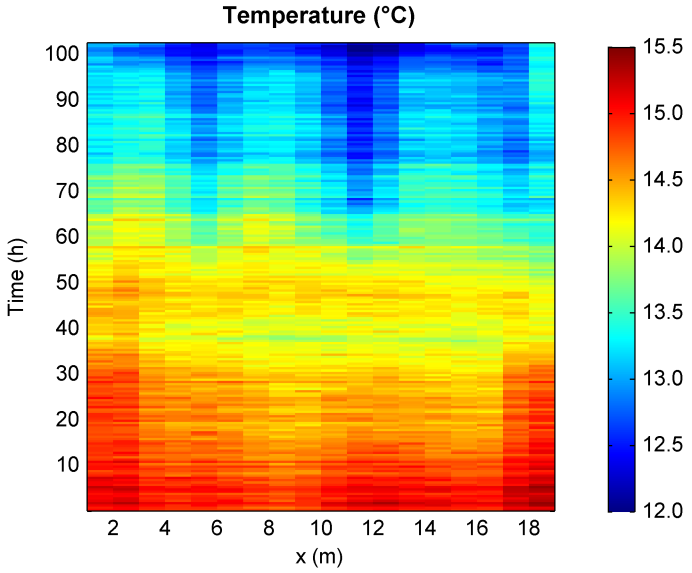

(b)

FIGURE 6.7: Spectrogram of the temperature measured at the most downstream line (y = 13.8 m)

as reported in Fig. 6.8, reveals how the pipes generate the thermal anomalies shown in Fig. 6.6 and 6.7. A minor detail to notice is that the temperature is not uniform along the x-axis (except downstream), neither in absence of flow (t=0) nor with seepage flow. The temperature is higher at the centre than at the borders. This can be ascribed to the

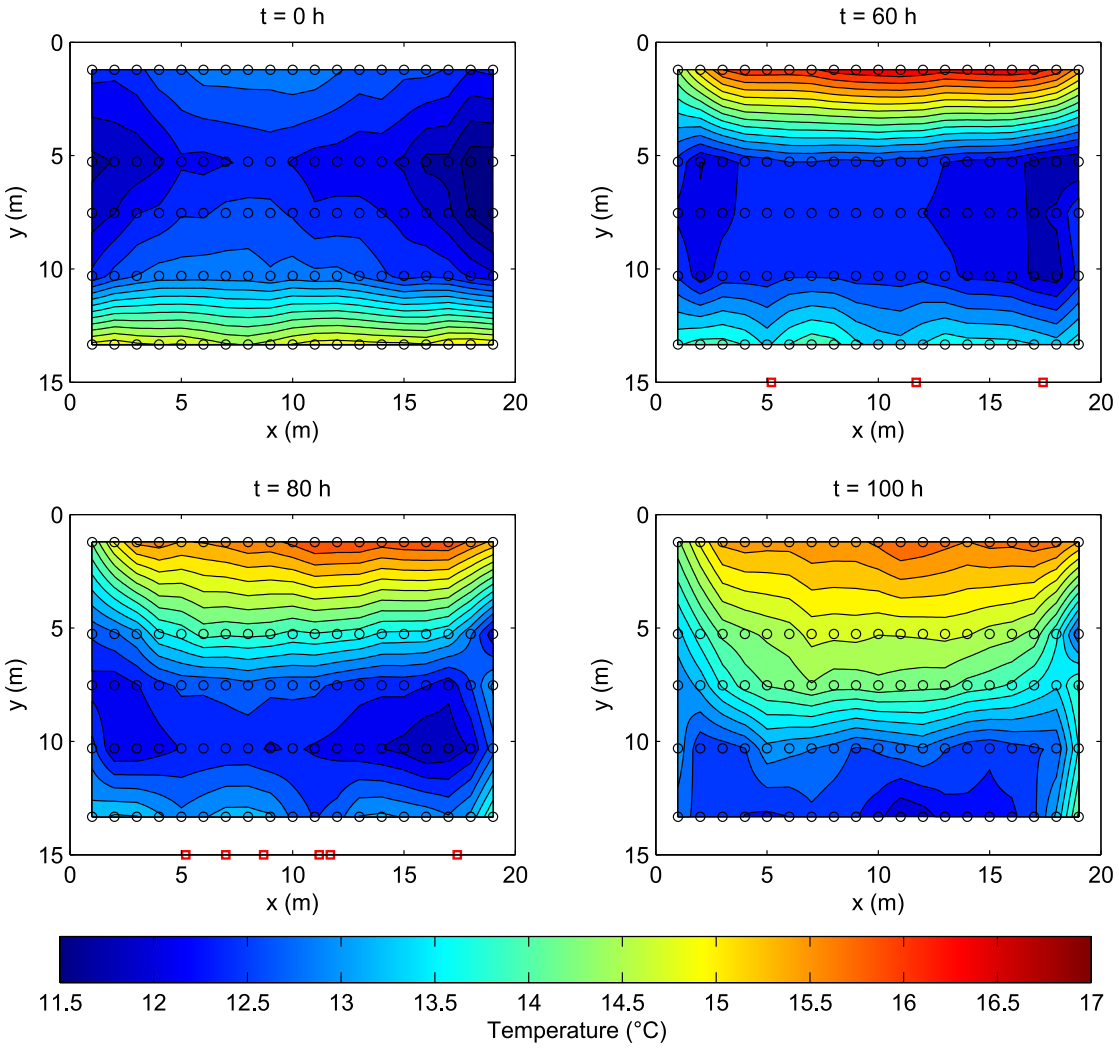

FIGURE 6.8: Temperature under the dike at 0, 60 , 80 and 100 h from the beginning of the test. The circles indicate the points at which real data were provided for interpolation. The squares on the x-axis indicate the position of the sand boils

three-dimensionality of the piping facility, in opposition to a real dike where the large extension in the longitudinal direction with respect to the transversal dimension makes the problem bi-dimensional. More importantly, it can be noted that the inflowing water causes the temperature to increase upstream, and pushes the cold water, initially present under the dike crest, towards downstream. When the pipes develop, temperature variations arise in their surroundings because the cold water coming from underneath the dike crest travels faster in the pipes. In addition, in the 100 h contour plot, preferential flow paths can be observed at the sides, that bring warm water downstream faster than how it travels in the centre of the dike. This is more pronounced at the right side. As no sand boil was observed at the sides, these preferential paths are believed to be a consequence of the discontinuity between the soil and the impermeable foil. These minor

leakages could not be identified by the interpretation of the pore pressure readings.

6.5.1.2 Discussion

Whether a thermal front can propagate in the dike foundation from upstream up to the downstream toe depends on several factors: the main actor is the hydraulic conductivity of the soil but a not negligible role is also played by the geometry of the seepage domain (see § 4.4). It was inferred inferred from the test that the time scale of the process of heat propagation along the seepage path might be comparable with the duration of typical flood events. Therefore, the time factor cannot be neglected when studying how heat is transferred under a dike. Differently from what happens to porewater pressure, which transmission can be assimilated to that of a body wave, heat transfer by advection requires that the water particle entered upstream reaches downstream while maintaining its initial temperature. As a consequence, heat travels much slower than porewater pressure.

In situations like the one presented here, where the thermal front does not propagate much along the seepage path, a second phenomenon might allow leakages to produce thermal anomalies: the thermal gradient initially present in the foundation, in absence of seepage. This gradient is due to the geometry of the dike, that makes the distance between the embankment base and the surface to vary in the direction of the seepage path.

In our test dike, being the piping prone layer close to the surface, the gradient existing between line 4 and 5 in absence of flow was significant. As seepage occurred, the flow velocity was everywhere high enough to alter the initial gradient. However the gradient in the seepage direction varied faster at the pipe locations than in the sound part of the dike, producing the thermal anomalies observed. The temperature gradient in the seepage direction is shown in Fig. 6.9 for two locations: one close to a pipe (x=11 m) and one not affected by piping (x=14 m). The graph also shows that, at the pipe location, after 90 h the gradient turns negative, meaning that the warm thermal front coming from upstream has reached the pipe at the measuring point.

Both the propagation of a thermal front and the existence of an initial thermal gradient are examined in Chapter 7 with the aid of numerical modelling.

Despite appropriate graphical representation of data can be effective in identifying leakages ex post, real-time identification requires quantitative and automatable criteria.

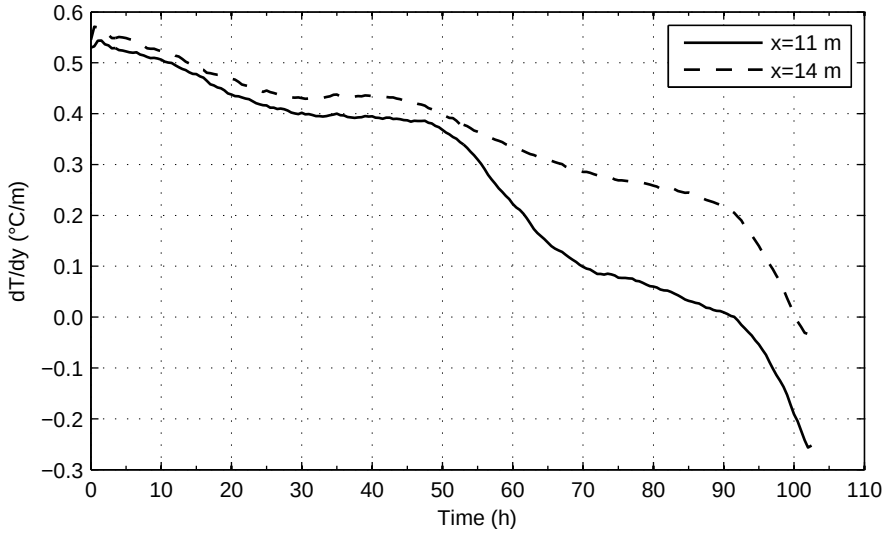

FIGURE 6.9: Temperature gradients in the direction of the seepage flow at a location where piping was observed (x=11 m) and at a location where no piping was detected (x=14 m)

Figure 6.10 shows the spatial temperature gradients calculated along the most downstream measuring line. At locations x=5 m and x=11 m, where sand-boils have been

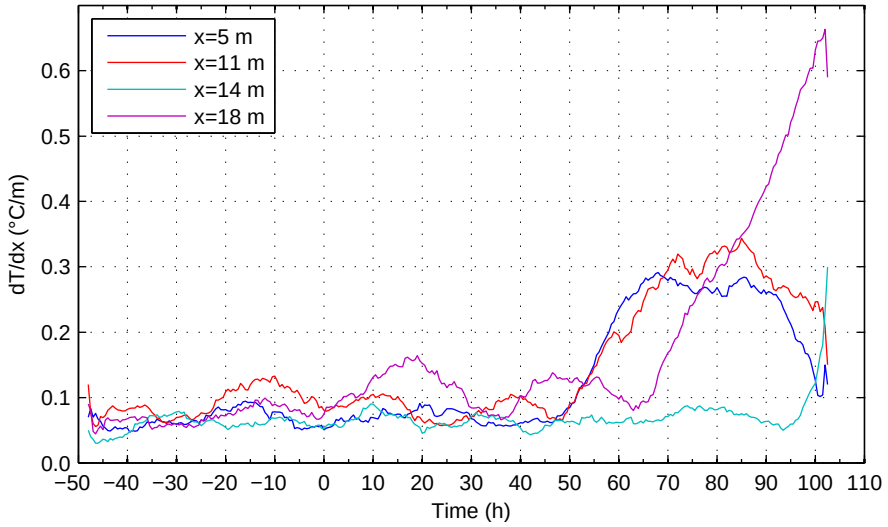

FIGURE 6.10: Spatial temperature gradients for significant points along the most downstream line

observed, the gradients start to increase at 50 h, reach a value of about 0.3 and stabilize between about 65 and 85 h, when the drainage tube is open. The gradients decrease when, after 85 h, the hydraulic load is increased continuously. A possible explanation is that new sand boils appeared and old pipes branched, so that a new *homogeneous* condition was reached, in which most of the dike was affected by piping. At x=18 m, where a sand-boil was observed starting from 60 h, the high spatial gradient comes from

the superposition of two effects: the negative anomaly caused by piping at that location and the positive anomaly caused by the leakage along the foil at x=19 m. For comparison, the graph also reports the gradients at x=14 m where no sand boil was observed, at least not up to 90 h when visual inspection was stopped for safety reasons.

The 1 m spatial resolution of the sensor is much larger than the width of a single pipe (few centimetres). For this reason, it was initially believed to be partially liable for the small extent of the temperature variations detected. However, when the pipes developed, the temperature difference between line 4 and 5, which was responsible for the anomalies around the pipes, was less than 1°C. Thus, the measurements would not probably have benefited from a higher spatial resolution. The development of a branched net of pipes behind a single sand boil, as observed in medium-scale experiments (Weijers and Sellmeijer, 1993a), could be positive in this sense. The 0.1°C accuracy was sufficient but higher accuracy could be advantageous.

6.5.2 Downstream slope

The temperatures measured in the central part of the dike (x=10 m) by the three lines of optical fibre deployed on the slope (bottom, middle and top line) are illustrated in Fig. 6.11.

The difference in delay and damping observed at the three positions with reference to the air temperature, is ascribable to a slightly different installation depth. Small variations are also observed along the single lines, as can be seen in Fig. 6.12 that shows all the measurements. This remark reveals that at small depths (< 1 m) even slight variations of the depth of the sensor can translate in significant differences in the temperatures recorded.

Figure 6.11 also shows that, during all the measuring period, amplitude and average value of the temperature at the bottom line decrease with reference to the amplitude and average value of the temperature at the middle and top line. This is possibly the effect of the superposition between the soil response to daily excursion and to yearly excursion of the air temperature.

No clear indication of seepage can be traced in the plots in Fig. 6.11 and 6.12. The adoption of a monochrome scale for spectrograph in Fig. 6.12 did not highlighted any new element.

The analysis of the data did not progress further, as the main focus of this work is erosion across foundation soils.

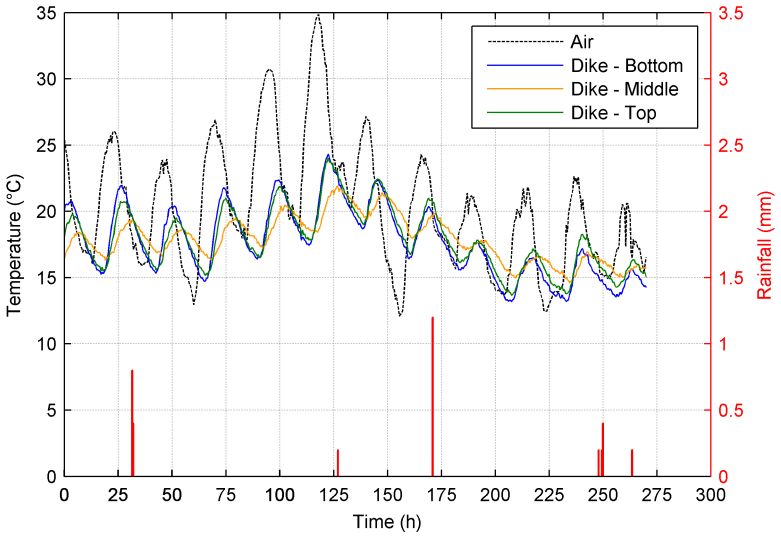

FIGURE 6.11: Temperature measured under the surface of the downstream slope

Two images of the downstream slope taken by the infrared camera are depicted in Fig. 6.13. At the piping locations the temperature decreases up to 3 ℃ compared to the surrounding region.

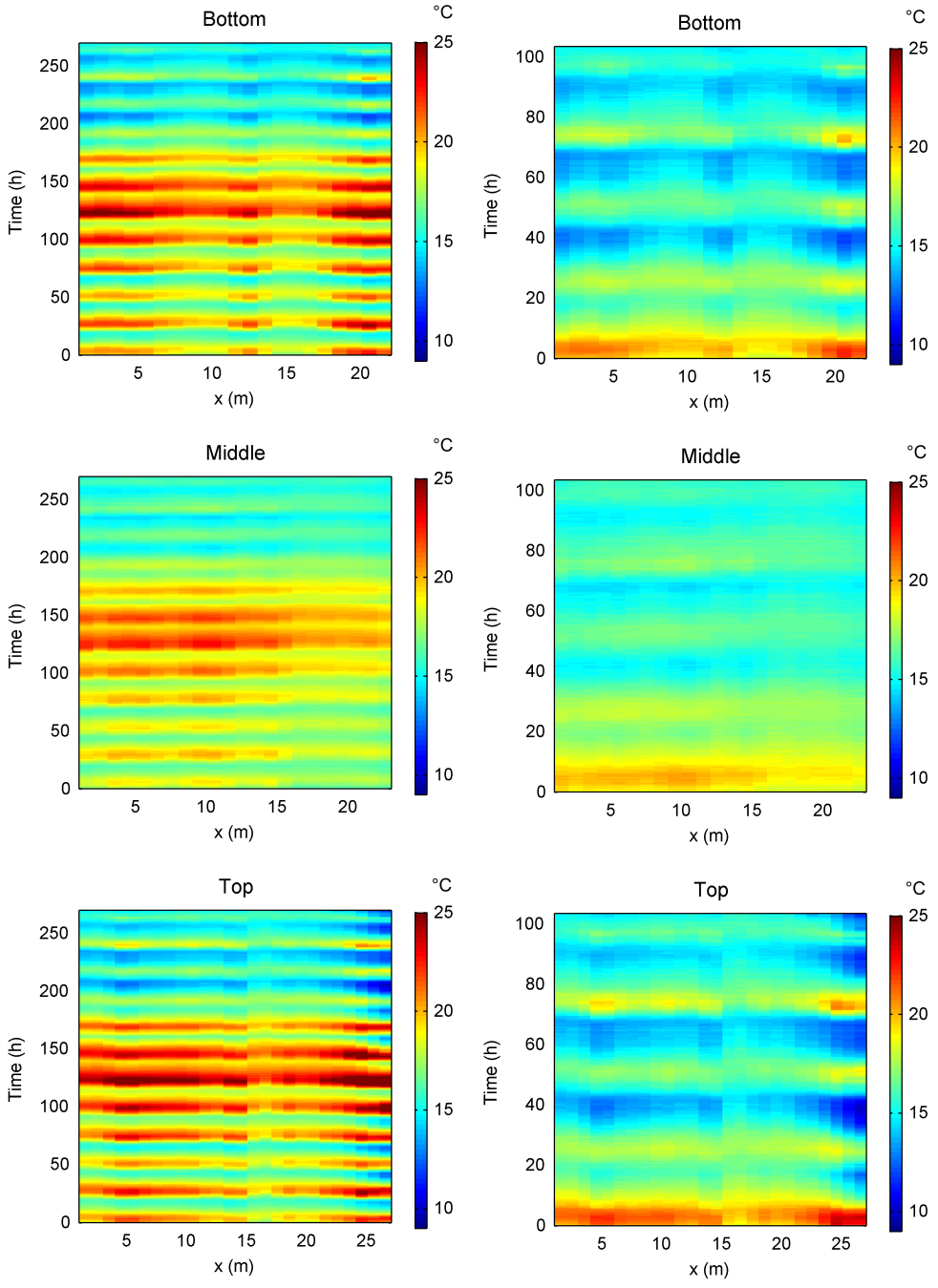

FIGURE 6.12: Spectrogram of the temperature measured at the bottom, middle and top of the downstream slope during the whole measuring period (a) and only during the test (b).

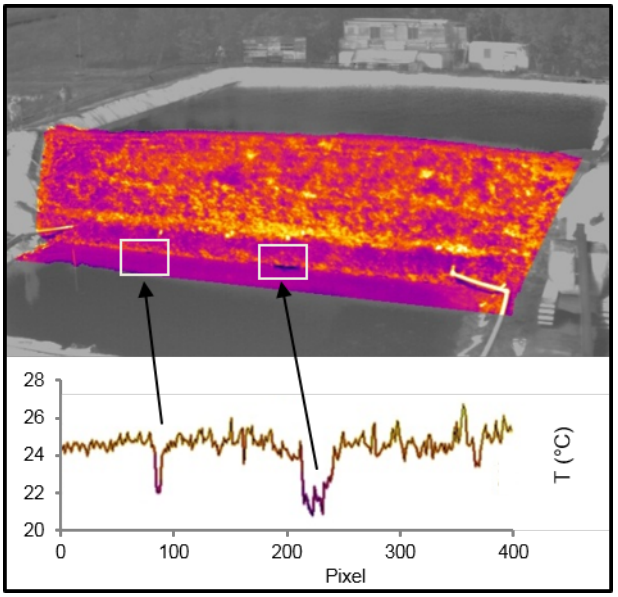

(a)

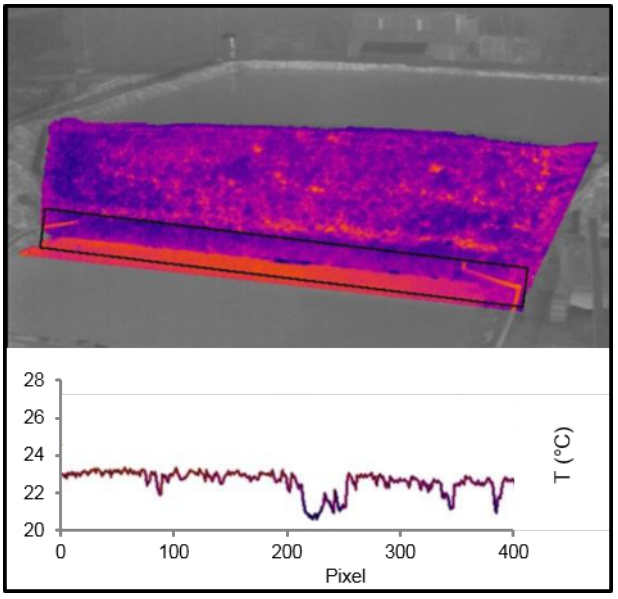

(b)

FIGURE 6.13: Surface temperature of the downstream slope and of the downstream toe (graph) measured by the infrared camera at t=94.5 h (a) and t=96 h (b)

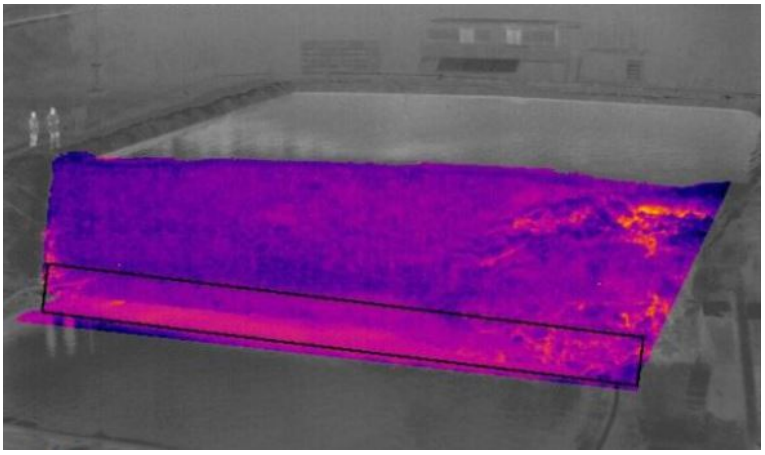

(a)

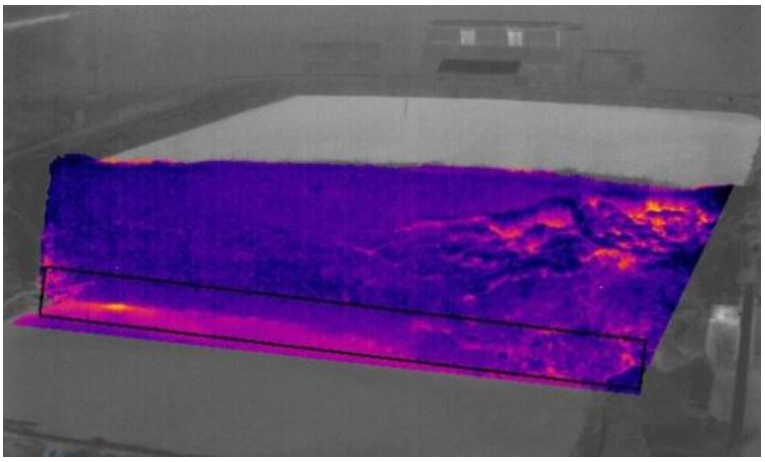

(b)

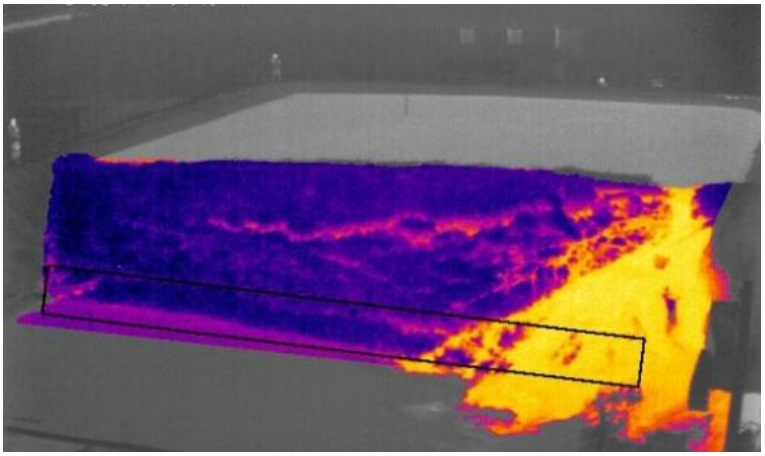

(c)

FIGURE 6.14: Surface temperature of the downstream slope measured by the infrared camera at three subsequent stages of the dike failure.

Chapter 7

Numerical modelling and dimensional analysis

In this chapter it is shown how, starting from a simple one-dimensional numerical model and gradually adding degrees of complexity, it was possible to define a model capable of reproducing the measurements of the large-scale experiment described in Chapter 6. At the aim, a commercial finite element code, COMSOL Multiphysics®, was used. Numerical modelling was of big help in extrapolating the experimental results to a larger time horizon and in connecting the experimental data to the analytical tools presented in Chapter 4. The analytical tools, in turn, enabled to extend the findings of the large-scale experiment to a wide range of geometries and seepage velocities typical of piping-prone dikes.

7.1 One-dimensional benchmark

The proper functioning of the numerical model was tested solving a one-dimensional problem for which an analytical solution was available. Bear (1972) reports the case of a semi-infinite column of porous medium ($x > 0$) maintained at constant specific discharge u in the x-direction and adjacent to a reservoir containing a tracer solution of constant concentration ξ_0. It is assumed that at $x = 0$ the concentration reaches its ultimate value ξ_0 immediately upon commencement of flow. The differential equation is:

$$\frac{\partial \xi}{\partial t} = D' \frac{\partial^2 \xi}{\partial x^2} - \frac{u}{\varepsilon} \frac{\partial \xi}{\partial x}, \tag{7.1}$$

where D' is the coefficient of hydrodynamic dispersion. Initial and boundary conditions are:

$$\begin{aligned} &t \le 0, \qquad x \ge 0, \qquad \xi = 0, \\ &t > 0, \qquad x = 0, \qquad \xi = \xi_0, \\ &t > 0, \qquad x = \infty, \qquad \xi = 0. \end{aligned} \tag{7.2}$$

Equation (7.1) is equivalent to Eq. (4.24), with the unknown being the temperature instead of the tracer concentration. In Eq. (4.24) D' is replaced by λ/C and ε is replaced by C/C_w. Under the following initial and boundary conditions:

$$\begin{aligned} &t \le 0, \qquad x \ge 0, \qquad T = 0, \\ &t > 0, \qquad x = 0, \qquad T = \Delta T, \\ &t > 0, \qquad x = \infty, \qquad T = 0, \end{aligned} \tag{7.3}$$

the solution becomes:

$$T(x,t) = \frac{\Delta T}{2}\left[\operatorname{erfc}\frac{x-(uC_w/C)t}{2(\lambda t/C)^{1/2}} + \exp\left(\frac{ux}{\lambda/C_w}\right)\cdot\operatorname{erfc}\frac{x+(uC_w/C)t}{2(\lambda t/C)^{1/2}}\right] \tag{7.4}$$

where erfc is the complementary error function. The solution is illustrated in Fig. 7.1 for $\Delta T = 1$ °C.

Since the problem of heat transfer under a dike is a two-dimensional one (three-dimensional if the pipes are included), there was interest in testing 2-d finite elements. Therefore the column of the problem described above was modelled by 2-d finite elements. The initial and boundary conditions of the model were:

$$\begin{aligned} &t \le 0, \qquad 0 \le x \le 15\,\text{m}, \qquad T = 0\ ^\circ\text{C}, \\ &t > 0, \qquad x = 0, \qquad\qquad\quad T = 1\ ^\circ\text{C}, \\ &t > 0, \qquad x = 15\,\text{m}, \qquad\quad T = 0\ ^\circ\text{C}. \end{aligned} \tag{7.5}$$

Darcy velocity was set equal to 10^{-5} m/s.

The size of the mesh was chosen so as to meet the stability condition $Pe_h < 2$, as described in § 7.2 and § B.2. For $u = 10^{-5}$ m/s the stability condition gives $h < 10$ cm, where h is the size of the grid.

The choice of the time step is regulated by the Courant-Friedrichs-Lewy condition:

$$\frac{|\mathbf{v}_T|\Delta t}{h} < 1, \tag{7.6}$$

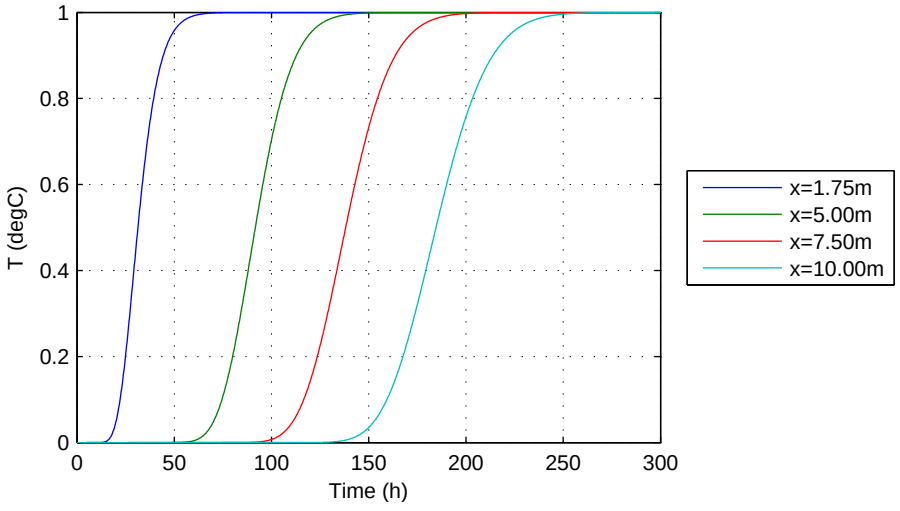

(a)

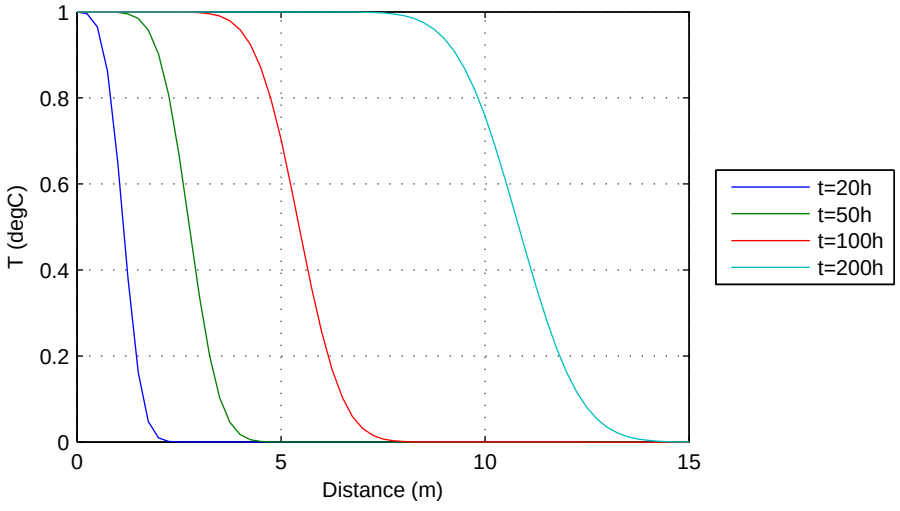

(b)

FIGURE 7.1: Analytical solution of the one-dimensional advection-diffusion equation for $\lambda = 2.77$ W/(m K), $C = 2.8$ MJ/(m^{3}K), $C_w = 4.186$ MJ/(m^{3}K) and $u = 10^{-5}$ m/s.

which assures that the process does not run faster than the advection velocity.

A perfect match between the analytical and numerical solution was obtained, confirming the validity of the numerical model.

7.2 Numerical stability of the heat transfer equation

The underlying finite element (FE) discretization method in COMSOL Multiphysics (as in most FE codes) is the Galerkin method. This method might fail in providing accurate numerical results when the diffusion term is small compared to the advection term.

The theory at the base of these instability issues is presented in Appendix B. The general stability condition derived in Appendix B is $Pe_h > 2$, where Pe_h is the element Péclet number, i.e. the ratio between the advective and conductive fluxes over an element of size h.

In this section the stability of the Galerkin method when it is applied to heat transfer problems is tested with the aid of the 1-d model described in § 7.1. For $u = 10^{-5}$ m/s, i.e. the average Darcy velocity in the large-scale test described in Chapter 6, a mesh with maximum element size $h = 0.1$ m satisfies the condition $Pe_h < 2$ and does not produce oscillations in the solution, as the simulations show (Fig. 7.2a). For seepage velocities typical of more permeable materials, the same mesh produces oscillations in proximity of the downstream boundary, where a Dirichlet condition is applied (Fig. 7.2b). As explained in (Zienkiewicz et al., 2005) and in § B.1, when diffusion is small, the downstream boundary condition is felt in only a very small region close to the boundary; therefore a local refinement of the mesh can resolve the boundary layer and confine the spatial oscillations in a small region (Fig. 7.2c). If the mesh is refined to meet the condition $Pe_h < 2$ in the boundary layer, the oscillations disappear (Fig. 7.2d). When also this strategy is not applicable because the seepage velocity is too high, it is necessary to resort to other numerical techniques, as finite volumes or mixed finite elements.

7.3 From 1-d to 2-d

In hydrogeological systems, heat transfer is generally a two-dimensional problem. In dike foundations advection mainly occurs horizontally, i.e. in the main direction of the water flow, while conduction occurs in both horizontal and vertical direction.

One-dimensional and two-dimensional solutions were compared in order to understand if, and within what limits, the simple analytical solution of a 1-d problem could work as a rough estimate of the solution of a 2-d problem.

With this aim the advection-diffusion equation was solved in a rectangular domain 3 by 15 metres, which is an approximation of the portion of the sand layer underneath the dike in the large-scale piping test. The thermal boundary and initial conditions

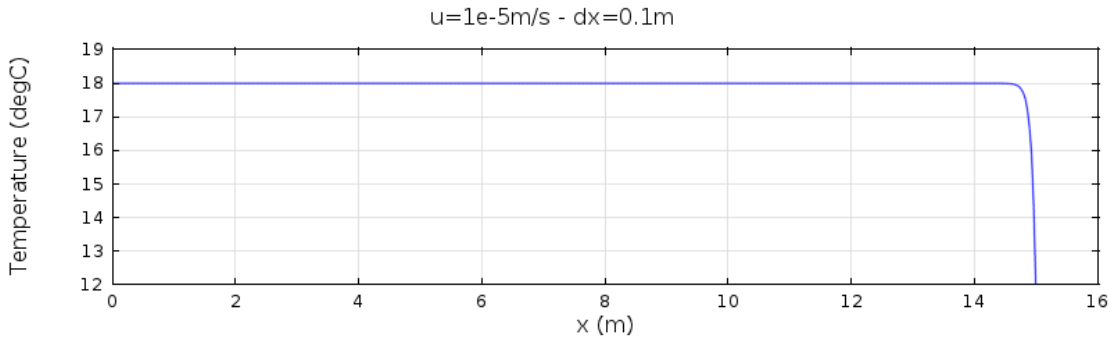

(a)

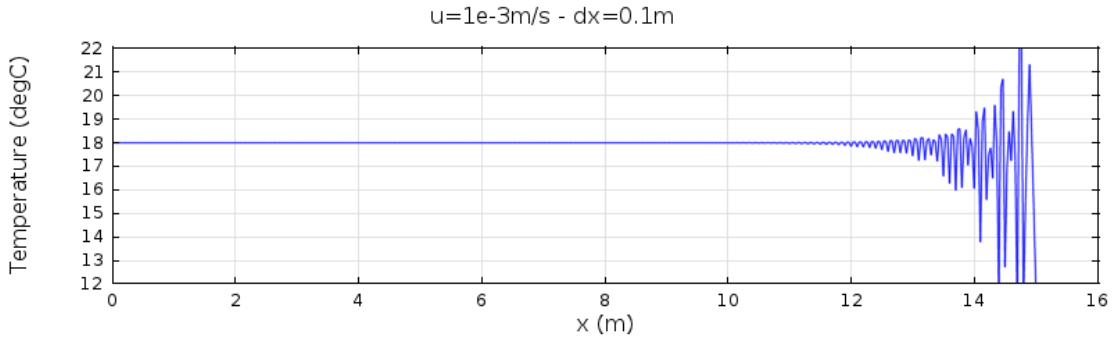

(b)

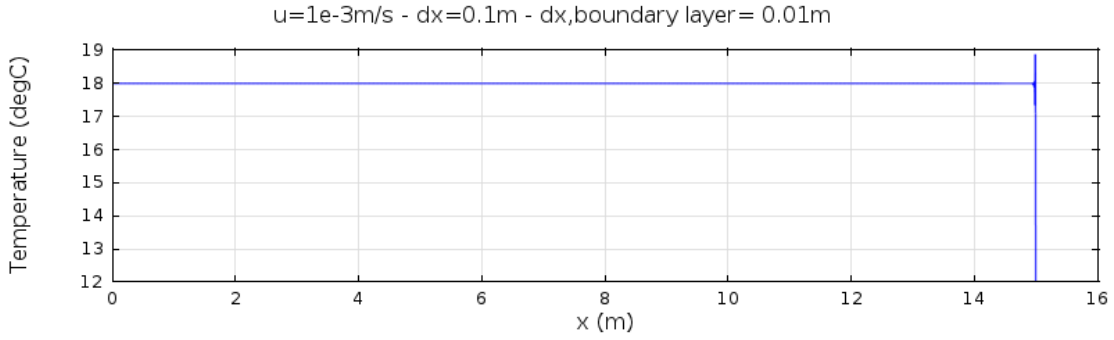

(c)

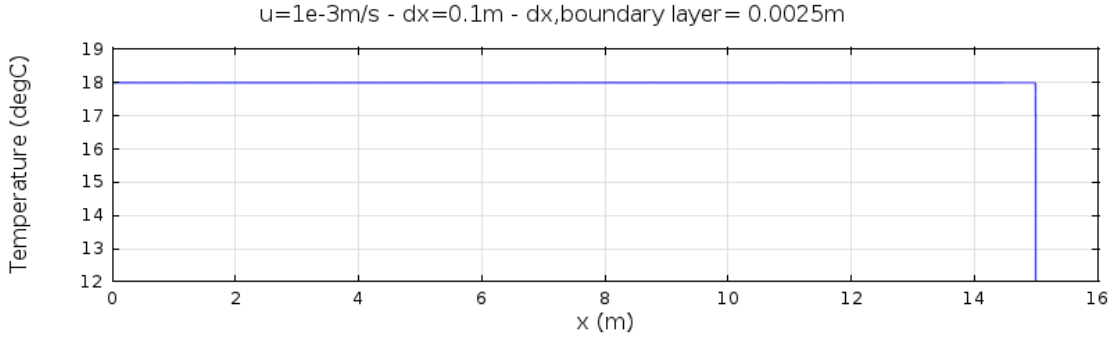

(d)

FIGURE 7.2: Steady-state solution of the advectio-diffusion equation using Galerkin finite elements. For high Darcy velocity, oscillations arise close to the downstream boundary, where a Dirichlet contition is applied (b). By refining the mesh in the boundary layer, the oscillations are confined in a small region (c) and, after a further refinement to meet the condition $Pe_h < 2$ in the boundary layer, they are eliminated (d).

were:

$$\begin{aligned} &t \leq 0, \qquad \forall (x,y) \in D, && T = 0\ ^\circ\mathrm{C}, \\ &t > 0, \qquad \forall (x,y) \in \partial D \mid x = 0, && T = 1\ ^\circ\mathrm{C}, \\ &t > 0, \qquad \forall (x,y) \in \partial D \mid x = 15\,\mathrm{m} \vee y = 0 \vee y = -3\,\mathrm{m}, && T = 0\ ^\circ\mathrm{C}. \end{aligned} \tag{7.7}$$

Darcy velocity was set again equal to 10^{-5} m/s.

Comparing the results presented in Fig. 7.3 with the 1-d solution in Fig. 7.1, it is evident that the 1-d and 2-d solutions are quite different. While in the 1-d case advection dominates over conduction, in the 2-d case the system manifests an intermediate behaviour: the temperature profiles lie above the curve depicting pure conduction at the steady state (u=0, t=inf.) but the temperature does not homogenize along the seepage path even after long time.

7.3.1 Péclet number of dike foundations

In this section the validity of the geothermal Péclet number (§ 4.4) for describing the problem of heat transfer in a permeable dike foundation layer is addressed. Differently from the situation depicted in § 4.4, conduction in the vertical direction occurs both upwards and downwards if it is assumed that the soil temperature both at the top and at the bottom of the permeable layer is significantly different from the temperature of the waterbody. It is more appropriate to calculate the geothermal Péclet number assuming $D/2$ instead of D.

The advection-diffusion equation was solved numerically in a rectangular domain of 1 by 200 metres, under the following initial and boundary conditions:

$$\begin{aligned} &t \leq 0, \qquad \forall (x,y) \in D, && T = 0\ ^\circ\mathrm{C}, \\ &t > 0, \qquad \forall (x,y) \in \partial D \mid x = 0, && T = 1\ ^\circ\mathrm{C}, \\ &t > 0, \qquad \forall (x,y) \in \partial D \mid x = 200\,\mathrm{m} \vee y = 0 \vee y = -1\,\mathrm{m}, && T = 0\ ^\circ\mathrm{C}. \end{aligned} \tag{7.8}$$

In Fig. 7.4 the vertical temperature profiles obtained at progressive distances from upstream (L) and for different Darcy velocities are plotted. These results (and many other obtained varying the thickness of the aquifer) confirm that for geothermal Péclet numbers much less than 1 the system is conduction dominated, while for values significantly grater than 10 the system is advection dominated.

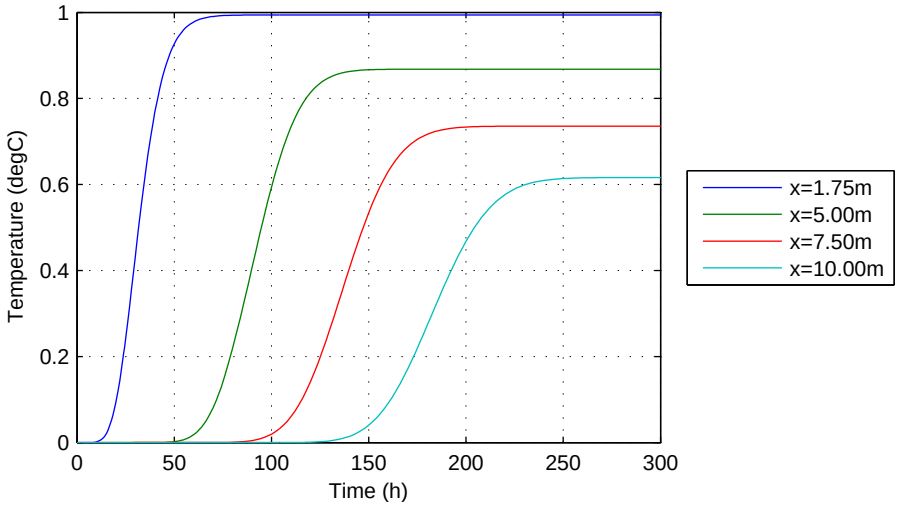

(a)

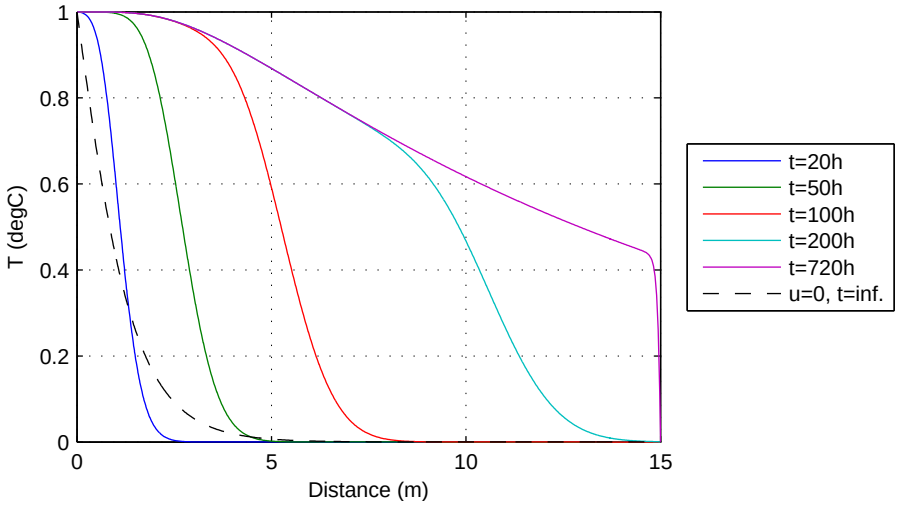

(b)

FIGURE 7.3: Numerical solution of the advection-diffusion equation in a two-dimensional domain. Data are sampled along the mid-line ($y = -1.5$ m) and the following parameters are assumed: $\lambda = 2.77$ W/(m K), $C = 2.8$ MJ/(m^{3}K), $C_w = 4.186$ MJ/(m^{3}K) and $u = 10^{-5}$ m/s.

The 2-d solutions presented so far are a rough simplification of the actual problem for mainly two reasons: (1) they neglect conduction in the direction of the flow and (2) the upper and lower boundary conditions are placed at the same boundaries of the flow domain.

Let us consider the case in which only a central strip of the domain is affected by the water flow, so that the thickness of the layer where advection occurs, D_H, is smaller than the vertical size of the domain D. In such case the energy exchanged by advection is proportional to D_H, while the conductive heat flow is inversely proportional

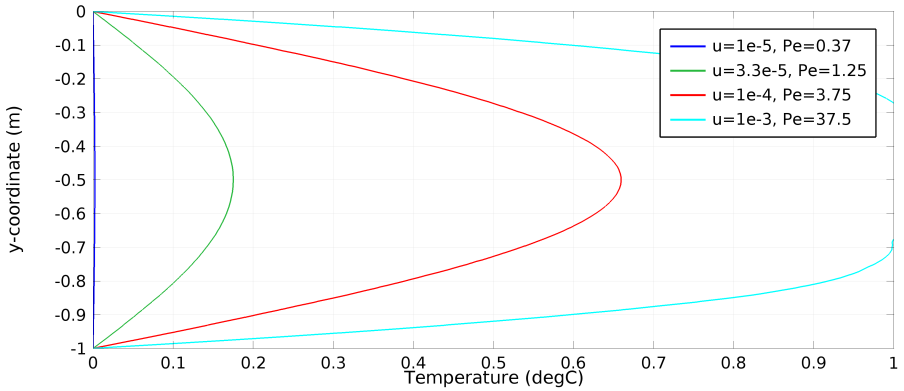

(a) L=10 m

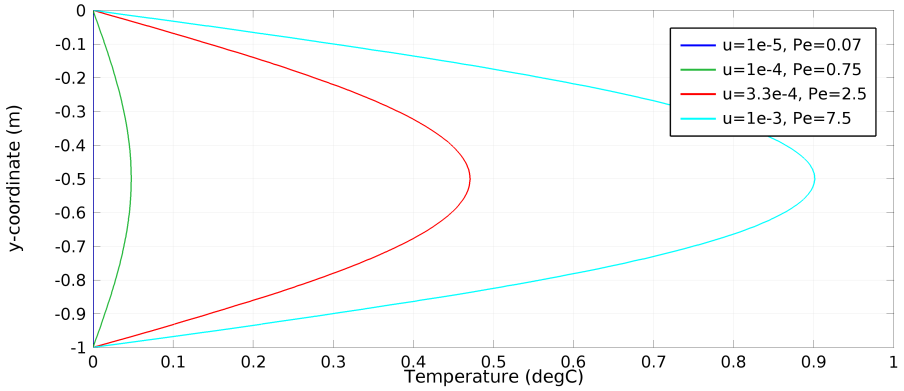

(b) L=50 m

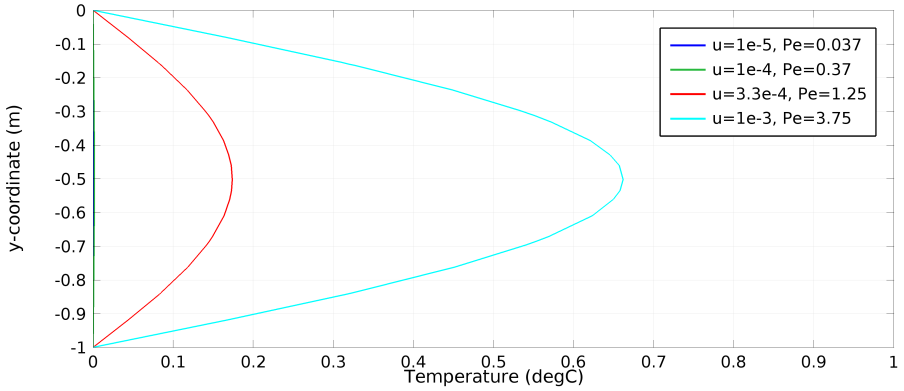

(c) L=100 m

FIGURE 7.4: Vertical temperature profiles at progressive distance from upstream (L) for different Darcy velocities

to D. In other words, if the position where the boundary conditions are applied changes, the solution consistently changes. This is a well known problem affecting elliptical and parabolic partial differential equations: it does not matter how far boundary conditions are applied, their value and position will always affect the steady state solution. While the correct position of the upper boundary is straightforward, as it coincides with the soil surface, it is hard to give a rule for a correct positioning of the lower boundary.

However, if the boundaries are far enough from the region of interest, the solution of the transient problem will not be influenced by the boundary conditions. Being less sensitive to the boundary conditions, transient analysis is always recommended. It still remains important to verify that the vertical size of the domain is sufficiently large that the solution does not change if the boundaries are moved farther.

7.4 Numerical simulation of the IJkdijk piping test

Figure 7.5 illustrates the model that reproduces a cross-section of the test dike. Seepage occurs in the blue domain, which represents the sand layer. The dike (domain 3) is assumed to be impervious and clayey. Domain 1 is also impervious and clayey; it needs to be included because of its influence on the temperature field but for the pressure field it can be ignored because of the impervious foil placed between the sand layer and the in situ soil. Considering domain 3 impervious is instead an approximation, since some pressure can actually dissipate in it. Since the base of the test dike had a high clay content and was compacted very well, the dissipation was of course smaller than it would be expected in a normally constructed dike. Thus in a real dike this approximation should be considered with more care.

The soil parameters used in the model are seen in Table 7.1. The thermal conductivity is calculated using the geometric mean model in Eq. (4.41); the heat capacity is calculated according to the weighted average in Eq. (4.46).

In conformity with the convention used in Chapter 6, the cross-section of the dike lies in the yz-plane, with the origin placed at the upstream toe of the dike and the z-axis

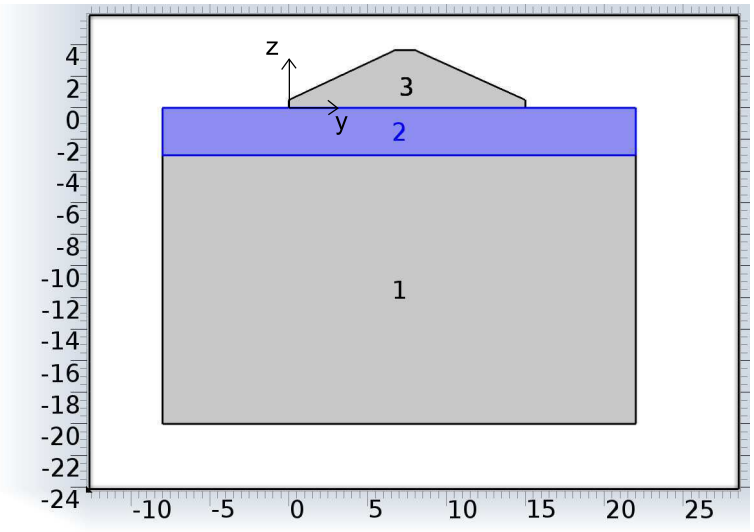

FIGURE 7.5: Model of the large-scale test

TABLE 7.1: Soil parameters used in the model simulating the large-scale piping test

Soil parameter	**Value**	**Unit**
ε (sand)	0.4	-
ε (clay)	0.3	-
K	$1.5 \cdot 10^{-4}$	m/s
λ_w	0.6	W/(m·K)
λ_q	7.7	W/(m·K)
λ_o	2.0	W/(m·K)
λ (sand)	2.77	W/(m·K)
λ (clay)	1.39	W/(m·K)
c_w	4186	J/(kg·K)
c_s	710	J/(kg·K)
ρ_w	1000	kg/m^3
ρ_s	2650	kg/m^3
C (sand)	$2.8 \cdot 10^6$	J/(m^3·K)
C (clay)	$2.5 \cdot 10^6$	J/(m^3·K)

pointing upwards. The boundary and initial thermal conditions are assumed as follows:

$$\begin{aligned} &t \leq 0, \quad && T = 12\,^\circ\mathrm{C} && \forall (y,z) \in D \\ &t > 0, \quad && T = 12\,^\circ\mathrm{C} && \forall (y,z) \in \partial D \mid z = -20\,\mathrm{m} \\ & && && \forall (y,z) \in \partial D \mid z \geq 0 \wedge y \geq 7\,\mathrm{m} \\ &t > 0, \quad && T = T_w && \forall (y,z) \in \partial D \mid z \geq 0 \wedge y < 7\,\mathrm{m} \end{aligned} \tag{7.9}$$

where T_w is the temperature of the reservoir water.

As the temperature measured at the base of the dike before the beginning of the test was quite uniform, a first attempt was made assigning a uniform initial temperature

throughout the domain, assuming that this simplification would not affect the solution in the region of interest.

At the bottom of the model the temperature is assumed constant. As a matter of fact, as seen in § 4.6, the temperature of the Earth is roughly constant in a zone extending from about 10 m to about 60 m depth, as a result of the complex interaction between heat flows from the atmosphere and heat flows from the earth interior.

The boundary condition at the top is approximated by a Dirichlet condition, although a rigorous modelling should consider multiple heat fluxes, including air convection and solar radiation.

At the inflow and outflow boundaries the measured hydraulic head is assigned. The maximum element size is 0.1 m in the flow domain and 0.25 m outside. The time step, chosen in accordance with Eq. (7.6), is 0.5 h.

Temperature data about the inflowing water was not available, so the input data for the model was varied until the best fitting between the numerical results and the measurements was achieved: Fig. 7.6 depicts the best fit obtained. In the comparison between numerical solution and measurements it is important to focus on the data recorded up to 67 h, as the first opening and successive adjustments of the drainage valve are not modelled. The decrease observed in the blue line after 60 h can be reproduced only assuming that $T_w(t)$ was not constant during the test. On the contrary, if T_w would be assumed constant, a monotonically increasing temperature would be obtained at every distance from upstream. The hypothesis of decreasing upstream temperature seems reasonable, as the reservoir was initially filled with 10 cm of water that was heated by a very shiny sun during the hours preceding the beginning of the test. The mixing with increasing quantities of cooler water supplied from a nearby channel would have caused the reservoir temperature to progressively decrease.

It is undeniable that calculated and measured arrival times of the thermal front at $y = 1.7$ m are much different. We considered three possible causes for this behaviour: (1) the hydraulic model provided inaccurate values for the seepage velocity, (2) the assumption made on the thermal initial conditions was unacceptable, (3) thermal dispersion was not negligible. The first two points will be addressed in the next sections, while for the last point a rigorous investigation is difficult because of both the lack of input data and the uncertainty related to the dispersivity models available to date.

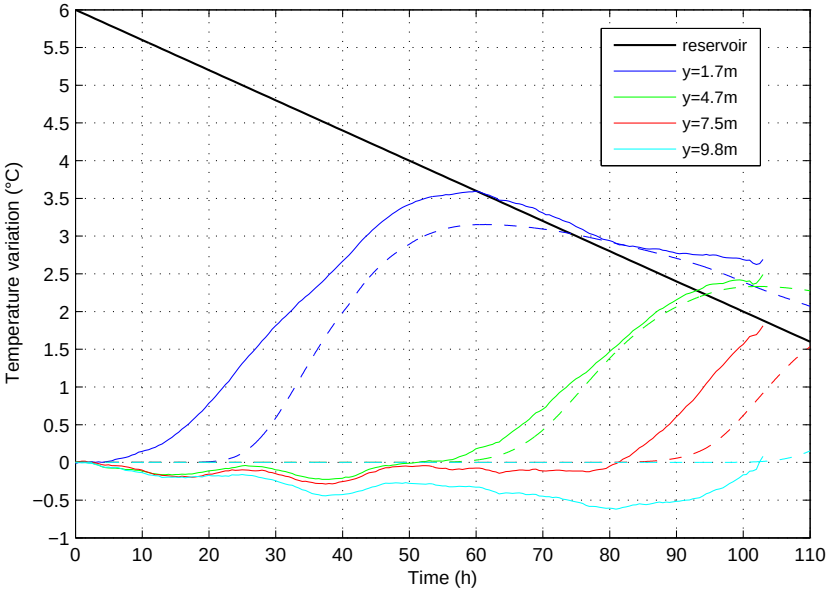

FIGURE 7.6: Comparison between measured (solid lines) and calculated (dashed lines) temperature variations induced by the seepage flow. As the reservoir temperature was not available, the function in the graph is the best guess.

7.4.1 Fine tuning of the hydraulic model

The model was refined to get the best fit between the solution and the pore pressures measured at four positions along the seepage path.

First, the compressibility of the porous matrix (§ 4.1), that had been initially neglected, was introduced. The water compressibility was again considered negligible for the pressures in play. In Fig. 7.7 the pore pressure measured by the transducers placed at $x = 6.8$ m is compared to the simulated pore pressure; the comparison is made form 0 to 40 h, as afterwards some events occurred that were not simulated (piping and opening of the drainage tube). As expected, the matrix compressibility influences only the transient phases, corresponding to the repeated raises of the reservoir level. The best fit is obtained for $X_m = 3 \cdot 10^{-7}$. During the first two hours the error is large as the pore pressure is of the same order of magnitude as the accuracy of the transducers (0.2 kPa). Figure 7.8 illustrates the effect of the matrix compressibility: if it is set too small, the pressure propagates faster in the model than in the reality; if it is set too large, the pressure propagation is too slow. Figure 7.9 shows the role played by the matrix compressibility on the flow velocity: introducing the compressibility the velocity increases at the beginning of the seepage path and decreases towards the end. This occurs only when the water level is being increased upstream (blue curves), while when the water level is stable, the matrix compressibility does not influence the seepage velocity

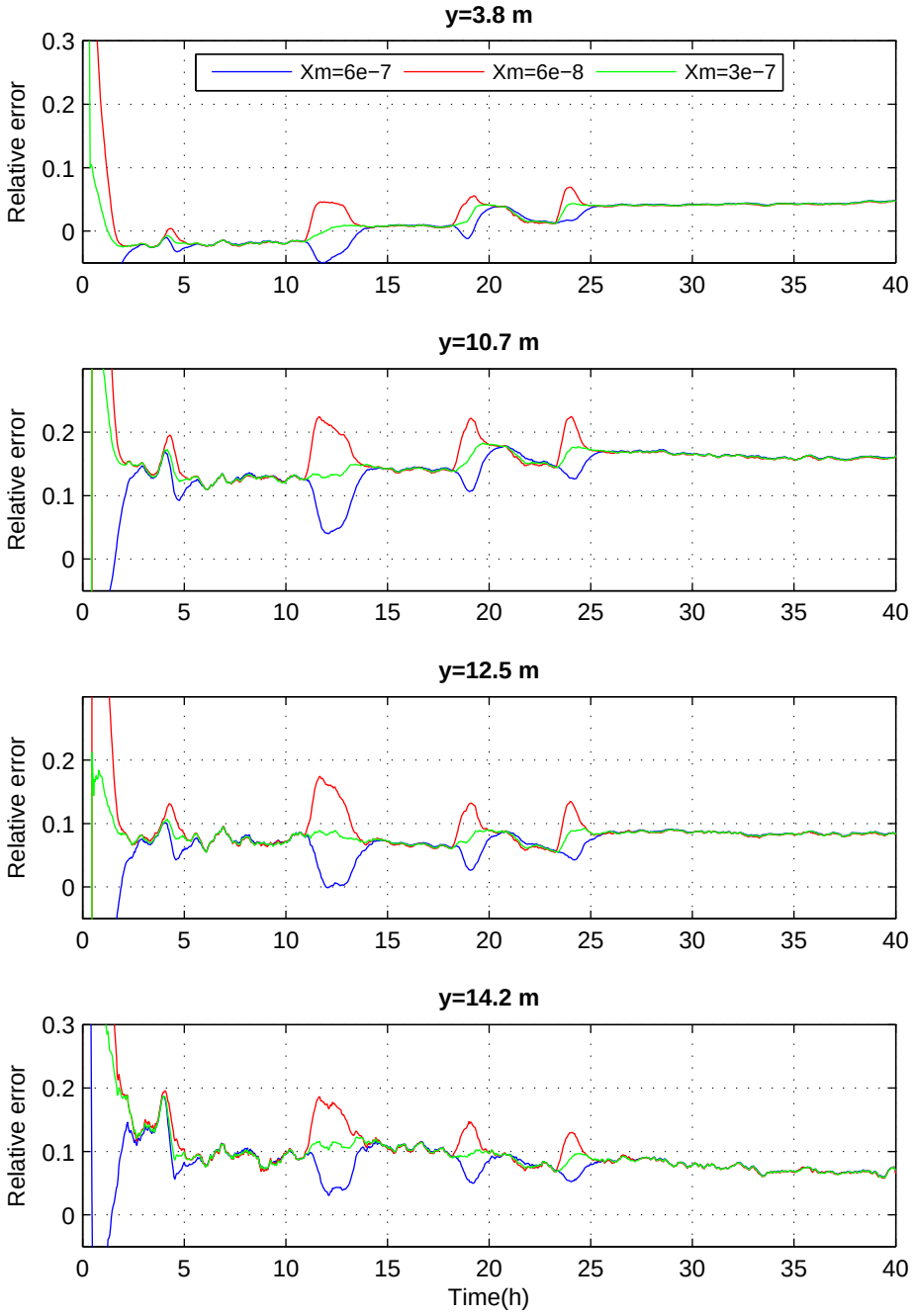

FIGURE 7.7: Difference between the pore pressure measured at x=6.8 m and the pore pressure calculated assuming different degrees of matrix compressibility X_m.

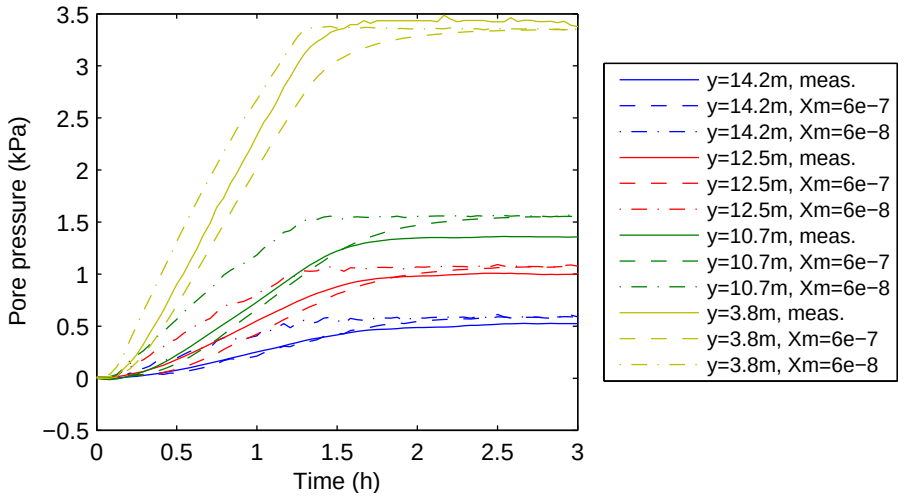

FIGURE 7.8: Pore pressure measured during the first 3 hours of the test and pore pressure calculated assuming two different degrees of matrix compressibility X_m.

(red curves). The increase of the Darcy velocity in the upstream region, consequent to the refinement of the hydraulic model, is, however, too small to produce the acceleration of the thermal front that was sought.

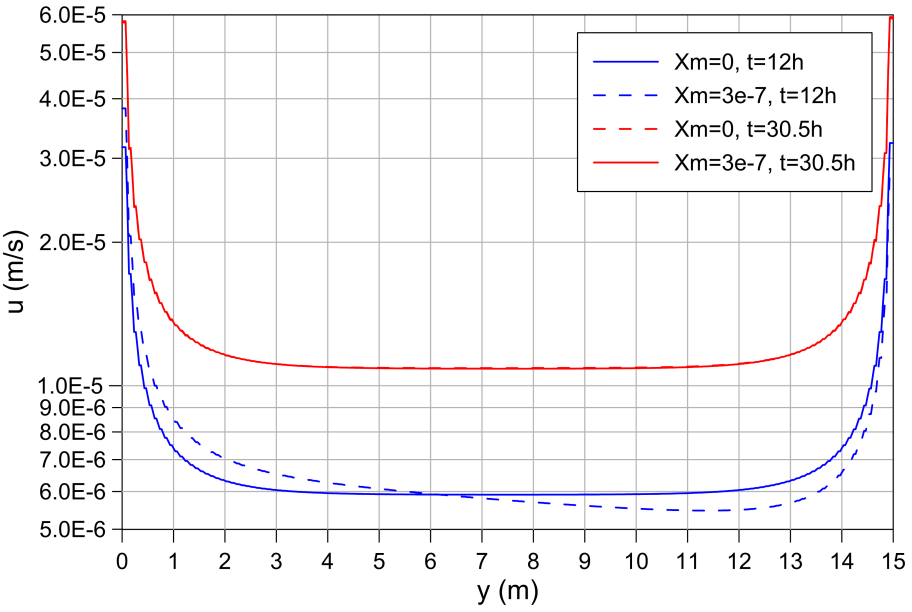

FIGURE 7.9: Effect of matrix compressibility on seepage velocity: blue curves refer to a transient phase, during the increase of the water level in the basin; red curves refer to an equilibrium phase, after the load had been maintained constant for hours.

Despite the modification made to the hydraulic model, it was noticed that an overestimation of the pore pressures of 5 to 10% was still present. The overestimation occurred even at equilibrium, where the compressibility of the matrix has no influence. At $y = 10.7$ m the overestimation was larger because at the x-coordinate that was

selected to perform the comparison ($x = 6.8$ m) the pore pressure was lower than at other points along the same line of sensors.

A further improvement of the hydraulic model consisted in introducing along the inflow boundary a thin layer affected by *clogging*. Clogging is the reduction of pore volume caused by deposition of fines suspended in the reservoir water and/or by biological processes. Clogging translates in a reduction of the permeability of a thin layer that, acting as a dissipator, causes a reduction of the pore pressures downstream. The thickness of the clogged layer in the model ($d_c = 0.3$ m) was dictated by the mesh size. The best fit of the data was obtained assigning to the clogged layer a hydraulic conductivity $K = 4 \cdot 10^{-6}$ m/s. As the thickness of the layer in the model is much larger than the thickness of a possible clogged layer in the reality, the meaningful data here is the transmissivity $T = K \cdot d_c = 1.2 \cdot 10^{-6}$ m^2/s. With this expedient the error in the pore pressure was reduced of about 5% at each position (Fig. 7.10). Sellmeijer et al. (2011) in their simulations of the piping tests performed at the same test site in 2009 also took into account sedimentation, reducing the actual hydraulic head by 5%, 10% and 0% in three different tests.

Since a low permeability layer has also a retardation effect on the propagation of the pore pressure, the value of the matrix compressibility giving the best fit between measured and simulated data was slightly lower for the new hydraulic model than for the previous model.

Also this improvement had no effect on the propagation of the thermal front.

It is likely that modelling the clayey base of the dike as an impermeable boundary removed from the model some dissipation that actually occurred in that layer. A further improvement of the hydraulic model would require to model the whole dike, but this path was not tried.

7.4.2 Modelling of the true initial conditions

This section describes the steps followed to determine the temperature distribution in the soil before the beginning of the test. Since the dike had been constructed few months before the test was run, it was necessary to (1) determine the temperature distribution in the soil before the construction and then (2) simulate the effect of the air temperature on the embankment in the months that separated the construction from the execution of the test.

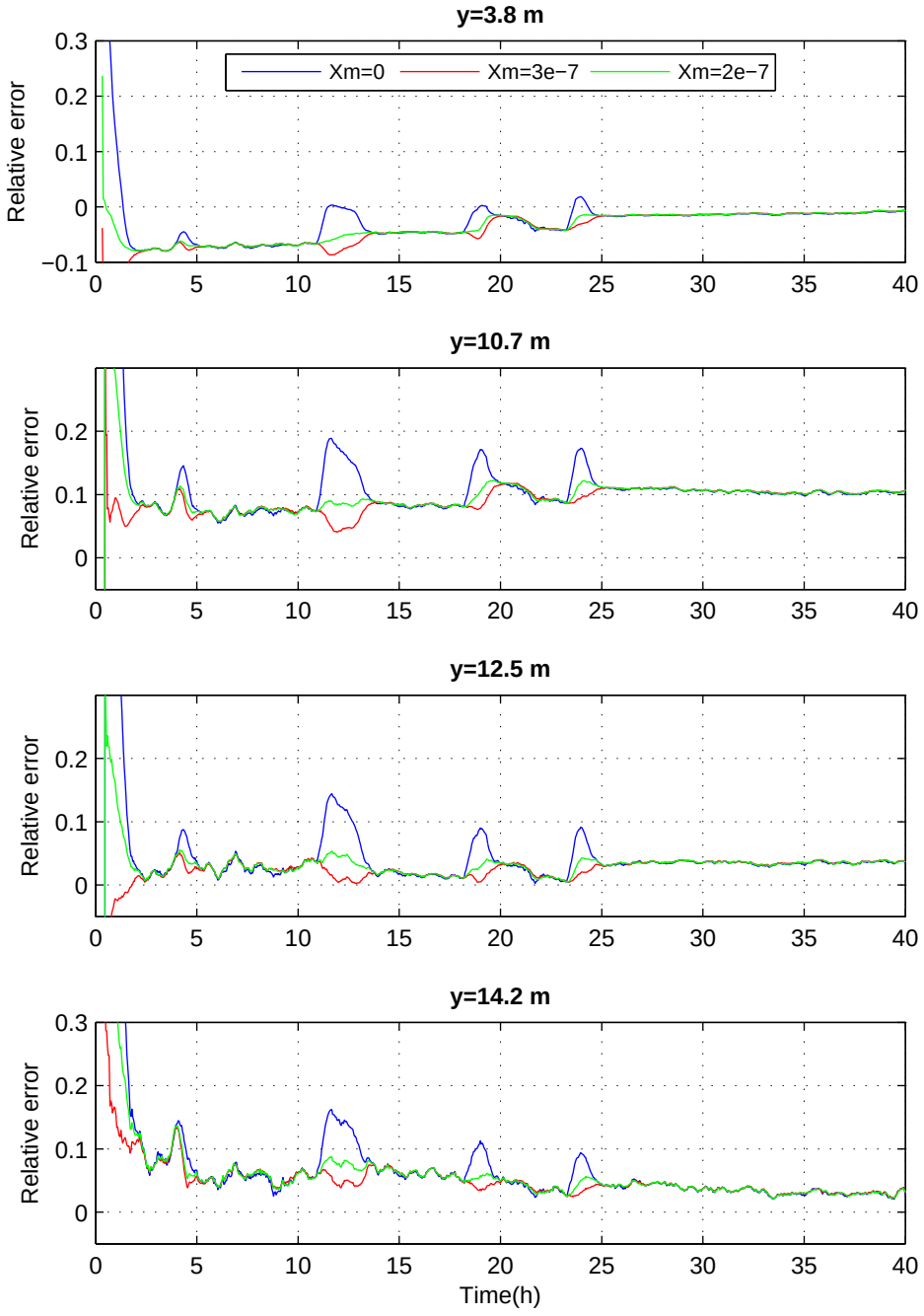

FIGURE 7.10: Difference between the pore pressure measured at x=6.8 m and the pore pressures calculated introducing a clogged layer upstream and assuming different degrees of matrix compressibility X_m.

1. The daily average temperature registered at Nieuw Beerta, the closest (about 3 km far) weather station among those of the KNMI (Koninklijk Nederlands Meteoroloigisch Instituut), was considered. The data of the preceding five years were interpolated using Eq. (4.50) and the parameters that minimized the mean error between measured and calculated values were determined. It was obtained: $T_a = 9$ °C, $A_0 = 8.5$ °C and $t_0 = 20$ days. Measured and calculated temperatures are reported in Fig. 7.11. Interpolation of the data relative to the period aug 2011 - aug 2012 produced slightly different results: $T_a = 10$ °C, $A_0 = 7$ °C and $t_0 = 23$ days.

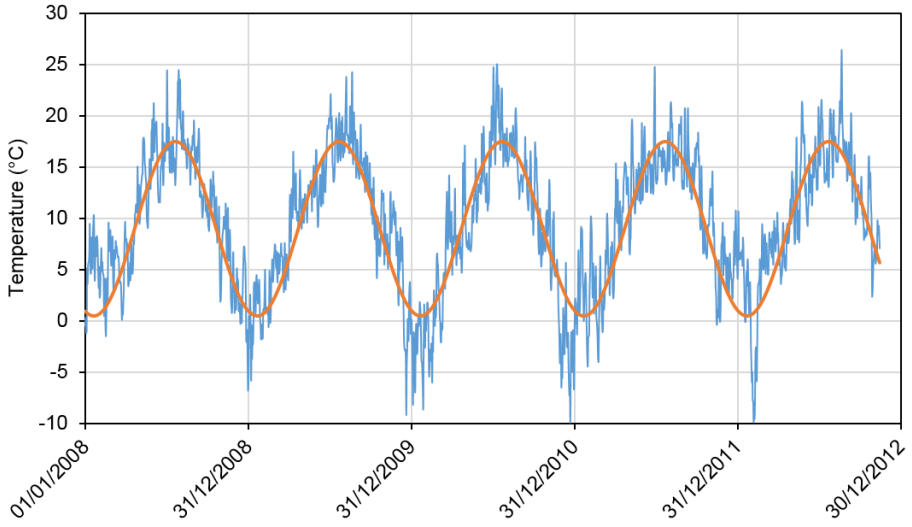

FIGURE 7.11: Daily average temperature measured at the weather station of Nieuw Beerta during the five years preceding the large-scale test (in blue) and interpolation of the data using a sinusoidal function (orange curve).

Using Eq. (4.51) and the parameters describing the yearly variation of the air temperature, the soil temperature distribution was determined for the moment when the test embankment was constructed, which was around 1st July 2012 ($t = 186$ days). Figure 7.12 shows the temperature distribution along depth. An average thermal diffusivity $a = 0.8 \cdot 10^{-6}$ m^2/s was assumed, from which it follows a characteristic penetration depth $d = 2.83$ m.

2. A homogeneous initial temperature was assigned to the embankment soil, which value was determined by trial and error.

   The following boundary conditions were assigned: temperature at the lower boundary equal to the average annual temperature T_a and temperature at the surface equal to the values registered at Nieuw Beerta between the construction of the dike

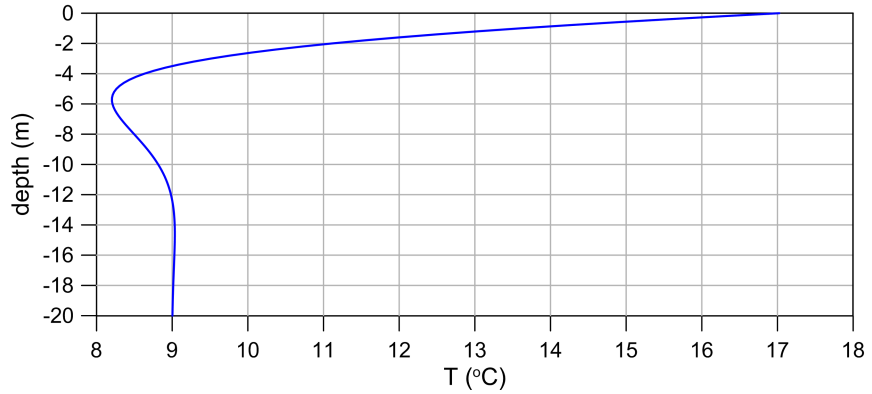

FIGURE 7.12: Calculated vertical distribution of the soil temperature at the moment when the test embankment was constructed (1st July 2012)

and the beginning of the test (1st Jul - 21st Aug 2012). The latter are illustrated in Fig. 7.13. The temperature measured by the weather station installed at the test location was compared with the temperature measured at Nieuw Beerta in the period 1st Aug - 21st Aug 2012 and an excellent agreement was found between the two.

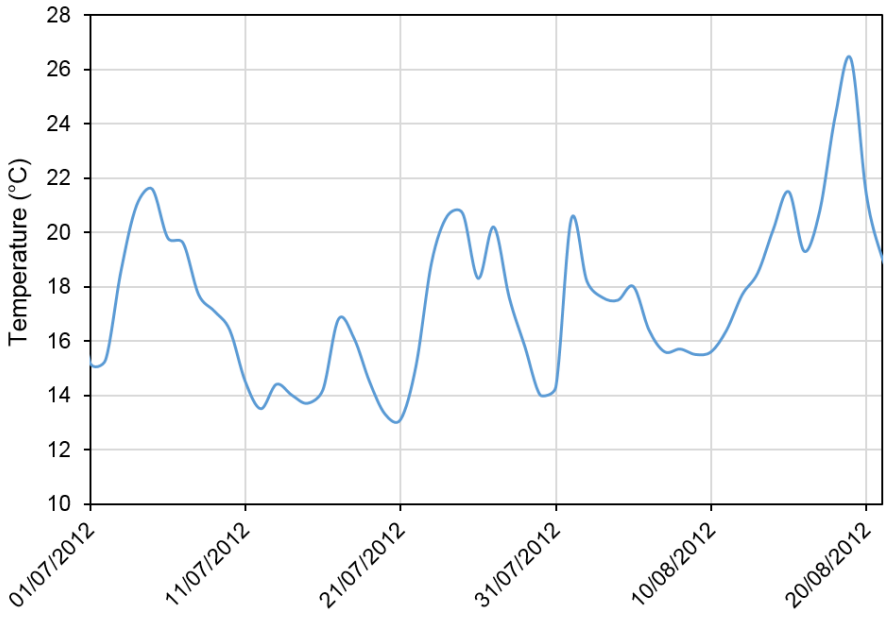

FIGURE 7.13: Daily average temperature measured at the weather station of Nieuw Beerta between the construction of the dike and the beginning of the test

The penetration of the conductive thermal front through the embankment was simulated for the period 1st Jul - 21st Aug 2012. Figure 7.14 shows the temperature distribution obtained at the base of the embankment. In order to achieve a good match between simulated and measured temperature values at the base at the

embankment, the thermal conductivity of the embankment had to be reduced from the first guess of 1.39 W/(m K) to 0.5 W/(m K). This value is typical of partially saturated materials (see Fig. 4.7). The best match was obtained assuming that the soil used to build the embankment had a temperature of 13 °C. Although Nofziger (2005) suggests to assume the surface temperature equal to the air temperature increased by 2 °C for bare soils, satisfactory results were obtained assuming the surface temperature equal to the air temperature on the South-oriented slope of the embankment and reducing the air temperature by 2 °C on the North-oriented slope. This possibly accounts for factors that were not taken into account: the effects of the grass cover as well as of the strong wind typical of the region.

The daily excursion, that affects the soil temperature up to 1 m depth, has not been taken into account. It is worth mentioning that any other simplification that was attempted in recreating the initial situation produced temperature values at the base of the embankment not compatible with the measurements made by the optical fibres.

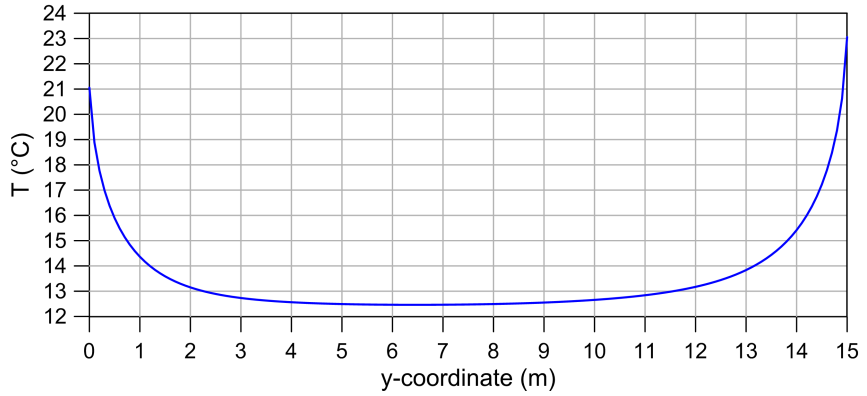

FIGURE 7.14: Temperature distribution at the base of the embankment at the beginning of the test as obtained by numerical simulation

The temperature distribution calculated following the procedure above, was used as initial condition for a new simulation reproducing the test. The new boundary conditions were:

$$\begin{aligned} T &= 9\ ^\circ\mathrm{C} \qquad \forall (y,z) \in \partial D \mid z = -20\,\mathrm{m} \\ T &= 17.5\ ^\circ\mathrm{C} \quad \forall (y,z) \in \partial D \mid z \geq 0 \wedge y \geq 7\,\mathrm{m} \\ T &= T_w \qquad \forall (y,z) \in \partial D \mid z \geq 0 \wedge y < 7\,\mathrm{m}. \end{aligned} \tag{7.10}$$

Assuming T_w linearly decreasing during the test between 18 °C and 16 °C, a good agreement was found between the simulation and the temperature measured by the most

upstream sensor (see Fig. 7.15, blue curves). There is also good agreement for what concerns the arrival time of the front at $y = 4.7$ m. As stated earlier, attention should focus on the data recorded up to 67 h, as the first opening and successive adjustments of the drainage valve are not modelled.

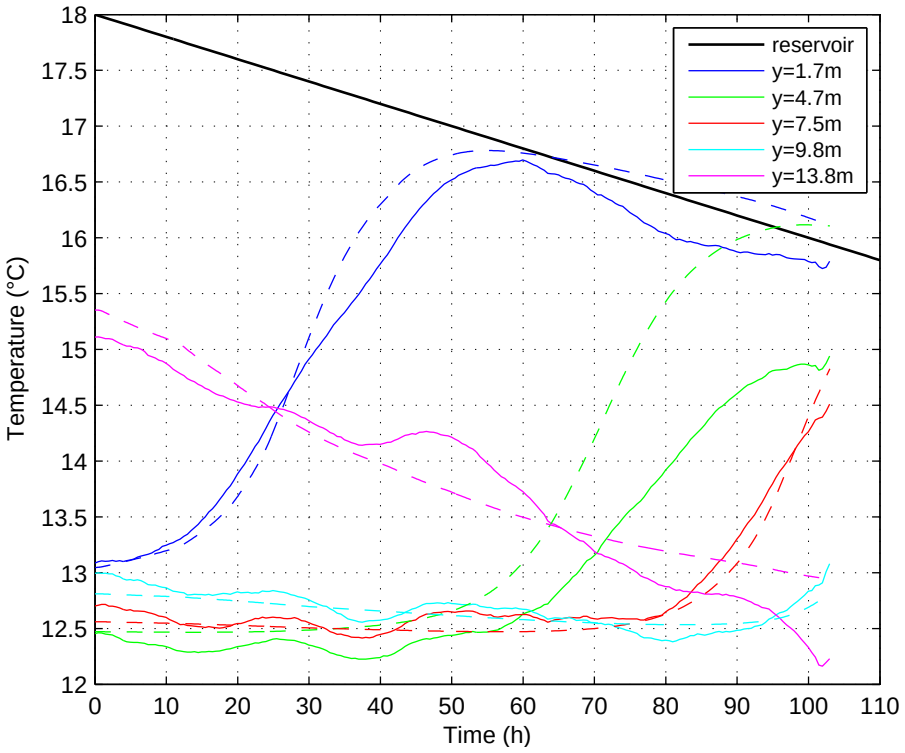

FIGURE 7.15: Comparison between temperature measured during the test (solid lines) and temperature calculated with improved initial conditions (dashed lines). As the reservoir temperature was not available, the function in the graph is the best guess.

7.4.3 Prediction of the dike behaviour over a longer time horizon

It was verified that the numerical model is reliable in reproducing the thermal variations induced by seepage flow in a saturated soil. Therefore, it can be used to project the observations made in the field over a time scale longer than the test duration.

The simplified model described at the beginning of § 7.4, with homogeneous initial thermal conditions and incompressible porous matrix, was used. It was assumed $T_w = \text{const}(t) = 16$ ℃ and a constant hydraulic load of 3 m ($u = 3 \cdot 10^{-5}$ m/s). Figure 7.16 shows how the seeping water preserves almost entirely its initial temperature up to the downstream toe. However more than 4.5 days (i.e. more than the duration of the measurements) are necessary for the thermal front to reach downstream.

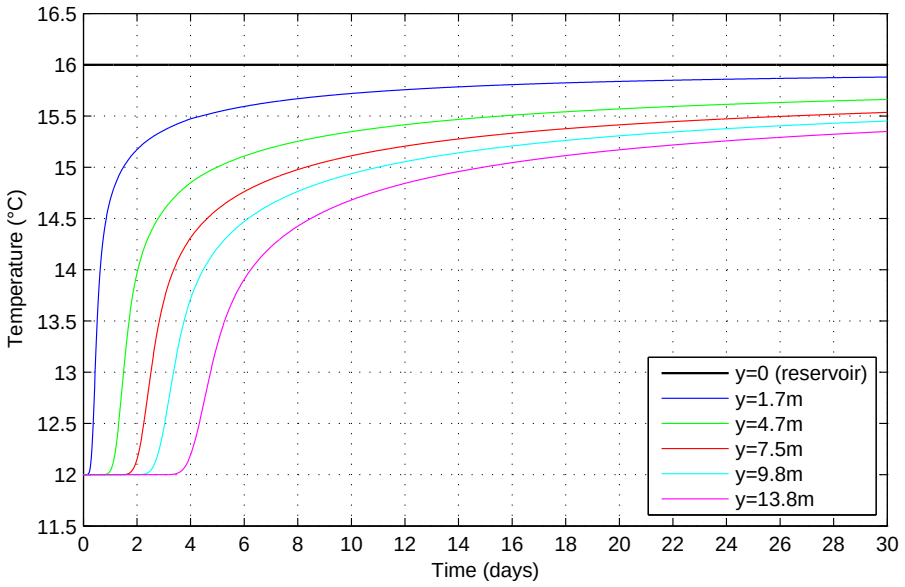

(a)

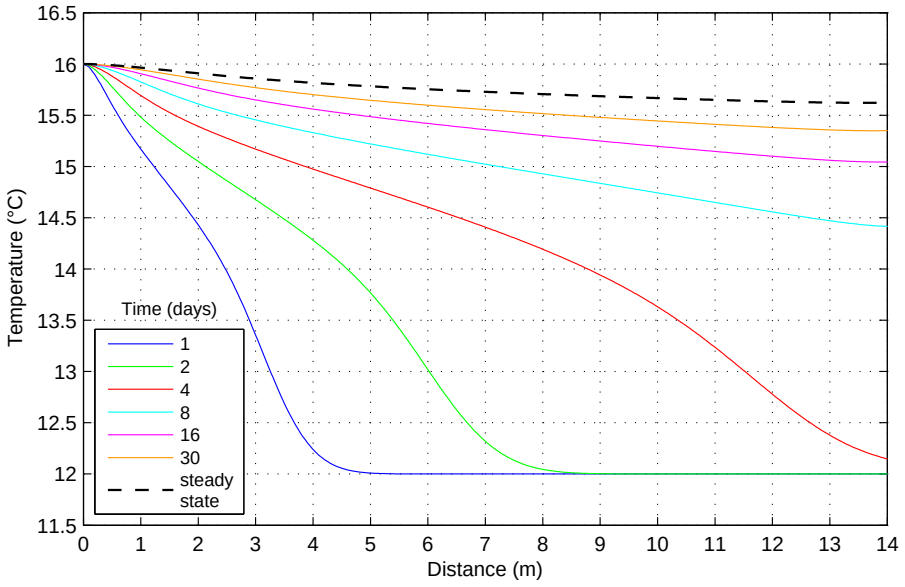

(b)

FIGURE 7.16: Simulation of the propagation of the thermal front in the test dike on a time scale longer than the duration of the test. Temperature is depicted as a function of time (a) and as a function of distance (b).

It can be concluded that in the large-scale test heat advection occurred in the sandy layer over the whole seepage length, not only in the pipes where the flow velocity is higher, but also in the intact soil. If the test would have progressed further, also the most downstream sensor would have registered a significant temperature variation.

At $y = 13.8$ m, $Pe_g \simeq 5$, which confirms the suitability of Pe_g for predicting the behaviour of 2-d hydrogeological systems. Moreover, the arrival time of the advective thermal front $t = 13.8$ m$/\mathbf{v}_T = 3.5$ d, where $\mathbf{v}_T$ is the (average) velocity of the thermal advective front defined in § 4.3, proved to be an acceptable estimate of the true arrival time of the thermal front.

7.5 Thermal anomalies induced by piping

The literature reports that leakage detection using the passive method relies on the existence of a temperature gradient between the waterbody and the soil. The outcomes of the large-scale test made clear, however, that what is actually needed for early detection of backward erosion piping is the existence of a difference between the temperature around the tip of the pipe and the soil at the location of the sensor, which is generally close to the tail of the pipe (or anyway more downstream then the tip of the pipe). This temperature difference will be called *effective thermal gradient*.

When the pipe is in its first stages (much earlier than its tip reaches upstream), a temperature gradient between the waterbody and the soil does not always translate in an effective thermal gradient. In other words, the existence of a temperature gradient between the waterbody and the soil is a condition not sufficient for the generation of thermal anomalies connected to piping. Section 7.5.1 presents the additional conditions.

Good news is that an effective thermal gradient might exist even with null temperature gradient between the waterbody and the soil. Section 7.5.2 clarifies the phenomenon that provides effective thermal gradients independently of the temperature of the waterbody.

7.5.1 Seepage-induced temperature gradients

An effective thermal gradient can develop if a thermal front propagates from upstream up to the tip of the pipe during a flood event. This occurs if all the following conditions are satisfied at the same time:

1. a temperature difference exists between the waterbody and the soil at the base of the dike;

2. advection prevails over the distance between the inflow point and the tip of the pipe;

3. the time necessary for the thermal front to reach the tip of the pipe is smaller than the duration of the design flood event.

With reference to point 1, the temperature at the base of the dike in case of no water flow or very slow flow varies seasonally and can be predicted using Eq. (4.51) or, in order to take rigorously into account the geometry of the dike, through numerical modelling, as seen in § 7.4.2. How the temperature of rivers and sea varies during the year was not investigated in this work.

Conditions 2 and 3 can be verified through numerical modelling or using the analytical tools discussed in the previous sections. The second approach is more approximate but can provide a better overview of the problem.

For what concerns point 2, advection prevails if the geothermal Péclet number of the dike foundation layer is greater than 1. In calculating the geothermal Péclet number the vertical size of the domain is assumed equal to half the thickness of the permeable layer.

For what concern point 3, the time necessary for the thermal front to reach the tip of the pipe can be calculated using the advective thermal velocity as reported in § 4.3: this is an upper bound for the arrival time of the thermal front, as conduction around the advective front is neglected. (A lower bound is given by the one-dimensional analytical solution.)

It must be recalled that some simplifying assumptions have been taken on the safe side and might have a not negligible influence on the results. Therefore the above conditions are sufficient for a thermal variation to be transmitted downstream, but could be not fully necessary. Also slightly lower parameters (lower seepage velocity or lower duration of the flood event) could produce a sensible thermal variation in the subsoil.

When the thermal behaviour of the foundation is intermediate between advective and conductive, a thermal gradient forms along the whole seepage path and it persists if a constant hydraulic head is maintained across the structure (Fig. 7.17, u=2e-6 m/s). When the thermal behaviour of the foundation is mainly advective, a gradient initially forms along the seepage path (u=2e-4 m/s, t=1 d; u=2e-4 m/s, t=3 d), and thus along

the pipe, but, if the hydraulic head is maintained over time, the temperature under the dike eventually equals the temperature of the waterbody (u=2e-4 m/s, t=inf), so that the possibility to detect leakages decreases with time.

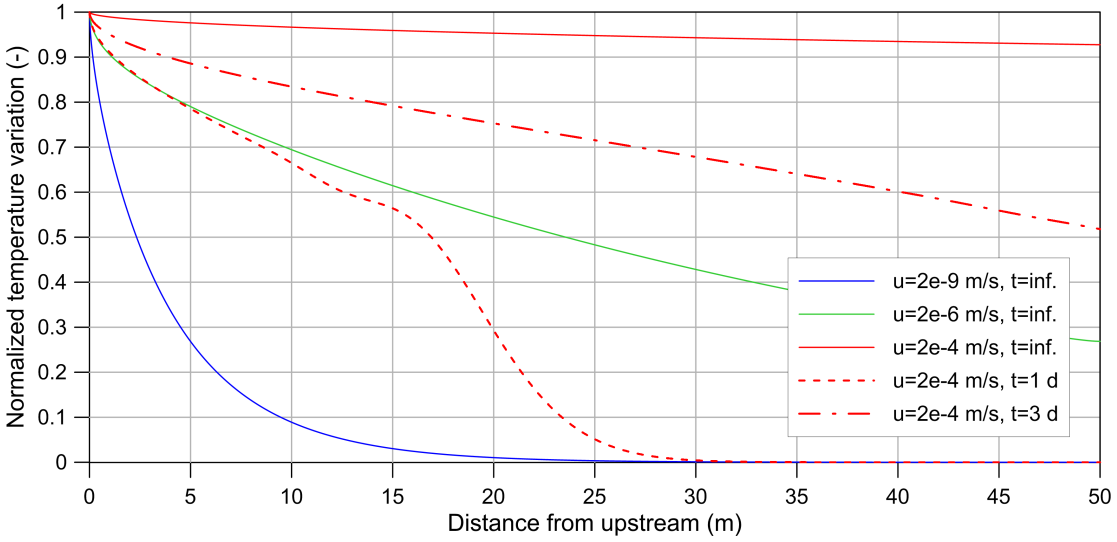

FIGURE 7.17: Horizontal temperature profiles for increasing Darcy velocity. Typical conductive (blue), intermediate (green) and advective (red) profiles are illustrated. The values are obtained by steady state analysis in a domain of size: L=50 m, D_H=3 m and D=10. For the higher Darcy velocity the evolution of the temperature with time is also depicted (dotted and dashed line).

It was investigated if conditions 2 and 3 were satisfied in piping-prone dikes for a wide range of geometries and seepage velocities. This was done, for condition 2, plotting the geothermal Péclet number as a function of distance (L) and of thickness of the sand layer (D) and, for condition 3, plotting the time required for the thermal front to reach a certain distance as a function of the distance itself. The distance can either be the seepage length or any other distance along the seepage path at which it is wished to know the behaviour. Figure 7.18 reports the plots made for two limit values of the seepage velocity expected in field situations. Fig. 7.18a depicts the case of a hydraulic conductivity typical of loose, coarse sands and a high average horizontal gradient equal to 0.2. Fig. 7.18b depicts the case of a hydraulic conductivity typical of dense, fine sands and an average horizontal gradient of 0.1. Typical horizontal gradients capable of triggering piping are around 0.1 or even lower.

Fig. 7.18a shows that in very permeable sands an intermediate or advective behaviour is expected. Only the arrival times need to be checked. The graph also shows that the difference between upper limit and lower limit of the arrival time (solid and

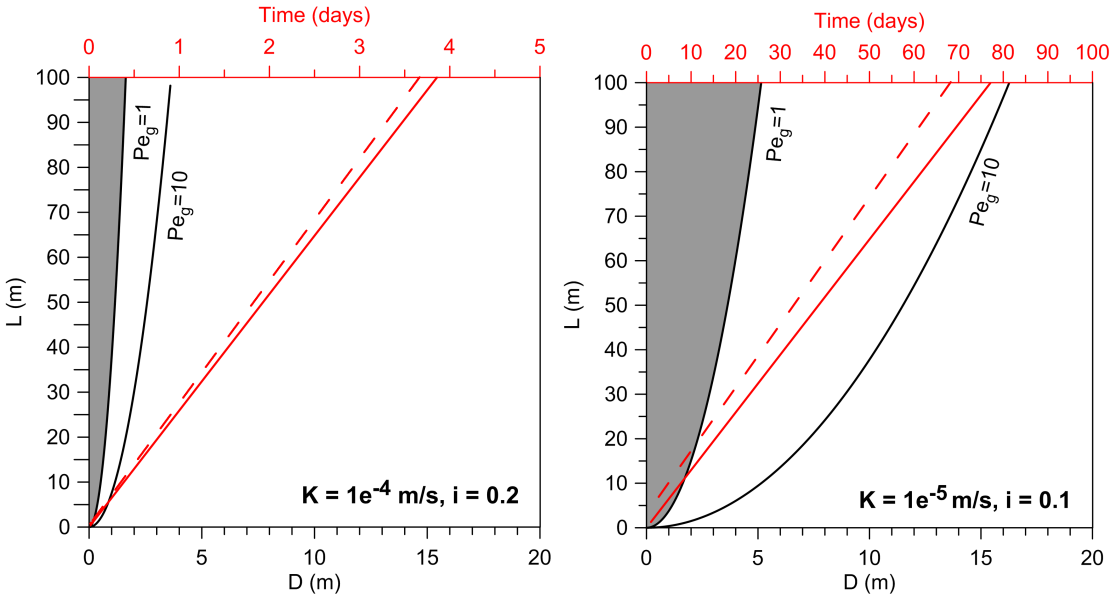

FIGURE 7.18: Approximate threshold values of the Geothermal Péclet number as a function of distance from upstream (L) and thickness of the sand layer (D), for two values of the Darcy velocity (u). On the upper x-axis the arrival times of the thermal front can be read: the solid red line indicates the upper limit (calculated using the velocity of the advective front) and the dashed red line indicates the lower limit (determined using the analytical solution of the 1-d problem).

dashed red line respectively) is relatively small. This confirms that estimating the arrival time of the thermal front using the velocity of the purely advective front does not introduce a large approximation.

Fig. 7.18b says that for less permeable sands the role of advection is limited when the sand layer is thin. Given the limitations concerning the non-dimensional parameters, these cases should be addressed with the aid of a numerical model. However it was also observed that the arrival times are large in comparison with the duration of flood events typical of the middle and final course of small and medium rivers or the duration of storm surges. For this reason, before proceeding with in-depth analyses, it is convenient to ascertain that the arrival time of the thermal front and the duration of the flood event are compatible. Comparing Fig. 7.18b with Fig. 7.18a it can also be observed that, as the Darcy velocity decreases and consequently the order of magnitude of the arrival time increases, the difference between lower and upper limit also increases. This seems reasonable, as the larger the time, the more the thermal front spreads around its centre of gravity because of heat conduction.

7.5.2 Initial temperature gradients

In § 7.5 it was seen that a flood event could be not long enough to allow the thermal front to reach downstream. However, the field data, supported by numerical modelling, have shown that a thermal variation can start to develop at the downstream toe shortly after the beginning of a flood event, exploiting another phenomenon: the alteration of a temperature gradient present under the dike before seepage occurs.

7.5.2.1 Horizontal gradient

At the base of a dike the distance from the surface increases when moving from the toes towards the crest. An increasing distance from the surface translates in increasing damping and phase shift of the annual excursion of the air temperature. It was seen in the field test that when the dike is built directly on a sand layer, and therefore the sensor is deployed at the very base of the dike, a significant temperature gradient is measured in the direction of the flow, close to the downstream toe, resulting in a continuous temperature variation at the toe during a flood event.

The common case of a dike built on agricultural soil, where the sand layer prone to piping is a few metres below the ground level, is now considered. The model is depicted in Fig. 7.19. Domain 2 and 3 are clayey and domain 1 is sandy. The soil parameters are again those reported in Table 7.1. Fig. 7.20 depicts the temperature

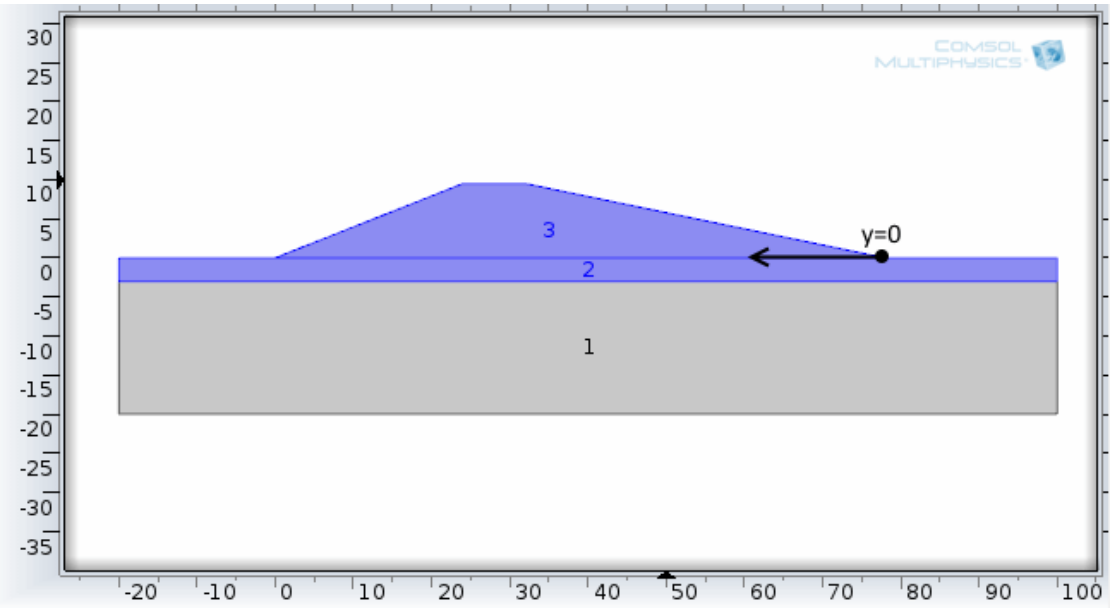

FIGURE 7.19: Model of a dike (domain 3) built on an agricultural soil (domain 2); the sand layer prone to piping (domain 1) is few metres below the ground level.

distribution under the dike obtained applying the boundary conditions in Fig. 7.11. As the distance from the ground level increases, the temperature gradients close to the downstream toe decrease, but still remains at a detectable level. The calculation has been repeated assuming that both the dike and the agricultural soil have a low water content: $\lambda_{unsat} = 0.5$ W/(m·K) and $C_{unsat} = 1.6 \cdot 10^6$ J/(m^3·K). This is a likely hypothesis for newly built dikes, as the test dike, but less likely for old dikes. Figure 7.21 depicts the results of the new calculation.

7.5.2.2 Vertical gradient

A piping channel basically works as a partially penetrating well rotated of 90 degrees. In a partially penetrating well water flows from the soil towards the well, entering both from the bottom and from the sides (Fig. 7.22). In a pipe, water enters both from the tip and along the pipe - through the sides and though the bottom.

Figure 7.23 shows the flow net below a piping channel. The deeper the sand layer the more the water entering from the bottom. However a value can be defined, above which the flow field around the pipe is not affected by a further deepening of the sand layer.

Although most of the water enters in the pipe in proximity of the tip, as testified by the density of the stream lines, the pipe produces a modification of the groundwater flow all along its length. Under the pipe the flow becomes mainly vertical and this can alter a pre-existing thermal vertical gradient. As seen in the previous section and displayed in Fig. 4.15, the thermal gradient decreases with depth. Thus, the deeper the pipe and the sensor, the lesser the temperature variation resulting from the modification of the water flow.

Superposition of the alterations of the horizontal and vertical gradient due to piping may be - borrowing terms from the weave theory - both constructive and destructive in producing thermal variations.

7.5.3 Temperature field in the vicinity of a pipe

In the previous sections the development of a temperature difference between the water flowing inside the pipe and the sound foundation soil far from the pipe was considered. This is likely what was measured in the large-scale test, where the sensor was installed

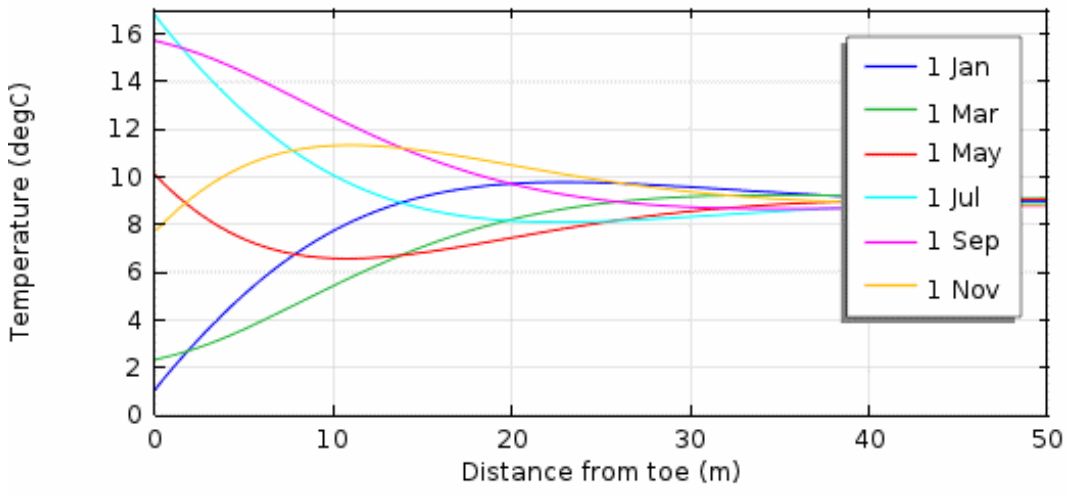

(a) z=0

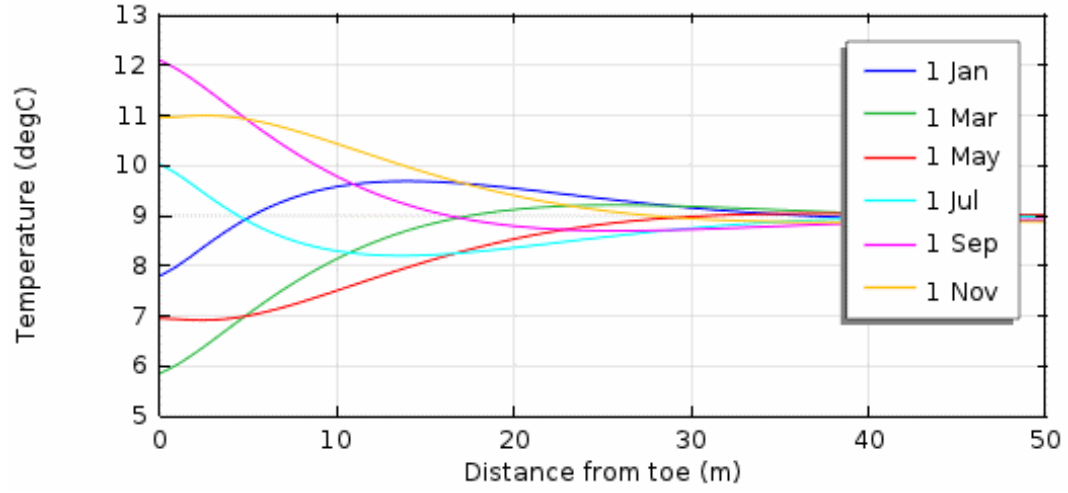

(b) z=-2 m

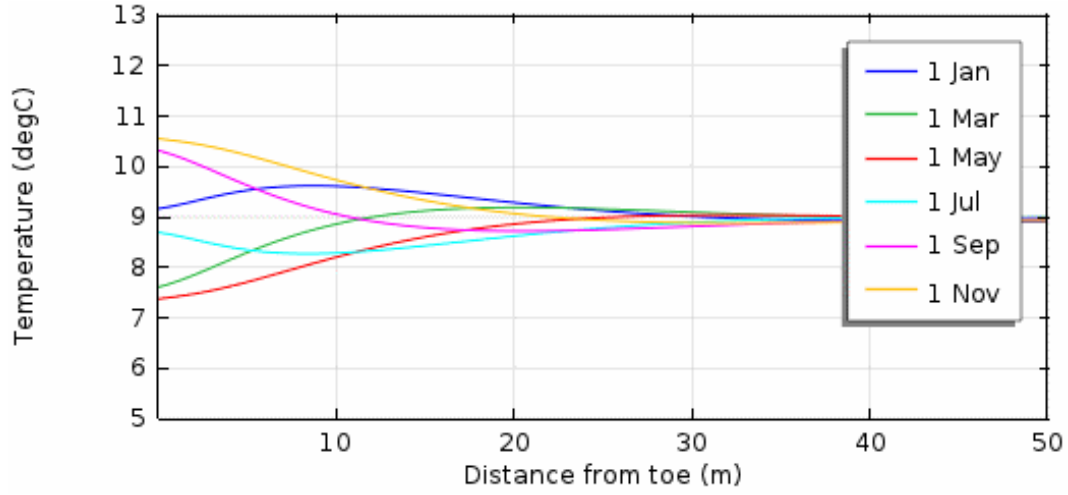

(c) z=-3 m

FIGURE 7.20: Horizontal temperature profile under the dike in Fig. 7.19 for different distances from the ground level (z) and different moments of the year. No seepage condition.

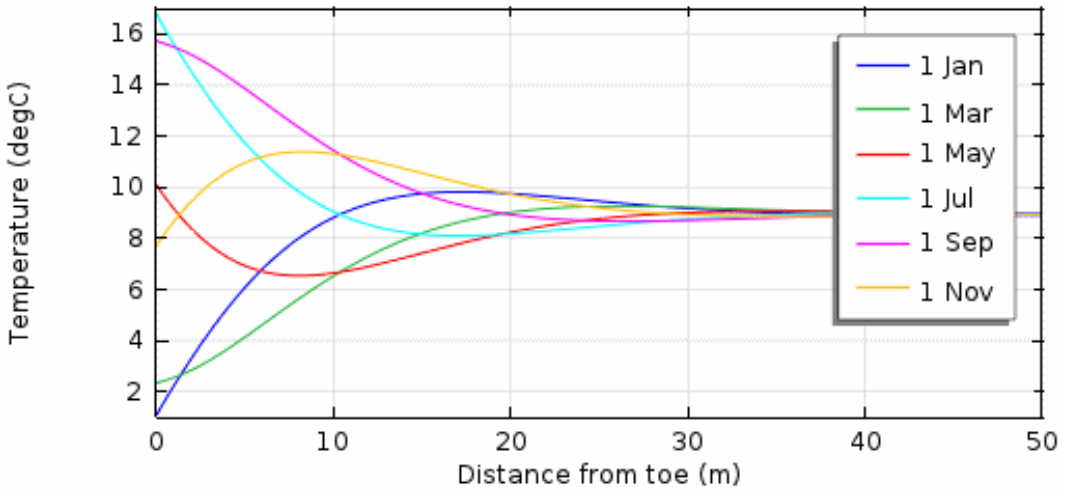

(a) z=0

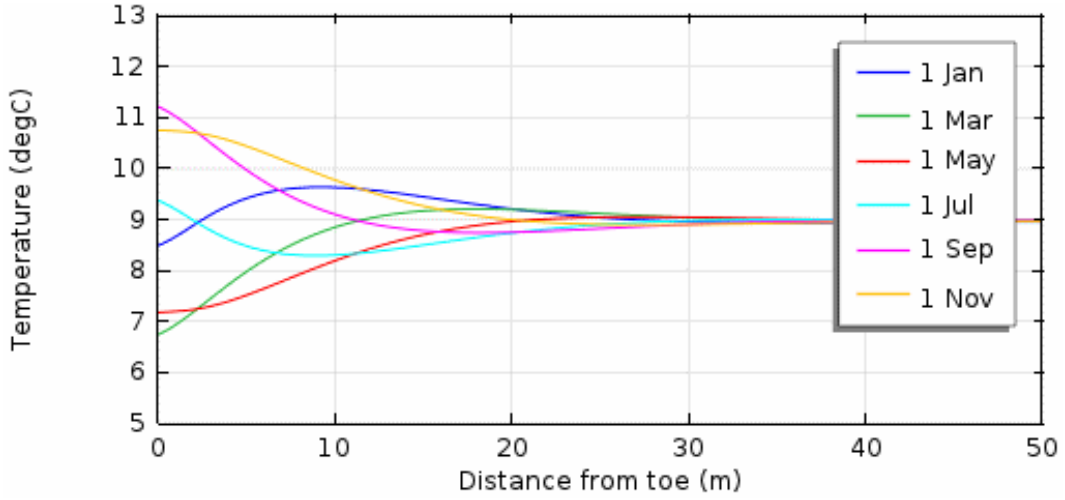

(b) z=-2 m

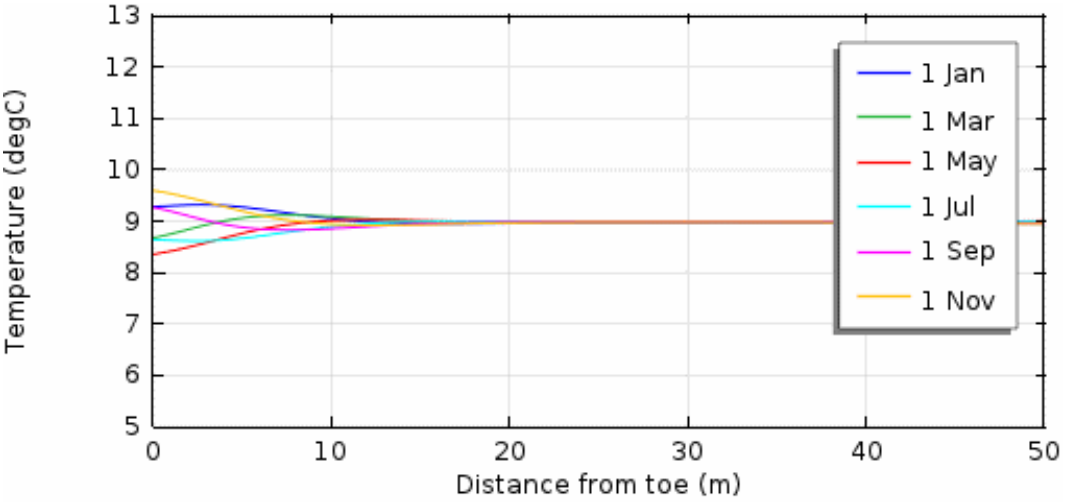

(c) z=-3 m

FIGURE 7.21: Horizontal temperature profile under the dike in Fig. 7.19 for different distances from the ground level (z) and different moments of the year. The water content of the dike and of the agricultural soil is assumed to be very low. No seepage condition.

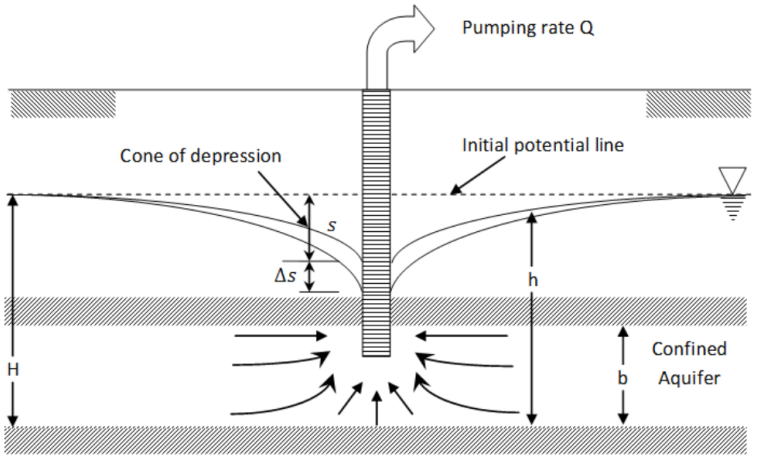

FIGURE 7.22: Partially penetrating well

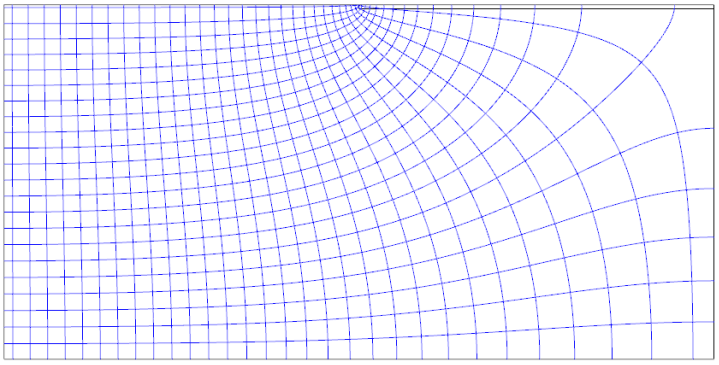

FIGURE 7.23: Flow net under a pipe extending for half the seepage length)

during the construction of the dike. Nevertheless, in practice, the sensor will be hardly located inside the pipe.

Backward erosion can affect a large area due to the branching of the pipes, but the thickness of the affected area remains very small up to failure. Theoretically, the sensor must be placed at the interface between the sand layer and the above clayey/silty cover, but a centimetric precision is hard to reach when working in the field. Moreover, the depth of the interface can slightly vary along the dike and complying with these variations requires great care.

It is therefore valuable investigating the thermal variations occurring in the surroundings of the pipes as a consequence of (1) heat conduction between the pipes and the soil and/or (2) variation of the flow field around the pipes.

Some interesting work in this direction has been done by Radzicki and Bonelli (2010a) using numerical analysis with finite volumes.

In this work the problem is not addressed in detail, but some examples and directions for further research are given. As explained in § 7.2, finite elements are not suitable for coupled modelling of mass and heat transport where high velocities and high velocity gradients occur, like in pipes. Convergence cannot be achieved with any reasonable mesh refinement. Therefore only the mass transport induced by a pipe was modelled using finite elements, while the modelling of the coupled problem is demanded to further research in which finite volumes should be employed.

A 3-d numerical model representing a slice of the foundation layer of the test dike was created. In the model a pipe was included. The size of the pipe was defined based of the observations reported in § 6.4.4: the pipe was 1 m long, 2 mm thick and 20 cm wide.

The results show that the pipe produces an increase of the y-component of the Darcy velocity (upstream-downstream direction) behind the tip of the pipe and a decrease of the same component at the sides of the pipe (Fig. 7.24). The latter is due to the flow around the pipe changing its main direction from parallel to perpendicular to the pipe walls. This is seen in Fig. 7.25, where the increment of the vertical velocity induced by the pipe is plotted.

Fig. 7.26 shows that an overall velocity increase occurs along the flow path towards the pipe. This promotes the advancing of a thermal front in the surroundings of the pipe. Again, the velocity does not increase close to the tail of the pipe.

It can be observed that the radius of influenced by the pipe decreases toward the tail.

Fig. 7.24 and 7.26 suggest that - for a plane type exit - a decrease of the velocity components perpendicular to the optical cable should be expected when the cable is located below the tail of the pipe. This is a useful information to keep in mind when piping detection relies on the active method, for which only the variations of the flow velocity at the position of the cable matter.

The radius of influence of a pipe is strongly dependent on the length of the pipe, both absolute and relative to the seepage length. Radzicki and Bonelli (2010a) showed that for pipe lengths ranging from 10 to 30 % of the seepage length the significant temperature changes are localized in the limited zone close to the upstream end of the pipe (which is in accordance with Fig. 7.24); however, when the pipe length equals about 50% or more of the seepage length, important changes in the thermal field almost touch the upstream side of the dike foundation.

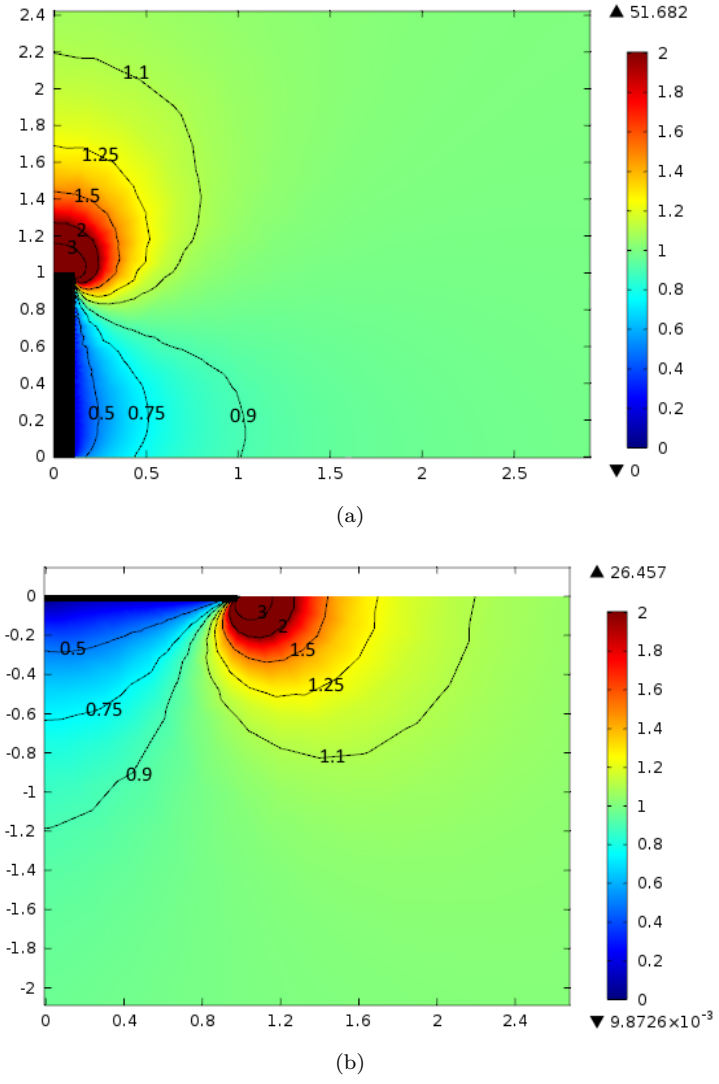

FIGURE 7.24: Variation of the y-component (from upstream to downstream) of the Darcy velocity in the surroundings of a pipe 1 m long. Top view (a) and side view (b). The velocity in the pipe is not plotted (black area). Values bigger than 1 indicate a velocity increase with reference to the situation with no pipe; values smaller than 1 indicate a decrease.

Radzicki and Bonelli (2010a) also investigated the effect of the hydraulic conductivity of the soil and the effect of the radius of the pipe. They showed that the first strongly determines the thermal field around a pipe, while the influence of the second is negligible.

Another factor that needs to be investigated is the configuration of the exit point (see Fig. 2.4). The presence of a landside blanket that requires the pipe to start at a crack or discontinuity in the blanket (hole type exit) causes the radius of influence on the pore pressure to be larger in comparison with the case of no blanket (plane exit), which also was the configuration of the large-scale test described in Chapter 6.

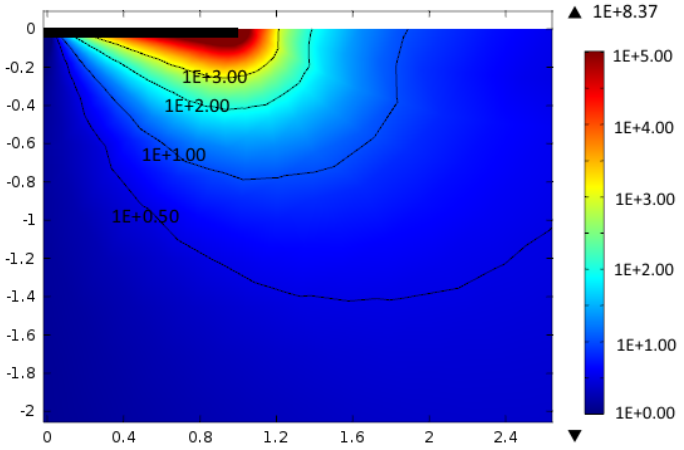

FIGURE 7.25: Variation of the vertical component of the Darcy velocity in the surroundings of a pipe 1 m long. Side view. The velocity in the pipe is not plotted (black area). Colorscale and contours are in a logarithmic scale. Values bigger than 1 (1E+0.00) indicate a velocity increase with reference to the situation with no pipe.

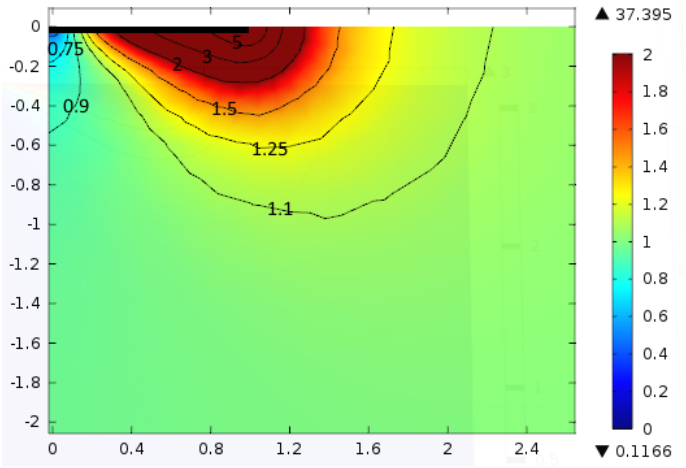

(a)

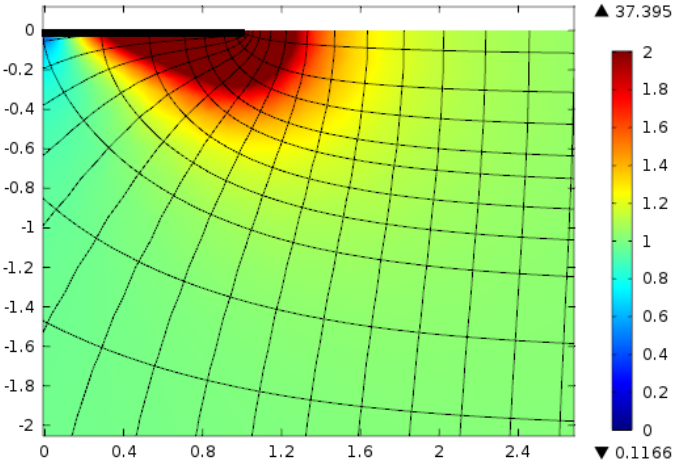

(b)

FIGURE 7.26: Variation of magnitude of the Darcy velocity in the surroundings of a pipe 1 m long. Side view. The velocity contour lines are added to the colorscale in (a) and the flow net is added in (b). The velocity in the pipe is not plotted (black area).

Finally, the effect of a network of pipes should be investigated.

7.5.4 Conclusions

The temperature field at the bottom of a dike is continuously changing, both seasonally and because of the discontinuous seepage flow. Considering the specific features of sea and river dikes prone to piping - high permeability and hydraulic loads of short/medium duration - it was demonstrated that a number of situations exist where backward erosion can induce thermal anomalies at the landside toe of the dike. It is likely that the upstream thermal front propagates up to the tip of the pipe during the flood event, but before the arrival of the thermal front or in case the front does not arrive at all, the combined effect of pre-existing horizontal and vertical thermal gradients close to the dike toe might also allow piping to generate a thermal anomaly.

Another issue that could not be investigated deeply in this work but it is believed to deserve further research is the spatial distribution of the thermal anomaly around the pipe. This is important because it is unlikely that the sensor will be located exactly in the pipe, given the small thickness of the pipe (or pipe network).

The results obtained so far are promising but more research is needed, supported by field data, in order to verify that passive thermometry is effective in all situations.

Chapter 8

Small-scale modelling

In comparison to large-scale field tests, small-scale modelling allows better control over boundary conditions and model parameters, as well as better repeatability at much lower costs. In the study of flow through porous media, sand box models are extensively used when the equations of motion and/or the boundary conditions are too complex to permit a purely analytical or even a numerical prediction of the prototype behaviour. In this chapter a sand box model adapted to study backward erosion piping is presented. It incorporates a distributed temperature sensor to measure temperature variations induced by piping. Downscaling of the phenomenon under study was addressed, for the first time to the author's knowledge, adopting a distributed sensing technology characterized by very high spatial resolution. In the chapter, details of the setup are given together with preliminary results and illustration of the difficulties connected to the integration of the novel sensor in the model that are progressively being solved.

8.1 Scaling rules

Studying the scaling effects is very important when designing experiments because it is fundamental to know beforehand how the process studied in the laboratory represents a field situation. In each system (prototype and model) there are several variables and dimensional or dimensionless coefficients. The conditions for which a model reproduces all the aspects of the behaviour of the prototype that are intended to be studied are known as *conditions of similitude*.

Conditions of similitude are not easy to obeyed in a model that couples heat, fluid and sediment transport.

It is worth mentioning that investigating the scaling effects concerning the mechanics of internal erosion is beyond the scope of this study. However, understanding the issues related to the effects of scale on the pipe geometry is beneficial for this work: since a pipe acts as a drain, its influence on the surrounding flow and temperature fields depends indeed on its size and geometry. Few concepts/reflections on this topic will be given in Appendix C.

The most important condition to consider is the *thermal similarity*. It requires that the proportion between conductive and advective heat fluxes is preserved in the model. This occurs if the geometric similarity is fulfilled and prototype and model share the same Péclet number (4.33). In this case the geothermal Péclet number (4.37) is the best available parameter to describe the thermal similarity. An average value of the geothermal Péclet number for the small-scale tests described in this chapter has been calculated as follows:

$$Pe_g = \frac{K\, H/L\, C_w\, D^2}{\lambda\, L} = \frac{5 \cdot 10^{-4} \cdot 0.05/0.3 \cdot 4186000 \cdot 0.075^2}{2.77 \cdot 0.3} = 2.36\,. \qquad (8.1)$$

Given the value obtained, the expected behaviour is intermediate between conductive and advective. As Fig. 7.18 shows this value is typical of a number field situations. In determining the value of geothermal Péclet number the reduction of the geometry scale by a factor on the order of 100 is compensated by the large ratio D/L of the model, that is not always found in the field. In other words, the model qualitatively reproduces heat transfer as it occurs in the field situations under study; the main difference between model and prototype is that while the geometry of the model (and consequently the flow field) reproduces a thick prototype aquifer (large D/L), its thermal behaviour is more similar to that of a thin prototype aquifer (small D/L).

It must be noted however that the geothermal Péclet number does not take into account neither the three-dimensionality of the model nor the thermal insulation provided by the container. The latter, in particular, limits significantly the heat transmitted by conduction and thus the geothermal Péclet number might underestimate the heat transferred by advection.

The time scale of the processes should also be considered. As a matter of fact, the evolution of the advective heat transfer is related to the residence time, which is scaled linearly with geometry if the Darcy velocity is preserved unchanged in the model. On

the other hand, the time evolution of the conductive heat transfer is scaled quadratically with geometry. As a consequence, the relationship between time and geometry scale is linear only when advection prevails.

Accurate upscaling of the temperature field around a pipe is not trivial since the relationship between the pipe geometry in the model and prototype is not yet fully understood, as explained in Appendix C. It seems therefore necessary to rely on experimental evidence from large-scale tests to deduce information on the geometry and size of the pipes at the full scale, and then rely on numerical modelling to translate flow and temperature distributions from a scale to another.

8.2 Setup

The setup designed at the University of Padova upgrades the one designed at Deltares and described in Vandenboer et al. (2014). Thus, that model can be used as a reference for the results concerning sand transport and the attention can be focused on the main subject of the work: heat transfer.

The setup consists of a box (Fig. 8.1) with an aluminium base and PMMA lateral walls and top cover. PMMA stands for polymethyl methacrylate, better known as Plexiglass, which is one among its many commercial names. The transparency of PMMA allows observation of the pipes developing at the top of the sample.

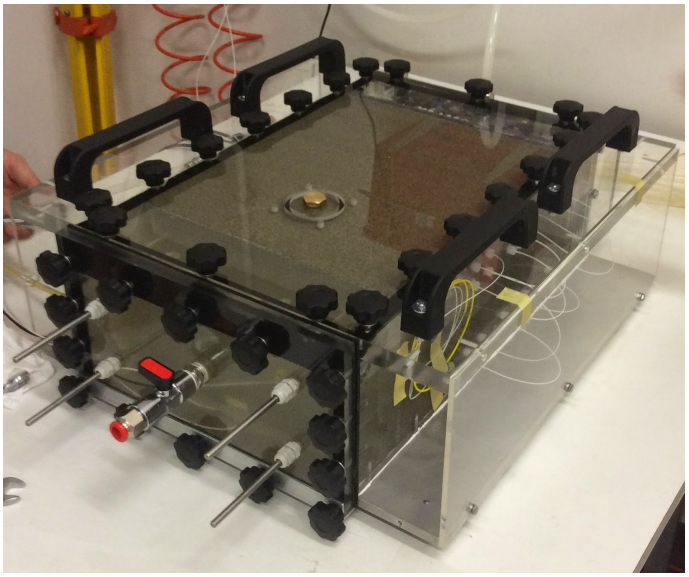

FIGURE 8.1: Sand box

The box contains a sand sample 30 cm wide and 15 cm high. The length (size of the sample in the flow direction) is variable up to circa 35 cm. The sand is retained upstream and downstream by filters consisting each one of a perforated steel plate and a nylon wire mesh of 255 μm aperture. The latter represents a good compromise between retention requirements (verified in accordance with Giroud, 2010) and permeability requirements. Avoiding head loss across the filters is important in order to know the exact load applied to the sample.

The upstream chamber is connected to a constant head reservoir, while the downstream chamber is connected to a free exit which height can be progressively adjusted during the test to apply the desired hydraulic head across to the sample. The setup is illustrated in Figs. 8.2a and 8.3.

The transparent cover has a circular hole located at a distance of 27 cm from the upstream filter and having a diameter of 8 mm. If the downstream tap is closed and water is let flowing from such hole, erosion takes place at the top of the sample as soon as the hydraulic load is above the head required for piping initiation. A cylinder is placed on top of the hole to allow the eroded sand to deposit next to the exit point. Finally, the cylinder is connected to a free exit of adjustable height. A schematic drawing of this alternative configuration is shown in Fig. 8.2b.

Configuration (a) allows a one-dimensional water flow through an intact sample to be realized, while configuration (b) promotes the initiation of backward erosion piping and its progression up to failure. The point exit (see Fig. 2.4) allows for better control over the progression phase. With a slightly modified downstream filter, configuration (a) transforms in a piping setup with a slope type exit.

8.3 Instrumentation

Five piezometer tubes depart from the side of the box to measure the water pressure in the upstream and downstream chambers and the pore pressure in the sample at three progressive distances. Manual reading of the piezometer tubes allows a millimetre precision.

A single standard telecom fibre encased in a tight teflon buffer and about 90 m long is arranged in 15 measuring lines orthogonal to the flow direction. As depicted in Fig. 8.4 the lines are organize in two top layers (2 and 4 cm from the top) and a bottom layer (3 cm from the bottom), each one made of five lines.

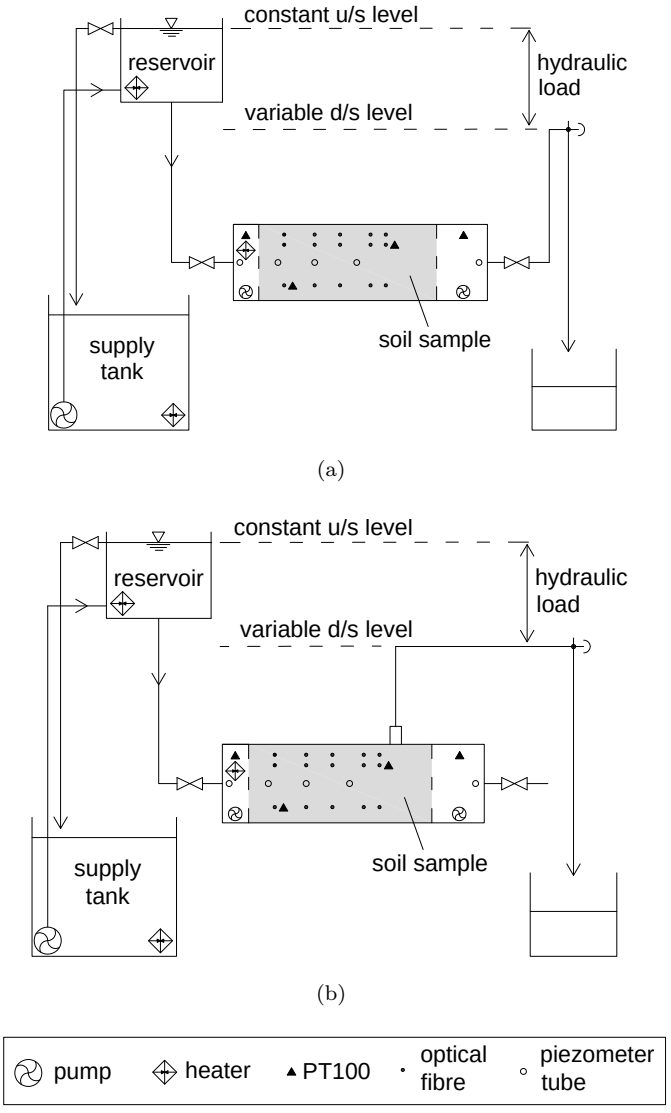

FIGURE 8.2: Schematic of the setup of the experiment. A system supplies hot water at constant temperature and constant hydraulic head; the hydraulic load across the sample is set by adjusting the height of flow exit point. The measuring system consists of 15 lines of optical fibre orthogonal to the flow direction, 4 resistive platinum sensors (PT-100) and 5 piezometer tubes departing from the lateral wall of the box. Small pumps are located in the upstream and downstream chamber to prevent thermal stratification of water.

FIGURE 8.3: Setup of the experiment

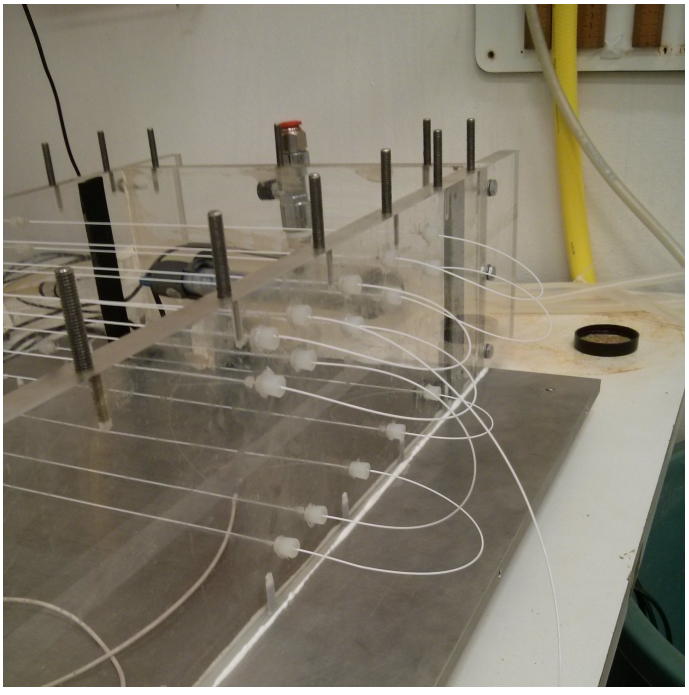

FIGURE 8.4: Arrangement of the optical cable in the box

The optical cable was clamped to the lateral walls to keep the fibre straight inside the sample and prevent any significant movement during the deposition and compaction of the sand. This is fundamental in order to fix the position of the optical sensor in the sample. Two lateral chambers, visible in Fig. 8.1, have been designed to protect the segments of fibre outside the sample. These chambers prevent any accidental movement of the fibre during the execution of the test and, in case the bare fibre (without any protective coating) is used, also protect the fibre from being damaged.

An Optical Backscatter Reflectometer (OBR) from Luna is used to interrogate the fibre. This device is a high resolution optical-frequency domain reflectometer, that measures the spectral shift in the local Rayleigh backscatter pattern (§ 5.2). As the spectral shift is both temperature and strain dependent, any strain must be avoided during the test in order to get meaningful temperature measurements. The knowledge of the temperature coefficient of the used cable allows then the calculation of the local temperature variation with regard to a reference measurement made at the beginning of the test. Temperature is measured with 0.1 ℃ resolution, sub-centimetre spatial resolution and frequency of 30 s. The acquisition and transformation of the data were performed by the colleagues from the Photonics and Electromagnetics group at the University of Padova.

Reference temperature measurements are taken within the sample by two resistive platinum sensors (Pt100) positioned as close as possible to a portion of fibre. Their sensing element is protected by a small teflon cylinder and they are class 1/3 DIN sensors, which means they have 0.15 ℃ accuracy @30 ℃. Other two Pt100 measure the temperature of the inflowing and outflowing water (class 1/10 DIN: accuracy = 0.045 ℃ @30 ℃). A Pt100 sensor with a flat cover which allows perfect contact with surfaces has been used to measure the temperature of the outside surface of the walls (class A: accuracy = 0.21 ℃ @30 ℃). Figure 8.5 shows the surface sensor and the small sensor used inside the sample. All the sensor cables have been kept as short as possible as they introduce an error which increases with length. The error introduced by a 2 m cable is around 0.1 ℃. The datalogger used, a PT104 Pico Technology, introduces a 0.01 ℃ error on the measurements, that is small compared to the accuracy of the sensors. The response time of the sensors were tested diving the sensors in a container and waiting until the response was stable. The operation was repeated for 7 temperature values between 25 ℃ to 35 ℃. For all the sensors it took less than 30 s, that is the acquisition frequency of the optical sensor, to reach the final temperature value. During the same

test it was also verified that the difference between the temperature measured by the sensors was within the accuracy declared by the producer.

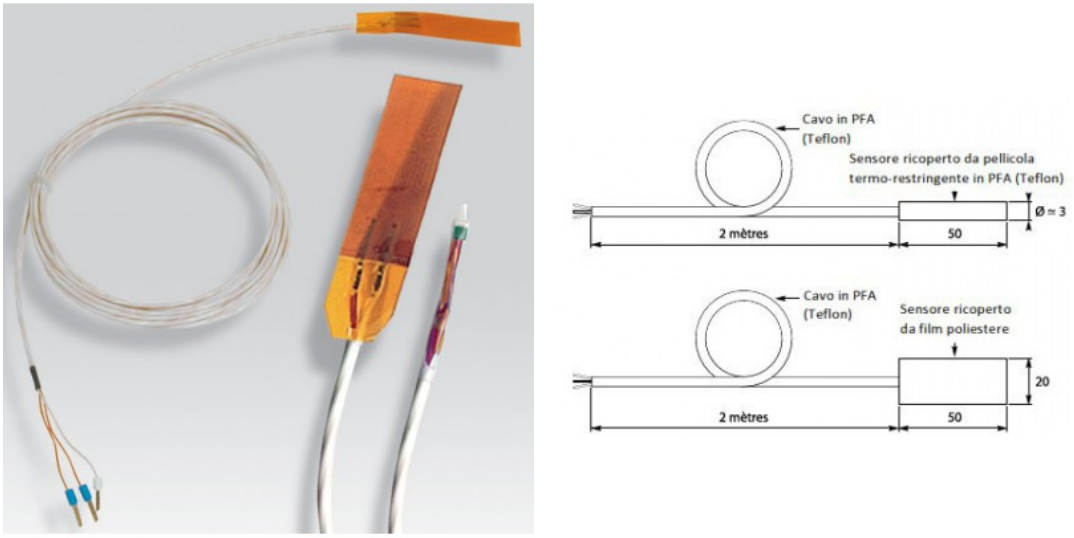

FIGURE 8.5: Resistive platinum sensors (Pt100): flat version for surface measurements and small version used inside the sample.

A camera suspended above the box takes pictures automatically during the test, allowing for the analysis of the pipe size throughout the test.

8.4 Sample material and preparation technique

For this work a washed river sand has been used. As depicted in Fig. 8.6 it is a uniform medium sand with average grain diameter d_{50} of 0.3 mm and uniformity coefficient of 1.5. The high specific gravity, $G_s = 2.73$, is in agreement with the significant amount of mica which is visible to the naked eye.

The sample is prepared using a technique developed at Delft Geotechnics (Van der Poel and Schenkeveld, 1998) that produces highly homogeneous and fully saturated samples with final relative densities between 30 and 70%. It is specifically suitable for poorly graded sands.

The preparation is done placing the box in vertical position as in Fig. 8.1 in order to ensure a good contact at the interface between the sample and the horizontal cover, that is where erosion is going to take place.

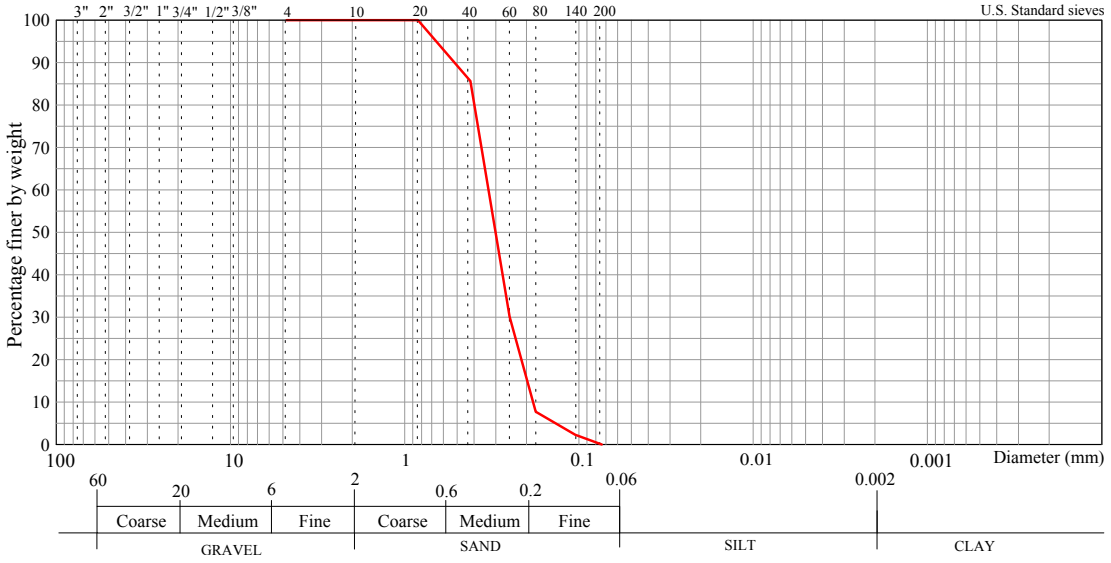

FIGURE 8.6: Grain size distribution of the test sand

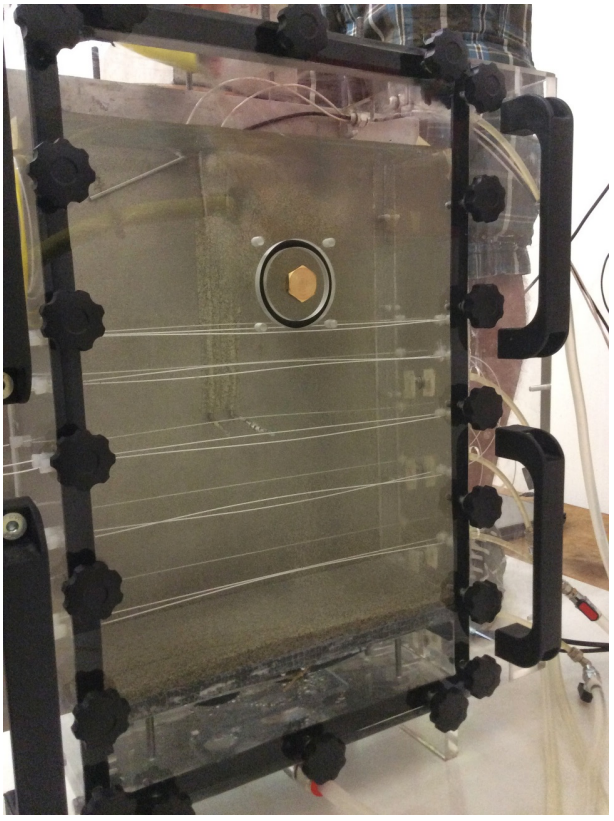

FIGURE 8.7: Box placed in vertical position and filled with water for the preparation of the sample.

TABLE 8.1: Size and bulk density of the tested samples

Sample n.	Dry mass (kg)	Area (cm^2)	Length (cm)	ρ_{dry} (kg/dm^3)	ρ_{sat} (kg/dm^3)	ε -
1	26.0	450	36.0	1.60	2.01	0.41
2	26.3	450	35.5	1.64	2.04	0.40
4	24.7	447	33.0	1.67	2.06	0.39

Dry sand is gradually poured into the box filled with de-aired water. During sedimentation, air inclusions in the dry sand vanish in the water. Then the sample is compacted with vertical shock waves. This is done by lifting the container and letting it fall (5 to 10 mm) on a rigid underground. The shock waves cause a temporary fluidisation of the sand, after which drainage of excess pore water pressures is allowed before the next shock is given.

Unlike compaction by tamping, this technique allows for the deployment of instrumentation in the container before or during deposition without and risk of damage for the instrumentation. Previous tests run at Delft Geotechnics have shown that during sedimentation and fluidisation, the sand flows around objects previously deployed in the container, preventing the formation of shaded regions.

The mass of the poured sand and the height of the sample - before and after compaction - should be recorded to determine initial and final bulk density.

8.5 Test 1

Test 1 was aimed at testing the functioning of the hydraulic and heating system and was performed before the deployment of the optical fibre.

There are two ways of creating a temperature gradient: heating or cooling. Heating was preferred because it is technically easier. Moreover, two options were identified: either flushing the sample at room temperature with hot water or heating the sample and flushing it with water at room temperature. The box has been designed with an aluminium base that, besides giving robustness to the container, is a good thermal conductor and allows the sample to be heated from below by means of a heat pad. However the first option, using hot water, was adopted in the tests run so far.

The characteristics of the sample are reported in Table 8.1.

A schematic of the setup is given in Fig. 8.8. The water in the chamber delimited by the upstream filter was heated by means of a 25-W aquarium heater. A small pump

mixed the water in the chamber to prevent thermal stratification. A closed hydraulic circuit was adopted.

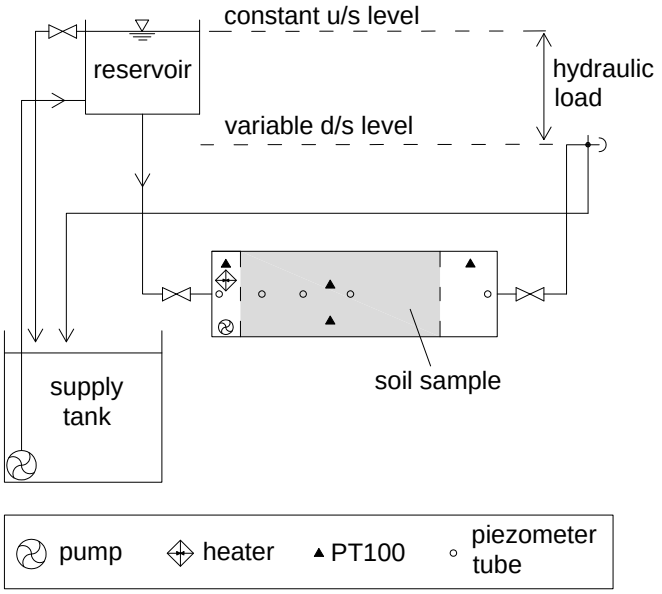

FIGURE 8.8: Setup for the test on sample 1

Tap water was used for sample preparation and execution of this calibration test. The heater was let working overnight before the flow test in order to collect data on the conductive behaviour of the system. A large amount of tiny bubbles at the inner surface of the transparent cover were observed the following morning, indicating that the increase of temperature in the sample had caused some air dissolved in the water to come out of solution. This leads to the conclusion that using de-aired water is even more important here than in groundwater flow experiments conducted at constant temperature.

The flow test consisted in progressively increasing the hydraulic head to generate a horizontal flow across the intact sample.

Pressure head measurements allowed quantification of the head losses occurring in the circuit. The nominal load (difference between the water level in the reservoir and the level of the exit point) and effective load (difference between the water levels recorded in the upstream and downstream chamber) applied during the test are depicted in Fig. 8.9.

The temperature measurements in Fig. 8.10a show that during the heating phase the temperature increases not only in the upstream chamber, but also inside the sample and in the downstream chamber because of heat conduction.

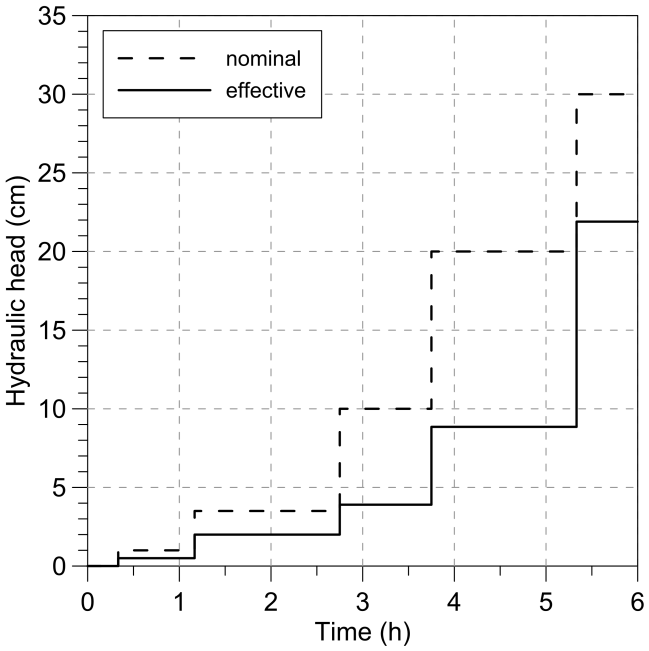

FIGURE 8.9: Nominal and effective load applied in test 1 (the error affecting the estimation of the nominal load is around 5 mm)

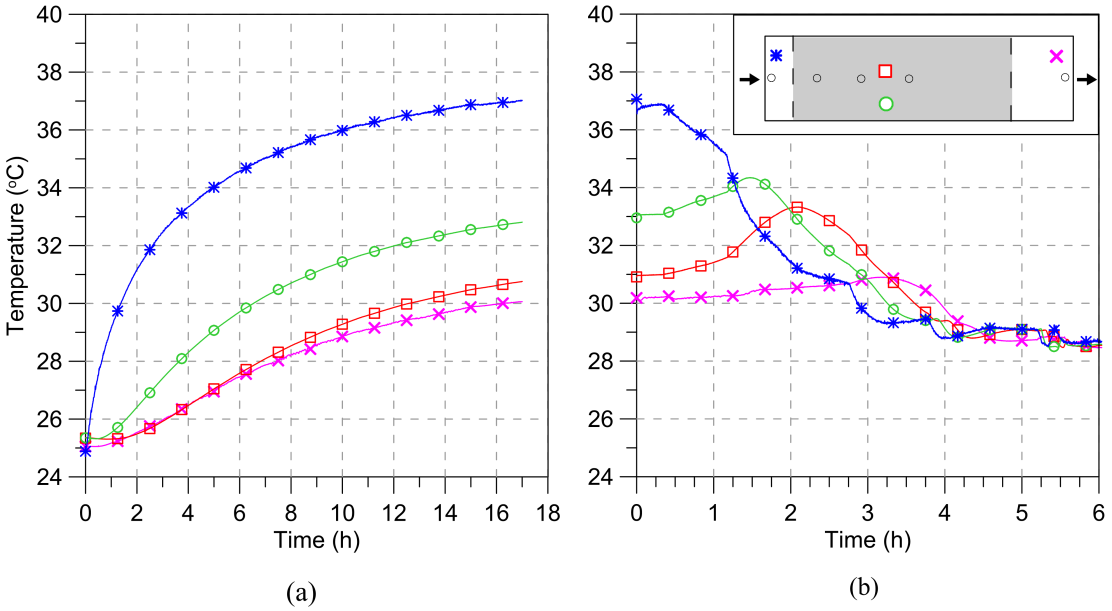

(a) (b)

FIGURE 8.10: Point temperature measurements in test 1: (a) heating phase, (b) water flow phase.

TABLE 8.2: Thermal properties of PMMA and aluminium

Material	ρ (kg dm^{-3})	λ (W m^{-1}K^{-1})	c (J kg^{-1}K^{-1})	α (m m^{-1}K^{-1})
PMMA	1.19	0.17	1470	$7 \cdot 10^{-5}$
Aluminium	2.70	205	910	$2.3 \cdot 10^{-5}$

An asymmetric thermal response is observed along the vertical direction, with the sensor in lower position showing a higher temperature. This was confirmed by 2-d numerical modelling of the experiment (see Fig. 8.11) and can be interpreted as a side effect of the presence of the aluminium base, since aluminium is a much better heat conductor than sand and PMMA (which conductivity is similar to glass and one order smaller than plastic). The thermal properties of PMMA and aluminium are reported in Table 8.2.

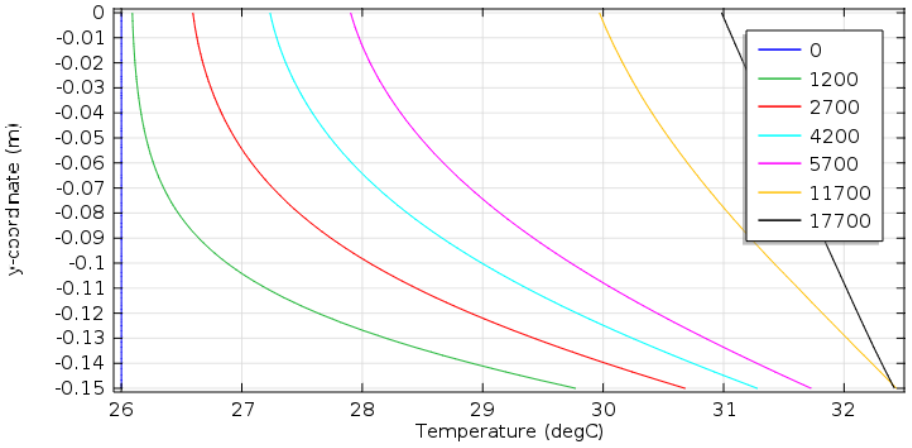

FIGURE 8.11: Numerical modelling of the heating phase of test 1. Vertical distribution of the temperature at 15 cm from upstream for different times from the beginning of the test (expressed in seconds in the legend). In the model a constant temperature of 35 °C is applied upstream. The initial temperature of the sample is 26 °C.

Soon after the water flow had started (Fig. 8.10b) the temperature in the upstream chamber began decreasing. At the other positions the temperature also decreases, after a first increase due to the passage of the hot water present inside the sample before the beginning of the flow. These data show that the heater placed in the upstream chamber had no sufficient power to heat the water quickly enough (a complete replacement of the water in the chamber takes a time in the order of 10 min).

The heating system was modified consequently: an additional heater was placed in the tank and one in the reservoir. The water was heated overnight and the heaters were left working during the test in order to maintain the temperature reached. However

the system was still not working as desired: the power of the heater in the tank (50 W) was not sufficient to compensate the cold water flowing out from the sample and going back to the tank. The definitive solution was an open cycle, where an amount of water sufficient to run the test was placed in the tank and heated over night (Fig. 8.2).

8.6 Test 2

Before the second test was run, an optical fibre protected by a 0.9 mm tight buffer was installed in the box. After installation, the position along the cable of the measuring lines in the box was mapped by reading the response of the fibre to a progressive filling of the box with hot water.

The size and bulk density of the second sample are reported in Table 8.1: they are comparable to those of the first sample tested.

8.6.1 Flow test

The test consisted in creating a flow of hot water through the sample, with the sample initially at room temperature. A constant 6.7 cm (effective) head difference was applied to the sample throughout the test. Figure 8.12 shows the progressive temperature increase under constant hydraulic head.

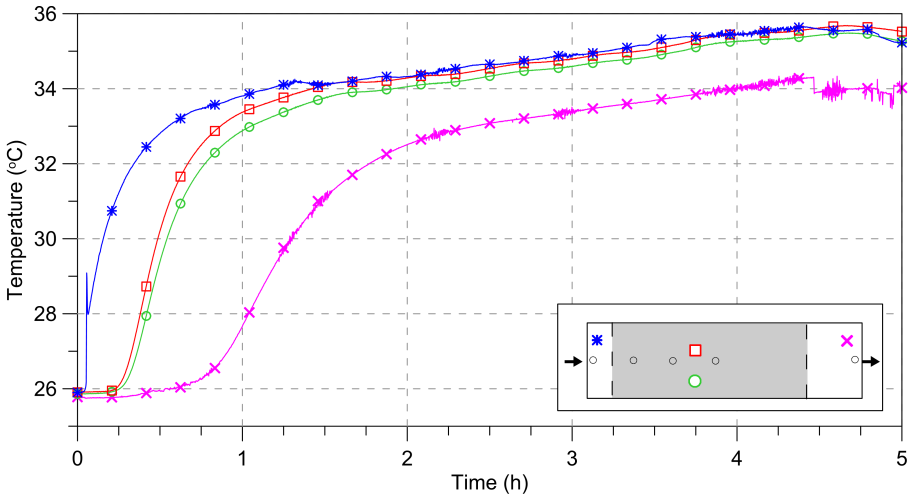

FIGURE 8.12: Point temperature measurements in test 2

Comparison with Fig. 8.10a highlights that a different vertical distribution of the temperature occurs when advection prevails. In this case the sensor in higher position measures a slightly higher temperature. This sensor is indeed closer to the middle of the sample and since the heat transferred by advection is dissipated at the walls, the

temperature in the middle of the sample is slightly higher than at the boundaries. Two-dimensional numerical modelling of the flow experiment also shows that in this case the different thermal properties of the top and bottom walls do not promote any significant asymmetry (Fig. 8.13).

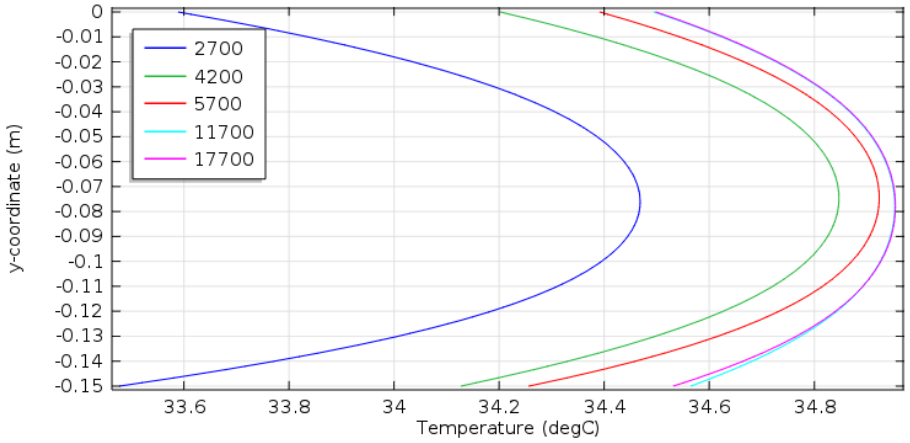

FIGURE 8.13: Numerical modelling of the flow phase of test 2. Vertical distribution of the temperature at 15 cm from upstream for different times from the beginning of the test (expressed in seconds in the legend). In the model a constant water flux of 10^{-4} m/s at a temperature of 35 ℃ is applied upstream. The initial temperature of the sample is 26 ℃.

Four flow measurements were performed during the test by weighing the water collected at the exit point in 30 s. It emerged that the hydraulic conductivity of the sample increased over time from $(5.1 \pm 0.4) \cdot 10^{-4} \pm 0.4$ m/s to $(6.6 \pm 0.4) \cdot 10^{-4}$ m/s. The increment is not so significant compared to the accuracy of the measurements but the trend was clear and was confirmed in test 4. It is believed that the increase in hydraulic conductivity is a consequence of the increase of the average temperature in the sample and subsequent decrease of the average water viscosity. This proves that if the temperature dependency of viscosity is neglected in the numerical modelling of the tests some small errors are introduced.

Figure 8.14 depicts the frequency shift measured by the optical fibre during the flow test for three moments during the test. For what concern the coordinate system: the z-axis is aligned with the main direction of the water flow, the y-axis is vertical and points upwards and the x-axis is taken consequently, according to a laevorotatory Cartesian coordinate system. It is here recalled that the OBR always provides relative measurements; in this case the reference measurement was taken at the beginning of the test and all the data presented are referred to that initial measurement.

A significant difference between the frequency variation measured at the bottom and at the top is observed, as well as a much larger increase at the centre of the sample than at the sides.

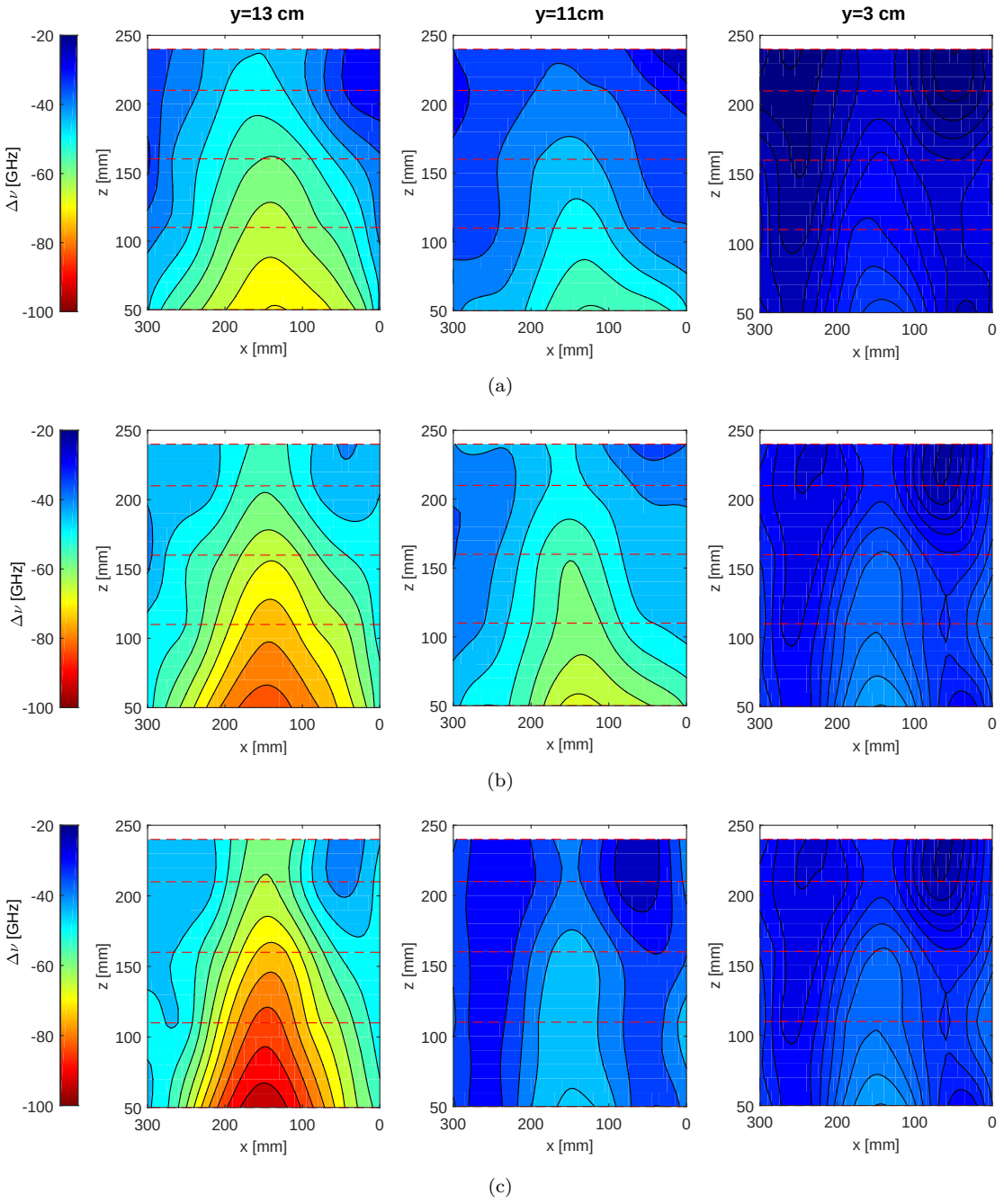

FIGURE 8.14: Frequency shift measured by the optical fibre during the flow phase in test 2 at 1.5 h (a), 3 h (b) and 5 h (c) from the beginning of the test. The water flow coincides is aligned with the positive direction of the z-axis.

In order to translate frequency shifts in temperature variations the temperature coefficient of the fibre is needed. This was obtained by calibration of the fibre with

coating in a climatic chamber, which results are depicted in Fig. 8.15. The temperature was increased in the chamber from 2 to 42 ℃ in steps of 5 ℃; each step was maintained for 2 h while moving from each step to the next one took 0.5 h. From 2 to 23 ℃ the relationship between frequency shift and temperature variation is linear, with a proportionality coefficient of -7 GHz/℃. Above 23 ℃ linearity, which is paramount for a sensor, is lost. Moreover, the fibre behaviour becomes time-dependent, with the measured frequency shift increasing over time at constant temperature. Also in the linear range the behaviour is far from what was expected, since the temperature coefficient of a standard fibre is around 1.25 GHz/℃. The high frequency shift registered is due to a thermoelastic effect, i.e. the mechanical interaction between the fibre and the tight buffer, caused by differential thermal expansion. As a matter of fact, teflon has a coefficient of thermal expansion an order of magnitude larger than that of an optical fibre. Differential thermal expansion induces stress on the fibre which is translated into frequency shift because of the sensitivity of the Rayleigh shift to strain. Up to 23 ℃ the thermoelastic effect has a positive implication as it increases the sensitivity of the sensor. This effect cannot be exploited in this experiment, but seems to have some potential for subsoil temperature measurement, where the temperature is lower. Above 23 ℃ the non linear and time-dependent response of the sensor makes its use not recommended.

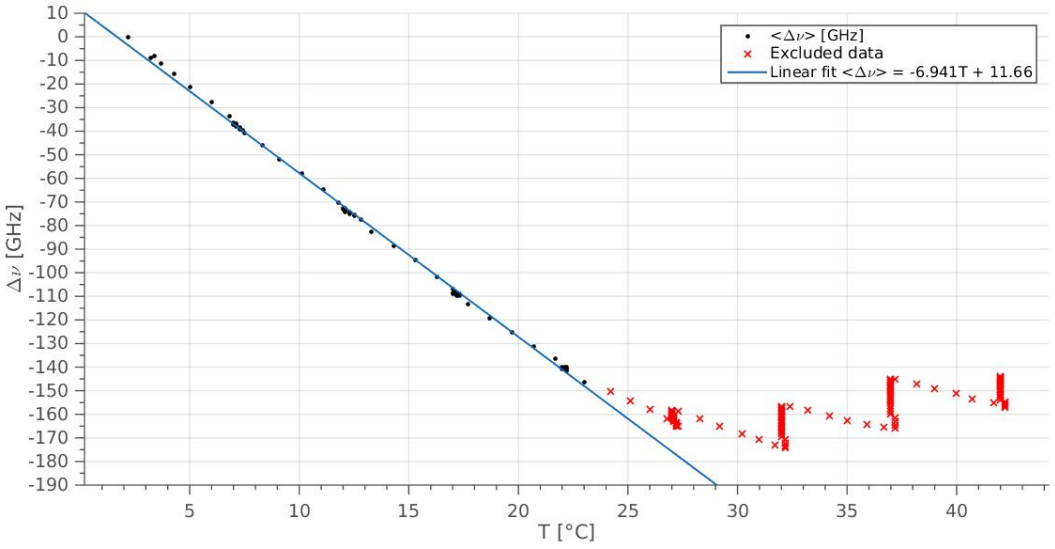

FIGURE 8.15: Fibre calibration curve

Going back to Fig. 8.14, it is clear that a much larger frequency variation occurred in the higher part of the sample than in the lower part. This was not supported neither by comparison with point measurements nor by numerical modelling (Fig. 8.13). It is

believed that this was again due to a thermoelastic effect involving the container. The different coefficient of thermal expansion of aluminium and PMMA has likely caused differential expansion of the bottom and top plate of the box, inducing a more intense tensile stress in the higher lines than in the lower one.

The graph in Fig. 8.16 shows the frequency shift of the three lines closer to the water inlet (z = 5 cm). The bottom fibre (y=3 cm) shows an interesting W-shaped pattern. Some hypothesis were made about this unexpected pattern: (1) preferential water flow along the walls, (2) buoyancy fluxes in the porous matrix, (3) curvature of the fibre because of soil settlements occurring during the test.

The likelihood of occurrence the second hypothesis was verified resorting to the well known criterion by Rayleigh the provides the condition for the onset of

As demonstrated by Elder (1967), the condition for the onset of buoyancy convection in a porous medium under an adverse temperature gradient is that the Rayleigh number is bigger than a critical value:

$$Ra = \frac{\kappa\gamma g\Delta T D}{a^*\nu} \geq 4\pi^2 \,. \tag{8.2}$$

The average Rayleigh number of the physical model was calculated assuming the permeability $\kappa = 5 \cdot 10^{-11}$ m^2, the coefficient of cubical expansion $\gamma = 3 \cdot 10^{-4}$, $\Delta T = 10$℃, the thickness of the domain $D = 0.15$ m, the modified thermal diffusivity $a^* = \lambda/\rho c_f = 6.6 \cdot 10^{-7}$ m^2/s and the fluid viscosity $\nu = 0.8 \cdot 10^{-6}$m^2/s. The result is $Ra = 0.42$, which is at least 100 times lower than the critical value. As a matter of fact, the material used by Elder in his experiments are spheres with minimum diameter of 3 mm, i.e. a more permeable material than medium sand.

8.6.2 Piping

In the second phase of the test piping was induced letting the water flow from the hole in the cover plate. The hydraulic load was increased in steps; each step was undertaken only when an equilibrium condition had been achieved, i.e. when sand transport had stopped.

Sand boiling started at a (nominal) hydraulic load of 3 cm. The setup was confirmed to offer a good control over the pipe growth as Table 8.3 shows. The progression of the pipe is depicted in Fig. 8.17.

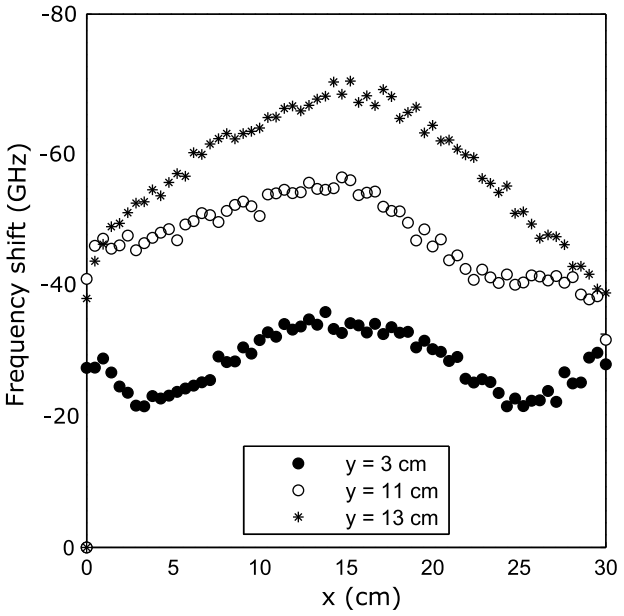

FIGURE 8.16: Frequency shift measured along the three lines closer to the water inlet (z=5 cm) after 4 h from the beginning of the test

TABLE 8.3: Equilibrium stages of pipe growth in test 2

Nominal head (cm)	Pipe length at equilibrium (cm)
6.0	5.0
7.0	8.5
8	10.0

When a hydraulic load of 9 cm was reached, the pipe bended of 90 degrees and the sand transport continued at a very small rate. Given the necessity to conclude the test, the load was increased to 10 cm. The pipe reached upstream but it got repeatedly clogged. Vibrating the box produced restarting of sand transport, but the very breakthrough only occurred at a load of 15 cm. As can be appreciated in Fig. 8.17e the width of the pipe was around 1 cm and was nearly constant over length.

The fibre-optic measurements in Fig. 8.18 show some differences respect to the flow phase (Fig. 8.14) that appear interesting, although only qualitative conclusions can be draws given the limitations of the measurements that are explained above. Two instants are plotted, that correspond to the situations depicted in Fig. 8.17d and 8.17e respectively. In the higher layers (y=13 cm, y=11 cm) the more downstream contours, i.e. in the region where the pipe bifurcated, are nearly "w" shaped. Moreover, some asymmetry evident at t= 4 h 25 min might be related to the geometry of the pipe.

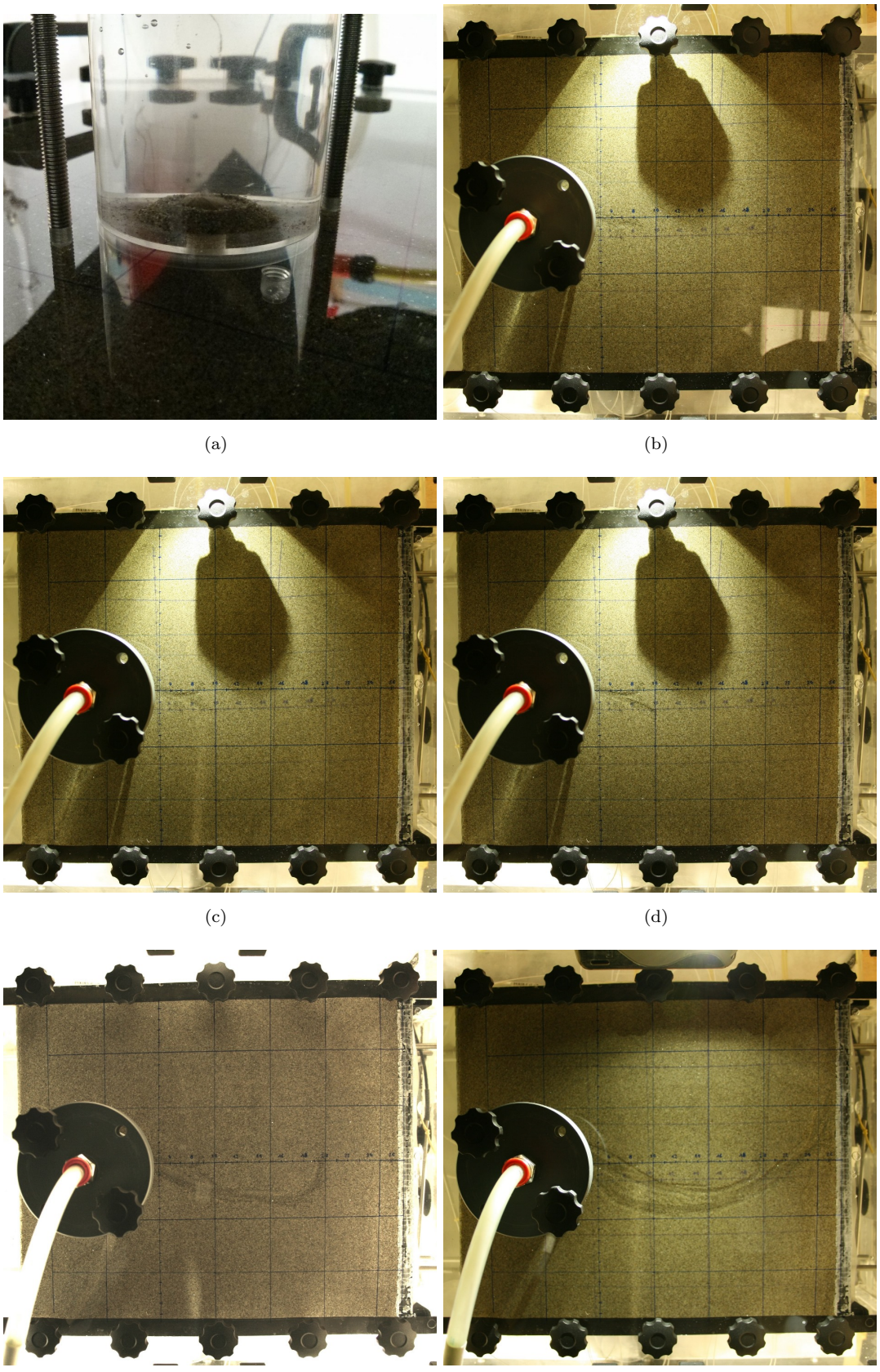

(a) (b)

(c) (d)

(e) (f)

FIGURE 8.17: Progression of the pipe in test 2: (a) beginning of sand boiling, (b) equilibrium at l=8.5 cm, (c) bifurcation, (d) equilibrium at l=10 cm, (e) very small sand transport at l=20 cm, (f) widening.

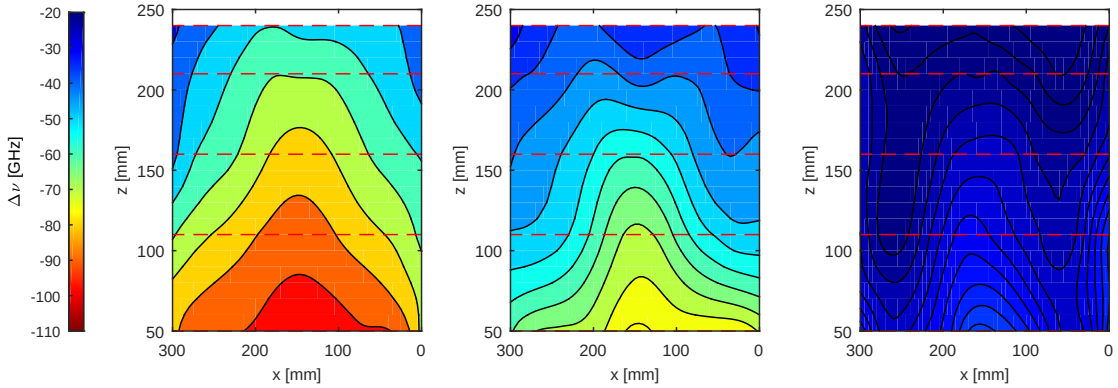

(a) t=3 h 25 min

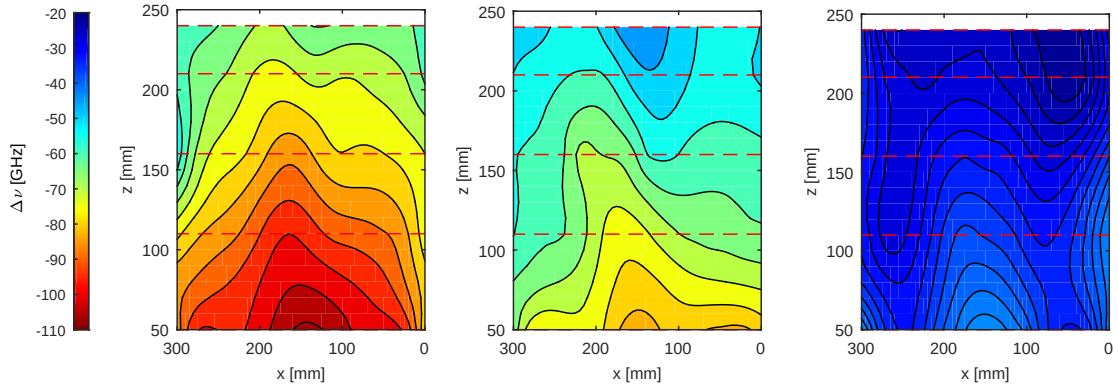

(b) t= 4 h 25 min

FIGURE 8.18: Frequency shift measured by the optical fibre during the piping phase in test 2. (a) Pipe length $l = 10$ cm, distance from upstream 165 mm; (b) pipe length $l = 20$ cm, distance from upstream 65 mm.

8.7 Test 3

Test 3 was run after a small pump was added in the downstream chamber to avoid thermal stratification. The numerical solution of the advection-diffusion equation - and thus the back-analysis of the results - requires indeed that all the boundary conditions are known. Ensuring a homogeneous temperature distribution in the downstream chamber is the simplest way to achieve the goal, being the creation of an adiabatic boundary much more difficult for this setup.

The test aimed at verifying that the pumps were effective in homogenizing the temperature in both chambers. Two temperature sensors were installed in each chamber at different height. The water in the upstream chamber and in the tank was heated overnight while the pumps were switched off. In the morning the data acquisition was started and a few minutes later the pumps were turned on. The water flow started after 27 min from the beginning of data acquisition, indicated in the graph by a spike in one

of the measurements. The data in Fig. 8.19 show that in absence of flow and with no pump working the stratification in the upstream chamber is significant.

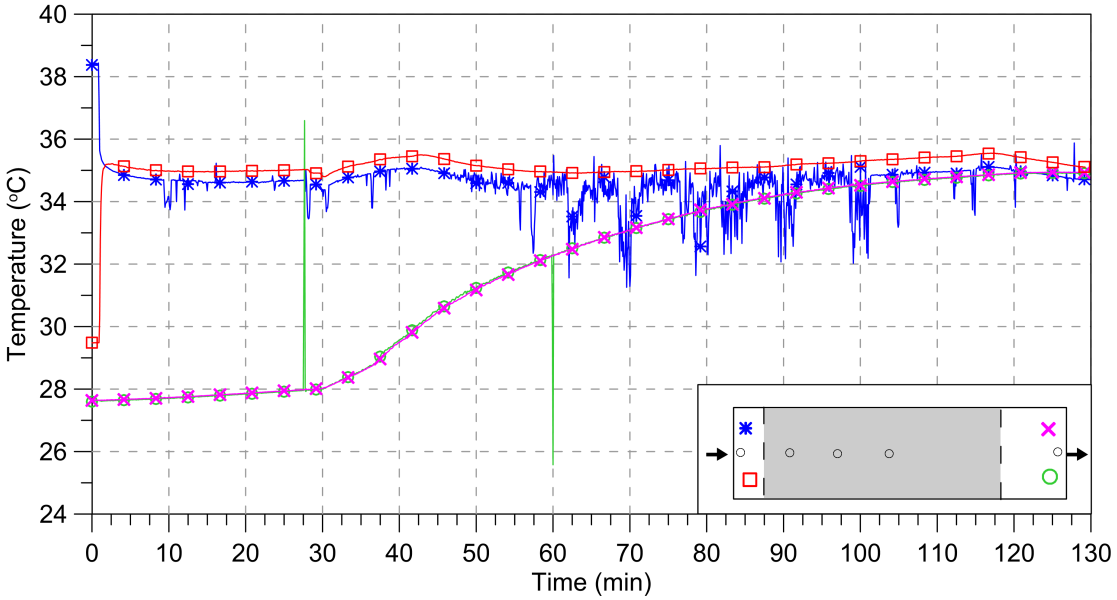

FIGURE 8.19: Point temperature measurements in test 3

After the pumps are turned on the temperature homogenizes in the upstream chamber, although a small difference persists between the two measurements throughout the test. Such difference might be ascribed to the malfunctioning of one of the sensors due to loss of waterproofness: after dismantling the setup it was verified that the damaged sensor slightly underestimated the actual temperature. In the downstream chamber the temperature is initially homogeneous and equal to the room temperature. Therefore it does not show significant changes after the pump is turned on, except a slight increases over time in absence of flow which was likely due to joule effect.

In conclusion, the test showed that (1) ensuring continuous mixing of the water in the chambers is essential as thermal stratification is otherwise significant and (2) the pumps installed fit to the purpose.

Note: The initial temperatures are consistent with those measured in test 1 at the end of the heating phase (Fig. 8.10) if few things are considered: in test 3 the room temperature was higher and the thermostat of the heater was set to a lower value (35 °C) than in test 1.

8.8 Test 4

In order to overcome the thermoelastic effects that affected the optical measurements in the previous tests, test 4 was run with the fibre installed in a strain-free configuration. First loose tubes were fixed to the walls of the box (Fig. 8.20a) and then the fibre was inserted in the tubes and glued to the tubes ends in few points to avoid significant displacements that would hinder the accurate mapping of the measurements (Fig. 8.20b).

A bare fibre was also installed on the inner face of the cover plate, where piping occurs and thus temperature measurements are more interesting. As illustrated by Fig. 8.21 the fibre was protected by a rough layer of silicon, that also had the aim of creating an interface between the sand layer and the cover that was more representative of field conditions. The scheme of deployment of the optical fibre on the cover plate is depicted in Fig. 8.21: the fibre is arranged in 13 lines spaced 3 cm; the first two lines are in the upstream chamber ($z < 0$) and the last lines are downstream of the exit point.

The fibre inside the box and the one on the cover were series-connected.

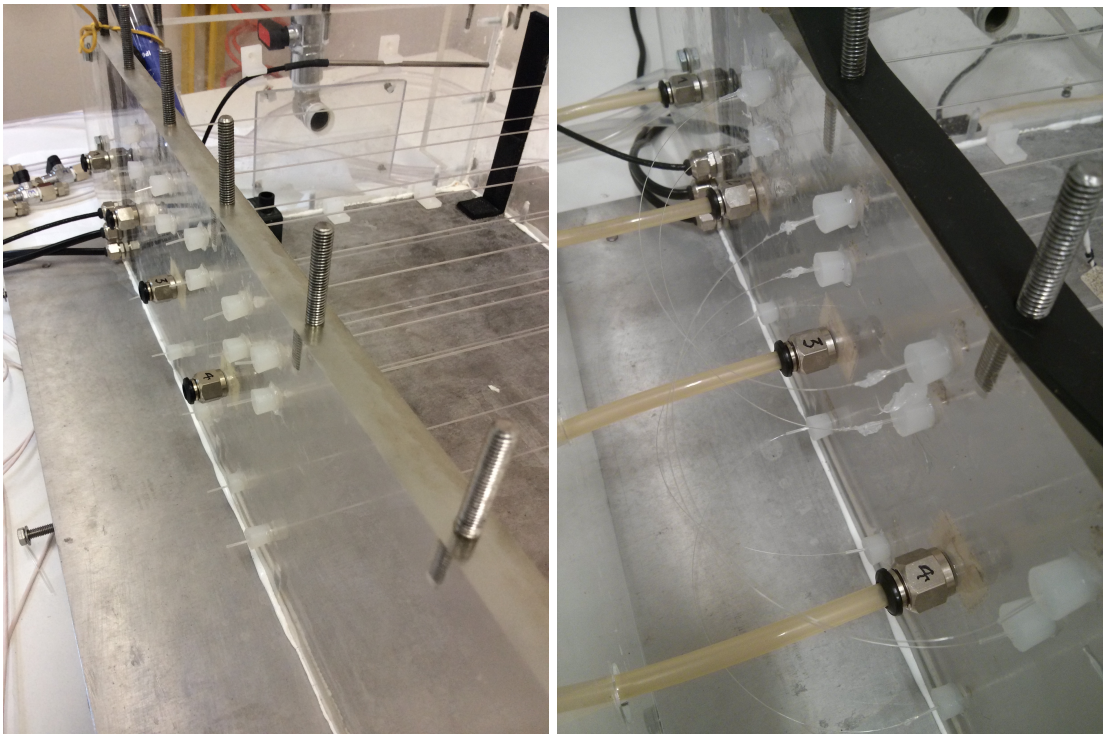

(a) (b)

FIGURE 8.20: Installation of the fibre in strain-free configuration: (a) loose tubes, (b) fibre glued to the tubes in a few points

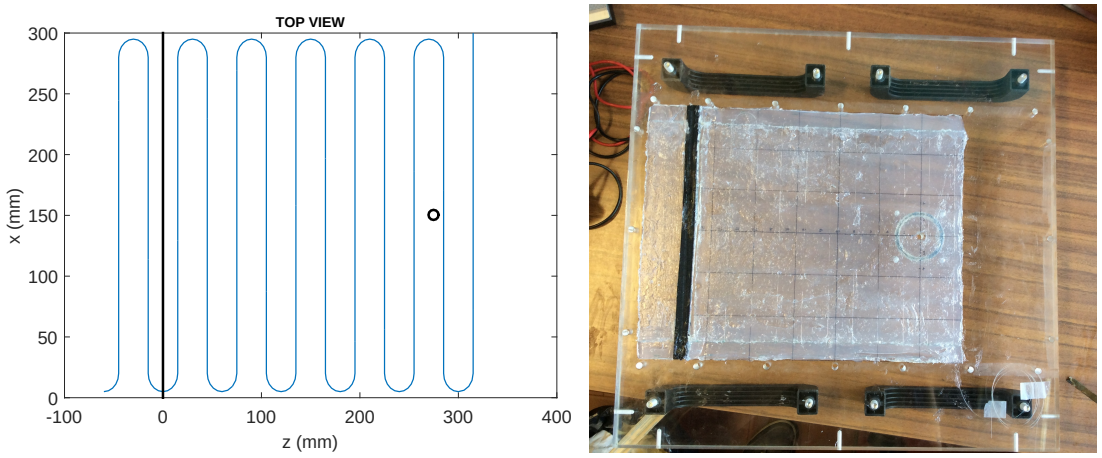

(a) (b)

FIGURE 8.21: Bare optical fibre on the inner face of the cover plate: (a) top view of the scheme of deployment, (b) bottom view of the deployment with a silicon protective layer.

The size and bulk density of the second sample are reported in Table 8.1: they are similar to those of the other sample tested.

8.8.1 Flow test

The test consisted in creating a flow of hot water through the sample by applying a constant 7.9 cm (effective) head difference throughout the test.

This time also the water in the upstream chamber was heated overnight. The procedure is not very efficient won't be replicated in future tests. The sample is in fact partially preheated with this test procedure, because of heat conduction from the adjacent upstream chamber. The initial condition is therefore quite complex, with the lower part of the sample warmer than the upper part (see Fig. 8.11) and the upstream part warmer than the downstream part. Figure 8.22 displays the temperature measured during the test by the point sensors.

The optical measurements at four instants during the test are reported in Fig. 8.23. The magnitude of the measured frequency shifts indicates that the fibre has mostly been freed from the stress that affected the measurements in test 2: the measured shifts were indeed 5 times lower than in test 2 while the maximum temperature variation was 2/3 of the maximum temperature variation in test 4. However the response of the sensor cannot be entirely ascribed to temperature variations. As a matter of fact, a 20 GHz shift would imply a temperature variation of about 16 ℃ over the test (assuming 1.25 GHz/℃ as temperature coefficients of the bare fibre), while the effective variation was

less than 6 °C. Therefore, although the fibre has been made independent on the box displacements, some stress persisted, likely arising from the interaction of the fibre with the soil.

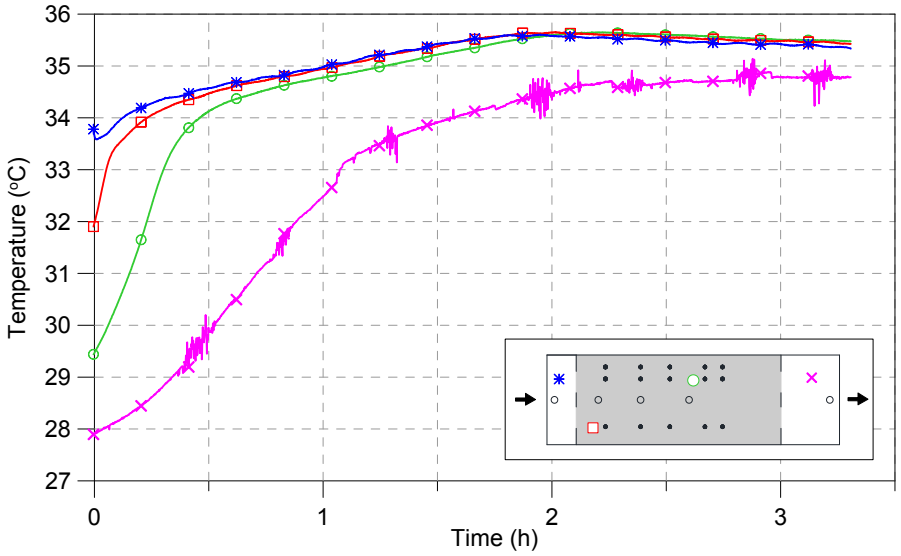

FIGURE 8.22: Point temperature measurements in test 4, flow phase

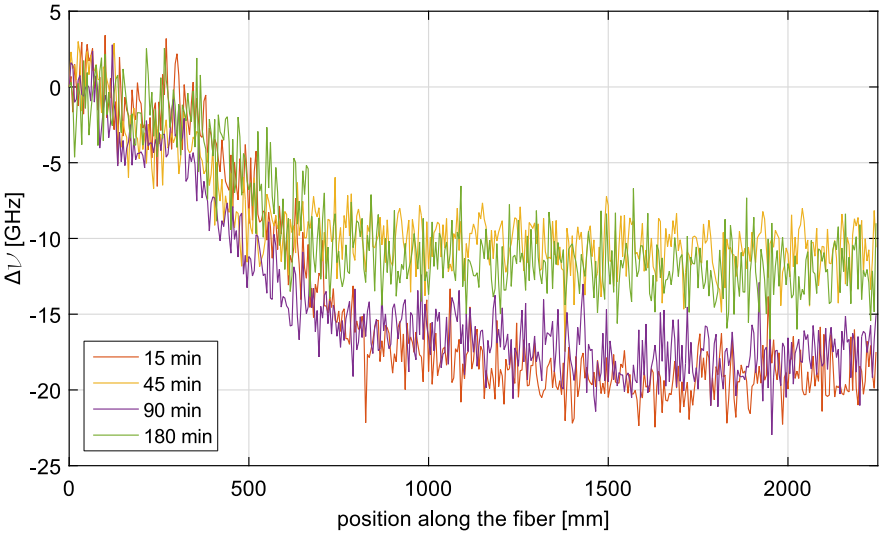

FIGURE 8.23: Fibre optic measurements in test 4, flow phase, for four instants during the test

8.8.2 Piping

The sample had been heated before the test by the heater in the upstream chamber. The hydraulic head was then increased in steps. No sand transport was observed until the hydraulic head reached 10 cm. At this point a large, straight pipe grew in few minutes

up to failure. Differently from test 2, the progression of the pipe occurred at constant head.

Although the illumination of the sample had been improved adding lateral LEDs, the pipe was hardly visible to the naked eye and impossible to see in the pictures because of the thick silicon layer. Difference of pictures shot at consecutive instants could however highlight the particles in movement and thus give a picture of the the piping channel (Fig. 8.24). The image processing was made easier by the non-uniform colour of the sand that contained some mica particles.

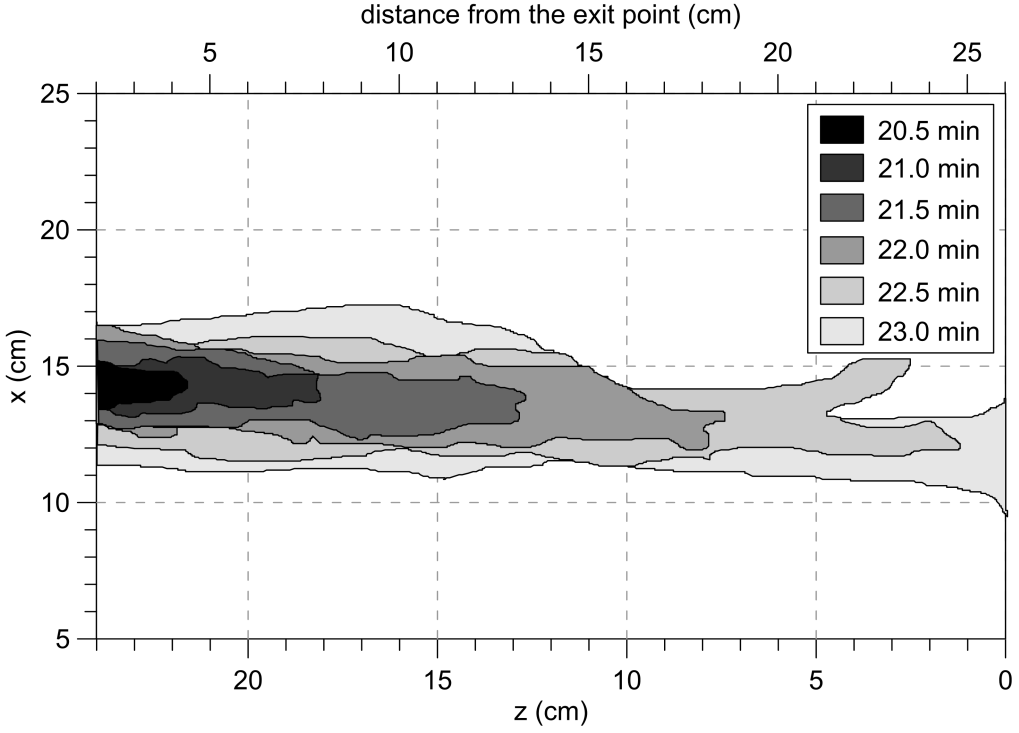

FIGURE 8.24: Backward progression of the pipe in test 4

The optical measurements on the cover cannot be interpreted univocally as they are affected by the strain created by the interaction between the silicon and the bare fibre. However this preliminary installation proved to be successful in that it allowed to detect some changes connected to the formation of the pipe.

Figures 8.25 and 8.26 show that the shift measured in proximity of the exit point and in the pipe is much larger than the shift measured in the upstream chamber (first two lines) and drastically increases during the progression of the pipe (between 21 and 25 min). This is in agreement with the point temperature measurements that show smaller temperature variations during the test in the upstream chamber (that was preheated) and at the beginning of the sample, and larger variations more downstream. Another

possible explanation is that the pressure drop, first progressively applied to the exit point to promote the water flow and later occurring in the pipe, has indirectly caused some stress in the fibre.

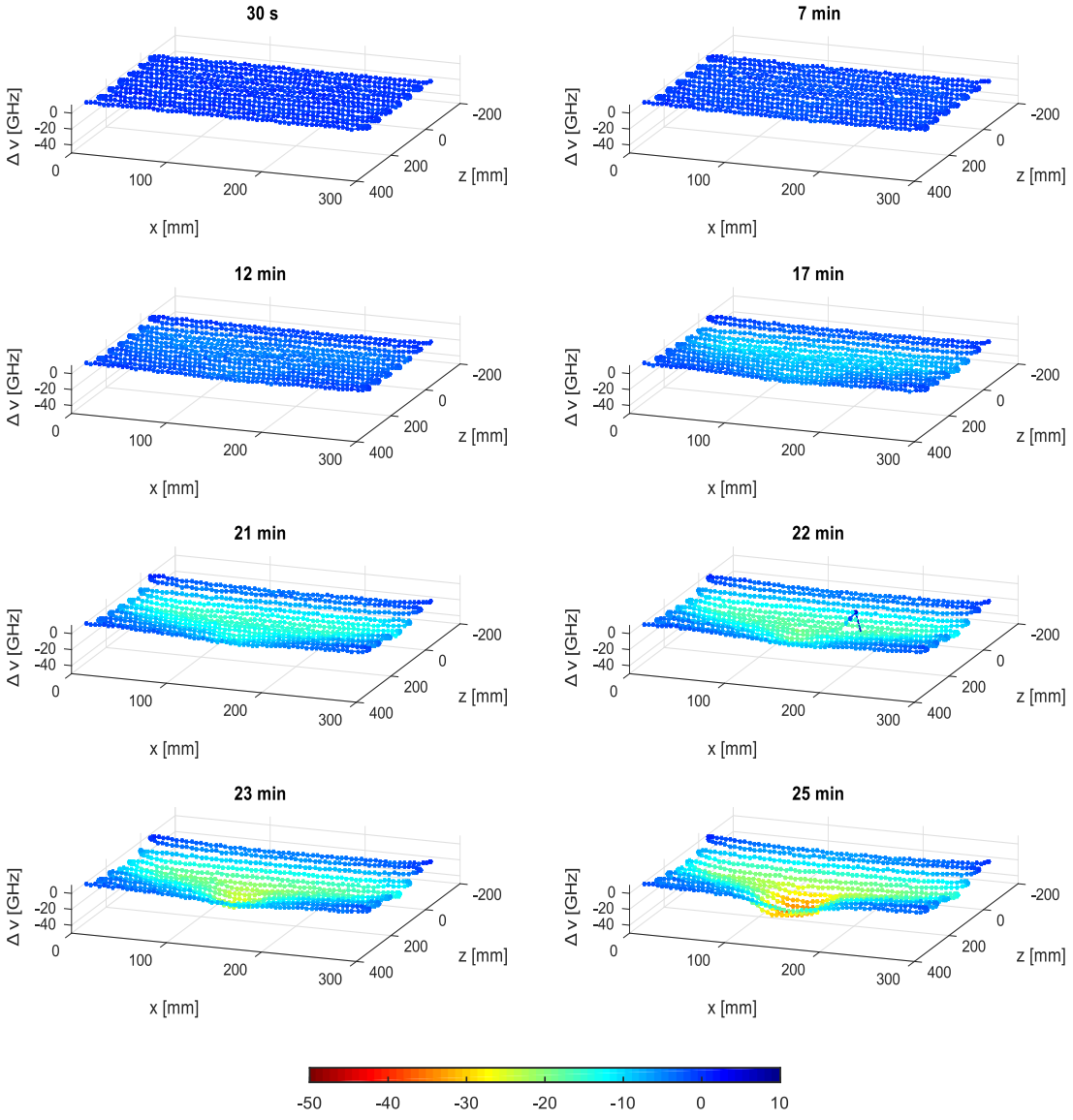

FIGURE 8.25: Map of frequency shift experienced by the optical fibre on the cover during the piping test

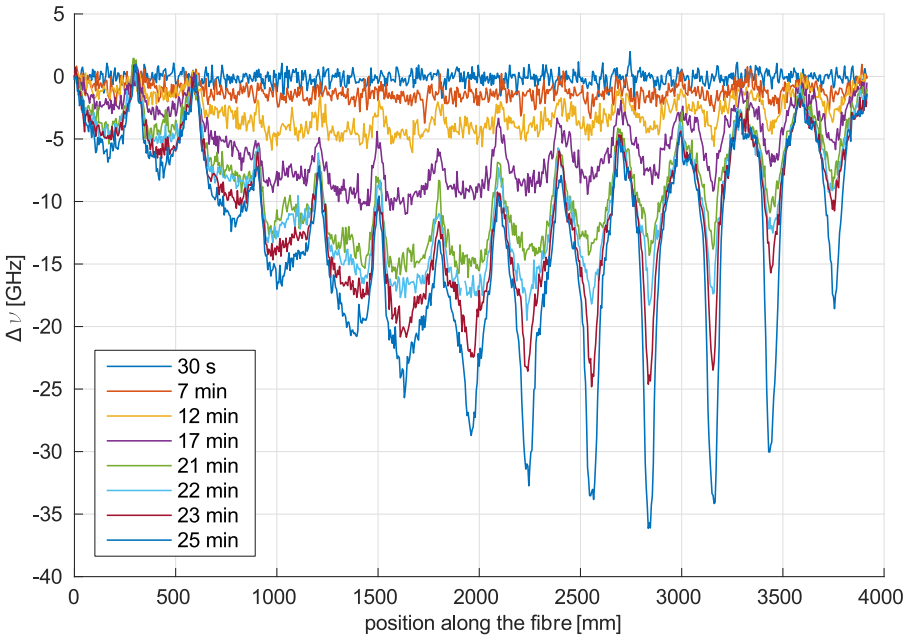

FIGURE 8.26: Frequency shift experienced by the optical fibre on the cover during the piping test expressed as a function of the cable length

Chapter 9

Conclusions

9.1 Dike monitoring and detection of internal erosion

Monitoring a dike is a complex task since it requires to control large distances and, at the same time, to maintain a high level of detail. This necessity can be addressed using a multiscale approach that combines extensive technologies with more accurate measurements performed along a few segments identified as critical. Suitable extensive technologies are remote sensing and those geophysical techniques that do not require contact of the instrumentation with the soil. Accurate measurements in cross-sections representative of critical dike segments are mostly performed by conventional geotechnical instrumentation: pore pressure meters, inclinometers, water content probes etc.

Detection of internal erosion cannot rely on conventional geotechnical instrumentation even at the local scale, because of the point nature of the measurements that these instruments provide. Since internal erosion is a highly localized process, technologies capable of performing spatially nearly-continuous measurements are required. Distributed fibre-optic temperature sensing, thermal imaging and geophysical methods that require contact with the soil, such as Electrical Resistivity Tomography and Self-Potential, provide the continuity required over distances that range between a few hundreds metres to a few kilometres. Distributed fibre-optic temperature sensing offers very good spatial resolution and temperature accuracy: Raman reflectometry, the technique traditionally used in the field, allows to reach 1 m spatial resolution and an accuracy of 0.1 ℃ over a couple of km.

Nevertheless, temperature is an indirect indicator of seepage velocity and depends on many factors other than seepage. This can make the interpretation of the data

ambiguous. Seepage velocity itself is an indirect indicator of internal erosion, so the uncertainty doubles.

The theory of conductive-advective heat transfer in soils is in large part well known and so are the numerous sources and mechanisms that contribute to the exchange of heat between the Earth and the atmosphere. However, this multitude of sources, combined with the soil heterogeneity, makes temperature measurements difficult to interpret when they are performed at small depth, where the influence of the external environment is not negligible. Heterogeneity means, in fact, a high variability in the response to the different sources.

Previous research dealing with detection of internal erosion in dikes through distributed temperature sensing focused on devising data interpretation techniques to extract from the measurements the information related to internal erosion. In this work a number of minor factors that affect the temperature distribution in a dike have been neglected in order to focus on few key factors, the influence of which has been analysed in depth.

9.2 Outcomes of the large-scale test

In a large-scale dike failure experiment porewater pressure and temperature were monitored to follow the development of piping. The sensors were deployed at the interface between the impervious base of the dike and the sandy foundation during the construction works. The temperature was measured by means of distributed fibre-optic sensors encased in a geotextile strip. A spatial density was achieved in the measurements in both directions - parallel and perpendicular to the dike - that would be impossible to achieve by instrumenting an existing dike.

The temperature measured at the base of the dike before the beginning of the test already provided interesting information. The temperature was higher at the toes and lower under the crest, as a consequence of the different influence of the air temperature at different depths. Also the orientation of the dike had a significant effect on the distribution: the temperature under the South-oriented slope was significantly higher and more rapidly changing as a function of solar radiation than the temperature under the South-oriented slope.

After gradual application of a hydraulic load, piping occurred at several positions, but erosion did not progress beyond 1/5 or 1/4 of the seepage length.

Pore pressure measurements confirmed that, as claimed in the literature, the influence of piping on the flow field is highly localized. For an effective monitoring a measurement would be needed every couple of metres. It follows that conventional point sensors are not suitable for detection of backward erosion piping.

The seepage flow promoted the progression of a warm thermal front under the dike, being the water in the reservoir warmer than the initial temperature at the base of the dike. However, unexpectedly, at the locations where piping was detected a temperature decrease was observed. The extent of the thermal anomalies (i.e. the difference between anomalous and regular measurements) was less than 1 ℃.

A careful look at the measurements (see Fig. 6.8) made clear how the anomalies developed. The inflowing warm water pushed the cold water - initially present under the dike crest, towards downstream - where the temperature was higher because of the smaller depth. At the piping locations the cold water travelled faster than in the intact regions, thus producing negative temperature variations close to the landside toe, where the sensor was located. Only after almost four days of continuous seepage flow, the warm thermal front reached the tip of the pipes.

In brief the test showed that:

1. In a permeable soil, as those prone to backward erosion piping are, and under a global horizontal gradient capable of triggering piping, an advective thermal front can propagate along the seepage path, i.e. a significant amount of heat is transported by advection.[1]

2. The duration of typical flood events (comparable with the duration of the test) could not be sufficient in order that the advective thermal front reaches the landside area.

3. If the advective thermal front does not reach the landside - or before this happens - piping induced thermal anomalies can arise due to the alteration of an initial thermal gradient at the base of the dike, since such alteration happens faster in the pipes than in the intact soil.

[1]It might seem more efficient talking about seepage velocities capable of triggering piping, instead of splitting the problem in hydraulic conductivity and hydraulic load. If seepage velocity is considered, it is important to recall that the parameter to refer to is the *average* velocity along the seepage path, which is different from the local velocity capable of promoting the displacement of the soil grains. The relationship between average velocity and local velocity depends on the configuration of the dike foundation.

Attention is focused on the landside because the aim of the monitoring is the detection of pipes that have not progressed much towards the waterside; at the contrary, detection of piping might occur too late to intervene successfully.

Real-time identification of piping requires automatable procedures. This means identifying appropriate parameters for which quantitative thresholds can be determined. In the test, the temperature gradients calculated along the sensor proved to be a good indicator of piping. However, in the field, the soil response to a seepage flow - but also to rain and other external factors is influenced by heterogeneity. In a sinuous dike also the exposition (South/North) of the slopes can vary and thus the influence of solar radiation on the temperature distribution can differs along the dike. Consequently, either the data are processed to eliminate the influence of external factors and heterogeneities other than piping or specific threshold values must be set for different regions along the dike. It goes without saying that the definition of site-specific threshold values requires a protracted observation of the system.

9.2.1 Performances of the DTS system

An accuracy of 0.1 ℃ combined with a 1-m spatial resolution was sufficient to detect piping induced thermal anomalies promoted by a the temperature gradient in the order of 1 ℃. Although the width of a single pipe is expected to be much smaller than the resolution of the sensor, it is likely that the development of a branched network of pipes covering a large area behind a single sand boil overcomes the limitations related to the spatial resolution of the sensor.

Adoption of systems with lower accuracy and spatial resolution is not recommended, even in the case that the active method is adopted. As a matter of fact, the active method is capable of providing large temperature variations between eroded and intact soil in unsaturated and low permeability soils, but small anomalies arise when internal erosion occurs in saturated sands. In very permeable sands the expected variation is smaller than 1 ℃, as demonstrated both theoretically and by lab experiments.

The measurement frequency adopted may be too low for early-warning purposes. When the anomalies are of very small extent, as in this case, recognizing a trend in the measurements is very important. Since more measurements are necessary to define a trend, two measurements per hour means at least a couple of hours to produce an alarm. Planning the desired acquisition frequency in advance with the system supplier

is important, because sometimes, in DTS systems, the adjustment of the acquisition frequency can be performed only at the expenses of accuracy and spatial resolution.

9.3 Propagation of an advective front

If advection dominates over conduction in the foundation layer of a dam or dike under the hydraulic loads of interest - as it occurred in the large-scale test - piping detection cannot be based on the principle generally exploited in less permeable structures as dam cores: advection predominance in the eroded regions and conduction predominance in the intact regions. More specifically, piping detection cannot be based on a different damping of the thermal load between eroded and intact regions (as depicted in Fig. 5.9). Nevertheless, piping detection can still rely on the existence of a time-lag between the thermal signal travelling in eroded regions and the signal travelling in intact regions.

The time-lag of the thermal front is exploitable for early piping detection only if the front can reach the tip of the pipe at the initial stage of the erosion process, which means to progress significantly towards the landside toe of the dike. With the aid of a 2-d finite element model and dimensional analysis, the conditions required for the propagation of an advective thermal front in a permeable dike foundation were determined.

Condition 0. Necessary condition for the propagation is that a gradient exists between the temperature of the waterbody and the temperature of the foundation soil. This gradient varies throughout the year and is said to be minimum in the intermediate seasons. This condition being well known and quite case-specific it was not investigated in this work. Attention was focused on the importance of the advective transport and on the duration of the hydraulic load.

Condition 1. As dimensional analyses teaches, in hydrogeological systems the importance of advection depends on:

- thermal properties of soil and water;
- average seepage velocity, which in turn depends on hydraulic conductivity and hydraulic gradient;
- thickness of the flow domain;
- length of the domain: in this case the length must be considered as the distance between the inflow point - the waterside toe or further outside if a waterside

blanket is present - and the point at which the information is required (landside toe or other).

The above factors are summarized in the geothermal Péclet number, that expresses the relative importance of advection in hydrogeological systems. The Péclet numbers are not characterized by the existence of a critical value below which the system is conductive. However, in this case for values much less than unity, the system is conduction dominated, while for values significantly greater than unity the system is advection dominated. It must be recalled here that this way of dealing with the problem is not rigorous and the above values have to be considered as approximate indications. A numerical modelling of the problem in transient conditions can provide more accurate information.

The analytical approach however was very useful to deduce some indications about the thermal behaviour of dike foundations for a wide range of sizes (thickness of the sand layer and seepage length) and different hydraulic conductivities. It was discovered that in very permeable sands an intermediate or advective behaviour ($Pe_g > 1$) is expected, except for very thin sandy layers; in less permeable sands there is a wider range of geometries for which advection seems to be not relevant but yet in many cases advection does play a role (Fig. 7.18).

Condition 2. Whether the advective thermal front reaches the head of the pipe depends on the velocity of the thermal front, which can be conservatively assumed around 1.5 times the Darcy velocity. The time required for the thermal front to reach the landside is in the order of typical flood events for very permeable sands, while for less permeable sands the arrival times are too large for the front to reach the landside during a flood event (Fig. 7.18).

9.4 Alteration of an initial gradient

In the shallowest portion of the subsoil a vertical gradient exists because of the interaction between the Earth and the atmosphere. Such gradient is neither linear nor monotone, it varies throughout the year and decreases with depth becoming negligible beyond 10 m on average. Under a dike also a horizontal gradient exists (in the absence of water flow) since the distance from the surface increases when moving from the toes towards the crest. Such gradient is significant only in proximity of the toe, where the base of the dike is shallower.

It is said in the literature that piping detection at the downstream toe of a dam or dike can rely on the principle that advection predominates in the eroded regions masking the influence of the external environment, which is instead preserved in the intact regions where conduction prevails. If advection dominates over conduction in the whole foundation layer, both sound and eroded parts, again the principle advection vs conduction cannot be exploited. However the initial horizontal gradient translates in a continuous temperature variation at the toe during a flood event, since the water that is displaced maintains its temperature. Again, in the pipes the temperature variation will occur faster since the seepage velocity is higher.

The effectiveness of this mechanism is limited by the depth of the layer where piping occurs (and where the sensors are placed). In many dikes, the soil layer prone to piping is often overlain by a less permeable layer and thus deeper than in the large-scale test. Calculations showed that if the interface where piping is expected is not farther than 2 m from the ground level the horizontal gradient is comparable or greater than the gradient capable of generating the anomalies in the large-scale test (> 1 ℃).

In the large-scale test, a large part of the horizontal gradient responsible for piping detection derived from the South exposition of the downstream slope and the strong solar radiation that heated the soil before the beginning of the test. Therefore in summer, when the external temperature is higher than the temperature under the dike, a strong solar radiation has a positive effect on the detection of anomalies.

9.5 Numerical issues

The numerical solution of the advection-diffusion equation by means of Galerkin finite elements is affected by instability issues. Instability arises when conduction (diffusion in case of solute transport) is small compared to advection. The general stability condition is that the element Péclet number, i.e. the ratio between the advective and conductive fluxes over an element, is smaller than 2. In our problem an element size of 10 cm satisfied the condition. The same mesh size was seen to work also for higher seepage velocities if the mesh was refined in a very thin layer close to the downstream boundary. If piping has to be modelled, however, no reasonable mesh refinement can avoid instability, because of the very high velocities and gradients occurring inside the pipes and at the interface between pipes and soil matrix. In brief, Galerkin finite elements are suitable to model heat transfer in a permeable dike foundation, but to model heat transfer in the presence

of piping it is necessary to resort to other numerical techniques, such as finite volumes or mixed finite elements.

Fluid flow in soils affected by piping can be conveniently modelled using the Darcy's law, both in the soil matrix and in the pipe, under the reasonable assumption that the flow in the pipe is laminar. A fictitious permeability has to be assigned in the pipe in order that the Darcy's law coincides with the formula that describes laminar flow in tubes: the Hagen-Poiseuille formula.

It may seem trivial, but it deserves to be stressed that in the attempt to reproduce the results of the large-scale test, it was noticed that correct initial conditions are paramount for obtaining reliable outputs.

9.6 Small-scale modelling

A small-scale setup has been developed that, thanks to a distributed fibre-optic sensor, enables a 3-d mapping of the temperature in a sand sample prepared by pluvial deposition. The setup includes a system that provides the sample with water at constant temperature. Although it was designed to study internal erosion and enables the development of a pipe in the sample, the setup is suitable for studying different kinds of problems related to heat transfer in porous media.

A sub-centimetre spatial resolution is achieved along the fibre adopting a novel sensing technology, in which the spectral shift of the Rayleigh backscatter is measured using optical frequency-domain reflectometry. High spatial resolution comes however to a price: the cross-sensitivity of the sensor to temperature and strain.

The cross-sensitivity was faced inserting the fibre in loose flexible tubes. This freed the measurements from most of the strain that the fibre had experienced in the first test - where it was encased in a tight buffer and clamped to the walls of the container - but it was not sufficient. Future tests will make use of more rigid loose tubes in the attempt of mechanically isolating the fibre from the sample.

9.7 Future outlooks

Distributed temperature monitoring proved to be an effective technique for piping detection in dike foundations. However, the factors that control the temperature distribution

in a dike are so many, and the data from real river and sea dikes so little, that further research is needed before distributed temperature measurements can be completely relied upon for real-time detection of piping.

The research undertaken will be completed by the study of the temperature variations occurring in the surroundings of a pipe. This will be achieved coupling small-scale modelling and finite volume modelling. It seems valuable investigating this aspect since the expected thickness of the pipes is so small that a sensor deployed in a groove at the toe of an existing dike will be hardly located exactly inside the pipe. In this study the influence of the "exit type", i.e. the configuration of the exit point of the flow, will also be considered because it strongly influences the flow field.

The next big step will be the installation in an existing river dike of a distributed temperature monitoring system. The pilot will provide data affected by all the factors that were not taken into account in this work, such as soil heterogeneity, rain, solar radiation, wind etc. Another factor that could be investigated in the field is the influence of the spatial resolution of the sensor on its capability of detecting temperature anomalies. Application of the high resolution technique used in the lab to field measurements seems viable, although more expensive and complex than the conventional technique. The cross-sensitivity to temperature and strain should be faced (and after the problems encountered in the lab there is some skepticism concerning the feasibility of the task). Since the interrogator is not field-proof it should be maintained in a protected environment. Also increasing the "spatial vertical range" of the monitoring system by deploying more cables at slightly different heights could provide useful information for research purposes.

From a wider perspective, a key point for a successful monitoring is the activation of a communication channel between the people that operate on the territory and the people who design and manage the monitoring system. In case the management of the monitoring system, after some time of testing, is entrusted to the people that operate on the territory, proper technical formation of these people is paramount.

On the other hand, the tools that the technology has made available, first of all web-based GIS (geographic information systems), should be used to collect historic information and the memories and knowledge gained by the people that for years worked on the territory. In this way lots of data will be easily available and it will be avoided that precious information is lost. These databases would be on one side a valuable tool to have an overview of the critical points and prioritize intervention, including installation

of monitoring systems, and on the other side a container for new information, including the information gained from the monitoring systems.

Appendix A

Large-scale piping test - pictures

FIGURE A.1: Comprehensive view of the test site with indication of the North direction.

(a)

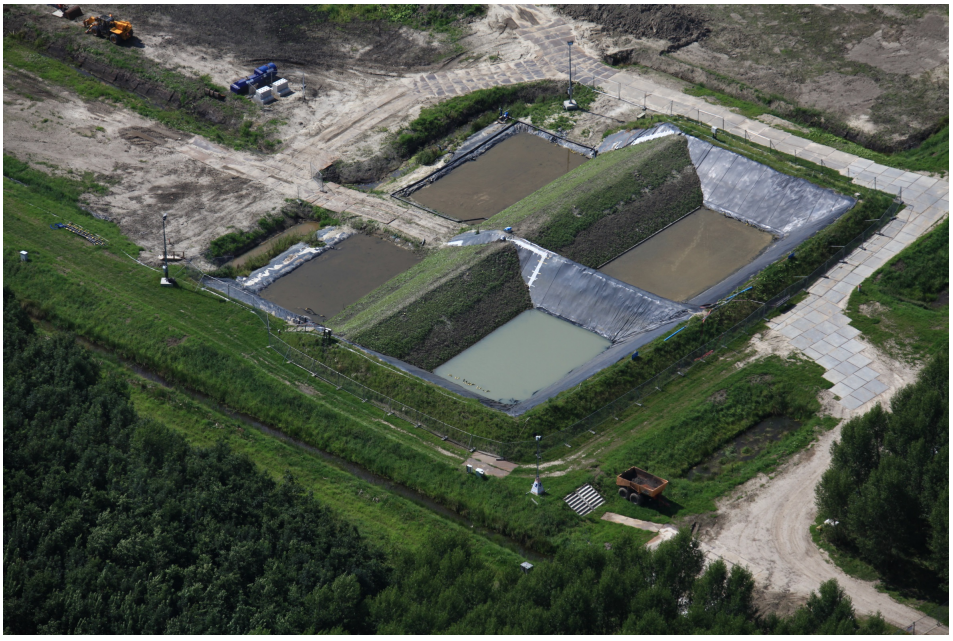

(b)

FIGURE A.2: Piping facility before and after the construction of the test dikes. Pictures are taken looking South-West; West dike is on the right.

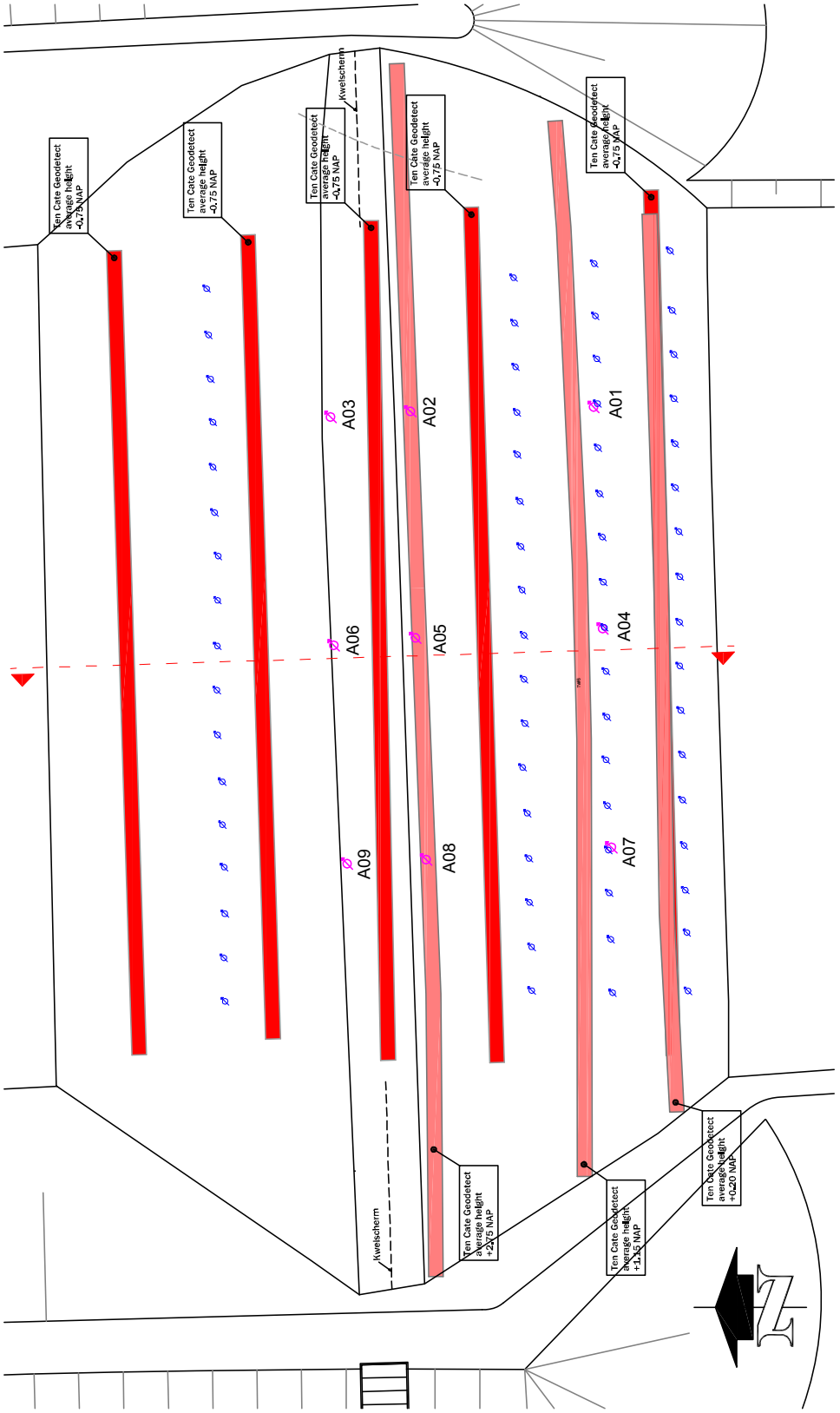

FIGURE A.3: Plan view of the West dike with positions of the instruments: blue and purple circles indicate the pore pressure sensors of the reference monitoring and red lines indicate distributed temperature sensors.

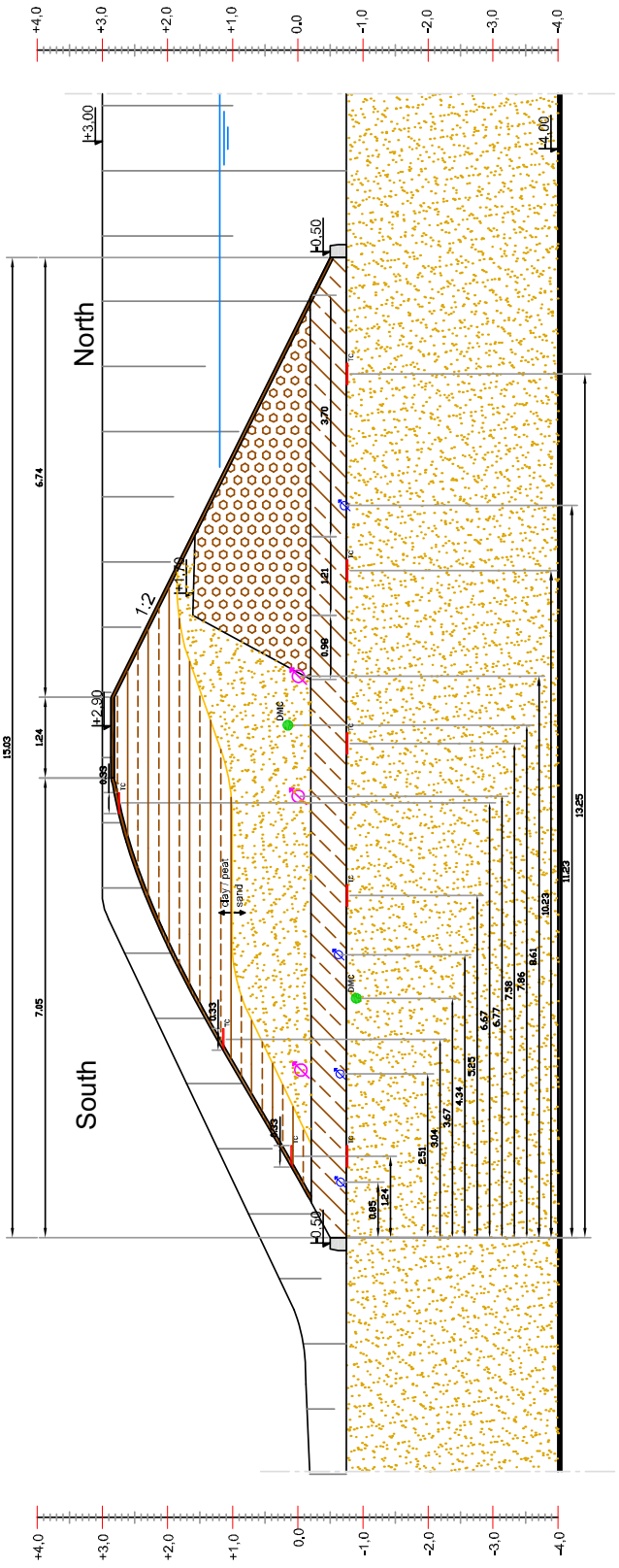

FIGURE A.4: Cross-section of the West dike with positions of the instruments: blue and purple circles indicate the pore pressure sensors of the reference monitoring,red lines indicate distributed temperature sensors and green circles indicate the controllable drainage tubes

FIGURE A.5: Piping facility before reconstruction works

FIGURE A.6: Piping facility during deposition of the new sand

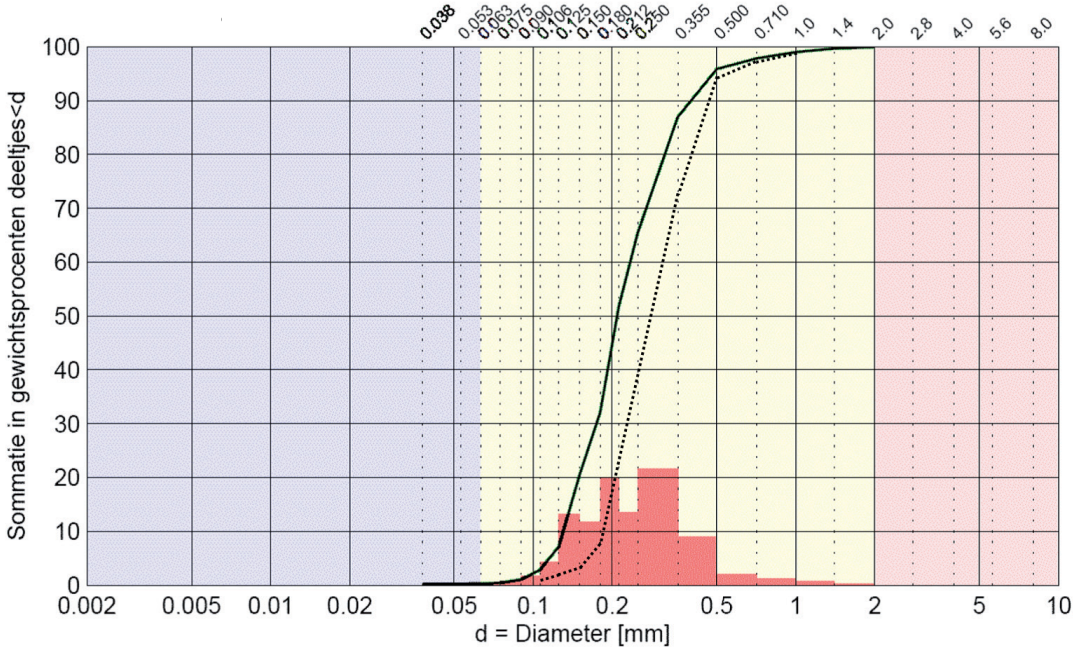

FIGURE A.7: Grain size distribution of the test sand (solid line and histogram). The dotted line refers to the sand used to replaced the upper part of the layer.

FIGURE A.8: Installation of the controllable drainage tube, surrounded by a sand filter.

FIGURE A.9: Installation of pore pressure sensors and optical fibres at the dike base.

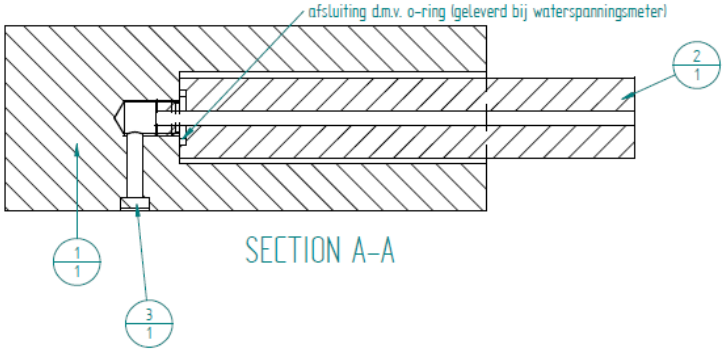

(a)

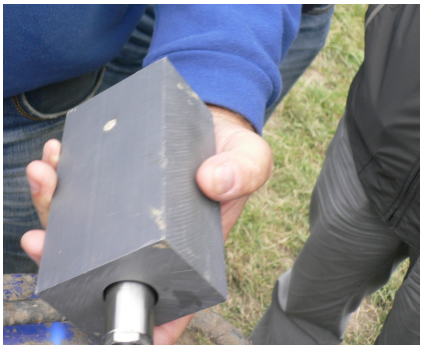

(b)

FIGURE A.10: Pore pressure sensors adopted for the reference monitoring: 1) plastic case, 2) liquid level sensor and 3) filter.

FIGURE A.11: Visual inspection performed from a crane.

FIGURE A.12: Infrared cameras pointing to the downstream West and East slopes.

FIGURE A.13: Distributed temperature and strain sensors: 4 optical fibres encased in a 33 cm wide geotextile strip.

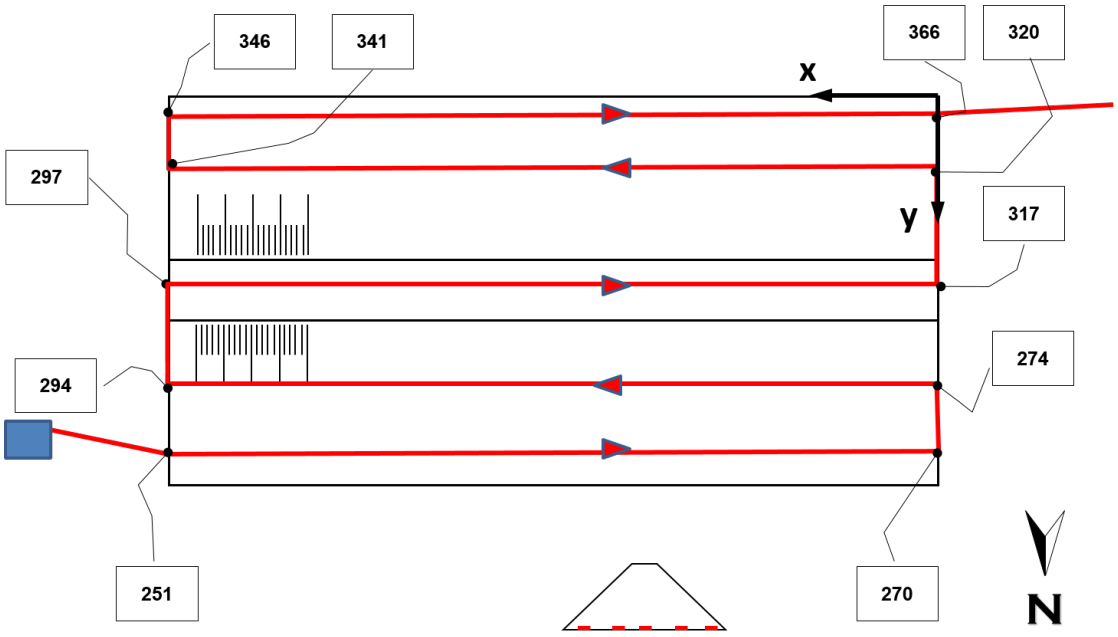

FIGURE A.14: Scheme of deployment of the optical fibres at the base of the dike. The text boxes indicate the progressive distances (in m) from the beginning of the cables. The scheme is fundamental to determine the position of every point of reflection along the fibre.

FIGURE A.15: Detail of the optical fibres at the base of the dike: bending between two profiles.

FIGURE A.16: Installation of the optical fibres in a trench on the downstream slope

FIGURE A.17: Extra lump of clay placed near the sides in order to avoid failure at the ends

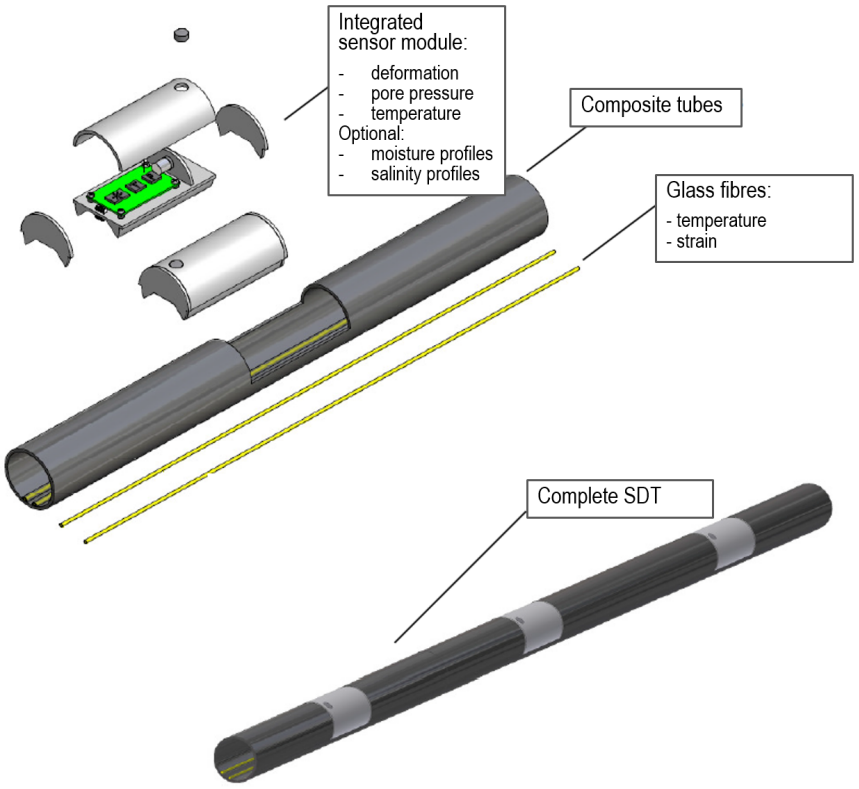

(a)

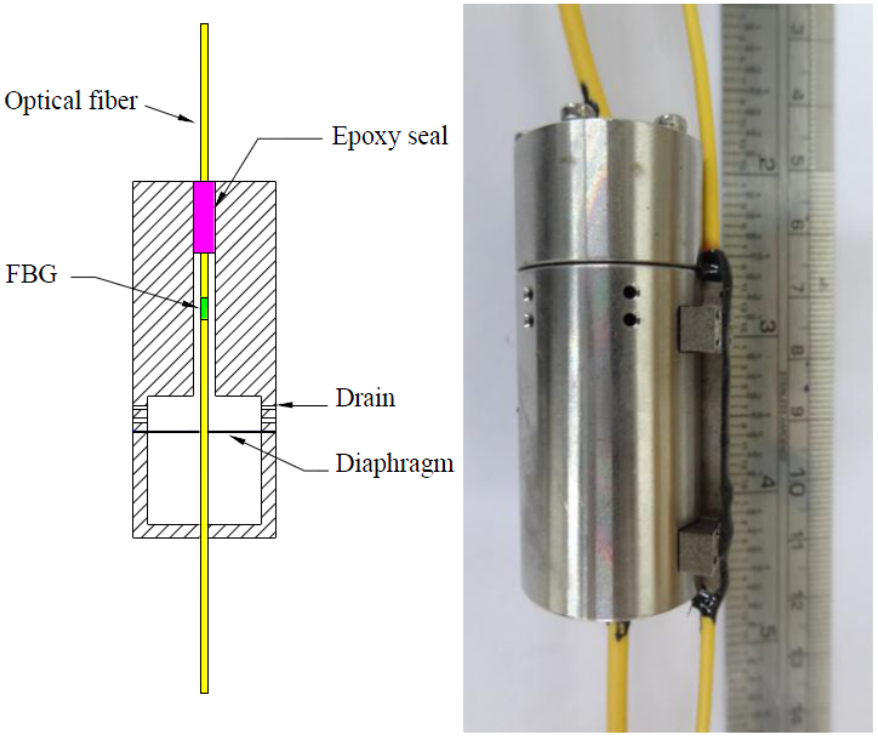

(b)

FIGURE A.18: Fibre optic FBG sensors installed in the dike: (a) FGB strain and temperature sensors, (b) FBG pore pressure sensors.

FIGURE A.19: Ground-based radar pointed to the downstream slope.

FIGURE A.20: Ground Penetrating Radar guided from a distance along the dike crest.

FIGURE A.21: First sand boil observed.

FIGURE A.22: Second sand boil observed.

FIGURE A.23: First crack appeared on the crest

FIGURE A.24: Cracks on the upstream slope

FIGURE A.25: First sliding of the downstream slope

FIGURE A.26: Buldge of the downstream toe

FIGURE A.27: Further sliding of the downstream slope

FIGURE A.28: Further buldge of the downstream toe

FIGURE A.29: Breaching of the dike

FIGURE A.30: Emptying of the upstream basin nearly complete

Appendix B

Numerical stability of the advection-diffusion equation

B.1 A basic analytical solution

To keep the analysis simple, the following elementary two-point boundary value problem will be considered, as reported in (Quarteroni et al., 2007):

$$\begin{cases} -\alpha u''(x) + \beta u'(x) = 0 \quad 0 < x < 1 \\ u(0) = 0, \qquad u(1) = 1 \end{cases} \tag{B.1}$$

where α and β are two positive constants such that $\alpha \, \beta \ll 1$ (which means that advection dominates over diffusion). The global Péclet number is defined as

$$Pe_{gl} = \frac{|\beta| L}{\alpha} \tag{B.2}$$

where L is the size of the domain (equal to 1 in this case).

By imposing $u(x) = e^{\lambda x}$ the characteristic equation associated to the differential equation (B.1) is found:

$$-\alpha\lambda^2 + \beta\lambda = 0, \tag{B.3}$$

which admits roots

$$\lambda_1 = 0, \qquad \lambda_2 = \beta/\alpha. \tag{B.4}$$

Imposing the boundary conditions yields

$$c_1 = -\frac{1}{e^{\beta/\alpha} - 1}, \qquad c_2 = -c_1 \tag{B.5}$$

and thus

$$u(x) = \frac{e^{\frac{\beta}{\alpha}x} - 1}{e^{\frac{\beta}{\alpha}} - 1}. \tag{B.6}$$

If $\beta/\alpha \ll 1$ the exponential can be expanded up to the first order, obtaining

$$u(x) = \frac{1 + \frac{\beta}{\alpha}x + ... - 1}{1 + \frac{\beta}{\alpha} + ... - 1} \backsimeq \frac{\frac{\beta}{\alpha}x}{\frac{\beta}{\alpha}} = x, \tag{B.7}$$

thus the solution is a straight line interpolating the boundary data.

However, if $\beta/\alpha \gg 1$ the exponential attains big values, so that

$$u(x) \backsimeq \frac{e^{\frac{\beta}{\alpha}x}}{e^{\frac{\beta}{\alpha}}} = e^{-\frac{\beta}{\alpha}(1-x)}. \tag{B.8}$$

Since the exponent is big and is negative for $x \,\epsilon\, [0, 1]$, the solution is almost equal to zero everywhere, except in a small neighbourhood of the point $x = 1$ where the term $1 - x$ becomes very small and the solution joins the value 1 with an exponential behaviour. The width of the neighbourhood is of order α/β and thus quite small: in such an event it can be said that the solution exhibits a *boundary layer* of width $\mathcal{O}(\alpha/\beta)$ at $x = 1$. Figure B.1 shows the trend of the solution for different values of α/β.

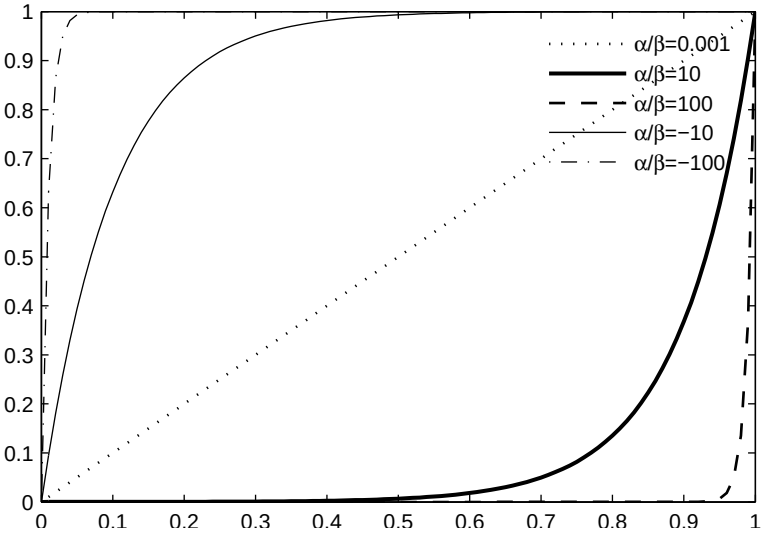

FIGURE B.1: Solution of the advection-diffusion equation for different values of α/β (advection/diffusion)

B.2 Centred finite differences approximation

In order to examine the numerical behaviour of the advection-diffusion equation the finite difference method (FD) is recalled, which is simpler to develop but equivalent to the linear Galerkin FE method.

Again the one-dimensional problem (B.1) is considered, with a uniform grid size h. To ensure that the local discretization error is of second order the derivatives $u'(x_i)$ and $u''(x_i)$, $i = 1, ..., n-1$, is approximated by the centred finite differences. The scheme can be derived recalling the Taylor's expansions

$$u(x_i + h) = u(x_i) + h\,u'(x_i) + \frac{h^2}{2}u''(x_i) + o(x_i^2), \tag{B.9}$$

$$u(x_i - h) = u(x_i) - h\,u'(x_i) + \frac{h^2}{2}u''(x_i) + o(x_i^2). \tag{B.10}$$

Equation (B.10) is subtracted to Eq. (B.9) to obtain

$$u'(x_i) = \frac{u(x_i + h) - u(x_i - h)}{2h} \tag{B.11}$$

and Eq. (B.10) is summed to Eq. (B.9) to obtain

$$u''(x_i) = \frac{u(x_i + h) - 2u(x_i) + u(x_i - h)}{h^2}. \tag{B.12}$$

Using a more compact notation:

$$u_i' = \frac{u_{i+1} - u_{i-1}}{2h}, \qquad u_i'' = \frac{u_{i+1} - 2u_i + u_{i-1}}{h^2}, \tag{B.13}$$

the following FD problem is obtained:

$$\begin{cases} -\alpha\dfrac{u_{i+1} - 2u_i + u_{i-1}}{h^2} + \beta\dfrac{u_{i+1} - u_{i-1}}{2h} = 0 \qquad i = 1, ..., n-1 \\ u_0 = 0, \qquad u_n = 1. \end{cases} \tag{B.14}$$

Multiplying (B.14) by h/α and defining the *element Péclet number* to be

$$Pe_h = \frac{|\beta|h}{\alpha} \tag{B.15}$$

the following is finally obtained:

$$(Pe_h - 2)u_{i+1} + 4u_i - (Pe_h + 2)u_{i-1} = 0. \tag{B.16}$$

This is a linear difference equation which can be solved imposing that the solution is of the kind $u_i = \lambda^i$. Rewriting (B.16) as

$$(Pe_h - 2)u_{i+2} + 4u_{i+1} - (Pe_h + 2)u_i = 0 \tag{B.17}$$

and substituting u_i with λ^i the following is obtained:

$$\lambda^i[(Pe_h - 2)\lambda^2 + 4\lambda - (Pe_h + 2)] = 0, \tag{B.18}$$

which admits roots

$$\lambda_{1,2} = \frac{-2 \pm \sqrt{4 + Pe_h^2 - 4}}{Pe_h - 2} = \begin{cases} \dfrac{2 + Pe_h}{2 - Pe_h} \\ 1. \end{cases} \tag{B.19}$$

The general solution to the equation (B.16) is the linear combination

$$u_i = c_1\lambda_1^i + c_2\lambda_2^i, \tag{B.20}$$

where the constants are to be determined by imposing the boundary conditions. The general solution thus results

$$u_i = \frac{1 - \left(\dfrac{2 + Pe_h}{2 - Pe_h}\right)^i}{1 - \left(\dfrac{2 + Pe_h}{2 - Pe_h}\right)^n} \qquad i = 1, ..., n. \tag{B.21}$$

It should be noted that if $Pe_h > 2$, a power with a negative base appears at the numerator, which gives rise to an oscillating solution. This is clearly visible in Fig. B.2 where for several values of the local Péclet number, the solution of Eq. (B.16) is compared with the exact solution corresponding to a value of the global Péclet equal to 50. Oscillations in space can arise where the Péclet number exceeds 2 and any of the following occur (COMSOL Inc., 2012):

- a Dirichlet boundary condition leading to a solution containing a steep gradient

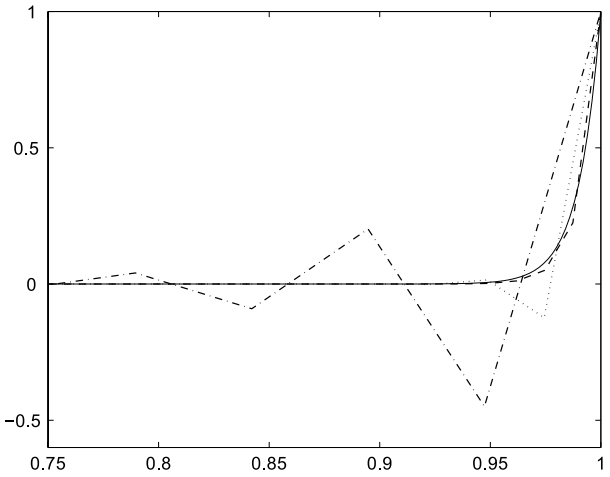

FIGURE B.2: Finite difference solution of the advection-diffusion problem (B.1) (with $Pe_g = 100$) for several values of the element Péclet number. Solid line:exact solution, dot-dashed line: $Pe_h = 5.26$, dotted line: $Pe_h = 2.56$, dashed line: $Pe_h = 1.26$. (Quarteroni et al., 2007)

near the boundary: if the mesh cannot resolve the boundary layer, this creates a local disturbance;

- a space-dependent initial condition: if not resolved by the mesh it can cause a local initial disturbance that propagates through the computational domain;
- a small initial diffusion term close to a non-constant source term or a non-constant Dirichlet boundary condition: this again can result in a local disturbance.

The simplest remedy for preventing oscillations consist of course in choosing a sufficiently small grid size h in such a way that $Pe_h < 2$. However, this approach is sometimes not feasible because it can require a very dense mesh. In these cases, other strategies can be pursued, as will be addressed in the next section.

B.3 Upwind schemes and artificial diffusion

The instability in the FD solution is due to the fact that the discretization scheme is a *centred* one. A possible remedy consists in approximating the first derivative by a one-sided finite difference according to the direction of the transport field. Precisely, the backward difference is used here if the convective coefficient β is positive and the forward difference otherwise. The resulting scheme when $\beta > 0$ is

$$-\alpha\frac{u_{i+1} - 2u_i + u_{i-1}}{h^2} + \beta\frac{u_i - u_{i-1}}{h} = 0 \qquad i = 1, ..., n-1. \tag{B.22}$$

This one-sided discretization of the first derivative is called *upwind* differencing. The price to be paid for the enhanced stability is a loss of accuracy, since the upwind finite difference introduces a local discretization error of $\mathcal{O}(h)$ and not of $\mathcal{O}(h^2)$ as happens using centred finite differences. Noting that

$$\frac{u_i - u_{i-1}}{h} = \frac{u_{i+1} - u_{i-1}}{2h} - \frac{h}{2}\frac{u_{i+1} - 2u_i + u_{i-1}}{h^2} \tag{B.23}$$

the upwind finite difference can be interpreted as the sum of a centred finite difference approximating the first derivative and of a term proportional to the discretization of the second-order derivative. Consequently, Eq. (B.22) is equivalent to

$$-\alpha' \frac{u_{i+1} - 2u_i + u_{i-1}}{h^2} + \beta\frac{u_{i+1} - u_{i-1}}{2h} = 0, \tag{B.24}$$

where $\alpha' = \alpha + \dfrac{\beta h}{2}$. We observe that the new Péclet number is

$$Pe'_h = \frac{\beta h}{\alpha + \dfrac{\beta h}{2}} \leq 2 \qquad \forall h > 0. \tag{B.25}$$

Therefore, the scheme is always stable.

The operations above amount to having replaced the differential equation (B.1) with the perturbed one

$$-\alpha' u''(x) + \beta u'(x) = 0 \tag{B.26}$$

and then using centred finite differences to approximate both u' and u''. The perturbation $-(\beta h/2)u''$ is called *numerical viscosity* (terminology that comes from the Navier-Stokes equations) or *numerical diffusion* or also *artificial diffusion*.

For the solution to be accurate, the numerical diffusion must be much smaller than the physical diffusion. This occurs if the size of the grid is such that $\beta h/2 \ll \alpha$.

With FE it is possible to proceed similarly, i.e. adding a diffusive term conveniently created. It is also possible to apply numerical diffusion only along the direction of the motion: the common SUPG method (*Streamline Upwind Petrov-Galerkin*) is so resorted. More advanced schemes also exist, which are basically based on the introduction of a minimal amount of numerical diffusion only where and when needed.

Appendix C

Conditions of similitude in piping modelling

C.1 Groundwater flow

In groundwater flow modelling the concepts of geometric, kinematic and dynamic similarity are recognized.

Geometric similarity implies that the ratios between all corresponding lengths in the two considered systems is the same. Let $(\delta x)_p$, $(\delta y)_p$ and $(\delta z)_p$ denote certain characteristic lengths in the prototype and $(\delta x)_m$, $(\delta y)_m$ and $(\delta z)_m$ be their corresponding lengths in the model. Their ratios are the length scales $\Lambda_i = (\delta i)_p/(\delta i)_m$ where $i = x, y, z$. Exact geometric similarity requires that $\Lambda_x = \Lambda_y = \Lambda_z = \Lambda$. However, often a distorted model with $\Lambda_x \neq \Lambda_y \neq \Lambda_z$ is employed. Angles are not preserved in this case.

Kinematic similarity means similarity of the flow net composed of streamlines and equipotentials, i.e., the two flow nets are geometrically similar. Kinematic similarity implies that the direction of the velocity remains unchanged and that the ratio between velocities at all homologous points in the two systems is the same throughout the domain. Since the boundaries of the flow domain will form some of the streamlines or equipotentials, kinematically similar flows must also be geometrically similar. In the range of laminar flow, the converse is also true. In a distorted model it is impossible to maintain kinematic similarity.

Dynamic similarity requires that forces at homologous points and homologous times acting on homologous elements of fluid mass are be the same throughout the two

systems. For confined flows the most relevant parameter to preserve is the ratio between inertial and viscous forces, called Reynolds number:

$$Re = \frac{u\, l^*}{\nu} \tag{C.1}$$

where l^* is some characteristic length and u some characteristic velocity. When referring to flow in tubes, the diameter of the tube is assumed as the characteristic length and the average velocity is considered as the characteristic velocity. For flow through porous media the characteristic length should be chosen as a dimension representing the elementary channels of the porous medium: d_{10} or d_{50} are often used. The pore velocity is assumed as the characteristic velocity.

C.2 Backward erosion piping

Let us apply the concepts expressed in § C.1 to the physical modelling of piping. First of all, the kinematic similarity requires that aquifer thickness and seepage length are scaled by the same geometrical factor. The aspect ratio of the aquifer does indeed have an influence on the flow field and thus on the dynamic forces.

Secondly, the dynamic similarity in groundwater flow modelling is fulfilled if the Darcy velocity is the same in prototype and model at every point. However, according to Sellmeijer's theory (Weijers and Sellmeijer, 1993a), the responsible factors for piping progression are not only the forces acting within the soil matrix but also the tangential stress at the wall of the pipe. In this framework, well established scaling laws for sediment transport in open channels come useful to understand some scaling issues in piping modelling. A non-dimensional parameter important in sediment transport is the Particle Reynolds Number:

$$Re_p = \frac{u_* d}{\nu}. \tag{C.2}$$

It represents the ratio of the viscous forces to the inertial forces acting on an individual grain of diameter d. u_* is called shear velocity and is the shear stress on the bed written in terms of velocity; it is linked to the average flow velocity in the channel. Another important parameter is the Shield Number:

$$\Theta = \frac{\rho u_*^2}{g(\rho_s - \rho)d}\ . \tag{C.3}$$

It represents the ratio of the shear stress on the bed, $\tau = \rho u_*^2$, to the submerged weight of the particle and is useful in characterizing incipient motion of particles on the bed.

The sediment transport similarity basically requires that prototype Particle Reynolds Number and Shield Number are preserved in the model. According to Sellmeijer's theory, this translates into a non-linear relationship between the critical head and the geometry scale factor:

$$(H_c)_p = \Lambda^{2/3}(H_c)_m \,. \tag{C.4}$$

This scale effect is supported by experimental evidence (Van Beek et al., 2013). If Sellmeijer's formula holds, and thus Eq. (C.4) holds, conservation of the Shield parameter requires that also the thickness of the slot (the 2-d analog of the pipe) varies non-linearly with scale:

$$(b)_p = \Lambda^{1/3}(b)_m \,. \tag{C.5}$$

Comparison between small-scale and large-scale experiments shows that the size of the pipes does not vary much with scale (Van Beek et al., 2013) but they rather branch as a result of micro-heterogeneities in the sand bed, covering a large area (see Fig. 2.6). This feature of the problem cannot be modelled by Sellmeijer's theory which is a 2-d approximation of a definitely 3-d process. The effect of three-dimensional flow in backward erosion is currently under investigation in The Netherlands and Belgium. In addition, Van Beek et al. (2014b) have highlighted the possibility that detachment of sand grains is triggered by groundwater flow towards the pipe rather than by the flow in the pipe. If this hypothesis is confirmed and the theory revised, it is likely that the scaling rules C.4 and C.5 will also be revised.

Most difficulties arise in physical modelling of piping because the size of the grains is not scaled, while the linearity of the laminar groundwater flow causes the flow velocity distribution to be linearly dependent on scale. Scaling of the grains is not feasible as reducing their size would mean increasing the grain surface forces (typical of clayey materials) with the reference to grain body forces acting, so that the erosion process in the new materials would be non comparable to that occurring in the prototype material.

The strategy adopted by researchers so far consists in using the same grains and fluid in the model as in the prototype, being aware that some scaling issues exist. Experimental investigation at different scales and theoretical investigation can subsequently cope with the drawbacks of a not perfect scaling.

For example, Van Beek et al. (2014a) by means of small-scale physical modelling

investigated the critical gradient for uplift of sand grains at the dike toe. Subsequently, by means of numerical and theoretical modelling of groundwater flow, they determined the effect of scale on the critical gradients, and thus on the hydraulic head that causes initiation of piping.

For what concern the modelling of piping progression, further research is needed to define appropriate scaling rules for the complex interaction between groundwater flow, pipe flow and sediment transport.

When the progression phase is studied, the model is representative of field conditions if the cross-section of the model is large enough for the radius of influence of the pipe to be contained in the model; on the contrary it should be taken into account that the flow field is influenced by the presence of the lateral boundaries.

References

Aanstoos, J. V. (2012). "Screening of levees by Synthetic Aperture Radar." *SERRI Report 90008-01*, OAK RIDGE National Laboratory. Prepared for U.S. Department of Homeland Security.

Aanstoos, J. V., Hasan, K., O'Hara, C. G., Prasad, S., Dabbiru, L., Mahrooghy, M., Nobrega, R., Lee, M., and Shrestha, B. (2010). "Use of remote sensing to screen earthen levees." *IEEE 39th Applied Imagery Pattern Recognition Workshop*.

Al Nakahabandi, G. and Kohnke, H. (1965). "Thermal conductivity and diffusivity of soils as related to moisture tension and other physical properties." *Agricultural Meteorology*, 2(4), 271–279.

Albalat, C. and Garnero, E. (1995). "Mesure de fuites sur le canal de Jonage avce un capteur de température á fibre optique continûment sensible." *Rapport EDF D4007/23/GC/95-3018*.

Bear, J. (1972). *Dynamics of fluids in porous media*. Elsevier, New York.

Bear, J. and Verruijt, A. (1987). *Modeling groundwater flow and pollution*. Springer Netherlands.

Beavers, G. and Joseph, D. (1967). "Boundary conditions at a naturally permeable wall." *Journal of Fluid Mechanics*, 30(1), 197–207.

Beck, Y. L., Khan, A. A., Cunat, P., Guidoux, C., Artires, O., Mars, J., and Fry, J. J. (2010). "Thermal monitoring of embankment dams by fiber optics." *Proceedings of 8th ICOLD European Club Symposium on dam safety*, ATCOLD Austrian National Committee on Large Dams.

van Beek, V. M., Bezuijen, A., and Zwanenburg, C. (2010). "Piping: Centrifuge experiments on scaling effects and levee stability." *Physical Modelling in Geotechnics:*

Proceedings of the 7th International Conference on Physical Modelling in Geotechnics (ICPMG 2010), S. Springman, J. Laue, and L. Seward, eds., Vol. 1, CRC Press, 183–189.

van Beek, V. M., Knoeff, H., and Sellmeijer, H. (2011). "Observations on the process of backward erosion piping in small-, medium- and full-scale experiments." *European Journal of Environmental and Civil Engineering*, 15(8), 1115–1137.

van Beek, V., Bezuijen, A., and Sellmeijer, H. (2013). "Backward erosion piping." *Erosion in Geomechanics Applied to Dams and Levees*, 193–269.

van Beek, V. M., Bezuijen, A., Sellmeijer, J. B., and Barends, F. B. J. (2014a). "Initiation of backward erosion piping in uniform sands." *Géotechnique*, 64(12), 927–941.

van Beek, V. M., Vandenboer, K., van Essen, H. M., and Bezuijen, A. (2014b). "Investigation of the backward erosion mechanism in small scale experiments." *8th international conference on Physical Modelling in Geotechnics*, Vol. 2, CRC Press-Taylor and Francis Group, 855–861.

Bergström, J. (1998). "Geophysical methods for investigating and monitoring the integrity of sealing layers on mining waste deposits." Ph.D. thesis, Luleå, Sweden.

van den Berg, F. P. W. and Koelewijn, A. R. (2014). "IV-Keten. Veiligheid als basis. Monitoringsfilosofie en proeftuinen." *Report 1207933-000-VEB-0001, 2nd version*, Deltares.

Blackwell, D. D. and Steele, J. L. (1989). "Thermal conductivity of sedimentary rocks: Measurement and significance." *Thermal History of Sedimentary Basins*, N. D. Naeser and T. H. McCulloh, eds., Springer New York, 13–36.

Bligh, W. G. (1910). "Dams, barrages and weirs on porous foundations." *Engineering News*, 64(26), 708–710.

Bolève, A., Janod, F., Revil, A., Lafon, A., and Fry, J.-J. (2011). "Localization and quantification of leakages in dams using time-lapse self-potential measurements associated with salt tracer injection." *Journal of Hydrology*, 403(34), 242–252.

Brinkman, H. C. (1949). "A calculation of the viscous force exerted by a flowing fluid on a dense swarm of particles." *Applied Scientific Research*, 1(1), 27–34.

Burns, B., Barker, R., and Ghataora, G. S. (2006). "Investigating internal erosion using a miniature resistivity array." *NDT & E International*, 39(3), 169–174.

Calabresi, G., Colleselli, F., Danese, D., Giani, G. P., Mancuso, C., Montrasio, L., Nocilla, A., Pagano, L., Reali, E., and Sciotti, A. (2013). "Research study of the hydraulic behaviour of the Po river embankments." *Canadian Geotechnical Journal*, 50(9), 947–960.

Cao, D. (1994). "Countermeasures for seepage erosion of Yangtze River main dikes." *Yangtze River*, 25(1), 25–30.

Case, J. S. (2012). "Inspection of earthen embankment dams using time lapse electrical resistivity tomography." M.S. thesis, Department of Civil Engineering, University of Mississippi, Oxford, MS.

Ciravegna, F. (2013). "WeSenseIt: Citizen observatories of water", <`http://ec.europa.eu/research/environment/geo/pdf/january_2013_workshop/plenary_session/wesenseit_ciravegna_general_introduction.pdf`>. Last visited 9th June 2014.

CIRIA, Ministry of Ecology, and USACE (2013). *The International Levee Handbook*. CIRIA, London, UK, <`http://www.ciria.org/ItemDetail?iProductCode=C731&Category=BOOK&WebsiteKey=3f18c87a-d62b-4eca-8ef4-9b09309c1c91`>.

Claesson, J., Hellström, G., and Johansson, S. (2001). "Temperature analyses for evaluation of water flow in aquifers and embankment dams." *in Software package for evaluation of temperature field in embankment dams (manual for DamTemp ver 1.0)*, HydroResearch and NeoEnergy, <`http://www.hydroresearch.se/en/temperature/evaluation`>.

Colleselli, F. and Cortellazzo, G. P. (1992). "Foundation behavior of a levee in the Po Delta." *Symp. on Prediction versus performance in geotechnical engineering*, Vol. 1, Bangkok, 15–20.

Colleselli, F., Jommi, C., and Vinciguerra, D. (2004). "Analisi delle condizioni di sicurezza di un'arginatura nel Delta del Po." *XXII CNG*, Palermo, 475–488.

Comité Européen de Normalisation (CEN) (2004). *BS EN 1997-1: Eurocode 7: Geotechnical design - Part 1: General rules*. Brussels, Belgium.

COMSOL Inc. (2012). *CFD module user's guide* Version 4.3.

Corwin, R. F. (2007). "Interpretation of self-potential data for dam seepage investigations." *CEATI Report No. T992700-0205B-3*, CEATI International Inc., Dam Safety Interest Group, Montreal, Quebec, Canada.

Cosanti, B. and Lo Presti, D. C. F. (2014). "A monitoring system to study seepage through river embankments." *IEAG XII Congress*, Torino.

Côté, A., Carrier, B., Gervais, R., and Noël, P. (2009). "Water seepage detection and localization using optical fiber at the Péribonka dam." *International Workshop On Internal Erosion in Dams and Foundations.*

Cunat, P. (2012). "Détection et évaluation des fuites à travers les ouvrages hydrauliques en remblai, par analyse de températures réparties, mesurées par fibre optique." Ph.D. thesis, Université de Grenoble, Grenoble, France.

Cunat, P., Beck, Y. L., Fry, J. J., Courivaud, J. R., Fabre, J. P., Faure, Y. H., and Radzicki, K. (2009). "Surveillance of dike ageing by distributed temperature measurement along a fiber optic." *Proceedings of HYDRO 2009*, Hydropower & Dams, Aqua Media International Ltd, Wallington, UK, 338–341.

Cundill, S., Hack, R., and van der Meijde, M. (2012). "Investigation of remote sensing for dike inspection." *International Geoscience and Remote Sensing Symposium IGARSS 2012*, IEEE Geoscience and Remote Sensing Society.

Cundill, S., Hack, R., van der Meijde, M., van der Schrier, J., and Ngan-Tillard, D. (2013). "Quality of peat dykes evaluated by remote sensing." *Comprehensive Flood Risk Management - Research for Policy and Practice*, Klijn and Schweckendiek, eds., London, UK, Taylor & Francis Group.

Dabbiru, L., Aanstoos, J. V., and Younan, N. H. (2010). "Classification of levees using polarimetric Synthetic Aperture Radar (SAR) imagery." *IEEE 39th Applied Imagery Pattern Recognition Workshop.*

Dacome, A. and Bersan, S. (2014). "Verifiche in situ della permeabilità di argini fluviali mediante traccianti chimici." *XXV CNG*, Baveno (4-6 giugno).

Dahlin, T., Sjödahl, P., and Johansson, S. (2008). "A guide to resistivity investigation and monitoring of embankment dams." *CEATI Report No. T992700-0205B-4*, CEATI International Inc., Dam Safety Interest Group, Montreal, Quebec, Canada.

D'Alpaos, L., Brath, A., Fioravante, V., Gottardi, G., Mignosa, P., and Orlandini, S. (2014). "Relazione tecnico-scientifica sulle cause del collasso dell'argine del fiume Secchia avvenuto il giorno 19 gennaio 2014 presso la frazione San matteo". Regione Emilia Romangna.

Del Grande, C. (2008). "Sistema sperimentale di preallarme per il rischio di collasso arginale lungo l'asta dei Fiumi Uniti, del F. Montone, del F. Lamone e del F. Savio quale misura non strutturale di difesa idraulica della città di Ravenna e delle localitá in provincia di Ravenna 1° Lotto." *Document no. 3: Technical report and specs*, Prepared for: Settore Ambiente e suolo, Provincia di Ravenna, <http://www.google.it/url?sa=t&rct=j&q=&esrc=s&source=web&cd=2&cad=rja&uact=8&ved=0CCgQFjAB&url=http%3A%2F%2Fwww.provincia.ra.it%2Fcontent%2Fdownload%2F16751%2F226272%2Ffile%2FPeziometriElaboratiProgettuale3.pdf&ei=rDyEVcKdNqa17gaIyaMQ&usg=AFQjCNH8f2ifc02uI4-LGt_AMYwd2bMjKQ&sig2=dQAeg5v2tMv2Vp7a6ySmag&bvm=bv.96042044,d.ZGU>. Last visited 22nd June 2015.

Di Prinzio, M., Bittelli, M., Castellarin, A., and Rossi Pisa, P. (2010). "Application of GPR to the monitoring of river embankments." *Journal of Applied Geophysics*, 71(2–3), 53–61.

Discacciati, M. and Quarteroni, A. (2009). "Navier-Stokes/Darcy coupling: modeling, analysis, and numerical approximation." *Revista Matemática Complutense*, 22(2), 315–426.

Dornstädter, J. (2013). "Leakage detection in dams - state of the art." *Proc. Int. Symp. Dam engineering in Southeast and Middle Europe*, Slovenian National Commitee on Large Dams (SLOCOLD), Ljubljana, Slovenia.

Douglas, K., Allen, R., Fell, R., and Peirson, B. (2013). "Backward erosion piping of dams - experimental progress." *Abstracts of the 21st annual meeting of the European Working Group in Internal Erosion in Embamkment Dams & Their Foundations (EWGIE)*, 30.

DWA (Deutsche Vereinigung für Wasserwirtschaft, Abwasser und Abfall) (2007). *Merkblatt DWA-M 507: Deiche an Fließgewässern.* Hennef, Germany.

Eindhoven University of Technology (n.d.). *Periodic soil temperature fluctuations*, <http://archbps1.campus.tue.nl/bpswiki/images/6/6a/H3.pdf>.

Elder, J. W. (1967). "Steady free convection in a porous medium heated from below." *Journal of Fluid Mechanics*, 27(1), 29–48.

European Parliament and Council (2007). *Directive 2007/60/EC on the assessment and management of flood risks (OJ L 288, 6.11.2007).*

Farouki, O. (1981). *Thermal properties of soils.* Monograph 81-1. Cold Regions Research and Engineering Laboratory, Hanover, NH.

Fell, R., Wan, C. F., Cyganiewicz, J., and Foster, M. (2003). "Time for development of internal erosion and piping in embankment dams." *Journal of Geotechnical and Geoenvironmental Engineering*, 129(4), 307–314.

FOA (Fiber Optic Association) (2010). *Guide to fiber optics premises cabling - Outside plant fiber optic network installation*, <http://www.thefoa.org/tech/ref/OSP/install.html>. Last visited 9th June 2014.

Foster, M., Fell, R., and Spannagle, M. (2000). "The statistics of embankment dam failures and accidents." *Canadian Geotechnical Journal*, 37(5), 1000–1024.

Fry, J. J. (1997). "Internal erosion and surveillance." *ICOLD 19th Congress*, Vol. V, 255–268.

Fry, J. J., Vogel, A., Royet, P., and Courivaud, J.-R. (2012). "Dam failures by erosion: lessons from ERINOH data bases." *Six International Conference on Scour and Erosion ICSE6*, International Society for Soil Mechanics and Geotechnical Engineering (ISSMGE), 273–280. paper n. 290.

Galiana, M. (2005). "Internal erosion as failure mechanism of inner dike slope clay cover by wave overtopping." *Extensive report of MSc-internship, GeoDelft report no. CO-418010/5*, GeoDelft.

Gamboloati, G. (1973). "Equation for one-dimensional vertical flow of groundwater. 1. The rigorous theory." *Water Resources Research*, 9(4), 1022–1028.

Gifford, D., Soller, B., Wolfe, M., and Froggatt, M. (2005). "Distributed fiber-optic temperature sensing using Rayleigh backscatter." *31st European Conference on Optical Communications - ECOC 2005*.

Giroud, J. P. (2010). "Development of criteria for geotextile and granular filters." *Proceedings of the 9th International Conference on Geosynthetics*, Vol. 1, 45–64.

de Groot, M., Mastbergen, D., Bezuijen, A., and Stoutjesdijk, T. (2011). "Micro-instability at dike inner slopes." *A feeling for soil and water: A tribute to prof. Frans Barends*, M. Van, ed., Deltares Select Series 07/2011, Deltares, 65–74.

Günzel, U. and Wilhelm, H. (2000). "Estimation of the in-situ thermal resistance of a borehole using the distributed temperature sensing (DTS) technique and the temperature recovery method (TRM)." *Geothermics*, 29(6), 689–700.

Hagerty, D. (1991). "Piping/sapping erosion. I: Basic considerations." *Journal of Hydraulic Engineering*, 117(8), 991–1008.

Harteveld, C. (2010). "Balancing play, meaning and reality: The design philosophy of Levee Patroller." *Simulation & Gaming*, 41(3), 316–340.

Hausner, M. B., Suárez, F., Glander, K. E., van de Giesen, N., Selker, J. S., and Tyler, S. W. (2011). "Calibrating single-ended fiber-optic Raman spectra distributed temperature sensing data." *Sensors*, 11(11), 10859–10879.

Hazma, V. M., Cardoso, R. R., and Alexandrino, C. H. (2010). "A magma accretion model for the formation of oceanic lithosphere: Implications for global heat loss." *International Journal of Geophysics*, 2010(doi:10.1155/2010/146496).

Hillel, D. (1982). *Introduction to soil physics*. Academic Press, San Diego, CA.

Hoes, O. A. C., Schilperoort, R. P. S., Luxemburg, W. M. J., Clemens, F. H. L. R., and van de Giesen, N. C. (2009). "Locating illicit connections in storm water sewers using fiber-optic distributed temperature sensing." *Water Research*, 43(20), 5187–5197.

Horai, K. (1971). "Thermal conductivity of rock-forming minerals." *Journal of Geophysical Research*, 76, 1278–1308.

Horlacher, H. B., Heyer, T., Carstensen, D., Bielagk, U., Bielitz, E., and Müller, U. (2007). "Analysis of dyke breaks during the 2002 flood in Saxony/Germany." *Lake*

Abaya Research Symposium LARS 2007, University of Siegen, FWU Water Resources Publications, 58–66.

Hurtig, E., Großwig, S., Jobmann, M., Kühn, K., and Marschall, P. (1994). "Fibre-optic temperature measurements in shallow boreholes: experimental application for fluid logging." *Geothermics*, 23(4), 355–364.

ICOLD (International Commission on Large Dams) (2015). *Internal erosion of existing dams, levees and dikes, and their foundations – Volume 1: Internal erosion processes and engineering assessment.* Bulletin 164, Paris, France.

Imre, E., Nagy, L., Lőrincz, J., Rahemi, N., Schanz, T., Singh, V. P., and Fityus, S. (2015). "Some comments on the entropy-based criteria for piping." *Entropy*, 17 (accepted for publication).

Imre, E. and Rétháti, L. (1991). "Complex geotechnical examination of river dykes." *Report No. 86/86/XXIX OTKA*, FTV, Budapest, Hungary.

Jessop, A. M., Hobart, M. A., and Sclater, J. G. (1976). "The world heat-flow data collection - 1975." *Geothermal Series Number 5*, Ottawa, Canada.

Johansen, O. (1975). "Thermal properties of soils." Ph.D. thesis, Nowegian Institute of Technology, Trondheim.

Johansson, S. (1997). "Seepage monitoring in embankment dams." Ph.D. thesis, Royal Institute of Technology, Stockholm, Sweden.

Johansson, S., Friborg, J., Dahlin, T., and Sjödahl, P. (2005). "Long term resistivity and self potential monitoring of embankment dams experiences from Hällby and Sädva dams, Sweden." *Elforsk report 05:15*, Elforsk/Canadian Electricity Association - Dam Safety Interest Group (CEATI DSIG), Stockholm.

Johansson, S. and Hellström, G. (2001). *Software package for evaluation of temperature field in embankment dams (manual for DamTemp ver 1.0).* HydroResearch and NeoEnergy, <`http://www.hydroresearch.se/en/temperature/evaluation`>.

Johansson, S. and Sjödahl, P. (2004). "Downstream seepage detection using temperature measurements and visual inspection – Monitoring experiences from Røsvatn field test dam and large embankment dams in Sweden." *Proceedings Stability and Breaching of Embankment Dams*, Norwegian Electricity Industry Association (EBL), Oslo, Norway.

Johansson, S. and Sjödal, P. (2009). "A guide for seepage monitoring of embankment dams using temperature measurements." *CEATI Report No. T062700-0214*, CEATI International Inc., Dam Safety Interest Group, Montreal, Quebec, Canada.

van der Kamp, G. and Bachu, S. (1989). "Use of dimensional analysis in the study of thermal effects of various hydrogeological regimes." *Hydrogeological Regimes and Their Subsurface Thermal Effects*, A. Beck, G. Garven, and L. Stegena, eds., Vol. 47 of *Geophysical Monograph Series*, AGU, Washington D.C., 23–28.

Kappelmeyer, O. (1957). "The use of near surface temperature measurements for discovering anomalies due to causes at depths." *Geophysical Prospecting*, 5(3), 239–258.

Kersten, M. S. (1949). "Laboratory research for the determination of the thermal properties of soils." *Final report*, Minnesota Univ. Minneapolis, Engineering Experiment Station.

Khan, A., Vrabie, V., Mars, J., and Girard, A. (2008a). "A least square approach for bidimensional source separation using higher order statistics criteria." *16th European Signal Processing Conference*, European Association for Signal Processing, 1–5.

Khan, A. A., Vrabie, V., Mars, J. I., Girard, A., and d'Urso, G. (2008b). "A source separation technique for processing of thermometric data from fiber-optic DTS measurements for water leakage identification in dikes." *Sensors Journal*, 8(7), 1118–1129.

Khan, A., Vrabie, V., Mars, J., Girard, A., and d'Urso, G. (2010). "Automatic monitoring system for singularity detection in dikes by DTS data measurement." *Instrumentation and Measurement*, 59(8), 2167–2175.

Koelewijn, A. R., de Vries, G., and van Lottum, H. (2013). "Full-scale field validation of innovative dike monitoring systems." *Proceedings of the 18th International Conference on Soil Mechanics and Geotechnical Engineering*, 931–934. Paris.

Koelewijn, A. R., de Vries, G., van Lottum, H., Förster, U., van Beek, V. M., and Bezuijen, A. (2014). "Full-scale testing of piping prevention measures: Three tests at the IJkdijk." *Proceedings of the 8th International Conference on Physical modelling in Geotechnics (ICPMG2014)*, C. Gaudin and D. White, eds., CRC press, 891–897.

Kohno, I., Nishigaki, M., and Takeshita, Y. (1987). "Levee failure caused by seepage and preventive measures." *Natural Disaster Science*, 9(2), 55–76.

Koonce, J., Young, M., Devitt, D., Yu, Z., Wagner, A., and Fenstermaker, L. (2011). "Soil water and thermal gradients in the vadose zone: Assessing evapotranspiration, recharge rates and shifts in phreatophytic water source." *American Geophysical Union Fall Meeting 2011.*

Lam, K. S., Gill, P. W., and Zwang, L. W. A. (2013). "Implementation of new levee strength modules for continuous safety assessments." *Comprehensive Flood Risk Management - Research for Policy and Practice*, Klijn and Schweckendiek, eds., London, UK, Taylor & Francis Group.

Lane, E. W. (1934). "Security from under-seepage: Masonry dams on earth foundations." *Proceeding American Society of Civil Engineers*, 60(4), 929–966.

Laymon, C., Crosson, W., Soman, V., Jackson, T., Manu, A., and Tsegaye, T. (1998). "Multifrequency ground-based microwave remote sensing of soil moisture." *Geoscience and Remote Sensing Symposium IGARSS '98.*

Le Bars, M. and Worster, M. (2006). "Interfacial conditions between a pure fluid and a porous medium: implications for binary alloy solidification." *Journal of Fluid Mechanics*, 550, 149–173.

Levy, T. and Sanchez-Palencia, E. (1975). "On the boundary conditions for fluid flow in porous media." *International Journal of Engineering Science*, 13(11), 923940.

Lo Presti, D. C. F., Cosanti, B., Fontana, T., and Guidi, P. (2014). "Use of plastic diaphragms to improve the resistance of river embankments against hydraulic failures." *IEAG XII Congress*, Torino.

Luna Inc. (n.d.). *Distributed Temperature and Strain Measurements*, <`http://lunainc.com/obr4600ts`>. Last visited 20th July 2015.

Mansur, C. I., Postol, G., and Salley, J. R. (2000). "Performance of relief well systems along Mississippi river levees." *Journal of Geotechnical and Geoenvironmental Engineering*, 126(8), 727–738.

van der Meij, R. (2013). "Examples of data combining techniques for assessment of urban flood defences." *Comprehensive Flood Risk Management - Research for Policy and Practice*, Klijn and Schweckendiek, eds., London, UK, Taylor & Francis Group.

Mériaux, P., Monier, T., Tourment, R., Mallet, T., Lopes, S., Maurin, J., and Pinhas, M. (2012). "Monitoring of flood protection dikes: A concept still to be imagined." *Colloque CFBR 2012*, Comité Français des Barrages et Réservoirs, Le Bourget-du-Lac, France. In French.

Midttømme, K., Roaldset, E., and Aagaard, P. (1998). "Thermal conductivity of selected claystones and mudstones from England." *Clay Minerals*, 33(1), 131–145.

Molina-Gilardo, N., Bayer, P., and Blum, P. (2011). "Evaluating the influence of thermal dispersion on temperature plumes from geothermal systems using analytical solutions." *International Journal of Thermal Sciences*, 50, 1223–1231.

Mooney, M. (2014). "Mike Mooney @ Mines - Current Research, <`http://control.mines.edu/mooney/index.php?option=com_content&view=category&layout=blog&id=15&Itemid=32`>. Last visited 23rd May 2014.

Müller-Kirchenbauer, H., Rankl, M., and Schlötzer, C. (1993). "Mechanism for regressive erosion beneath dams and barrages." *Filters in Geotechnical and Hydraulic Engineering*, J. Brauns, M. Heibaum, and U. Schuler, eds., Balkema, Rotterdam, the Netherlands, 369–376.

Ng, G. and Oswalt, K. (2010). "Levee monitoring system - Better management through better information." *Engineering Systems*, April 2010, 1–12.

Nofziger, D. L. (2005). "Soil temperature changes with time and depth: Theory", <`http://soilphysics.okstate.edu/software/SoilTemperature/document.pdf`>.

Nygren, K. (2013). "Detection of sudden seepage changes in embankment dams". Bachelor's thesis, Stockholm University, Sweden.

Ochoa-Tapia, J. A. and Whitaker, S. (1995). "Momentum transfer at the boundary between a porous medium and a homogeneous fluid. I. Theoretical development." *International Journal of Heat and Mass Transfer*, 38(14), 2635–2646.

Palmieri, L. and Schenato, L. (2013). "Distributed optical fiber sensing based on Rayleigh scattering." *The Open Optics Journal*, 7, 104–127.

Peeters, P., Haelterman, K., and Visser, K. P. (2013). "About reinventing innovative technologies for levee monitoring." *ICOLD 2013 International Symposium*.

Perri, M. T., Boaga, J., Bersan, S., Cola, S., Cassiani, G., Deiana, R., Simonini, P., and Patti, S. (2014). "River embankment characterization: an integrated approach using geophysical and geotechnical techniques." *Journal of Applied Geophysics*, 110, 5–22.

Perzlmaier, S. (2007). "Verteilte filtergeschwindigkeitsmessung in staudammen." Ph.D. thesis, Munich Unversity, Germany.

Perzlmaier, S., Aufleger, M., and Dornstdter, J. (2007). "Detection of internal erosion by means of the active temperature method." *Assessment of the risk of internal erosion of water retaining structures: dams, dykes and levees: intermediate report of the European working group of ICOLD*, 193–207.

Pietrus, T. J. (1981). "An experimental investigation of hydraulic piping in sand." M.S. thesis, University of Florida, Dept. of Civil Engineering, Gainesville, FL, USA.

van der Poel, J. T. and Schenkeveld, F. M. (1998). "A preparation technique for very homogeneour sand models and CPT research." *Proceedings of the International Conference Centrifuge 98*, Kimura and Kusabe, eds., Balkema, 149–154.

Pyayt, A. L., Kozionov, A. P., Mokhov, I. I., Lang, B., Meijer, R. J., Krzhizhanovskaya, V. V., and Sloot, P. M. A. (2014). "Time-frequency methods for structural health monitoring." *Sensors*, 14(3), 5147–5173.

Quarteroni, A., Sacco, R., and Saleri, F. (2007). *Numerical Mathematics*. Springer Science and Business Media, 2nd edition.

Radzicki, K. and Bonelli, S. (2010a). "A possibility to identify piping erosion in earth hydraulic works using thermal monitoring." *Proceedings of 8th ICOLD European Club Symposium on Dam Safety*, ATCOLD Austrian National Committee on Large Dams, 618–623.

Radzicki, K. and Bonelli, S. (2010b). "Thermal seepage monitoring in the earth dams with impulse response function analysis model." *Proceedings of 8th ICOLD European Club Symposium on Dam Safety*, ATCOLD Austrian National Committee on Large Dams, 624–629.

Rau, G. C., Andersen, M. S., and Acworth, R. I. (2012). "Experimental investigation of the thermal dispersivity term and its significance in the heat transport equation for flow in sediments." *Water Resources Research*, 48(3) W03511.

Rau, G. C., Andersen, M. S., McCallum, A. M., Roshan, H., and Acworth, R. I. (2014). "Heat as a tracer to quantify water flow in near-surface sediments." *Earth-Science Reviews*, 129, 40–58.

Revil, A. and Bolève, A. (2007). "Self-potential as a detection method to evaluate fluid flow." *Assessment of the Risk of Internal Erosion of Water Retaining Structures: Dams, Dykes and Levees - Intermediate Report of the European Working Group of ICOLD*, Munich, Germany, Technical University of Munich, 167–179.

Richards, K. S. and Reddy, K. R. (2010). "True triaxial piping test apparatus for evaluation of piping potential in earth structures." *Geotechnical Testing Journal*, 33(1).

Richards, K. S. and Reddy, K. R. (2014). "Kinetic energy method for predicting initiation of backward erosion in earthen dams and levees." *Environmental & Engineering Geoscience*, 20(1), 85–97.

Rittgers, J. B., Revil, A., Planes, T., Mooney, M. A., and Koelewijn, A. R. (2015). "4-D imaging of seepage in earthen embankments with time-lapse inversion of self-potential data constrained by acoustic emissions localization." *Geophysical Journal International*, 200, 758–772.

Royet, P. (2012). "Rapid and cost-effective dike condition assessment methods: geophysics and remote sensing." *FloodProBE Project Report n. WP3-01-12-09*, Irstea.

Santamarina, J. (2012). "Thermal properties of soils." *ALERT Doctoral School 2012: Advanced Experimental Techniques in Geomechanics*, G. Viggiani, S. A. Hall, and E. Romero, eds., ALERT Geomaterials, Grenoble, FR, 261–265.

Schmertmann, J. H. (1995). "Report on flume tests for piping and scour erosion of HL-2 sands." IMC-AGRICO.

Schmertmann, J. H. (2000). "The non-filter factor of safety against piping through sands." *Judgment and innovation*, F. Silva and E. Kavazanjian, eds., Geotechnical Special Publication No. 111, American Society of Civil Engineers, Reston, VA, USA, 65–132.

Schmugge, T. (1998). "Applications of passive microwave observations of surface soil moisture." *Journal of Hydrology*, 212/213, 188–197.

Schweckendiek, T., Calle, E. O. F., and Vrouwenvelder, A. C. W. M. (2013). "Updating levee reliability with performance observations." *Comprehensive Flood Risk Management - Research for Policy and Practice*, Klijn and Schweckendiek, eds., London, UK, Taylor & Francis Group.

Selker, J., van de Giesen, N., Westhoff, M., Luxemburg, W., and Parlange, M. B. (2006a). "Fiber optics opens window on stream dynamics." *Geophysical Research Letters*, 33(24) L24401.

Selker, J. S., Thévenaz, L., Huwald, H., Mallet, A., Luxemburg, W., van de Giesen, N., Stejskal, M., Zeman, J., Westhoff, M., and Parlange, M. B. (2006b). "Distributed fiber-optic temperature sensing for hydrologic systems." *Water Resources Research*, 42(12) W12202.

Sellmeijer, J. B. (1988). "On the mechanism of piping under impervious structures." Ph.D. thesis, Technische Universiteit Delft, the Netherlands.

Sellmeijer, J. B. (2006). "Numerical computation of seepage erosion below dams (piping)." *Proceedings of the 3rd International Conference on Scour and Erosion*, CURNET, Gouda, the Netherlands, 596–601.

Sellmeijer, H., de la Cruz, J. L., van Beek, V. M., and Knoeff, H. (2011). "Fine-tuning of the backward erosion piping model through small-scale, medium-scale and IJkdijk experiments." *European Journal of Environmental and Civil Engineering*, 15(8), 1139 to 1154.

Sentenac, P., Jones, G., Zielinski, M., and Tarantino, A. (2013). "An approach for the geophysical assessment of fissuring of estuary and river flood embankments: validation against two case studies in England and Scotland." *Environmental Earth Sciences*, 69(6), 1939–1949.

Sentenac, P. and Zielinski, M. (2009). "Clay fine fissuring monitoring using miniature geo-electrical resistivity arrays." *Environmental Earth Sciences*, 59(1), 205–214.

Sheffer, M. R., Johansson, S., and Sjödahl, P. (2009). "Recent developments in the use of temperature, resistivity and self-potential methods for monitoring embankment dam performance." *CDA 2009 Annual Conference*, Canadian Dam Association, Toronto, Ontario, Canada.

Sillis, G. L. (2012). "Levee seepage (part 1)." *Levee design short course*, Floodplain Management Association. (Course material).

Silvis, F. (1991). "Verificatie piping model: proeven in de Deltagoot." *Report No. CO317710/7*, Grondmechanica Delft.

Simeoni, L., Tarantino, A., Pozzato, A., De Polo, F., and Bragagna, M. (2008). "Il progetto di un sistema di monitoraggio di un argine dell'Adige." *Rivista Italiana di Geotecnica*, 3/08, 73–94.

Simm, J., Jordan, D., Topple, A., Mokhov, I., Pyayt, A., Abdoun, T., Bennett, V., Broekhuijsen, J., and Meijer, R. (2013). "Interpreting sensor measurements in dikes experiences from UrbanFlood pilot sites." *Comprehensive Flood Risk Management - Research for Policy and Practice*, Klijn and Schweckendiek, eds., London, UK, Taylor & Francis Group.

Squeglia, N., Cosanti, B., and Lo Presti, D. C. F. (2013). "Stability analysis of the Serchio river flood plain embankments." *7th Int. Conf. on Case Histories in Geotechnical Engineering*, Paper no. 3.62a.

Steele-Dunne, S. C., Rutten, M. M., Krzeminska, D. M., Hausner, M., Tyler, S. W., Selker, J., Bogaard, T. A., and van de Giesen, N. C. (2010). "Feasibility of soil moisture estimation using passive distributed temperature sensing." *Water Resources Research*, 46(3) W03534.

Striegl, A. M. and Loheide, S. P. (2012). "Heated distributed temperature sensing for field scale soil moisture monitoring." *Ground Water*, 50(3), 340–347.

Suárez, F., Hausner, M. B., Dozier, J., Selker, J. S., and Tyler, S. W. (2011). "Heat transfer in the environment: Development and use of fiber-optic distributed temperature sensing." *Developments in Heat Transfer*, M. A. dosSantos Bernardes, ed., InTech.

Szepessy, J. (1983). "Tunnel erosion and liquefaction of granular and plastic soils in river dikes." *Vízügyi Közlemények*, 29, 23–35. In Hungarian.

Tarnawski, V. R., Momose, T., and Leong, W. H. (2011). "Thermal conductivity of standard sands. Part II. Saturated conditions." *International Journal of Thermophysics*, 32(5), 894–1005.

TAW (Technische Adviescommissie voor de Waterkeringen) (1999). *Technisch rapport zandmeevoerende wellen (Technical report on sandboils).* Delft, the Netherlands. (Draft English version, August 2002).

Terzaghi, K. (1922). "Der grundbruch an stauwerken und seine verhüting (The failure of dams by piping and its prevention)." *Die Wasserkraft*, 17(24), 445–449 . Reprinted in Terzaghi, K. (1960). From theory to practice in soil mechanics, Wiley, New York, NY, USA, 114–118.

Titov, K., Loukhmanov, V., and Potapov, A. (2000). "Monitoring of water seepage from a reservoir using resistivity and self polarization methods: case history of the Petergoph fountain water supply system." *First Break*, 18(10), 431–435.

Townsend, F. C., Bloomquist, D., Shiau, J.-M., and Martinez, R. (1988). "Analytical and experimental evaluation of piping and filter design for sands." *Report to the U.S. Bureau of Reclamation*, University of Florida, Dept. of Civil Engineering, Gainesville, FL, USA.

Trenberth, K. E., Fasullo, J. T., and Kiehl, J. (2009). "Earth's global energy budget." *Bullettin of American Meteorological Society*, 90 (3), 311–323.

Tyler, S. W., Selker, J. S., Hausner, M. B., Hatch, C. E., Torgersen, T., Thodal, C. E., and Schladow, S. G. (2009). "Environmental temperature sensing using Raman spectra DTS fiber-optic methods." *Water Resources Research*, 45(4) W00D23.

USACE (U.S. Army Corps of Engineers) (2000). *Design and construction of levees.* Manual no. 110-2-1913, Washington, DC, USA.

USACE (U.S. Army Corps of Engineers) (2005). *Design guidance for levee underseepage.* Technical letter no. 1110-2-569, Washington, DC, USA.

Vandenboer, K., Bezuijen, A., and van Beek, V. M. (2014). "3D character of backward erosion piping: Small-scale experiments." *Scour and Erosion: Proceedings of the 7th International Conference on Scour and Erosion (ICSE 2014)*, L. Cheng, S. Draper, and H. An, eds., CRC Press, 81–86.

Vogt, T., Schneider, P., Hahn-Woernle, L., and Cirpka, O. A. (2010). "Estimation of seepage rates in a losing stream by means of fibre-optic high-resolution vertical temperature proling." *Journal of Hydrology*, 380, 154–164.

de Vries, D. A. (1975). "Heat transfer in soils." *Heat and Mass Transfer In the Biosphere. Part 1*, D. A. deVries and N. H. Afghan, eds., Scripta Book Co., 5–28.

de Vries, G., ter Brake, C. K. E., de Bruijn, H., Koelewijn, A. R., Langius, E. A. F., van Lottum, H., and Zomer, W. S. (2013). *Dike monitoring: evaluation of measurement techniques and visualization systems. Final report All-In-One Sensor Validation Test.* STOWA/Stichting IJkdijk, Amersfoort. In Dutch.

Vrijling, J. K. (2010). "Piping - Realiteit of Rekenfout?". Rijkswaterstaat, Waterdienst.

Weijers, J. and Sellmeijer, J. (1993a). "A new model to deal with the piping mechanism." *Filters in geotechnical and hydraulic engineering*, 349–355.

Weijers, J. B. A. and Sellmeijer, J. B. (1993b). "A new model to deal with the piping mechanism." *Filters in geotechnical and hydraulic engineering*, J. Brauns, U. Schuler, and M. Heibaum, eds., Balkema, Rotterdam, the Netherlands, 349–355.

WES (U.S. Army Corps of Engineers Waterways Experiment Station) (1956). *Investigation of underseepage and its control. Lower Mississippi river levees.* Technical memorandum no. TM-3-424, Vicksburg, MS, USA.

Westhoff, M. C., Savenije, H. H. G., Luxemburg, W. M. J. ., Stelling, G. S., van de Giesen, N. C., Selker, J. S., Pfister, L., and Uhlenbrook, S. (2007). "A distributed stream temperature model using high resolution temperature observations." *Hydrology and Earth System Sciences*, 11(4), 1469–1480.

Wilhelm, T. (2000). "Piping in saturated granular media." Ph.D. thesis, Leopold-Franzens-Universität Innsbruck, Austria.

de Wit, J. M., Sellmeijer, J. B., and Penning, A. (1981). "Laboratory testing on piping." *Proceedings of the Tenth International Conference on Soil Mechanics and Foundation Engineering*, Rotterdam, the Netherlands, Balkema, 517–520.

Witte, H. J. L., van Gelder, G. J., and Spitler, J. D. (2002). "In situ measurement of ground thermal conductivity: a Dutch perspective." *ASHRAE Transactions*, 108(1), 263–272.

Woodside, W. and Messmer, J. H. (1961). "Thermal conductivity of porous media. I. Unconsolidated sands." *Journal of Applied Geophysics*, 32, 1688–1699.

Wu, J. and Nofziger, D. L. (1999). "Incorporating temperature effects on pesticide degradation into a management model." *Journal of Environmental Quality*, 28, 92–100.

Zienkiewicz, O., Taylor, R., and Nithiarasu, P. (2005). *The finite element method for fluid dynamics*. Elsevier, 6th ed. edition.